A Numerical and Observational Study of the Genesis of Concentric Eyewall Hurricanes

by

Shangyao Nong

M.S., Nanjing University (1993)

Submitted to the Department of Earth, Atmospheric and Planetary Sciences
in partial fulfillment of the requirements for the degree of

Doctor of Philosophy

at the

MASSACHUSETTS INSTITUTE OF TECHNOLOGY

September 1999

Author .....
Department of Earth, Atmospheric and Planetary Sciences
August 13, 1999

Certified by .....
Kerry Emanuel
Professor
Thesis Supervisor

Accepted by .....
Ronald G. Prinn
Chairman, Department Committee on Graduate Students

A Numerical and Observational Study of the Genesis of Concentric Eyewall Hurricanes

by

Shangyao Nong

Submitted to the Department of Earth, Atmospheric and Planetary Sciences
on August 13, 1999, in partial fulfillment of the
requirements for the degree of
Doctor of Philosophy

Abstract

This work attempts to understand the dynamics of the genesis of concentric eyewall hurricanes. More specifically, we focus on the effects of external eddy forcing associated with upper-level wave asymmetries in the environment of tropical cyclones, and through what processes these effects can be achieved. Our approach is a combination of numerical modeling and observational case studies. We have made use of two numerical models, namely a simple two-layer model and a two-dimensional cloud resolving non-hydrostatic model. The latter is called the full physics model for short. Owing to the lack of direct measurements of upper-level atmospheric conditions, we choose to use reanalysis data from National Centers for Environmental Prediction (NCEP) and National Center for Atmospheric Research (NCAR) and European Center for Mdeium-Range Weather Forecasts (ECMWF). A somewhat lengthy evaluation suggests that both datasets are marginally suitable for case studies of tropical cyclones.

Our major conclusions are as follows:

- Numerical simulations from the simple and full physics models suggest that the genesis of concentric eyewall hurricane results from finite-amplitude wind-induced surface heat exchange (WISHE) instability of the tropical atmosphere.

- The results from the full physics model suggest that the role of the eddy forcing is like the catalyst in a chemical reaction. The forcing helps manifest internal finite-amplitude instabilities which themselves are driven by surface enthalpy fluxes.

- The results from our extensive case studies suggest that a causal relationship does not always exist between environmental forcing and genesis of a secondary eyewall. Some cases, for example, Hurricane Allen of 1980, Hurricane Elena of 1985 and Hurricane Opal of 1995, show a good and clear relationship between their eyewall replacement cycles and their external forcings. Some cases, for example, Hurricane Gilbert of 1998 and Hurricane Andrew of 1992, show some

degree of causal relationship. Some cases, for example, Hurricane Emily of 1993 and Hurricane Gabrielle of 1989, show a weak or close to no causal relationship.

- With the results of Hurricane Frederic of 1979 and results from concentric eyewall hurricanes, we can conclude that the interaction between a tropical cyclone and its upper-level synoptic environment is neither sufficient nor necessary for the genesis and development of concentric eyewall cycles in reality.

- The maps of isentropic potential vorticity (PV) only provide qualitative information on the occurrence of the interaction. The strength of the interaction should be determined quantitatively by the eddy PV fluxes which should be calculated in a storm-moving coordinate system.

The discrepancy between the numerical results and the case studies' results leads us to hypothesis two mechanisms of the genesis. One is the interaction between a hurricane and the ocean underneath. The other is the tilting of high PV inner core with the storm and followed up projection of cyclonic vorticity down to the ocean surface.

Thesis Supervisor: Kerry Emanuel
Title: Professor

Acknowledgments

I would like to express heartful thank to my thesis advisor Prof. Emanuel, for his stimulating guidance and construtive criticism for my research work in the past five years.

I extend my sincere thanks to my thesis committee members, Prof. Chang, Prof. Plumb, and Prof. Newell, for reading my thesis in such a short time and offering me good comments.

I thank Vincent Larson carefully proofread and gave comments on this thesis. I would also thank my officemates for their moral support during the writing of this thesis.

I thank Marja Bister and Francoise Robe for their kindly support in my early stay at MIT. Thanks should also go to Linda Meinke who shares her tape drive with me and solve all kinds of computer problem.

At the end, I would also like to thank my family that puts up with me during my entire thesis writing.

Contents

List of Figures

List of Tables

Chapter 1

Introduction

1.1 Concentric Eyewall Hurricanes

The tropical cyclone has been one of the unresolved puzzles in fluid dynamics for decades. This is because its dynamics is characterized by interacting physical processes and multi-scale motions. To see through the complexity of the tropical cyclone, one has to know well almost all the subjects in atmospheric science. A few of the subjects include cloud physics, general circulation of the tropics, air-sea interaction, and radiative processes.

Fig. 1.1 is a schematic illustration of radar reflectivity in a northern hemisphere tropical cyclone with 50-60 m/s maximum wind. The echoes show two remarkable sets of features: concentric rings around the eye and open spiral rainbands. Within these entities individual echoes reach intensities of 32 to 45 dBZ, owing to active convection. Subsidence is normally present in echo-free areas such as the eye. Near the surface each convective ring has its own tangential wind maximum. Fig. 1.2 illustrates the vertical cross-section corresponding to Fig. 1.1. We can see each convective ring also has its own secondary circulation. This pattern of inner and outer convective rings is generally referred to as concentric eyewalls. At the time shown in Figs. 1.1 and 1.2, the inner eyewall is stronger than the outer one.

Observational studies (Willoughby et al., 1982; Willoughby, 1990; Black and Willoughby, 1992; Burpee et al., 1994) have shown that hurricanes with concen-

tric eyewalls often undergo characteristic cycles in which the outer eyewall contracts and intensifies, while the inner one weakens and dissipates. Typically about 10 to 24 hours later, the outer eyewall replaces the inner one at a larger radius, and becomes a new primary eyewall.

The eyewall replacement process coincides with changes in hurricane intensity. The appearance of the concentric eyewalls usually marks the end of intensification and the beginning of gradual weakening, i.e., the rise of the central pressure, the decrease of the maximum tangential wind, and the increase of the eyewall's radius. After the eyewall succession, hurricanes may resume intensification if they remain under favorable condition for development, e.g., no encounter with any surface obstacle or cold water.

To have a concrete idea what a concentric eyewall hurricane is, let us look at two famous hurricanes, Hurricane Gilbert of 1988 and Hurricane Allen of 1980. Both are Category 5 hurricanes.

Gilbert had one eyewall replacement cycle recorded by research aircraft during its life time. It had the record lowest minimum sea level pressure (MSLP), 888 hPa, in the Atlantic basin. Gilbert developed from a westward-moving tropical wave near the African coast on 3 September. It traversed the Caribbean, the Yucatan Peninsula and the southern Gulf of Mexico before final landfall in northeast Mexico. Fig. 1.3 shows the track of Gilbert for 11-17 September. Fig. 1.4 shows the changes in the tangential wind recorded in five of the six WP-3D flights[1] into Hurricane Gilbert for 1988 from 11 to 16 September (a), and time series of MSLP and radii of the inner and outer eyewalls (b). Fig. 1.5 shows time composites of the horizontal distribution of radar reflectivity.

Gilbert attained hurricane intensity in the Caribbean late on 10 September 1988 (Lawrence and Gross 1989). At 2152 UTC 13 September, Gilbert reached its maximum intensity. Fig.1.5a shows that the eyewall was a closed ring of intense convection ($> 36dBz$) encircling an echo-free eye of only 7km in radius. At radii larger than

[1]The flight levels are 700hPa on 11 and 14 September, 3km on 13 September, and 850hPa on 15 and 16 September.

70km, there are two higher reflectivity rainbands that later formed Gilbert's outer eyewall. After about eleven hours, these two spiral rainbands wrapped up and formed an outer eyewall about 100km from the center (Fig. 1.5b). A local tangential wind maximum accompanied the formation and development of the outer eyewall, and it moved inward gradually (Fig. 1.4a). During this process, there was an increase of MSLP (Fig. 1.4b) and a decrease of maximum tangential wind as shown in Fig. 1.4a. After the replacement of the inner eyewall by the outer one, Gilbert intensified again on late September 15 (Fig. 1.4a). However, it did not become as strong as it had been on September 13 because it made landfall at 2300 UTC 16 September.

Making landfall shortly after the eyewall replacement is one of the reasons we rarely see a full reintensification. Another reason is that even if a concentric eyewall hurricane intensifies again over the ocean, it is still difficult to obtain data showing a new cycle of intensification, simply because observing a concentric eyewall hurricane over an open sea is not an easy task. One has to differentiate persistent wind maxima controling the vortex development from transient asymmetric features induced by single convective cells now and then. To monitor the evolution and propagation of convective rings, one needs to pay careful attention to temporal and spatial continuity as well as comparison with radar reflectivity data.

To the best of our knowledge, only Allen regained its original intensity after its first eyewall succession (Willoughby et al., 1982). This is because it was over sea at that time. As shown in Fig. 1.6, there are three separate concentric eyewall periods in which the central pressure fell by more than 50mb, with interspersed periods of weakening.

After a very thorough and careful search, we have found the following concentric eyewall hurricanes in the Atlantic Basin documented in the literature. These hurricanes are:

1996: Bertha (3), Edouard (4), Fran (3), Hortense (4);

1995: Felix (4), Luis (4), Marilyn (3), Opal (4);

1993: Emily (3);

1992: Andrew (5);

1991: Claudette (4);

1990: Gustav (3),

1989: Gabrielle (4), Hugo (1989);

1988: Gilbert (5);

1985: Elena (3), Gloria (4);

1984: Diana (4);

1983: Alicia (3);

1980: Allen (5);

1979: David (5);

1978: Ella (4);

1977: Anita (5);

1969: Debbie (3);

1967: Beulah (5);

1961: Carla (5);

1960: Donna (5).

The number in the parenthesis is the Saffir-Simpson scale which classifies the strength of a tropical cyclone in terms of its minimum central pressure and its maximum tangential wind. A hurricane with a category number larger or equal to 3 is usually regraded as a major hurricane.

Even though the above concentric eyewall hurricanes are major hurricanes, this does not mean that only intense hurricanes have concentric eyewall cycles. The above list just states that in the hurricanes listed, at least one eyewall replacement cycle has been observed. There is no bias toward intense hurricanes. If there is a bias, it is that more attention is paid to major hurricanes than to weak hurricanes.

Tropical cyclones with concentric eyewalls also have been observed in other ocean basins. For example, Typhoon Sarah of 1956 (Fortner, 1958) and Typhoon Gloria of 1974 (Holliday, 1977) were observed to have concentric eyewall cycles over the Northwest Pacific ocean.

1.2 Motivation

From the above description of concentric eyewall hurricanes, we already know that intensity change is one of major characteristics of the eyewall replacement process. As a matter of fact, previous observational studies of tropical cyclones (Shapiro and Willoughby, 1982; Willoughby et.al., 1982, 1984; Willoughby, 1988) have shown that a large fraction of intensity changes are preceded by changes in eyewall radius or by formation of a secondary wind maximum outside the original eyewall. For example, Hurricane Andrew of 1992 almost regained its original peak intensity after an eyewall replacement cycle. It was speculated that the destructiveness of Andrew was related to the eyewall replacement (Willoughby and Black, 1996). On the other hand, according to Emanuel et al. (1995a), present forecast skill of hurricane intensity change is poor except after landfall of hurricanes. Therefore, understanding initial formation and the following development of outer eyewall should shed light on the intensity change associated with concentric eyewall cycles.

Though there exist no complete theories to explain the genesis and the successive evolution of the outer convective ring, two observational studies by Molinari and his colleagues (1989, 1990, 1992, 1995) suggested that the interaction between a tropical cyclone and an upper-level mid-latitude trough or a sub-tropical low played an important role in the intensity changes of Hurricane Elena of 1985 and Hurricane Allen of 1980. And it has been known and accepted in varying degrees that the initial intensification of a tropical cyclone usually occurrs after the presence of an upper-level trough to the northwest of the cyclone. Thus understanding the interaction between a hurricane and its upper level synoptic environment may help us gain insight into the hurricane intensity change due to eyewall replacement cycles. If this interaction proves important, forecasters might benefit from looking for an upper level signal prior to the appearance of secondary eyewalls.

In summary, the motivation for this thesis includes:

- Understanding the genesis of concentric eyewall hurricanes;
- Understanding intensity changes associated with the eyewall replacement cycles;

- Understanding the interaction between a hurricane and its environment at upper levels;

- Determining an upper level precursor for the formation of secondary eyewalls, e.g., time variation of the eddy potential vorticity flux. If there exists such precursor, then by what physical processes does the upper-level interaction lead to the formation of a secondary eyewall? And to what extent is the genesis due to the interaction rather than associated solely with internal processes of the storm?

1.3 Brief Review of Previous Work

Several mechanisms have been suggested for concentric eyewall formation. Here we will briefly review five of them. These mechanisms are:

1. Rainband theory (Willoughby et al.1982)

2. Downdraft theory (Willoughby et al.1982)

3. Symmetric instability (Willoughby et al.1982)

4. Genesis as a result of ice microphysics (Willoughby et al.,,1984, Lord et al.,,1985, Craig, 1996)

5. Topographic forcing (Hawkins, 1983)

The first mechanism was originally proposed by Willoughby (1979) to explain the formation of hurricane rainbands. The essence of the mechanism is that resonantly excited, radially propagating, asymmetric waves produce a convergence of the eddy momentum flux into their source region, and the convergence forces a radial outflow on the inward side of the wave source and thereby forms a saddle in the wind profile. Since a secondary eyewall usually evolves from inner spiral rainbands, it is straightforward to use a theory of hurricane rainbands to investigate the genesis of a secondary eyewall.

After analyzing aircraft flight-level data from 787 radial legs in 20 hurricanes from 1977 to 1989, Samsury and Zipser (1995) found that many rainbands were without wind maxima, while a secondary horizontal wind maximum (SHWM) was frequently associated with a mesoscale rainband. They also discovered that the kinematic structure of the composite SHWM is essentially the same as that associated with the primary eyewall, e.g., radial convergence occurrs near the radius of maximum wind (RMV), the preferred location of updrafts is just inside the RMV, and upward mass transport maxima are on the inward side of the RMV. Their results imply that a rainband can be formed in various ways, but the probability for the rainband to have a SHWM is small. Thus a rainband associated with a SHWM is already similar to an eyewall, so that it has a better chance of developing into a secondary eyewall if other conditions favorable for further development also exist, such as a sufficiently moist mid-troposphere and a persistent supply of energy from the surface heat fluxes. But a rainband without SHWM has little chance to evolve into a secondary eyewall since the definition of concentric eyewalls requires the coexistence of rainband and surface wind maximum. In conclusion, Samsury and Zipser's study suggests that a SHWM is a necessary condition for the genesis of a secondary eyewall.

In the second proposed mechanism, the downdraft theory, the negative buoyancy due to the evaporation of the precipitation falling from the overhanging cumulus anvil of the inner eye forces a downdraft surrounding the eye. Descent of low momentum air and low-level radial outflow induces a saddle in the wind profile. The pitfall of this mechanism is that downdrafts are always present, but no one can claim that every hurricane has eyewall replacement cycles. Therefore, the role of downdrafts in the genesis of a secondary eyewall requires more careful theoretical and observational studies.

In the third mechanism, symmetric instability arises from the small absolute vorticity and strong vertical shear at the base of the upper-tropospheric outflow layer. The discriminant for dry symmetric instability (Emanuel,1979) is

$$\sigma = (\frac{\partial v}{\partial r} + \frac{v}{r} + f)(\frac{2v}{r} + f) \times \frac{g}{\bar{\theta_v}}[\frac{\partial}{\partial z}(\theta_v + \bar{\theta_v})] - [(\frac{2v}{r} + f)\frac{\partial v}{\partial z}]^2. \qquad (1.1)$$

When $\sigma < 0$, the Eliassen's balance vortex equation (Eliassen, 1951) becomes a hyperbolic equation. Instability manifests itself as a ring of overturning air surrounding the center, and air is entrained into the outflow stream from the inertially stable lower troposphere where angular momentum is high. The overturning should increase relative vorticity and decrease the vertical wind shear, and thus remove the symmetric instability. When the effect of moisture is taken into account, the instability can occur even though σ has a positive value (Bennets and Hoskins, 1979). The reason is that the effective static stability can become small in moist atmospheres. In other words, dry symmetric instability occurrs when the Ertel potential vorticity becomes negative, while moist (conditional) symmetric instability occurrs when the saturated wet bulb potential vorticity (using wet-bulb potential temperature rather than usual potential temperature) is negative. However, observational studies (Riehl, 1979, Molinari and Vollaro, 1990) found that negative absolute vorticity rarely occurrs in the outflow layer. This is why we observe stable outflow. Therefore, the role of symmetric instability also requires further study.

The fourth mechanism was proposed by Willoughby et al.(1984), Lord et al.(1985), and Craig (1996) to explain their numerical results. They claimed that concentric eyewall cycles are more common with ice processes than with liquid water processes only. In the paper by Willoughby et al., microphysical processes are parameterized with the bulk method of Lin et al. (1983) and Orville and Kopp (1977). There are a total of 24 processes for six water variables in this complicated scheme. The microphysics scheme used by Craig is a Kessler-type warm rain scheme with a single additional variable for ice. Detailed results, however, are not available in either paper. Fig. 1.7 is the radius vs. time plot of vertical velocity at 4.6km of the numerical experiment I7A in 1984 Willoughby et al.'s paper (Lord et al. 1984). Several inward propagating rainbands can be seen in this figure. Due to the short time range of the figure, it is not certain that the primary eyewall had actually been replaced at a later time. So the claim made by Willoughby et al. and Lord et al. is suspect. Craig used concentric eyewall replacement events to explain the long timescale (30-40 hours) variability found in the time evolutions of maximum azimuthal wind and

minimum central pressure in his numerical experiment (Fig. 1 in Craig's paper). Again, detailed results and discussion are not presented in his paper. The problem for this mechanism is the same as that of the downdraft theory. Ice processes are ubiquitous but concentric eyewall cycles are not.

The last mechanism, topographic forcing, was proposed by Hawkins (1983) to explain some concentric eyewall hurricanes that formed outer eyewalls near shore. This, however, may reflect a bias toward landfalling storms because more data were collected during reconnaissance of hurricanes that threatened shore.

In conclusion, five mechanisms for the origin of a secondary eyewall have been reviewed briefly. Each one has its own strength as well as its own weakness. None of them successfully explains the genesis of the secondary eyewalls. Four of them tend to focus on the evolving characteristics of a cyclone vortex. The last mechanism tries to use the external forcing, i.e., topography, to explain the initiation of an outer eyewall.

At the end, we would like to point out that diverse mechanisms for origin are by no means mutually exclusive. For example, a given SHWM will cause an anomalous surface heat fluxes and thus reinforce the convective rainband. Because of their slow fall speed, frozen hydrometers could radially spread out in the outflow layer. More evaporation could happen, and a relatively large horizontal area could then be moistened. If the atmosphere becomes moist enough, downdrafts could no longer deplete the surface layer entropy. So surface heat fluxes could more efficiently raise the boundary layer entropy and thus the temperature of the free atmosphere aloft. The amplification of SHWM could now occur. This positive feedback process is essentially the wind-induced surface heat exchange (or WISHE) mechanism of Emanuel (1989, hereafter E89, 1993) and Emanuel et al. (1994). However, whether such a positive feedback could be realized in models as well as in nature depends on the initial strength of the SHWM.

1.4 Hypothesis and Some Supporting Evidence

1.4.1 Hypothesis

The hypothesis under examination in this thesis is that an upper tropospheric and low stratospheric environmental forcing, e.g., an upper tropospheric trough, induces the initial surface wind disturbance through interaction with the extant hurricane. When the disturbance becomes strong enough, and the environmental conditions are still favorable for the further development, e.g., weak vertical shear of horizontal wind, it triggers the formation of a secondary eyewall and the surface circulation amplifies through the WISHE mechanism of Emanuel.

1.4.2 Observational Evidence for the Hypothesis

The arguments presented in the Section 1.3, especially the observational findings from Samsury and Zipser (1995), suggest that it is undoubtedly important to have a sufficiently strong SHWM initially. The question is what processes might lead to the formation of such a perturbation. An environmental transient forcing might play a critical role in producing the perturbation, as in the case of tropical cyclogenesis. Recall that one of motivations of this study is to understand the role of the synoptic environment in the upper troposphere and lower stratosphere in the genesis of concentric eyewall hurricanes.

Several terminologies have to be defined before further discussion. The term "environmental forcing", as suggested by Molinari and Vollaro (1989), refers to the exchange of energy and angular momentum between a tropical cyclone and azimuthally asymmetric features in its environment. Origins of the features are in general independent of the existence of the tropical cyclone. A good example is a mid-latitude trough extending into the tropical area. In this thesis, two other terms, external forcing and eddy forcing, have the same meaning as environmental forcing.

The exchange of angular momentum, as originally proposed by Pfeffer (1958), is quantified by calculating angular momentum transport due to azimuthal eddies

in a storm-centered coordinate system. This coordinate system is often used in observational studies. The term "momentum" is defined as the scalar relative angular momentum around a vertical axis at the center of the moving storm. It is expressed as rv , where v is the storm relative tangential wind and r the radius. Since the inertial stability in the outflow layer is generally lowest, the greatest potential for interaction often occurrs there, as pointed out by Holland and Merrill (1984). In other words, it is easy to move an air parcel horizontally in a low-inertia environment

Consistent with our definition of the environmental forcing, the atmosphere and upper ocean will be considered together to make up the hurricane system, so that surface interactions and sea surface temperature effects will be regarded as internal to the hurricane system.

Two points should be kept in mind here. The first point is that in reality, the exchange of energy and angular momentum most likely represents a mutual interaction rather than a forcing and a response. In fact, the eddy fluxes must be interpreted as arising from an interaction between a tropical cyclone and its environment, and not as a simple forcing in one direction or the other. The second point is that the definition of environmental forcing certainly contains some ambiguity. No distinct boundary exists between the cyclone and its surroundings in nature. The term is used for convenience of narration.

In the following paragraphs, we will review effects of the environmental forcing on initial development of a tropical cyclone. The review ultimately leads us to consider the possible connection between the forcing and the genesis of concentric eyewall hurricanes.

A number of observational studies have shown that rapid intensification of an initially weak tropical cyclone often occurrs when an upper-level trough approaches the cyclone (e.g., Sadler, 1976, Gray, 1979, and Merrill, 1988a). Miller (1958) suggested that the presence of a trough to the northwest of a tropical cyclone allows well-defined anticyclonic outflow channels to be maintained, presumably providing an upper-level mass sink and momentum sources for the storm.

Pfeffer and Challa (1981) used a balanced, axisymmetric numerical model to con-

duct a series of experiments in which they introduced McBride and Zehr's (1981) observed eddy momentum fluxes. The eddy fluxes are shown in Fig. 1.8. Their results indicate that the composite developing storm forced by its associated organized eddy momentum fluxes (Fig. 1.8a) rapidly intensified to hurricane strength, while the composite non-developing storm with its weak and diffuse eddy fluxes (Fig. 1.8b) did not intensify even for a long time integration. Most significantly, without the eddy forcing, the prehurricane developing vortex failed to intensify into a hurricane. The same conclusion was reached by Challa and Pfeffer (1990), using the three-dimensional Naval Research Laboratory limited-area hurricane model.

The working mechanism envisioned by them is: the large-scale eddy momentum flux convergence exerts a cyclonic stress ($(\frac{\partial v}{\partial t})_{eddy} = \frac{1}{r^2}\frac{\partial}{\partial r}(-r^2\overline{u'v'})$, where the overbar represents the azimuthal mean, and the prime represents the eddy component) in the upper troposphere and lower stratosphere. This stress breaks the balance among the Coriolis, pressure gradient and centrifugal forces, thereby generating upper level outflow, tropospheric upwelling and lower level inflow over a broad area. The inflow in the planetary boundary layer brings air inward over a broad stretch of warm ocean where it picks up moisture and concentrates it into a central region. This organizes the convection and the release of latent heat, which intensifies the storm into a hurricane. Challa and Pfeffer also emphasized that only after the sea level circulation attains sufficient intensity does the CISK mechanism come into play. Similar physical arguments were offered by Holland and Merrill (1984) based on the calculation of balance vortex responses to idealized momentum and heat sources.

Potential vorticity (PV) analysis has been widely used in understanding conceptually the dynamics of midlatitude synoptic-scale weather system, and has proven productive. Its use is getting more widely appreciated in tropical systems (Thorpe, 1985, Schubert and Alworth, 1987, Schubert et al., 1991, Montgomery and Farrell, 1993). Reilly and Emanuel (1991) suggested that the triggering mechanism of tropical cyclogenesis might be viewed as the superposition of two positive PV anomalies, one corresponding to a low-level initial disturbance and the other to an approaching upper tropospheric trough. Bosart and Bartlo (1992) analyzed the initial develop-

ment of Hurricane Diana of 1984 in a baroclinic environment. They found that the cyclogenesis was nearly indistinguishable from a classical mid-latitude development.

But the reality is complex. There are documented cases (Merill, 1988b) in which troughs were present in some nonintensifying tropical cyclones. Two reasons may account for the lack of intensification. The first is that when tropical cyclones move over a cold ocean surface, their intensity decreases. The second reason is that the negative influence of the increased vertical wind shear associated with the trough overwhelms the positive influence of the eddy forcing. After calculating the eddy flux convergence (EFC) of relative angular momentum at 200mb for the named tropical cyclones in 1989-1991 Atlantic hurricane seasons, DeMaria et al.(1993) confirmed the above two reasons for the nonintensification of some tropical cyclones. They also found that one third of the cases, which are thirty-two storms in total, had at least one synoptic period of EFC, and the storm intensified just after the period of enhanced EFC. It is obvious that a clear mechanism for coupling synoptic-scale forcing to the mesoscale instability represented by hurricane intensification has not been well established. This will be an interesting future research topic.

Nevertheless, the above brief review provides evidence that an external forcing at upper levels plays an important role in the initial intensification of tropical cyclones. More important, it stimulates us to speculate whether such environmental forcing can also generate a secondary eyewall, and if it can, through what physical processes. The working mechanism might be the same as described by Challa and Pfeffer (1990), except that an enhanced surface circulation occurrs around 100-300km. The enhanced surface circulation then intensifies through internal processes, or under the influence of the external forcing, or a combination of both.

The first question that arises is why the enhanced surface circulation does not appear at the center, or just further enhances the extant surface circulation associated with the primary eyewall. A possible answer is that inertial stability (defined as $(f+\frac{2\bar{v}}{r})(f+\frac{\partial\bar{v}}{\partial r}+\frac{\bar{v}}{r})$) increases when a hurricane is intensifying or has developed. Fig. 1.9 shows the inertial stability in an observed intensifying hurricane (Holland and Merrill, 1984). Note that there is a three order-of-magnitude horizontal variation in

the inertial stability from a very stable core to a much less stable outer circulation. Furthermore, the lower troposphere is quite stable out to large radii, whereas the upper troposphere is only weakly stable. Moving an air parcel horizontally is much more difficult in a stable area than in an unstable area. Therefore the influence of the external forcing is unlikely to affect the hurricane core. But the external forcing may induce a SHWM outside the primary circulation. If this SHWM is persistent and strong, it can start the WISHE instability outside the hurricane core, and a secondary eyewall can then form. This reasoning is consistent with that at the end of the last section.

Now let us look at the results of two observational studies mentioned in Chapter 1.2. Their results have shown that there is a good correlation between the development of concentric eyewalls and an increased upper-level eddy angular momentum influx.

The first case is the study of Hurricane Elena of 1985 by Molinari et al. (1989, 1990). They convincingly showed that the development of Elena's secondary eyewall correlated at 30 hours lag with an increased upper level eddy angular momentum influxes. Fig. 1.10a shows the time variation of minimum central pressure with each horizontal bar indicating the occurrence time of each secondary eyewall. None of the three fits the classic behavior described by Willoughby et al. (1982). The first was diffuse and asymmetric, and neither it nor the third one was preceded by a period of filling or slow deepening. Both occurred during Elena's rapid deepening and did not dramatically extend the period of deepening. Fig.1.10b shows six-hourly tangential wind changes during the second event. In this event, the secondary eyewall formed at or outside of 120km between 0000UTC and 1200UTC 31 August and propagated into the storm core late on the same day. Only this eyewall replacement episode affected the pressure field. Pressure fell slowly during inward propagation of the SHWM, then fell rapidly for an extended period after the SHWM reached the innermost radius. As a result, a more classical, sharpened wind profile developed for the first time in Elena.

Fig. 1.11a gives the azimuthal eddy flux convergence of tangential velocity at

200mb[2]. The eddy spin up rate exceeded 25m/s/day at the 650km radius on August 31 and remained positive subsequently as it shifted inward to the storm core. Figs. 1.11b-11d show vertical cross sections of the radial convergence of eddy flux of angular momentum and eddy heat flux on 31 August [3].

After comparing Figs. 1.10 and 1.11, we can conclude that the major storm filling event (0006UTC 31 August - 0000UTC 1 September) and the following deepening event were both preceded by an inward shift of the eddy flux convergence. The eddy fluxes of angular momentum and heat were observed to be substantial for at least 36 hours. Fig. 1.11d indicates a cooling by eddies up to 5K/day at middle and upper tropospheric levels. This is because there was a cold trough in the hurricane volume. Since the tropopause was relatively low in the mid-latitude trough, the trough represented a warm anomaly at 100mb, and up to 8K/day warming by eddy heat fluxes occurred at that level. Also note that the zero line of the heat flux in the upper troposphere generally coincided with the level of maximum eddy angular momentum flux. By using Eliassen's balanced vortex equation, they also calculated the response of the hurricane vortex to eddy fluxes of heat and angular momentum. Their balanced solutions showed that the upward motion induced by the eddy sources reached the storm core simultaneously with the development of a SHWM.

The second case is the study of Hurricane Allen of 1980. Molinari (1992) found that the first weakening/reintensification cycle occurred as Allen encountered a shallow upper tropospheric positive vorticity anomaly. Fig.1.12 clearly shows that there was an upper tropospheric positive PV anomaly to the west of Allen before the appearance of its first secondary eyewall (see Fig.1.6).

One more case is Hurricane Gloria of 1985. When they calculated the PV distribution for Gloria, Shapiro and Franklin (1995) found an upper tropospheric positive PV anomaly west of Gloria prior to the development of Gloria's SHWM. The PV

[2]data source: international rawinsonde network, and high-level satellite-derived cloud motion vectors generated operationally by the National Hurricane Center. Detailed discussions on the quality of the data can be found in Molinari et al. (1989).

[3]data source: initialized three dimensional analyses from ECMWF on a 2.5^o latitude-longitude grid on seven standard pressure levels: 1000, 850, 700, 500, 300, 200, and 100mb. Detailed discussions on the quality of the data can be found in Molinari et al. (1990).

anomaly at $\theta = 350K$ is obvious in Fig. 1.13a. The local PV maximum occurrs at r $\sim$ 100km in Fig. 1.13b corresponds to Gloria's SHWM observed by Willoughby (1990).

To conclude this section, three known concentric eyewall hurricanes had an upper level synoptic-scale precursor, i.e., mid-latitude trough, before the development of a secondary eyewall. So it is natural to ask whether there is a real causal relationship between the environmental forcing and the genesis of a secondary eyewall. We will answer this question later on in this thesis.

The organization of this thesis is as following. Chapter 2 will use numerical models to test this hypothesis. Chapter 3 will present results from an observational study. Chapter 4 will summarize this thesis.

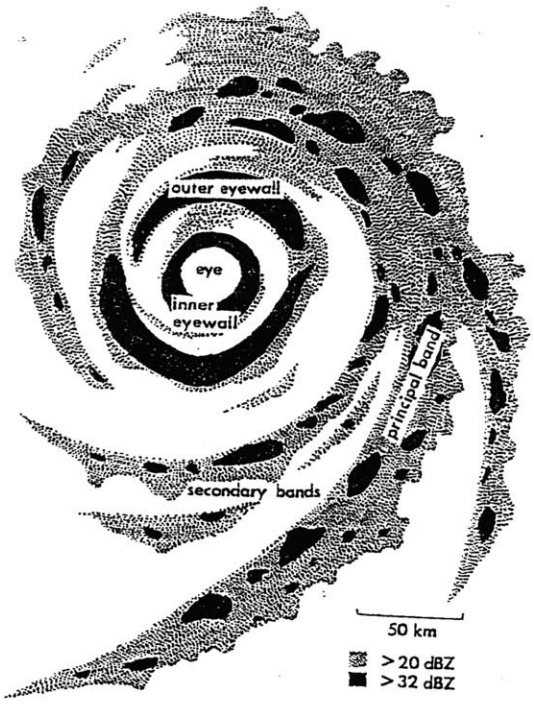

Figure 1-1: Schematic illustration of radar reflectivity in a northern hemisphere tropical cyclone with 50-60 m s^{-1} maximum wind (from Willoughby (1988)).

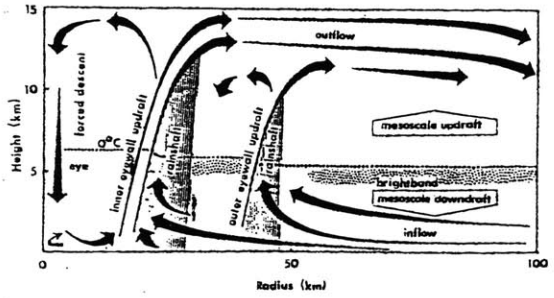

Figure 1-2: Schematic illustration of the secondary circulation and precipitation distribution for the situation shown in Fig.1 (from Willoughby (1988)).

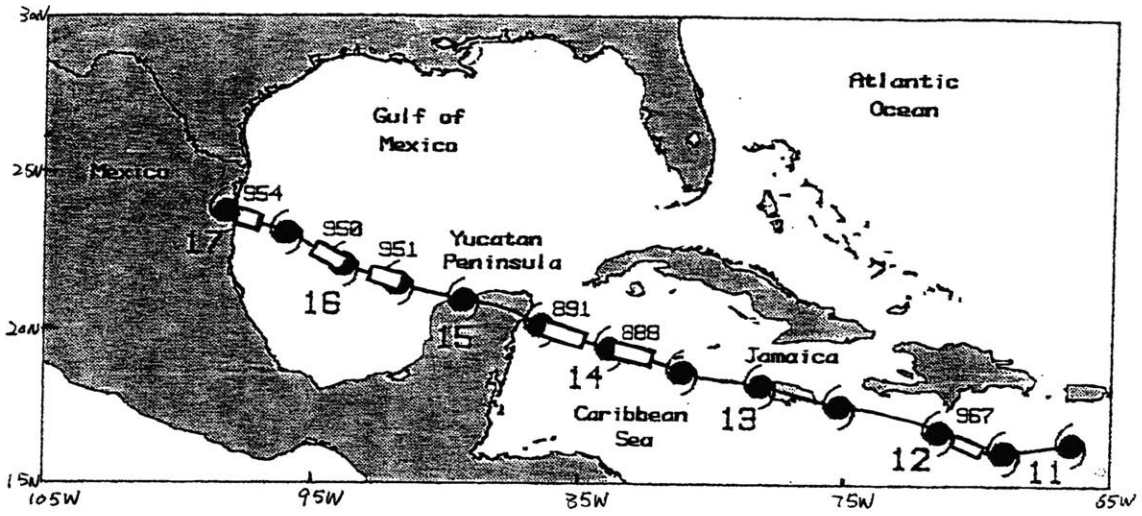

Figure 1-3: Track of Hurricane Gilbert for 11-17 September 1988. The hurricane symbols are plotted at 12-h intervals, and bold numbers indicate the date at 0000UTC each day. Rectangles along the track show the locations of the NOAA flights with the minimum sea level pressure (hPa) recorded on each flight plotted above the track (from Black and Willoughby (1992)).

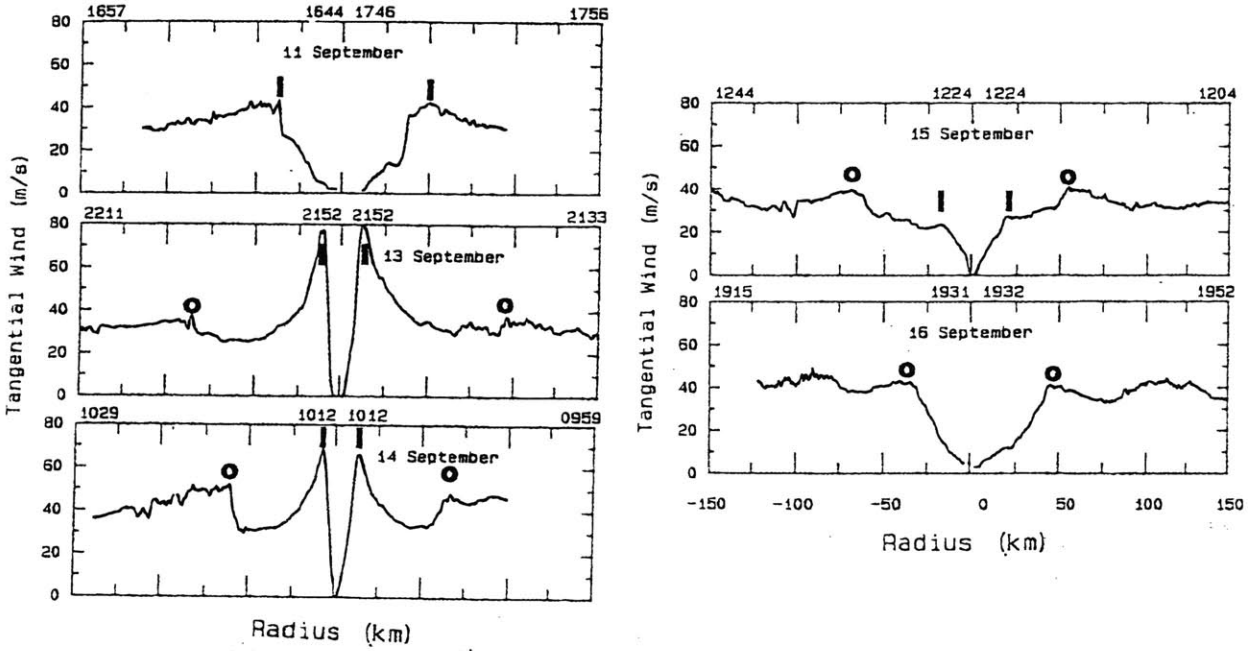

Figure 1-4: (a) Flight-level tangential wind speed from south-north traverses through the center of Hurricane Gilbert. Bold *I*'s and *O*'s denote the location of the inner- and outer-eyewall wind maxima, respectively. Times at the beginning and end of each radial pass are plotted at the top of the panels (from Black and Willoughby (1992)).

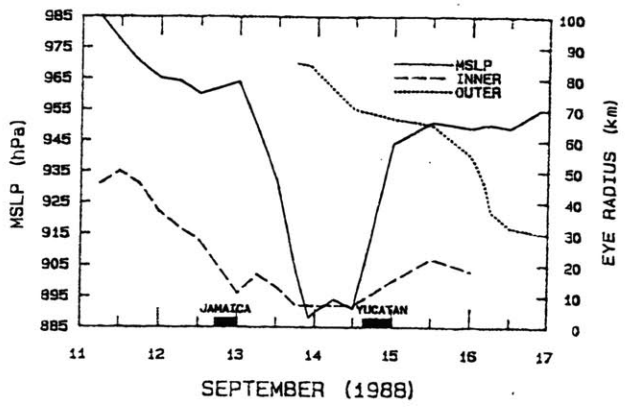

Figure 1-4: (b) Hurricane Gilbert's minimum sea level pressure and radii of the inner and outer eyewalls as a function of time, September 1988. Dates starts at 0000UTC. Solid blocks at the bottom indicate times over land (from Black and Willoughby (1992)).

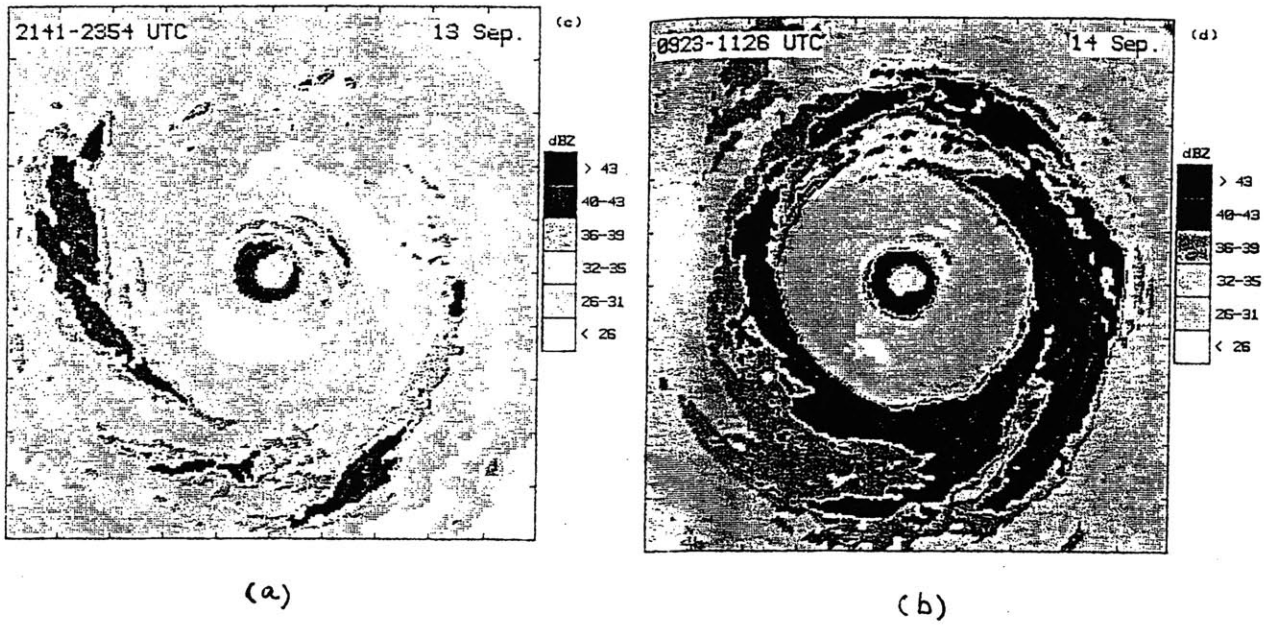

Figure 1-5: (a) time composite of the horizontal distribution of radar reflectivity on September 13 between 2141-2354 UTC (The hurricane center is in the middle of the image, north is at the top, and the domain is $240 \times 240 km^2$. Tick marks are at 24-km intervals.), (b) same as (a) but on September 14 between 0923-1126 UTC (from Black and Willoughby (1992)).

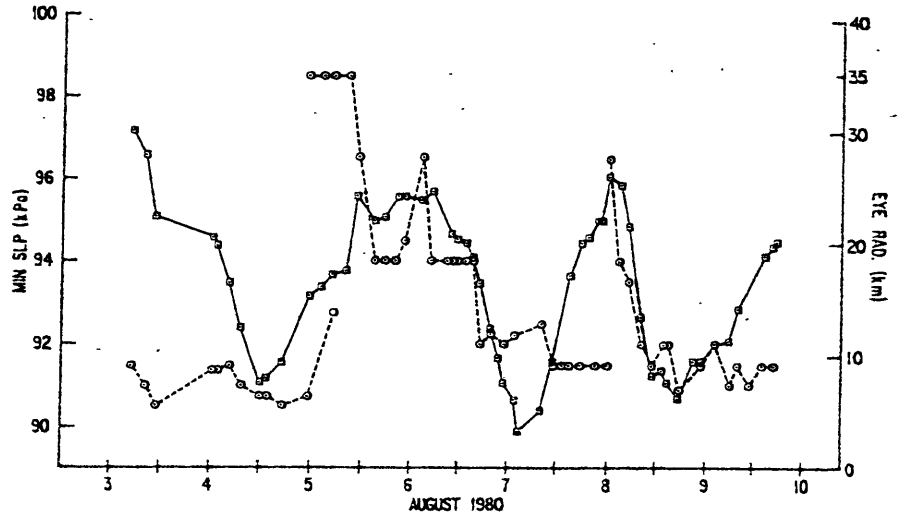

Figure 1-6: Time evolutions of central pressure (solid) and eye wall radius (dashed) in Hurricane Allen of 1980. Day numbers on the horizonal axis represent 1200 UTC (from Willoughby et al. (1982))

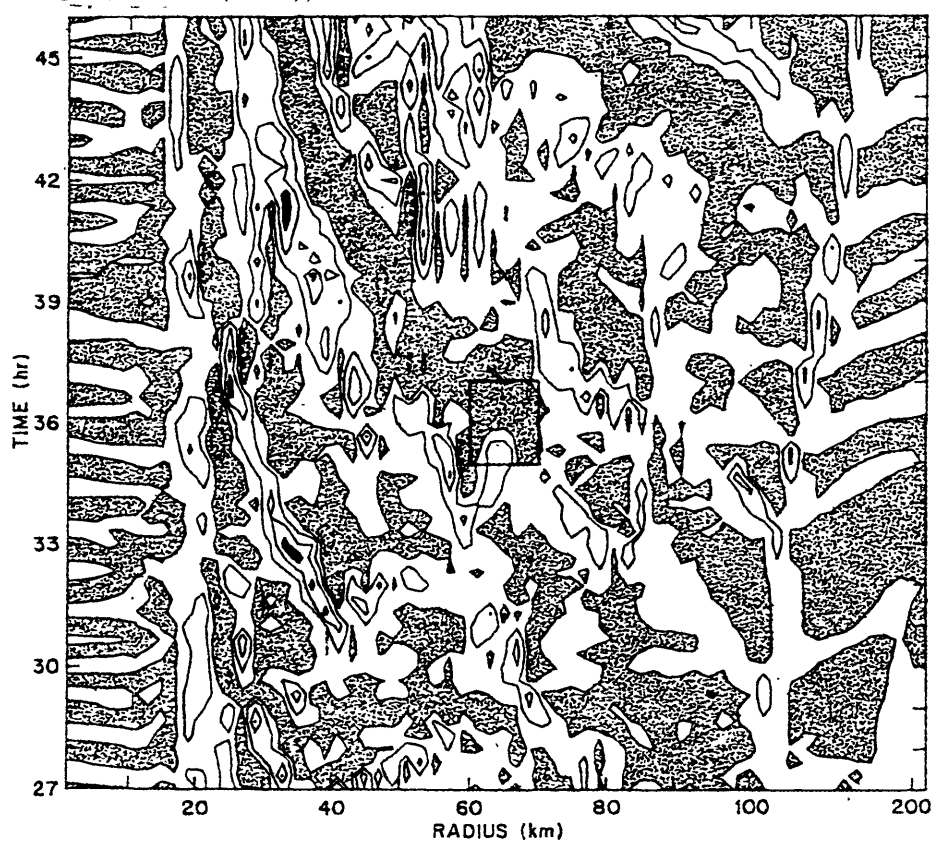

Figure 1-7: Radius via time plot of vertical velocity (m/s) at 4.6km of the numerical experiment I7A in 1984 Willoughby et al's paper. Negative area is shaded. The contour interval is not available from the original paper (from Lord et al. (1984)).

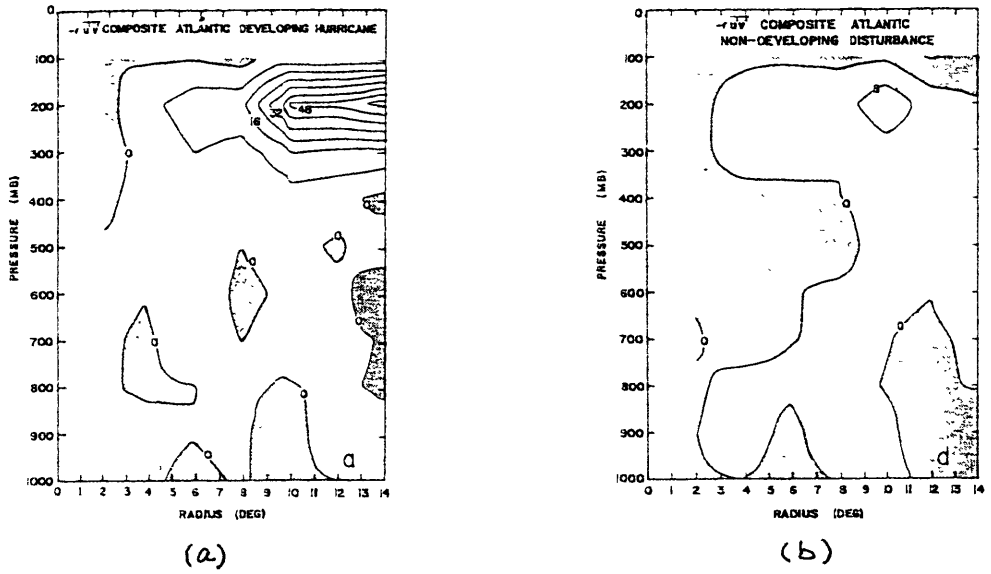

Figure 1-8: Distributions of inward eddy flux of momentum ($-\overline{ru'v'}$) for the composite developing (a) and non-developing Atlantic tropical disturbances (b). Unit is 10 deg $m^2 s^{-2}$ (from Pfeffer and Challa (1981)).

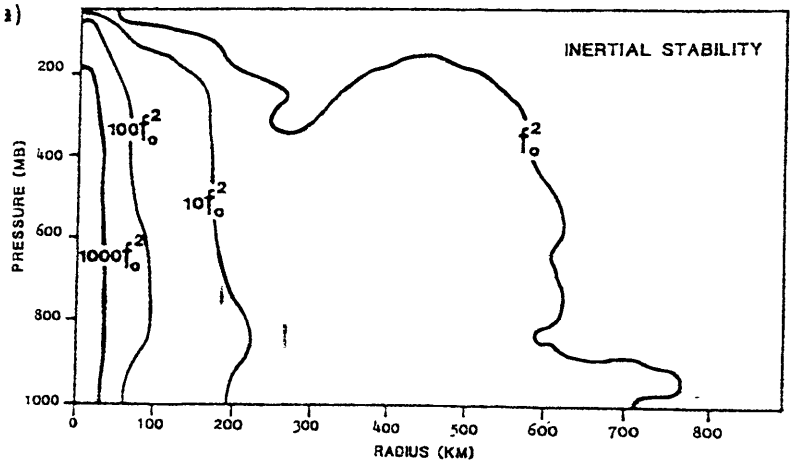

Figure 1-9: Axisymmetric vertical cross-sections of inertial stability (multiples of f^2) for the composite intensifying hurricane (from Holland and Merrill (1984)).

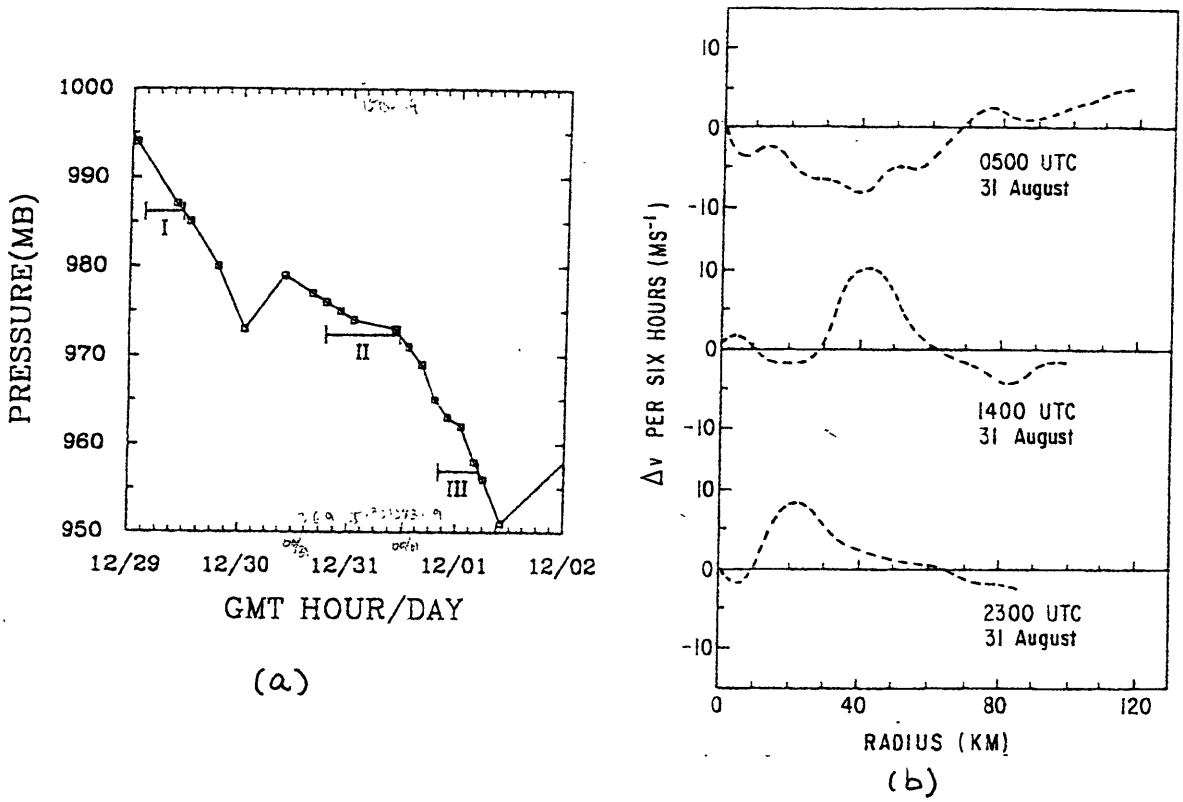

Figure 1-10: (a) Time variation of minimum central pressure in Elena with occurrences of secondary wind maxima superimposed. (b) Six-hourly changes in azimuthally averaged tangential velocity (m s^{-1}) centered on the times shown, indicating the inward shift of secondary wind maximum (from Molinari et al.(1990)).

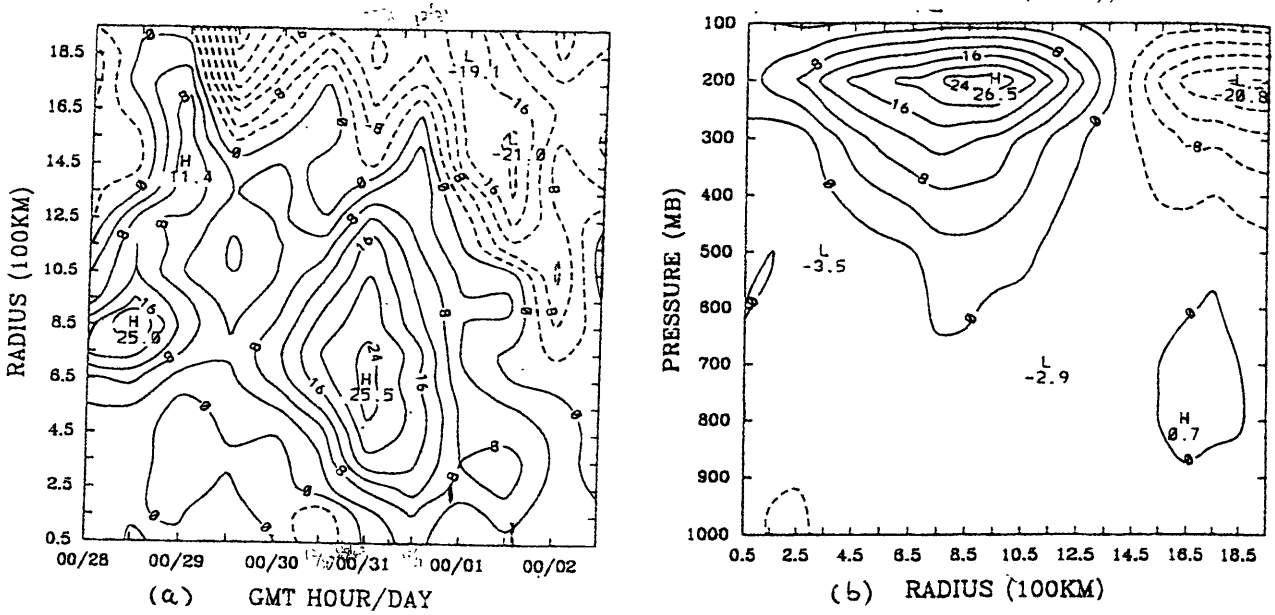

Figure 1-11: (a) Radius-time section of azimuthal eddy flux convergence of tangential velocity on 200mb. (b) Radial-vertical cross section of eddy flux convergence of relative angular momentum at 0000 UTC 31 August. Negative contours are dashed. Unit:m/s/day (from Molinari et al.(1989,1990))

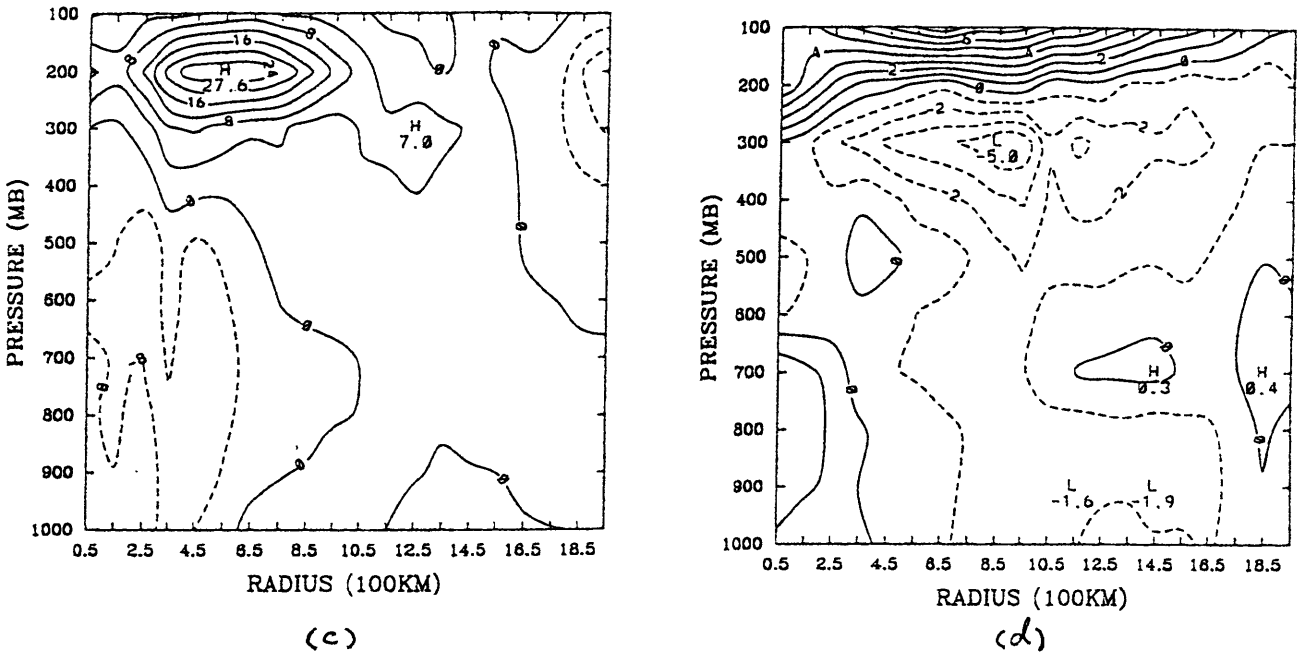

Figure 1-11: (c) same as (b) but at 1200 UTC 31 August. (d) Radial-vertical cross section of the lateral convergence of eddy flux at 1200 UTC 31 August. Unit: K/day. Negative contours are dashed (from Molinari et al.(1990)).

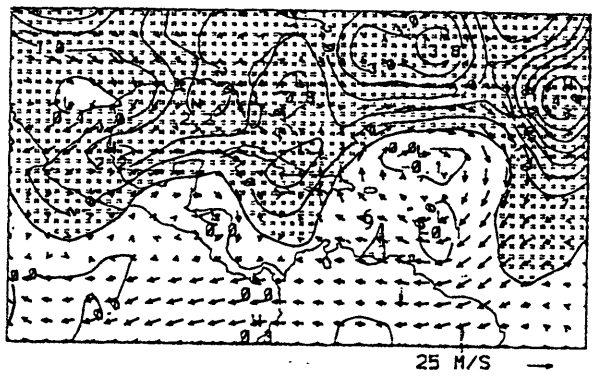

Figure 1-12: Isentropic potential vorticity at $\theta = 350K$ on 0000 UTC 5 August 1980. Hurricane Allen is shown by the hurricane symbol. Values greater than 0.5PVU are shaded (from Molinari (1992)).

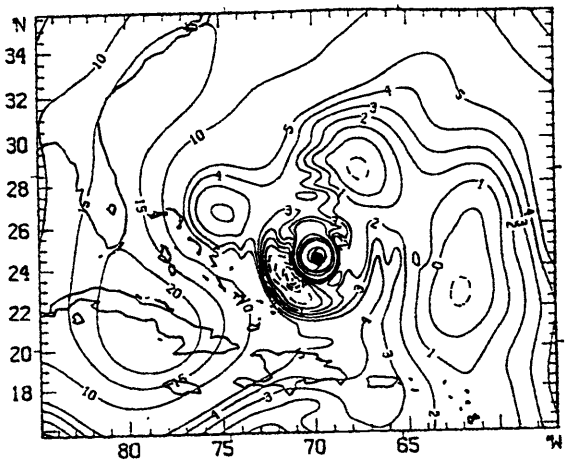

Figure 1-13: (a)Isentropic potential vorticity at $\theta = 350K$ for Gloria of 1985. Unit: 0.1 PVU (from Shapiro and Franklin (1995)).

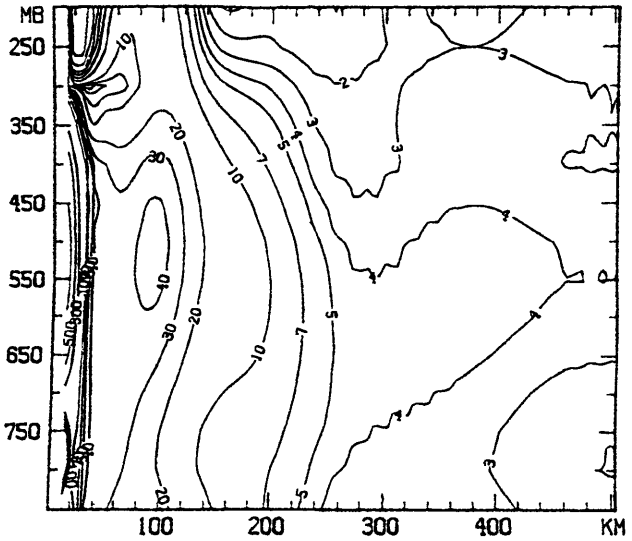

Figure 1-13: (b) Radial-height cross section of symmetric PV of Gloria of 1985. Unit: 0.1 PVU (from Shapiro and Franklin (1995))

Chapter 2

Numerical Models and Results

2.1 The Simple Model and Numerical Results

2.1.1 The Simple Model

The simple hurricane model was built and revised by Emanuel (E89, 1995b, hereafter E95b). Details of model derivations and discussions were given in both E89 and E95b. Here we will outline the model briefly.

The model structure is shown in Fig. 2.1. There are two parts in the model, a subcloud layer and the rest of the troposphere divided into two vertical levels. The subcloud layer is assumed to be in thermodynamic equilibrium. The rest of the troposphere is assumed to be in hydrostatic and gradient wind balance. The free atmosphere is also assumed to be neutral to slantwise moist convection, a condition approximated by constant saturation entropy along angular momentum surfaces above the subcloud layer.

The convective scheme in the model is based on subcloud layer entropy quasi-equilibrium. This equilibrium assumption states that in the subcloud layer, the time tendency of entropy is negligible in comparison to the surface enthalpy fluxes and input of low-entropy air into the subcloud layer by convective downdrafts; the latter two are assumed to be in equilibrium. The physical basis for this assumption has been thoroughly discussed by Raymond (1995).

Variable	Definition
χ_b (S_b), χ_m (S_m) and χ_t (S_t)	Entropies of the subcloud layer, lower troposphere and the tropopause
$\chi^*(S^*)$	Saturation entropy of the troposphere
r_b, r_i and r_t	Radii of R surfaces at the sea surface, midtroposphere and tropopause
v_b	Surface azimuthal wind
ψ_0 and ψ	Mass streamfunctions at the boundary layer top and in the midtroposphere
w_e and w_m	Clear air vertical velocity at the boundary layer top and in the midtroposphere
M_u and M_d	Convective updraft and downdraft mass fluxes at the boundary layer top

Table 2.1: Primary variables in the simple hurricane model

The model is axisymmetric with a potential radius, R, as the horizontal coordinate and pressure, P, as the vertical coordinate. R is proportional to the absolute angular momentum per unit mass surrounding the storm center:

$$\frac{f}{2}R^2 \equiv rv + \frac{f}{2}r^2. \tag{2.1}$$

where f is the Coriolis parameter (assumed constant), r the physical radius from the storm center and v the azimuthal velocity. In other words, R is the radius at which a parcel would attain zero tangential velocity if displaced radially away from the storm's center while conserving angular momentum.

The primary dynamic and thermodynamic variables in the model are listed in Table 2.1.

All the entropy variables have been replaced by a new quantity, χ, whose definition is

$$\chi \equiv (T_s - T_t)(S - S_{bi}), \tag{2.2}$$

where T_s and T_t are the surface and tropopause absolute temperatures (assumed constant), S is the entropy ($S = c_p \ln \theta_e$, where c_p is the heat capacity at constant pressure, and θ_e is moist potential temperature), and S_{bi} is the entropy of the ambient

Parameter	Name	Values
r_m	Radius of maximum wind	60km
r_0	Radius of vanishing wind	400km
V_m	Maximum azimuthal wind	15m/s
$\mathcal{H}_m$	Lower tropospheric relative humidity	60%

Table 2.2: Initial conditions of EX1

subcloud layer.

The model equations are in nondimensional form. The scalings of all the dependent and independent variables and their typical values can be found in E89 or E95b. The primary scaling in the model is χ_s, defined as

$$\chi_s \equiv (T_s - T_t)(S^*_{si} - S_{bi}), \tag{2.3}$$

where S^*_{si} is the ambient saturation entropy of the sea surface. χ_s measures the thermodynamic disequilibrium between the ocean and the atmosphere, and it controls the amplitudes of the azimuthal velocity and pressure in the model.

2.1.2 Numerical Experiments and Results

The physical parameters in our control simulation EX1 are the same as those in the control run of E95b. Table 2.2 gives the initial conditions of EX1. Experimental designs are summarized in Table 2.3.

Fig. 2.2 shows the time evolution of maximum surface azimuthal wind v_{max} and the radius of maximum wind r_{max} for the control run EX1. As we can see from the figure, the model vortex evolves into a hurricane after 8 days, and reaches a steady state after 10 days. Numerical results indicate that only one eyewall formed in the whole integration time. The fluctuation around 15 days has nothing to do with the eyewall replacement cycle. It may be caused by the activities of convective cells outside the eyewall.

[1]For reference, before adding the random perturbations, the range of the surface entropy fluxes

Experiment	Difference from the control experiment
EX1	—
EX2	$\mathcal{H}_m$ increased from 60% to 90% in the lower troposphere
EX3	same as EX2 except that surface wind at 8 days is used in the calculations of surface entropy fluxes after 8 days
EX4	same as EX1 except that Gaussian random perturbations with zero mean and standard deviation of 5[1] are added to the surface entropy fluxes at 9.4 days for one time step
EX5	same as EX4 except that the random perturbations begin at 9.5 days and last 7.5 hours.

Table 2.3: Descriptions of experiments done using the simple hurricane model

The time series of v_{max} and r_{max} from EX2 are shown in Fig. 2.3. Several significant fluctuations in the storm intensity can be seen from the figure. After checking the numerical results between 9 and 11 days, we have found a full eyewall replacement cycle. Fig. 2.4 gives the vertical cross sections of azimuthal velocity, radial velocity, and vertical velocity at 10 days. This figure indicates double surface wind maxima and double secondary circulations. The inner eyewall is around 20km from the center, and it has fully developed. The outer eyewall has just appeared and is located around 50km from the center. At this time, the inner eyewall is still dominant over the outer eyewall. With the passage of time, the outer eyewall propagates inward and replaces the inner one 12 hours later. The inward propagation of the outer eyewall can be seen from Figs. 2.4d-f. This eyewall replacement process corresponds to the intensity change seen between 9 and 11 days on Fig. 2.3. Therefore, an eyewall replacement cycle has been produced in the simple model, and the cycle resembles the observed one described in Chapter 1.1.

The explanation of the secondary eyewall genesis is as follows: when the moisture is increased in the lower troposphere, the entropy is increased too. This can be seen from Fig. 2.5 which gives the entropies of EX1 and EX2 at 10 days. If the

[1] at 9.4 days is from a maximum of 8.1 around the eyewall to a minimum of 0.01 at the outer edge of the horizontal domain.

lower tropospheric entropy is increased and can be maintained at a higher value, the precipitation-generated downdrafts at large radius as well as large-scale subsidence can no longer counter the moistening effect upon the subclound layer by surface entropy fluxes. Deep and high precipitation efficiency convection breaks out. The perturbation intensifies through the WISHE mechanism, just as in tropical cyclogenesis. In fact, numerical studies (E89, E95b, Rotunno and Emanuel, 1987, hereafter RE87) suggested that a moist lower and middle troposphere is conductive to tropical cyclogenesis.

But we should emphasize that without the WISHE mechanism, we would not have any development of concentric eyewall hurricanes in the model. To prove this, we did experiment EX3 in which the surface wind at 8 days is used to calculate the surface entropy fluxes after 8 days. The time evolution of v_{rmax} and r_{max} are shown in Fig. 2.6. No fluctuation in the intensity of the model hurricane can be seen from this figure. This is simply because the positive feedback between the surface wind and surface entropy fluxes has been artificially turned off in the model. The surface wind disturbance can not amplify by WISHE.

In order to further assess the unstable nature of the concentric eyewalls, we did two more numerical experiments in which Gaussian random perturbations were added to surface entropy fluxes. These experiments are EX4 and EX5. In experiment EX4, we started with the initial conditions of EX1, then at 9.4 days (only at this time step) we introduced random perturbations into the surface entropy fluxes and continued the integration to the end. The experimental design of EX5 is the same as that of EX4 except that the random perturbations started at 9.4 days and lasted 7.5 hours. Note that the random perturbations in EX5 changed with time. In both experiments, the variability of the random perturbations corresponded to Gaussian distributions with zero mean and standard deviation of 5.

The results from these two experiments are shown in Fig. 2.7 and Fig. 2.8. There are no concentric eyewall cycles in EX4 (Fig. 2.7), while several occur in EX5 (Fig. 2.8). A closer look at the numerical results of EX5 reveals that an eyewall replacement cycle occurs between 11.9 days and 13.1 days. More experiments were

carried out to find the critical time duration and the critical amplitude of the standard deviation of the random perturbations in order to have instability. The result is that the time duration and the standard deviation should not be less than 5.7 hours and 3.5, respectively, with the initial conditions of the control run EX1. There is no doubt that these values will depend on the initial conditions and physical parameters of the control experiment.

The results from all above experiments tell us several things. First, if the lower troposphere is not moist enough, concentric eyewalls do not arise spontaneously for certain parameter values in the simple model. Second, if we just have small anomalous surface entropy fluxes caused by small surface wind perturbations, we would not expect those fluxes to counter the drying effect of convective downdrafts and large-scale subsidence, as when tropical cyclones fail to develop. Third, the situation will change if there are finite-amplitude perturbations. As shown in EX5, when we have strong enough anomalous surface entropy fluxes, we can not only counter the cooling and drying effects due to the downdrafts and the subsidence, but also raise the subclound-layer entropy and thus the lower tropospheric entropy and saturation entropy aloft, so the occurrence of concentric eyewalls is possible.

2.1.3 Conclusions from the Simple Model

Based on the numerical experiments we have done with the simple model, we have reached the following conclusions:

1. If the lower troposphere is made moist enough, the simple model is able to produce concentric eyewall hurricane without external forcing. The concentric eyewalls in the model share the same characteristics as those in nature;

2. The WISHE mechanism is responsible for the development of secondary eyewalls in the model;

3. If the lower troposphere is not moist, the simple model needs substantial perturbations to produce concentric eyewalls. An initial finite-amplitude disturbance

is needed to trigger the concentric eyewall hurricane in the simple model. The physical rationale is that the precipitation-induced downdrafts and large-scale subsidence stabilize the outer region by depleting the subcloud-layer entropy. This effect is crucial to the development and maintenance of a tropical cyclone. However, infinitesimal perturbations will be diminished by these stabilzing effect, and only finite-amplitude perturbations can overcome this effect and then amplify.

2.2 The Full Physics Model and Numerical Results

2.2.1 The Full Physics Model

The full physics model was originally developed by Rotunno and Emanuel (RE87) and revised by Bister (1996, hereafter B96). The model is an axisymmetric, cloud resolving model with fully compressible, nonhydrostatic equations expressed in cylindrical coordinates. A detailed description of the model can be found in RE87 and B96. The main aspects of the model are highlighted here.

1. The microphysics process is a Kessler-type warm rain microphysics implemented by Bister (1996). In order to mimic ice processes, we use temperature conditions to determine the terminal velocity, v_T, of rain. When the temperature $T > 0^oC$, v_T will be the calculated value from the warm rain microphysical scheme; for $-15^oC < T < 0^oC, v_T = 1.0$m/s; for $-35^oC < T < -15^oC, v_T = 0.8$m/s; for $T < -35^oC, v_T = 0.2$m/s. So when the temperature is less than 0^oC, a rain drop will stay in air for a relatively long time, so that it can evaporate more in an unsaturated environment and thus can result in extra cooling. The strength of the downdraft can then be enhanced. A large horizontal area of moistening and cooling is expected, owing to the slow fall speed of rain water. Obviously this method is very crude. For example, latent heat release associated with the ice processes is not considered.

2. The turbulence parameterization is formulated following Mason and Sykes (1982), which is a first-order closure with a Richardson number-dependent eddy viscosity. An energy equation for turbulence is formed by assuming equilibrium conditions, as in Lilly (1962). The tangential stresses and vertical fluxes at the surface are given by bulk aerodynamic formulae.

3. The model uses Newtonian cooling to simulate radiative cooling in the tropical atmosphere. It relaxes the temperature profile back toward the initial state rather than toward a state of radiative equilibrium. The radiative relaxation time is 12 hours.

4. The prognostic equations are divided into acoustic and advective parts in order to have computational stability and efficiency. A large time step is used for advective and diffusive processes, while a small time step, e.g. one fifth of the large time step, is used for computations of the terms associated with sound waves.

5. A leap-frog scheme is used for time-integration, except for the sound wave integration. To suppress the splitting tendency of the leap-frog scheme, the model uses the weak Asselin time-filter described by Klemp and Wilhelmson (1978).

6. The model uses a spatially staggered grid in which the u and w points are computed at one-half of the grid sizes in the horizontal and vertical directions, respectively, away from the v point where the other dependent variables are defined (see Fig. 1 in RE87). Standard second-order conservative differences are used for the advection terms.

7. Open lateral boundary conditions are used to allow gravity waves to propagate out of the integration domain. A sponge layer is placed in the uppermost part of the model to damp out gravity waves before they can reflect from the rigid lid back into the lower troposphere.

At this point, one might ask whether it is appropriate to use a two-dimensional model to investigate the influence of eddy forcing on a hurricane. It is known that

the interaction between a hurricane and its synoptic environment is highly asymmetric. There is no doubt that it would be best to conduct the study using a three-dimensional, nonhydrostatic, convection-resolving model. But owing to the much greater amount of computation time and associated expense for such numerical integrations, it would seem reasonable to conduct three-dimensional integrations for this purpose only if the results of a symmetric model suggest the importance of the environmental forcing for the genesis of a secondary eyewall. The results obtained with the symmetric model could then be used as a guide to experiment with a three-dimensional model more efficiently. The second reason for using an axisymmetric model is that Challa and Pfeffer (1990) reached similar conclusions using an axisymmetric model and a three-dimensional model. These two reasons justify using an axisymmetric model to investigate the genesis of a secondary eyewall.

2.2.2 The parameterization of the eddy forcing

In order to account for the environmental forcing, we have to make some changes to the model equations. As a first step, we only consider the effect of eddy angular momentum fluxes and leave the effect of eddy heat fluxes for future study. According to Molinari and Vollaro (1990), the eddy heat fluxes act in the same direction as the eddy momentum fluxes, but often with less magnitude and smaller areal coverage.

We first rewrite the azimuthal momentum equation in RE87 in flux form by using the continuity equation, then divide all physical variables into azimuthal mean and the deviation from the mean, and then average azimuthally. The new azimuthal momentum equation in RE87 takes the following form,

$$\frac{dv}{dt} + (f + \frac{v}{r})u = D_v + F_v, \tag{2.4}$$

where the substantial derivative $\frac{d}{dt} = \frac{\partial}{\partial t} + u\frac{\partial}{\partial r} + w\frac{\partial}{\partial z}$; u, v, and w are the mean radial, azimuthal, and vertical velocity components in cylindrical coordinate system r, ϕ, and z, with its axis vertical and z measuring upward from the surface; t is time; f is the Coriolis parameter assumed constant; D_v is the azimuthal mean diffusion.

The term F_v in equation 2.4 is the azimuthal mean convergence of eddy angular momentum fluxes, which can be expressed as,

$$F_v = \frac{1}{r^2}\frac{\partial}{\partial r}(-\overline{r^2 u' v'}), \tag{2.5}$$

where the overbar denotes an azimuthal mean and a prime denotes a departure therefrom. Though F_v has the same mathematical form as the Reynold's stresses, F_v is here assumed to arise from the mutual interaction between a tropical cyclone and its environment. If it is well organized, as shown in Fig. 1.8a, it can help the initial intensification of a tropical cyclone or could trigger a secondary eyewall. If it is diffusive, as shown in Fig. 1.8b, it does no more than the diffusion term D_v. In the equation, $F_v > 0$ means that the eddy stress exerts a cyclonic torque on the axis. The mean cyclonic angular momentum will increase, and there is an energy transfer from eddy disturbances to the mean field. When $F_v < 0$, it means that the eddy stress exerts an anticyclonic torque about the rotation axis. The mean cyclonic angular momentum will decrease.

Based on Figs. 1.8, 1.11b and 1.11c, we parameterized the eddy forcing F_v as

$$F_v(r, z, t) = f_v(r) h_v(z) g_v(t), \tag{2.6}$$

where

$$\begin{aligned} f_v(r) &= sin(2\pi\frac{r - r_0}{l_r}), r_0 < r < r_0 + l_r, \\ h_v(z) &= sin(\pi\frac{z - z_0}{l_z}), z_0 < z < z_0 + l_z, \\ g_v(t) &= A_{efc} exp(-(\frac{t - t_{max}}{l_t})^2). \end{aligned}$$

In the above equations, A_{efc} represents the magnitude of the eddy forcing; r_0, the starting radius of the eddy forcing, l_r, the radial range of the eddy forcing; z_0, the starting height of the eddy forcing, l_z, the vertical height of the eddy forcing; t_{max}, the peak time of the eddy forcing, l_t, the half width of the eddy forcing duration time.

Here we use the following values for the parameters in the expression of F_v,

$$A_{efc} = 25 \text{ m/s/day},$$
$$r_0 = 80 \text{ km}, l_r = 1600 \text{ km},$$
$$z_0 = 5 \text{ km}, l_z = 12 \text{ km},$$
$$t_{max} = 130 \text{ hours}, l_t = 30 \text{ hours}.$$

Fig. 2.9 shows the vertical distribution of the eddy spin up rate at t_{max}. The major features of the observed eddy forcing have been captured by our parameterization. For example, the eddy spin up rate maximizes in the outflow-layer, and an area of anticyclonic spin up is outside an area of cyclonic spin up. Even though the observations show no sign of equal area between cyclonic spin up and anticyclonic spin up in the radius-height plane, equal area is chosen here for convenience. Because the model has to be a closed system while there is no boundary for a hurricane in nature, the terminating radius of anticyclonic spin up is somewhat arbitrarily chosen. Some experiments will be carried out to test the sensitivity to our chosen parameter values.

2.2.3 Numerical Experiments and Results

In this section, we present the results of some experiments. The experiments are listed in Table 2.4. Results of the sensitivity tests will be described in the next section.

All experiments start with an horizontally uniform sounding and a cyclonic vortex identical to those in the control run of RE87. More specifically, the sounding is neutral to convection in the model atmosphere. Also the maximum tangential wind, the radius of the maximum tangential wind and the radius at which the tangential wind vanishes are 15m/s, 86.25km and 416.25km, respectively. The sea surface temperature is equal to 300K. The Coriolis parameter is $5 \times 10^{-5}s$. The drag coefficients for momentum and heat (sensible and latent) are assumed to be constant. Both are equal to 1.5×10^{-3}.

In all experiments, the horizontal and vertical resolutions are 7.5km and 1.25km, respectively. The domain outer radius r_b is 2250km, and the top of the model is at

Experiment	Difference from the control experiment
EXP1	(no eddy forcing is added)
EXP2	same as EXP1 but initial relative humidity is 90% from 1.875km to 9.375km
EXP3	same as EXP1 with eddy forcing turned on and no limitation of Newtonian cooling.
EXP4	same as EXP3 but the WISHE mechanism is turned off by using the surface winds at 130 hours in the calculations of surface heat fluxes between 130 hours and 230 hours. After 230 hours, the WISHE is switched on again.

Table 2.4: Description of experiments done with the full physics model

30km. The large time step is 10 seconds, and the small time step is 2 seconds. The total simulation time is 320 hours.

Fig. 2.10 displays time series of v_{max} and r_{max} of EXP1. The eddy forcing is turned off in this experiment. It can be seen that the initial cyclonic vortex develops into a hurricane intensity vortex and reaches a quasi-equilibrium state after 100 hours. The development of v_{max} and r_{max} is smooth throughout the whole simulation. Only one eyewall forms in the whole integration time. Due to local conditional instability, deep convective elements occur locally from the lowest level in the outer region [1]. Their averaged life time is less than $5 \sim 10$ hours, and they do not have any local wind maximum. The dissipation of these convective elements is owing to the downdraft associated with them and the general subsidence outside the eyewall. The occasional occurrence of deep convection in the outer region may be responsible for the variation of v_{max} after 100 hours.

Fig. 2.11 shows v_{max} and r_{max} in EXP2. This figure tells us that there is no significant intensity change in this experiment. A closer look at the numerical output reveals that no concentric eyewalls formed in the experiment. This result contradicts the result from the simple model. After checking the numerical results of EXP1 and EXP2 carefully, we have found two common features in the mature model hurricanes.

[1] It is defined as the region extending from the radius of maximum wind to an outer radius where the surface tangential wind vanishes (Emanuel 1986, E95b).

These two features may be responsible for the absence of concentric eyewalls in EXP2.

The first common feature is that just above the top of the boundary layer, a strong inversion layer is present from 70km to 600km where the first appearance of a secondary eyewall is usually observed. The layer can be clearly seen in Fig. 2.12. A detailed heat budget study shows that the formation of the inversion layer is owing to the subsidence warming surpassing the Newtonian cooling in the experiment. A depression in the specific humidity field (figure not shown) also substantiates that next to the convective downdrafts which occur adjacent to the convective updrafts in the eyewall, there exists gentle downward motion through a relatively dry region outside the eyewall. In fact, the control run of RE87 has an inversion layer too (Fig. 5d in RE87). The presence of the inversion layer prevents the development of any deep convection in the outer region. In the simple hurricane model, however, no inversion layer can form since we only have two layers and assume constant saturation equivalent potential temperature along angular momentum surfaces.

The second common feature is that there exists radial inflow in the upper middle troposphere (Fig. 2.13). Owing to evaporation of rain water, convective downdrafts form outside the eyewall cloud, so there should be radial inflow in the upper middle troposphere to obey mass continuity. The radial inflow carries relatively cool and dry upper-middle tropospheric air with high angular momentum toward the outer edge of the eyewall, which leads to an increase of the evaporation of rain water as well as to a tendency for cyclonic rotation. The convective downdrafts are then enhanced, and most of the cyclonic tendency is advected to the lower atmosphere by the enhanced convective downdrafts. Therefore, as the tangential wind at the surface is further increased, so are the surface heat fluxes. The enhancement of the inner eyewall further stablizes the model hurricane and thus reduces the chance of an outer eyewall forming in the outer region. Note that such high level radial inflow has been observed (Rosenthal, 1978).

Besides the above two common characteristics, one more point should be made here. When the relative humidity is increased in the simple model, the mid-tropospheric entropy is increased and kept at a higher value. As stated in E89, the low θ_e of the

middle troposphere would limit the growth of the initial vortex. So after the mid-tropospheric entropy is at a higher value, disturbances outside the eyewall have a better chance to develop compared to when the mid-tropospheric entropy is low. In the full physics model, however, the initial extra moisture added in the experiment EXP2 was almost depleted in about 2 days owing to active convective elements in the outer region. The mid-tropospheric entropy thus cannot stay at a higher value after two days. As a result, disturbances do not grow in the full physics model.

In brief, the full physics model does not produce concentric eyewalls spontaneously by increasing the initial moisture in the troposphere. The presence of the inversion layer, the mid-tropospheric inflow, and the quick depletion of the initial moisture suggest that only finite-amplitude perturbations can trigger concentric eyewall cycles. This is consistent with the conclusion based on the randomized numerical experiments described at the end of Chapter 2.1.2.

The time series of v_{max} and r_{max} of EXP3 is shown in Fig. 2.14. A substantial variation of the model hurricane intensity can be seen in the figure. Between 200 and 220 hours, v_{max} decreases. After 220 hours, v_{max} increases again. At the turning point 220 hours, r_{max} jumps from 40km to about 120km.

Fig. 2.15 presents the radius vs. time plots of w at 1250m and v at 625m between 200 and 280 hours. There are two distinguishable rainbands (Fig. 2.15a), one centered around 40km, and another around 200km. Each rainband has its own surface tangential wind maximum (Fig. 2.15c). The well-organized rainband around the 40km radius is the primary eyewall (Fig. 2.15a) which appears with the spin-up of the initial vortex. The tangential wind associated with the primary eyewall is also well developed (Fig. 2.15c). The outer rainband around the 200km radius (Fig. 2.15a) is the secondary eyewall whose vertical kinematic structure is displayed in Fig. 2.16. The vertical structure of the primary eyewall can also be seen in the same figure. The secondary eyewall resembles the primary one, which is consistent with what Samsury and Zipser (1995) discovered. For example, it has its own surface tangential wind maximum (Fig. 2.16a) and its own in-up-out circulation (Figs. 2.16b and 2.16c).

The succession of the concentric eyewalls is clearly shown in Fig. 2.15. The outer

eyewall contracts and intensifies, while the inner one weakens and dissipates. After the outer eyewall replaces the inner one at the 120km radius around 220 hours, the outer eyewall continues to propagate inward and becomes more intense until it reaches its final position, which is also around the 40km radius (Figs. 2.15b and 2.15d). The above eyewall replacement picture is similar to the classical picture described by Willoughby et al. (1982).

So we conclude that a concentric eyewall hurricane has been produced, and the secondary eyewall in the model shares the same kinematic structure as its counterpart in the real world. The next step is to understand why it happens. After inspecting the numerical results, we can make the following observations:

Although in the outer region deep convection occurs more frequently in EXP3 than in EXP1, it is not organized until a substantial surface tangential wind maximum first appears around 160 hours at 350km from the center. With the passage of time, this wind maximum evolves into the SHWM seen in Fig. 2.16a. It is speculated that the WISHE mechanism plays a fundamental role in the evolution, because after 160 hours the external forcing is almost negligible. Experiment EXP4 is designed to test this speculation. Results of EXP4 will be presented later on.

Given the potential importance of the surface wind anomaly, the next question is where the anomaly comes from. With the aid of Fig. 2.17, we may use PV thinking to tackle this question. In the moist atmosphere, instead of using conventional potential vorticity defined in the paper of Hoskins et al.(1985), we need to use saturated moist potential vorticity [2]. When there is an upper-level trough several hundred kilometers to the west and poleward of a hurricane, the trough begins to interact with the hurricane. As is usually done in studying mid-latitude dynamics, the trough can be thought of as an upper-level moist PV anomaly, as shown in Fig. 2.17. Through the interaction process, the cyclonic vorticity associated with the trough projects along a characteristic surface. Here, the angular momentum surfaces function as characteristics surfaces in moist potential vorticity inversion. This argument was first

[2]To get the saturated moist potential vorticity, we just replace the potential temperature with the saturated moist potential temperature.

suggested by Emanuel (1997). Indeed, Molinari et al. (1990) observed the downward shifting of the maximum spin up rate from 200mb to 900mb; see Fig. 2.18. Once there is a wind anomaly formed at the surface, it may develop into a secondary eyewall through the WISHE mechanism given favorable conditions.

The second observation concerns the roles of evaporation-driven downdrafts and ice processes in the development of the SHWM. It should be kept in mind that so far no real ice processes have been included in the model. The term is used for the sake of narration. One notable feature in the vertical velocity field in Fig. 2.16b is that there is a significant branch of convective downdrafts next to the secondary eyewall. The downdrafts remain active until the secondary eyewall has replaced the primary one completely and reaches its final position.

From Fig. 2.16b, we can see that the downdrafts originate at about 5-6km height where $T < 0^oC$ (See Fig. 1.2). Extra evaporation of the precipitation happens owing to its slow fall speed. The extra evaporation of rain water results in extra cooling and thus enhances the downdrafts. The occurrence of the downdrafts, through mass continuity, leads to mid- to upper-level inflow (Fig. 2.16c). This radial inflow brings relatively low entropy and high angular momentum middle tropospheric air toward the outer edge of the secondary eyewall, which will increase the evaporation and the cyclonic rotation tendency there. The convective downdrafts will then be further enhanced. The convective downdrafts then transport most of the cyclonic tendency down to the surface. Therefore, the SHWM will be further increased, and so will the surface heat fluxes. Perhaps this is also the reason for a little stronger vortex after the eyewall replacement (see Fig. 2.14).

Furthermore, we speculate that since more cold air is brought close to the secondary eyewall at mid-level, the temperature gradient at that level becomes even stronger than it would otherwise be. This implies, through the hydrostatic relationship, that the surface pressure gradient will increase, and so will the SHWM, according to gradient wind balance.

The last role of the downdrafts is that they transport low entropy air to the subcloud layer, which prevents new deep convection from occurring near the secondary

eyewall. This process keeps the latent heat release in a small area (at least not outside the secondary eyewall). This means that the heating can more efficiently maintain, or even increase, the existing temperature gradient associated with the secondary eyewall at upper levels. Therefore, the SHWM will be strengthened.

In conclusion, the appearance of the convective downdrafts helps maintain and develop the SHWM. The effect of ice processes is achieved indirectly through enhancing downdrafts.

The third observation concerns which process is responsible for the demise of the primary eyewall: subsidence on the inner side of the outer eyewall, which is a byproduct of the outer eyewall itself; or taking up of the high angular momentum and entropy carried by surface inflow. Fig. 2.16b clearly shows that no direct subsidence is over the inner eyewall, while strong subsidence occurs just on the left side of the outer eyewall. The subsidence also can be easily seen on Fig. 2.16a since it drags down the contour of v significantly at upper levels. After tracking v and w continuously from 160 hours, we have found that only at the final stage of the eyewall replacement is the subsidence directly over the inner eyewall. But at that time, the inner eyewall is already fragile enough to be weakened by surface friction and the lack of the supply of high angular momentum and entropy air. Therefore, we believe that the depletion of the high angular momentum and entropy by the outer eyewall mainly accounts for the dying of the inner eyewall. By measuring the mass flux of a convective cell in a hurricane, Barnes et al. (1991) found that rainbands may partially obstruct inflow to the eyewall. Furthermore, we speculate that the subsidence on the inner side of the outer eyewall prevents deep convection there, which helps limit the area to be heated and thus helps retain the existing temperature gradient across the secondary eyewall. In short, the SHWM in the model survives in an unfavorable environment once it has gained a certain initial strength, at least in the model.

After we have discussed how the SHWM forms and develops, we now turn to an exploration of the mechanism by which the SHWM evolves into a secondary eyewall. Experiment EXP4 is the same as EXP3 except that we use the surface wind at 130 hours to calculate surface heat and moisture fluxes between 130 hours and 230 hours,

and after 230 hours we switch back to the normal way of calculating the surface fluxes. Fig. 2.19 shows the time development of v_{max} and r_{max} in the experiment. Compared to Fig. 2.14, we can say that no concentric eyewalls form in this experiment after turning off the WISHE mechanism, even though the eddy forcing is present. Our previous speculation is proved correct. The result is identical to what we found using the simple model, which essentially operates under the WISHE mechanism. So we do need to appreciate the importance of the positive feedback between the surface wind and the surface fluxes on the genesis of secondary eyewalls.

Based on the results from EXP3 and EXP4, we have the following general picture in our mind for the genesis of concentric eyewall hurricanes in the full physics model:

1. Upper level environmental forcing can induce an initial surface wind disturbance. This is achieved through the projection of a moist PV anomaly along angular momentum surfaces to the sea surface.

2. The development of an initial weak SHWM depends on the important role of evaporation-driven downdrafts. The primitive ice processes used in the model maintain or enhance the strength of the downdrafts through extra cooling, which then aids the development of the SHWM.

3. When the disturbance becomes strong enough, it triggers the formation of a secondary eyewall. The surface circulation intensifies through the WISHE mechanism, which is an internal processes by definition. Therefore, the genesis of a secondary eyewall is a finite-amplitude WISHE instability.

4. The presence of a secondary eyewall serves as a barrier to the inflow of high angular momentum and high θ_e air into the vortex center. It is the consumption of this inflow air by the secondary eyewall that causes the weakening of the primary eyewall in the model.

   It should be pointed out that points 1 and 2 are our speculations, point 3 has been tested in EXP4, and point 4 has the support from one observation.

2.2.4 Results of Sensitivity Experiments

In this subsection, we present the results of some sensitivity tests in order to see how the above conclusions vary with the parameters used in the eddy forcing. The design for each experiment is briefly described in Table 2.5, and the result of each experiment are summarized in Table 2.6.

Experiment	Difference from experiment EXP3
EXP5	no negative spin up
EXP6	no positive spin up
EXP7	A_{efc}=15 m/s/day
EXP8	A_{efc}=35 m/s/day
EXP9	A_{efc}=35 m/s/day but WISHE mechanism turned off
EXP10	$r_0 = 160$ km
EXP11	$r_0 = 300$ km
EXP12	$l_r = 1000$ km
EXP13	$z_0 = 7$ km
EXP14	$l_z = 10$ km
EXP15	$t_{max} = 115$ hours, $l_t = 15$ hours
EXP16	$l_r = 2000$km, $t_{max} = 140$ hours, $l_t = 35$hours, $r_b = 2625$km.

Table 2.5: Description of the sensitivity experiments

By trial and error, we have found the threshhold value for A_{efc} to produce concentric eyewall cycles under the conditions of experiment EXP3. This value is 19 m/s/day. Obviously, we can always make eyewall replacement cycles happen by combining different parameter values in the parameterization of the eddy forcing. The bottom line is that a strong enough external forcing is needed to generate a concentric eyewall hurricane in the model. Without doubt, the strength of the external forcing depends on the initial conditions and the other parameter values in the full physics model.

2.2.5 Conclusions from the Full Physics Model Simulations

Based on the numerical experiments done with the full physics model, we come to the following conclusions:

Experiment	Observations
EXP5	Concentric eyewalls form. The intensity change associated with the eyewall replacement is more pronounced than in EXP3.
EXP6	No concentric eyewalls form.
EXP7	No concentric eyewalls form.
EXP8	Multiple eyewall replacement cyles are found.
EXP9	No concentric eyewalls form.
EXP10	Concentric eyewalls form. The timing and the magnitude of the intensity change is similar to those of EXP3.
EXP11	No concentric eyewalls form.
EXP12	No concentric eyewalls form.
EXP13	No concentric eyewalls form.
EXP14	No concentric eyewalls form.
EXP15	No concentric eyewalls form.
EXP16	Two events of concentric eyewall cycles are found. The first one starts at 170 hours, and the second one starts at 270 hours. The second episode is stronger than the first one.

Table 2.6: Observations of the sensitivity experiments

1. The full physics model does not spontaneously produce concentric eyewalls just by increasing the initial moisture in the middle troposphere. This is probably due to three effects: (1) the quick loss of initial moisture through precipitation, (2) a strong temperature inversion layer above the boundary layer top and stretching from the eyewall to about 600km, where the observed concentric eyewalls likely form in the real world, and (3) a radial inflow in upper-middle levels of the model atmosphere. The quick loss of the moisture makes the mid-troposhere dry and thus it is destructive for any small disturbance. The strong inversion layer suppresses deep convection. The existence of the inversion is owing to the subsidence warming surpassing the limited radiative cooling in the model. The high level inflow enhances the cyclonic rotation by bringing in high momentum air, which in turn helps to maintain the subsidence in the outer region and so maintain the inversion layer. These two processes make the model hurricane remain stable. Therefore, finite-amplitude disturbances are needed to trigger concentric eyewall cycles.

2. After an external forcing is introduced into the model at upper levels, the model produces concentric eyewall cyclones. The external forcing induces a wind disturbance first at the sea surface. This initial disturbance develops into a SHWM under the influence of evaporation-driven downdrafts and ice microphysical processes which not only maintain but also enhance the strength of the downdrafts. When the SHWM becomes strong enough, it triggers the formation of a secondary eyewall through the WISHE mechanism.

3. The eddy forcing should be strong enough to produce an initial wind disturbance. If the initial disturbance is not strong enough, it will not survive the stabilizing effect of the downdrafts and the large scale subsidence in the outer region. Our sensitivity tests show that the eddy forcing should be present long enough, be close enough to the vortex center and the surface, and be broad enough horizontally and vertically. Our numerical results are in agreement with Holland's (1988) suggestions that an eddy forcing should reach a critical radius in order to interact with the storm's inner core. Clearly the critical strength of the eddy forcing is a function of initial conditions and parameter values of the full physics model.

4. The concentric eyewall cycles in the model share similar characteristics with those in nature; for example, the kinematic structure and the intensity change are similar.

5. The blocking by the outer eywall of the supply of high angular momentum and high θ_e air into the vortex center kills the inner eyewall. The subsidence associated with the outer eyewall prevents deep convection from occurring on the inner side of the outer eyewall. The subsidence only has the second-order effect on the demise of the inner eyewall.

We emphasize that the genesis of concentric eyewalls is a finite-amplitude WISHE instability. The origin of the finite-amplitude perturbations can be the upper-level external forcing. In the next chapter, we will look for such forcing in nature by

analyzing the synoptic environment of the concentric eyewall hurricanes listed in Chapter 1.1

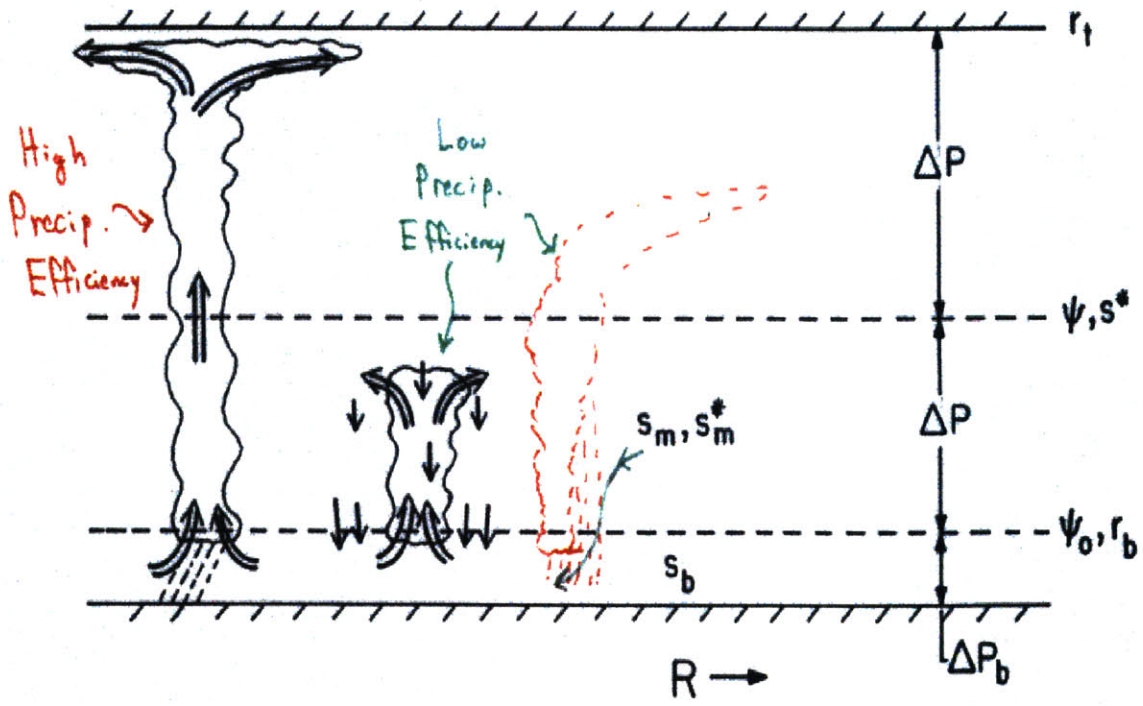

Figure 2-1:The model structure of the simple model. See text for the meaning of each symbol.(from Prof. Emanuel's web site. The web address is http://www-paoc/~emanuel/geosys/fig6.3.gif.)

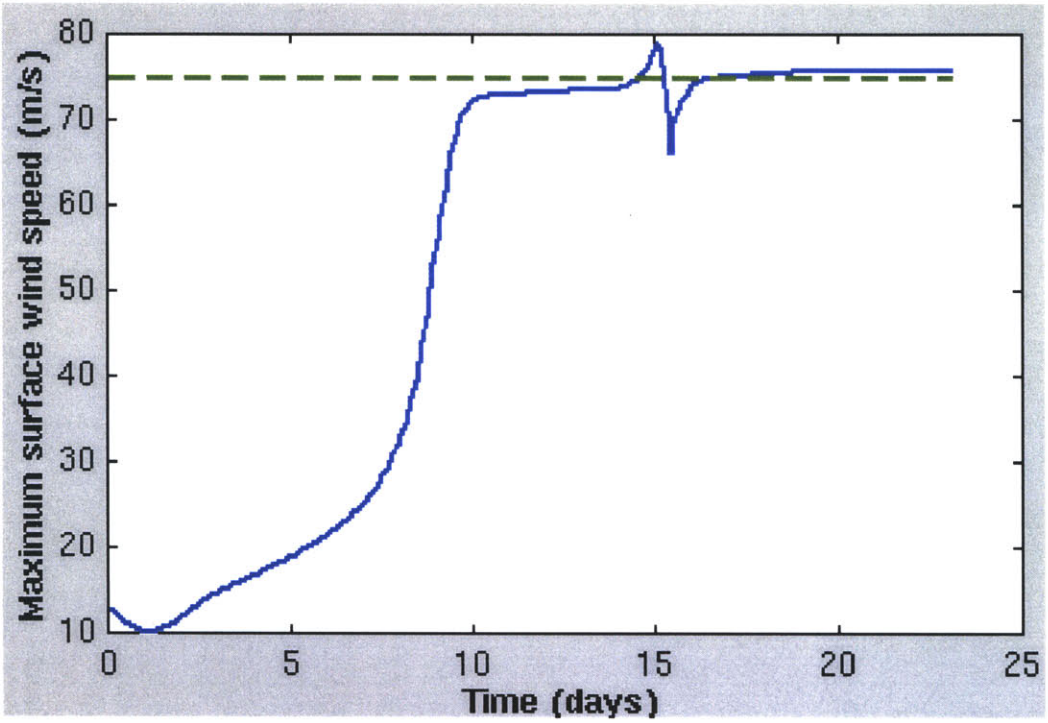

(a)

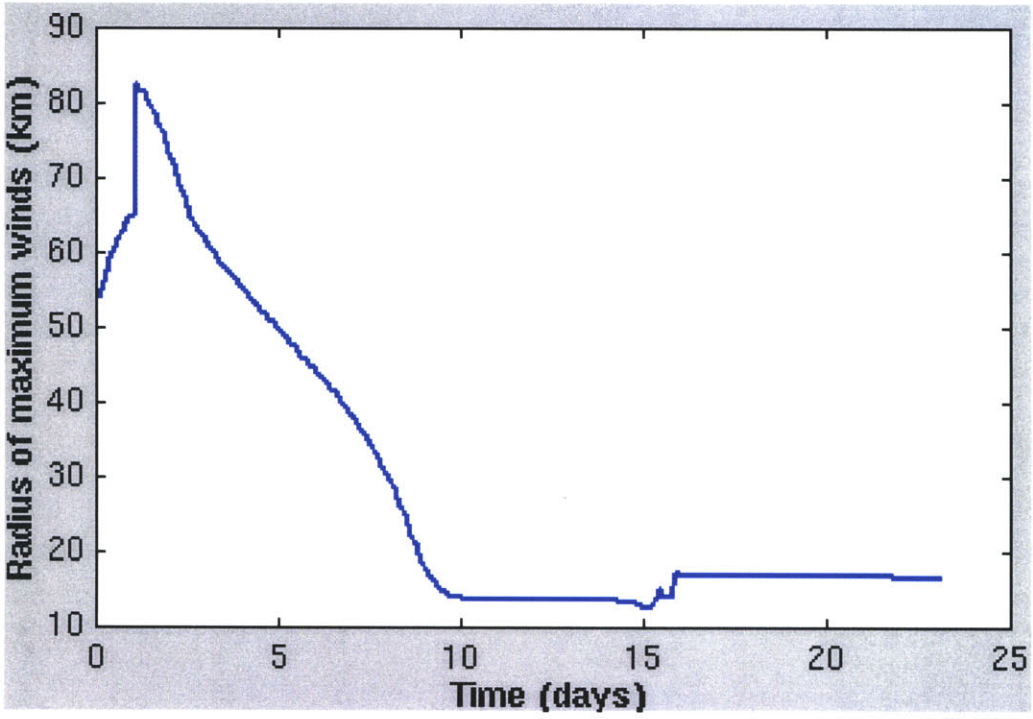

(b)

Figure 2-2:Time evolution of maximum azimuthal surface wind (a) and radius of maximum wind (b) of EX1.

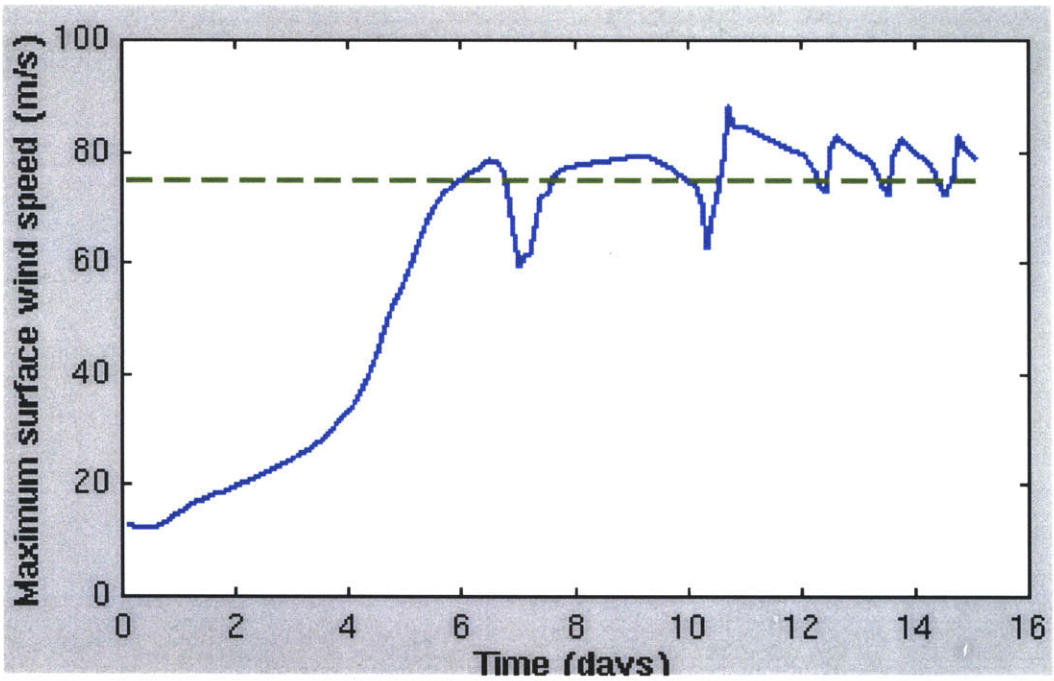

(a)

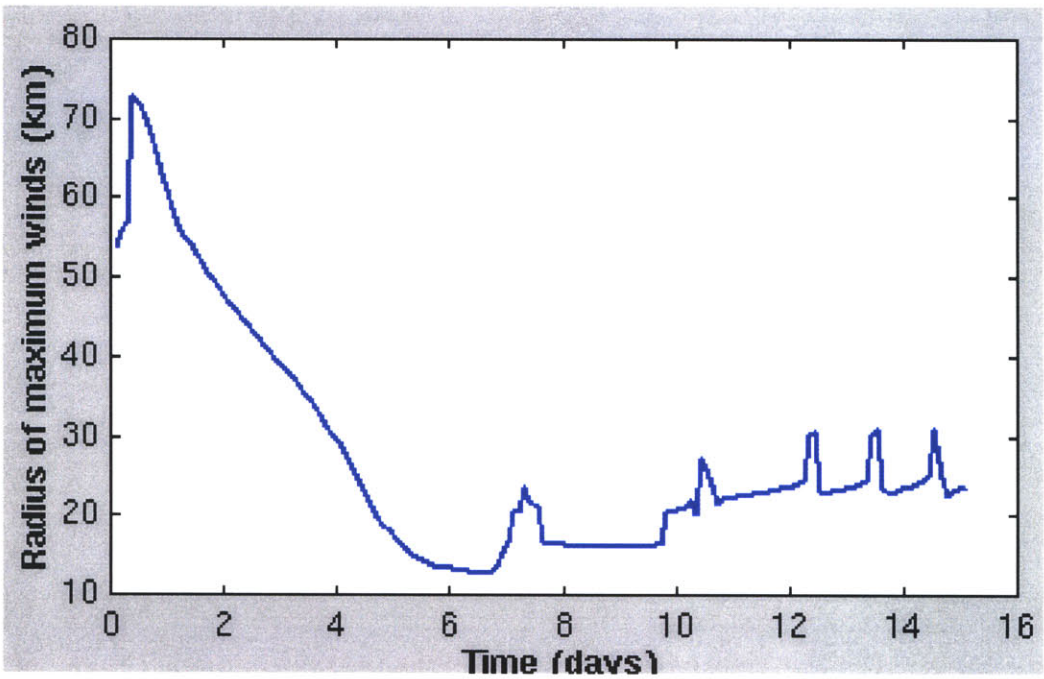

(b)

Figure 2-3: Time evolution of maximum azimuthal surface wind (a) and radius of maximum wind (b) of EX2.

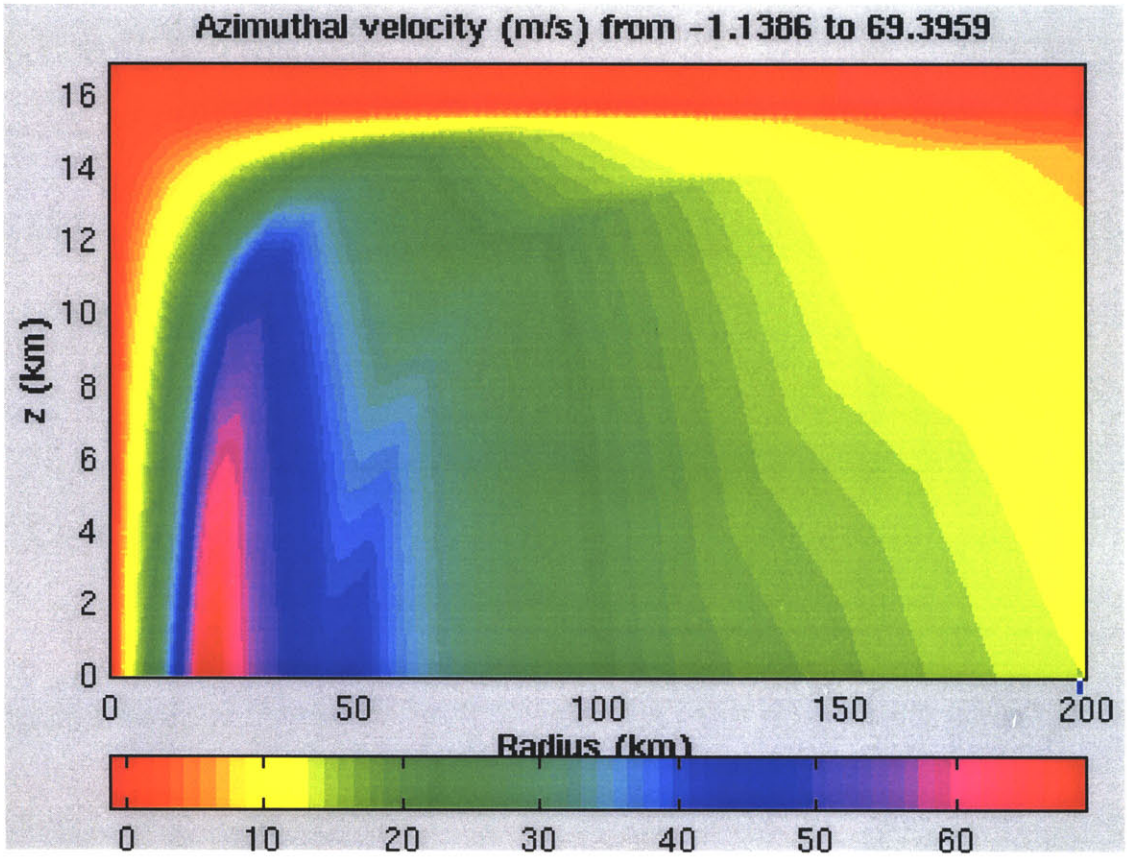

(a) Azimuthal velocity

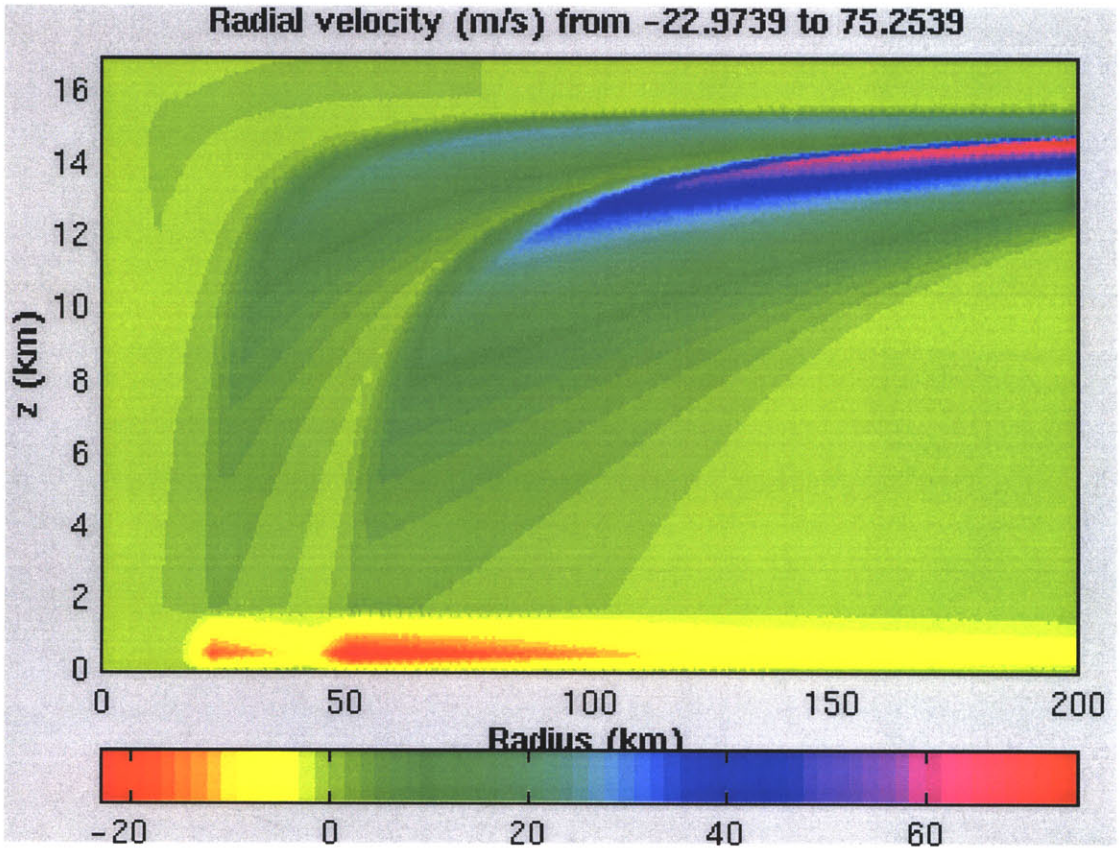

(b) Radial velocity

Figure 2-4: Azimuthal velocity (a) and radial velocity (b) of EX2 at 10.11 days;

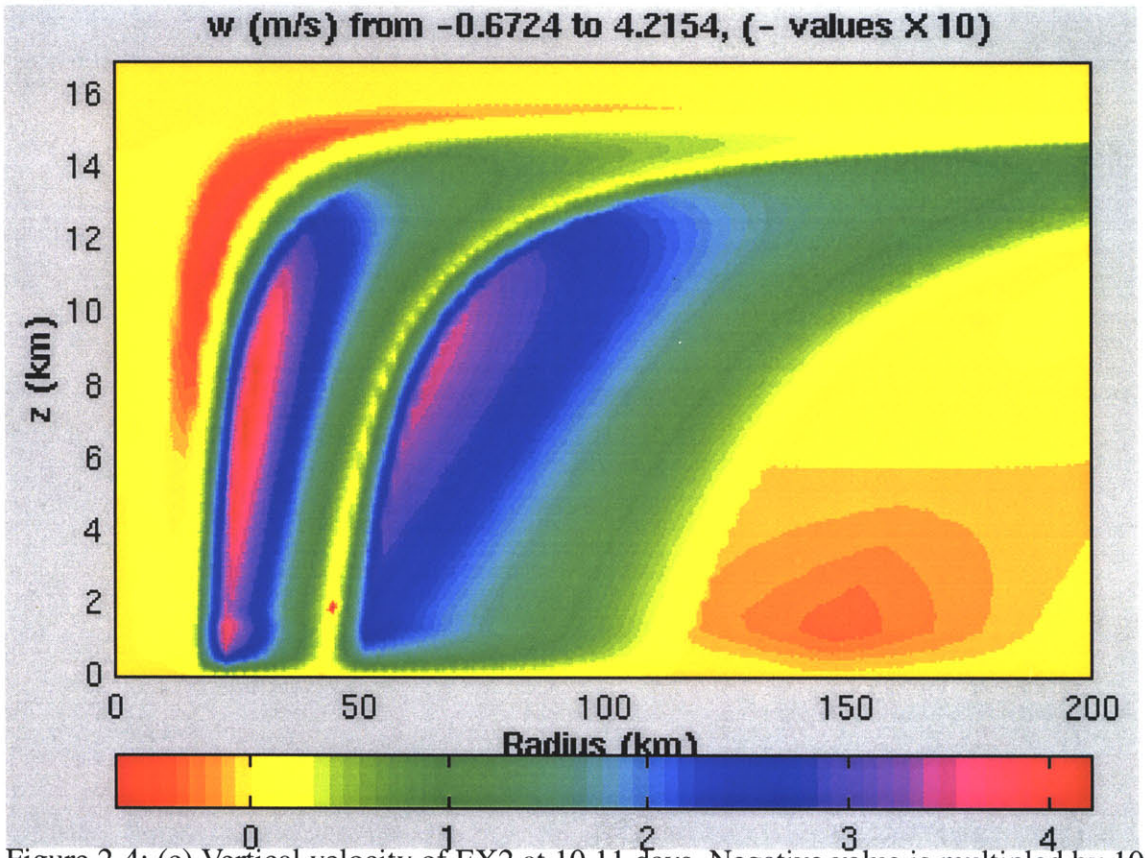

Figure 2-4: (c) Vertical velocity of EX2 at 10.11 days. Negative value is multipled by 10;

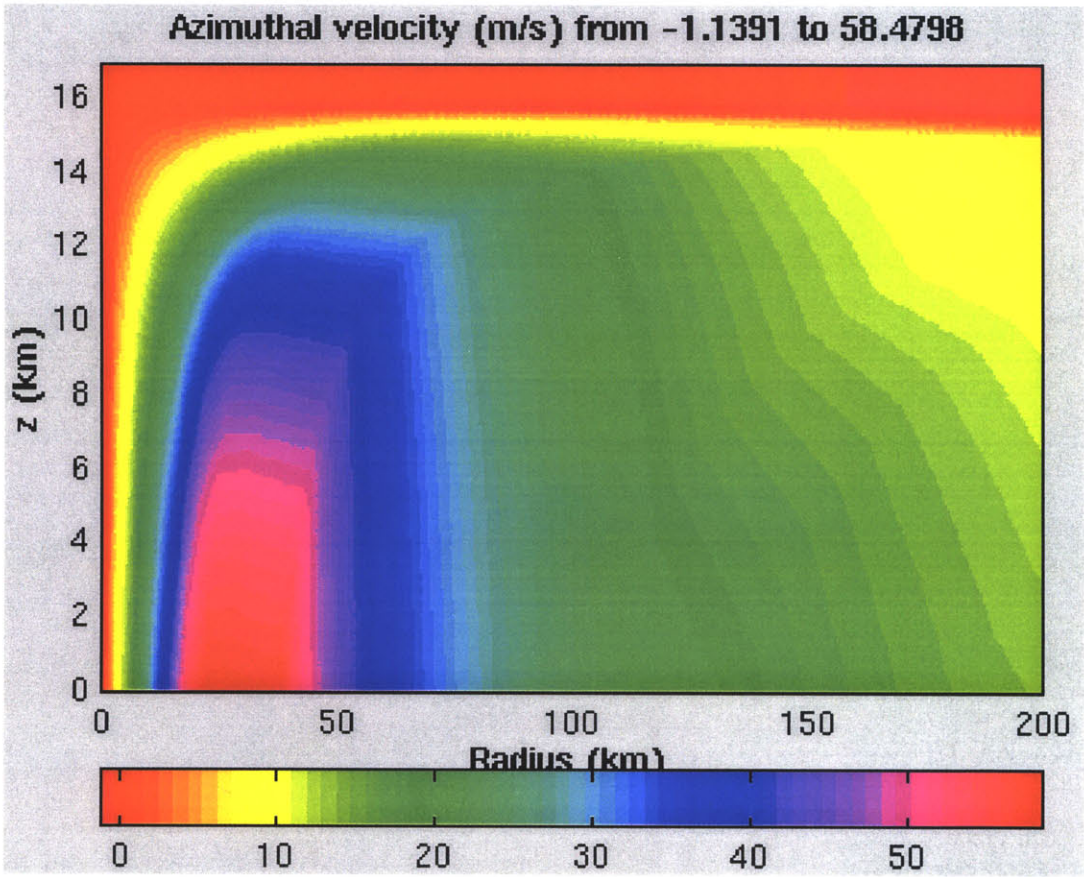

Figure 2-4: (d) Azimuthal velocity of EX2 at 10.225 days;

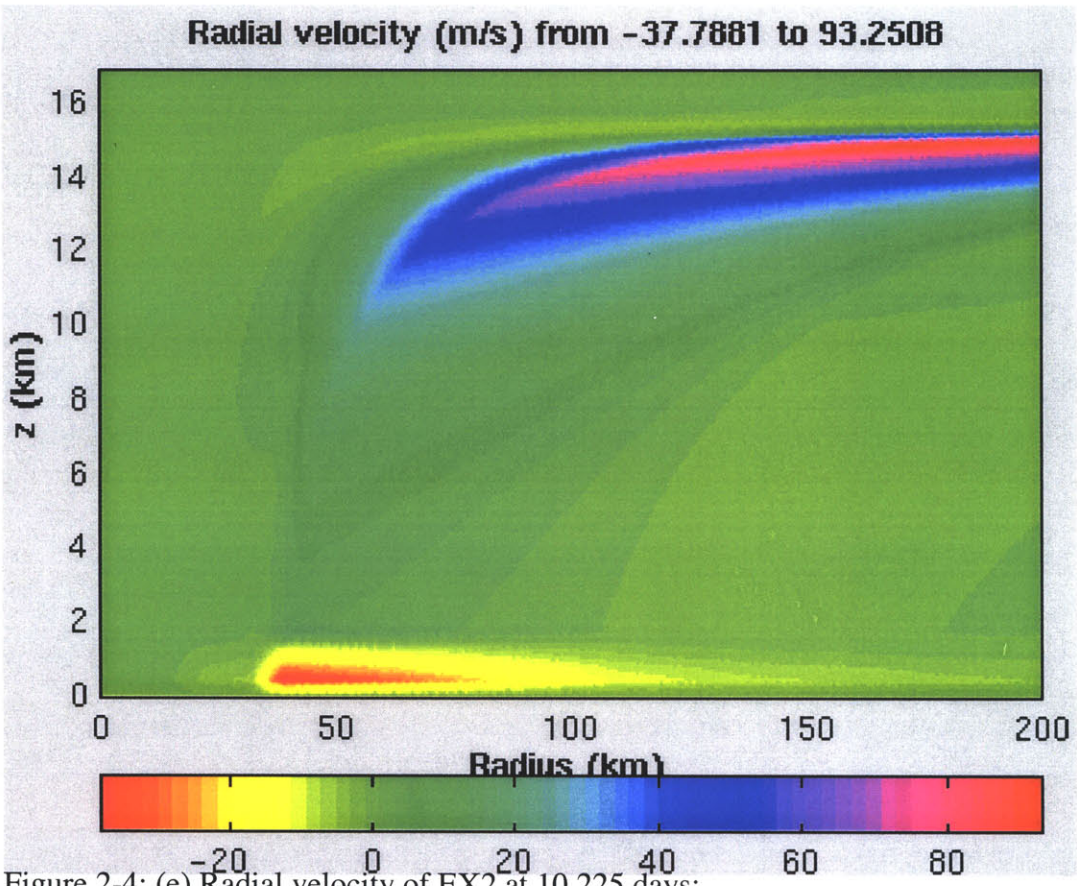

Figure 2-4: (e) Radial velocity of EX2 at 10.225 days;

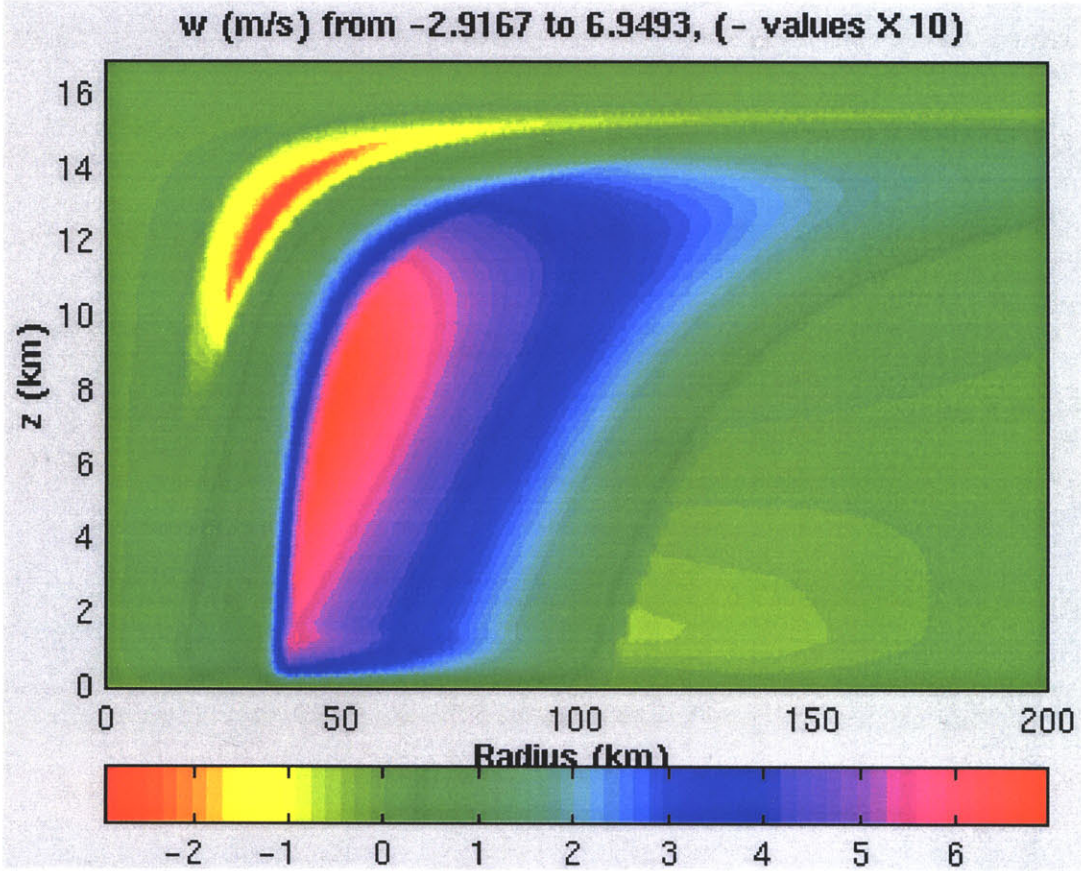

Figure 2-4: (f) Vertical velocity of EX2 at 10.225 days. Negative value is multipled by 10.

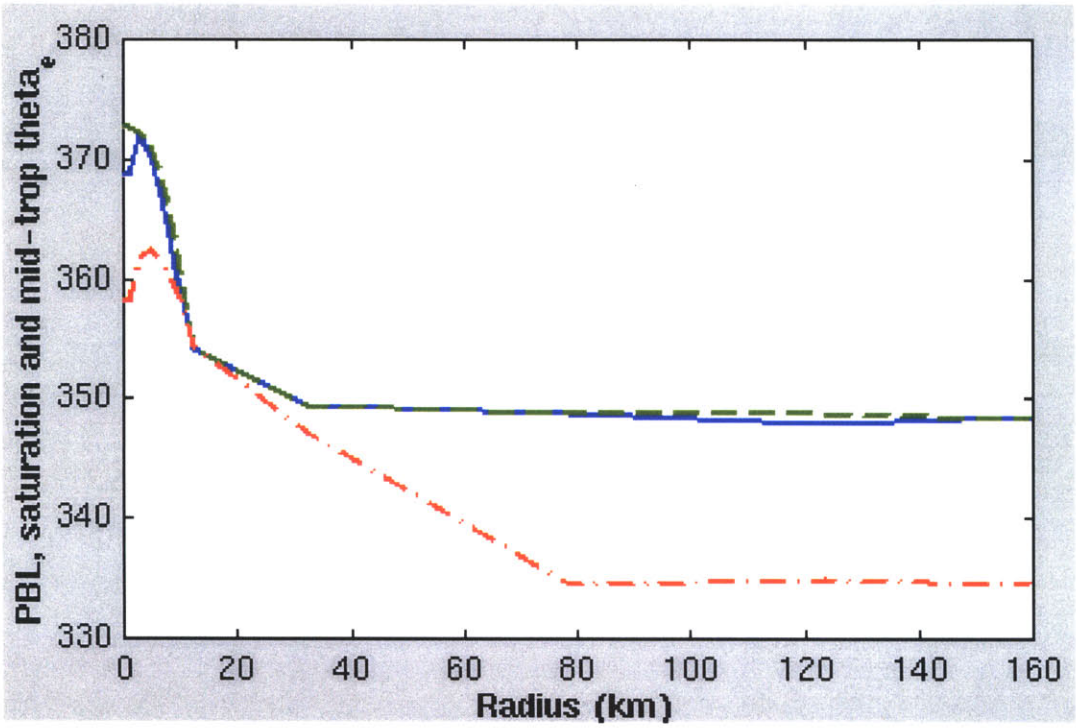

(a)

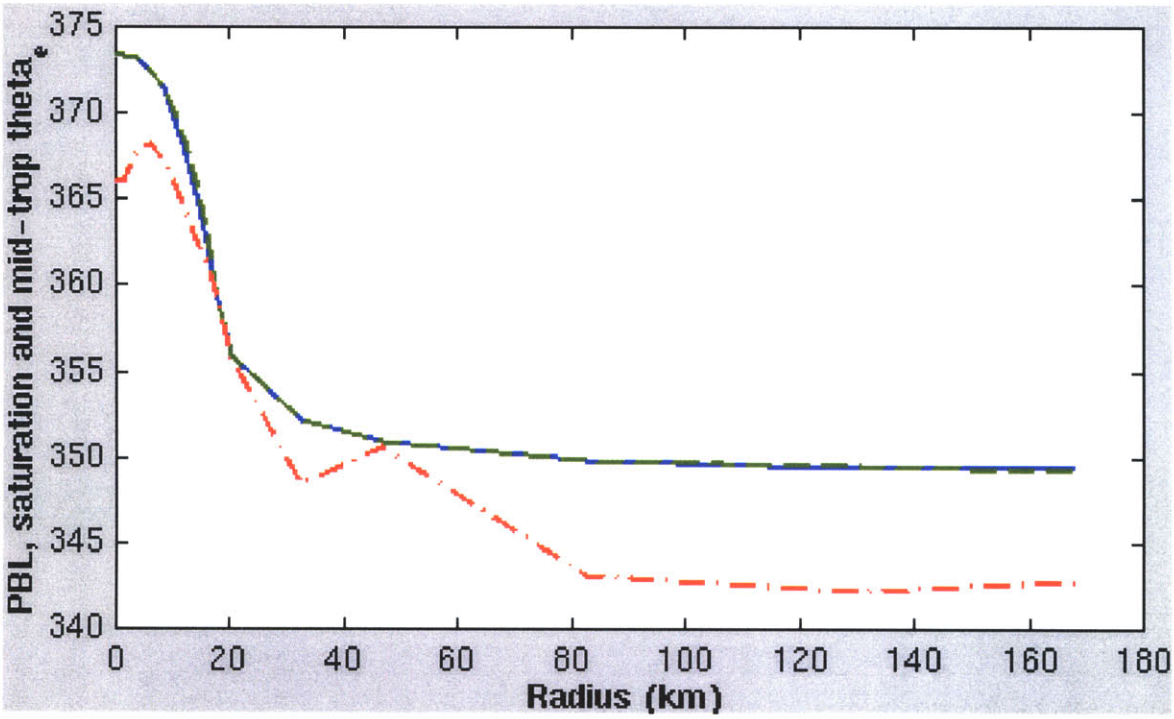

(b)

Figure 2-5:Moist potential temperature of EX1 (a) and EX2 (b) at 10.11 days. Solid, dashed and dash-dot lines are for PBL, saturation and mid-tropospheric moist potential temperature, respectively.

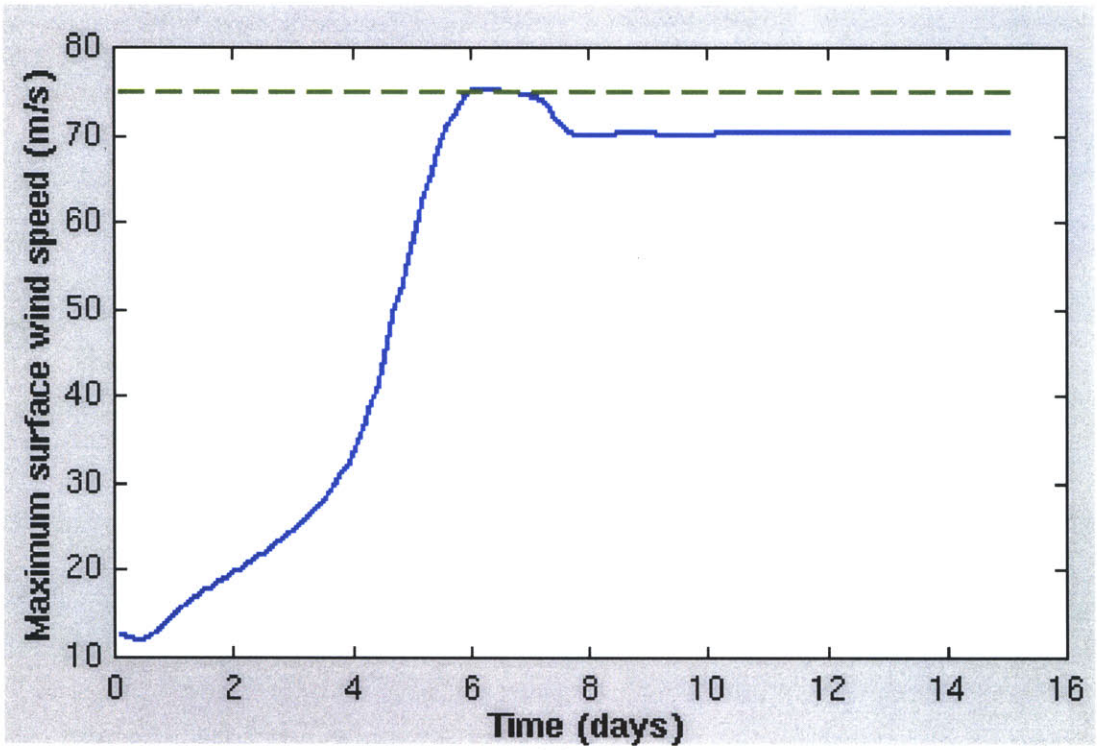

(a)

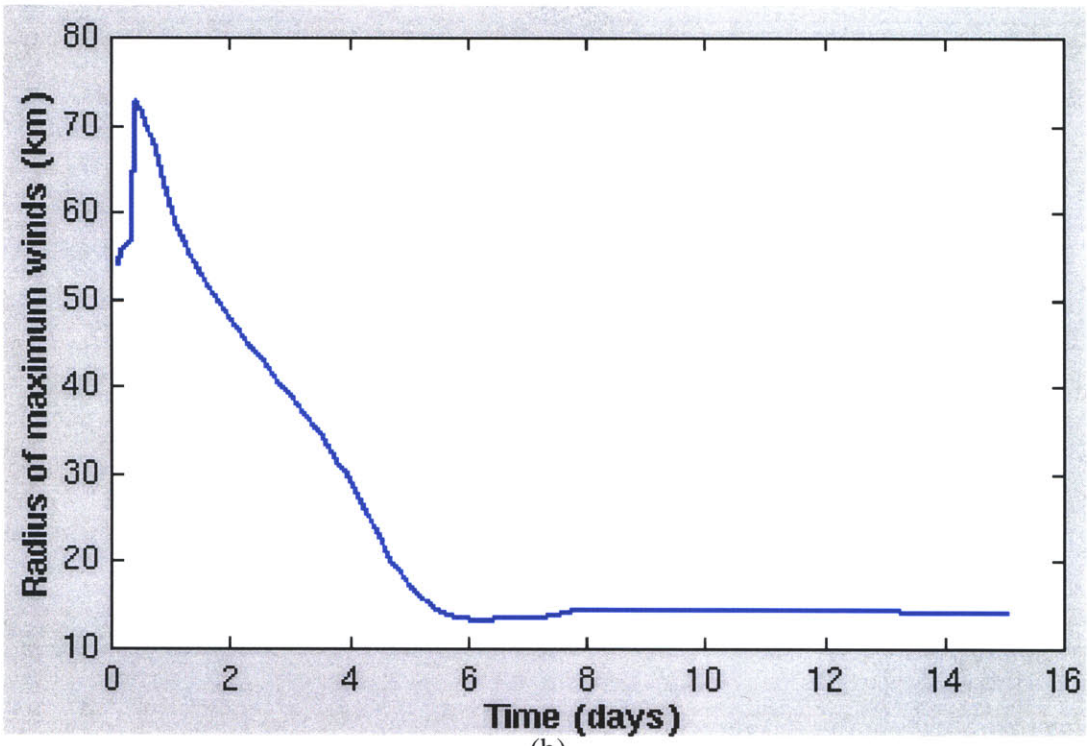

(b)

Figure 2-6:Time evolution of maximum azimuthal surface wind (a) and radius of maximum wind (b) of EX3.

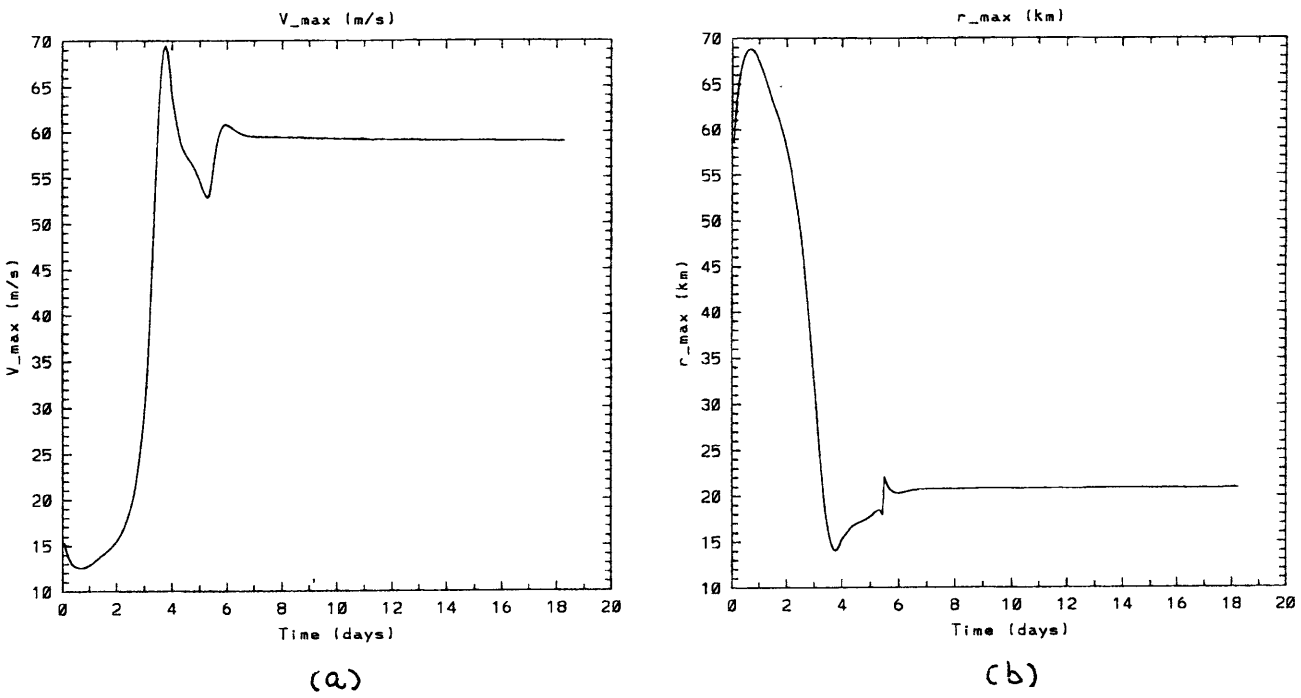

Figure 2-7: Time evolution of v_{max} (a) and r_{max} (b) of EX4.

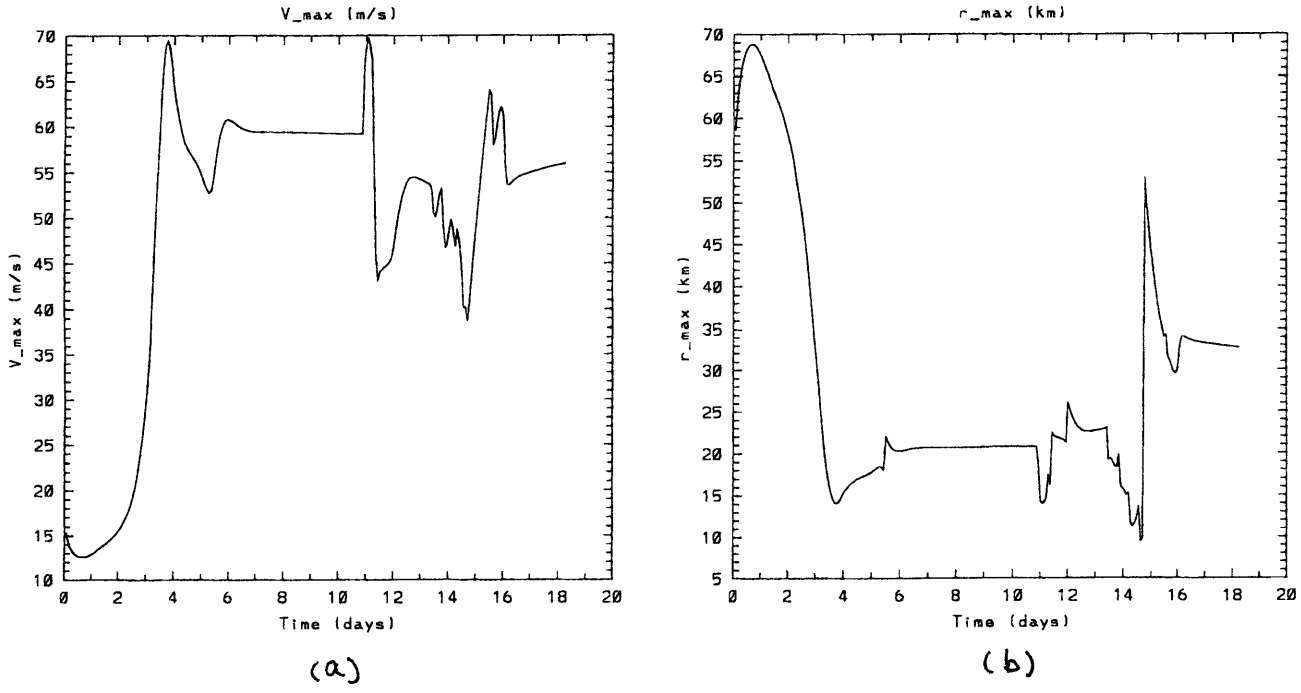

Figure 2-8: Time evolution of v_{max} (a) and r_{max} (b) of EX5.

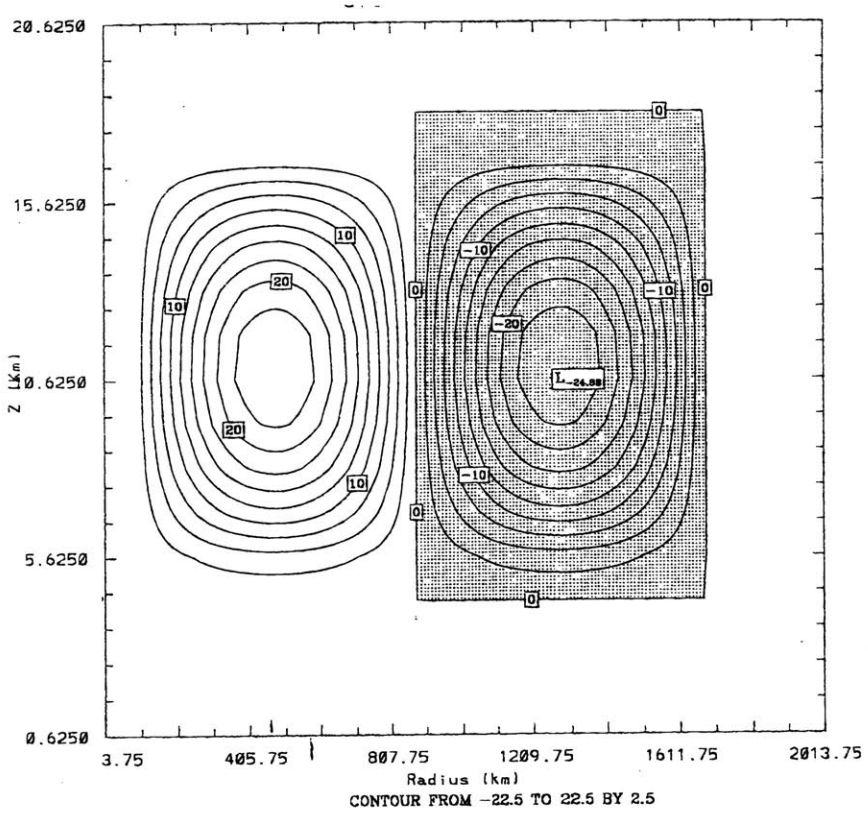

Figure 2-9: Eddy spin up rate at $t = t_{max}$ in EXP3 and EXP4. Negative area is shaded. Unit:m/s/day.

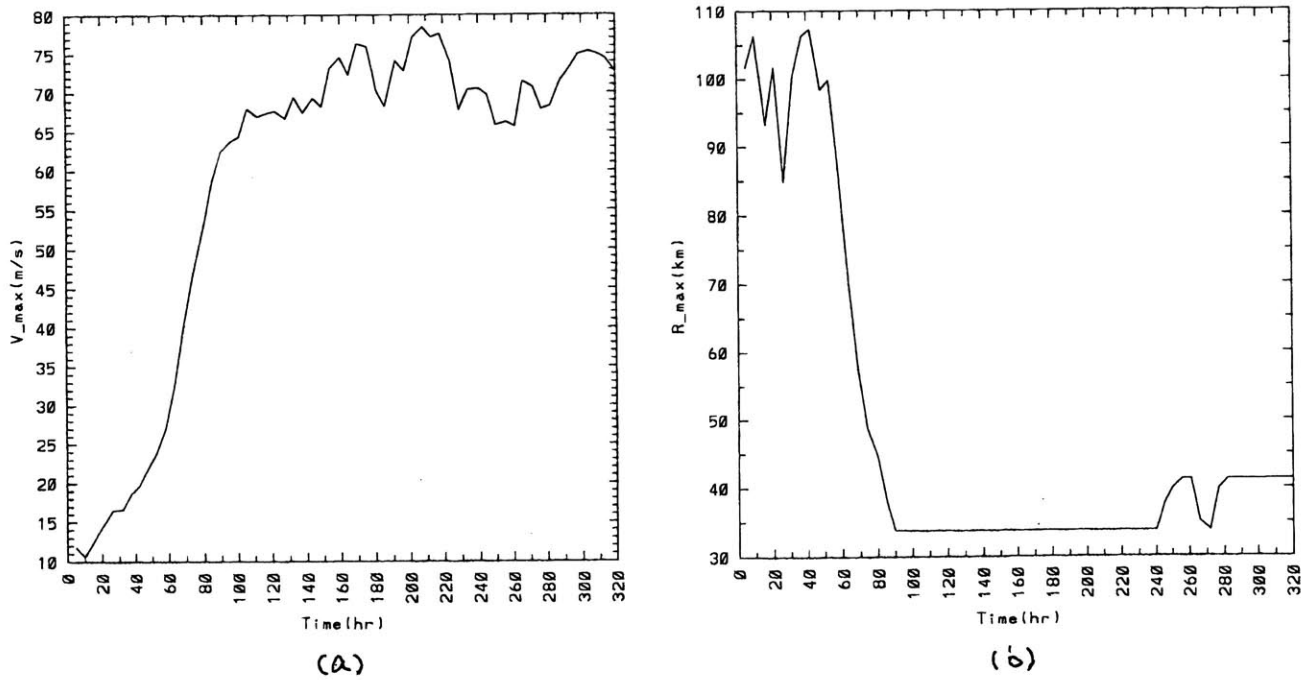

Figure 2-10: Time evolution of v_{max} (a) and r_{max} (b) of EXP1.

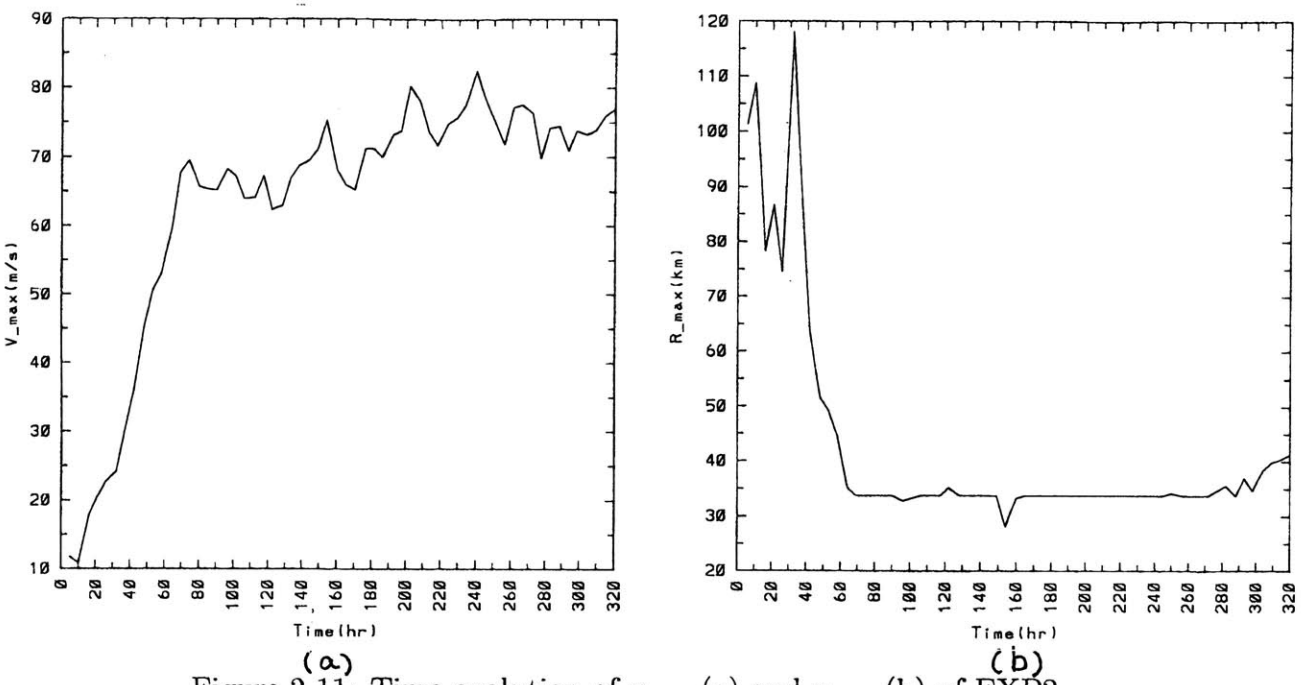

Figure 2-11: Time evolution of v_{max} (a) and r_{max} (b) of EXP2.

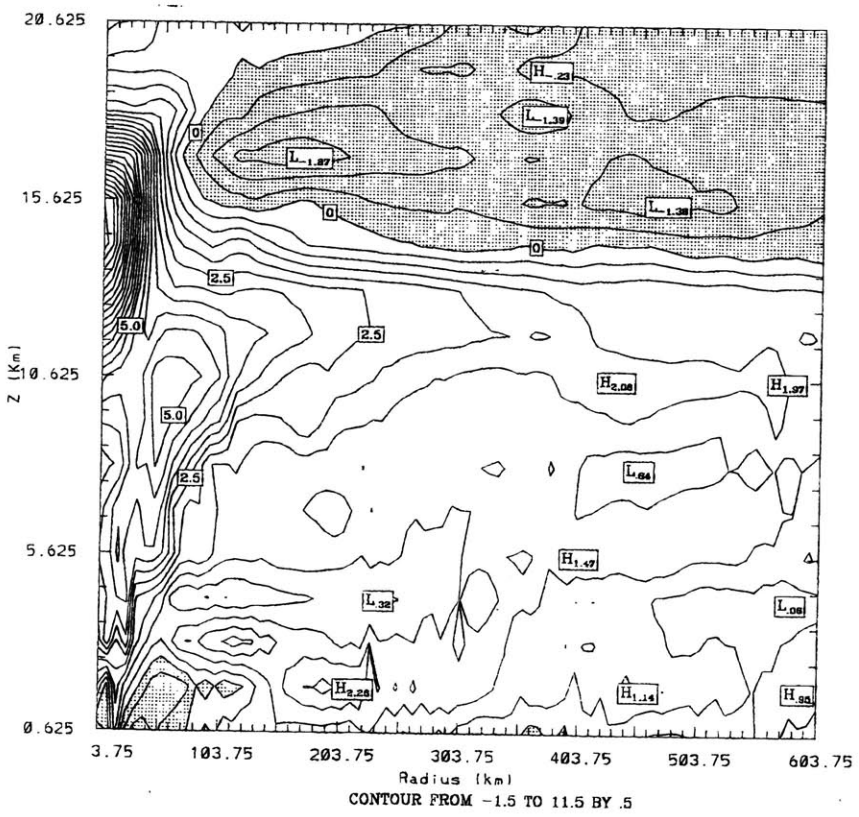

Figure 2-12: Five hour averaged temperature perturbations of EXP1 at t=150 hours. Negative areas are shaded.

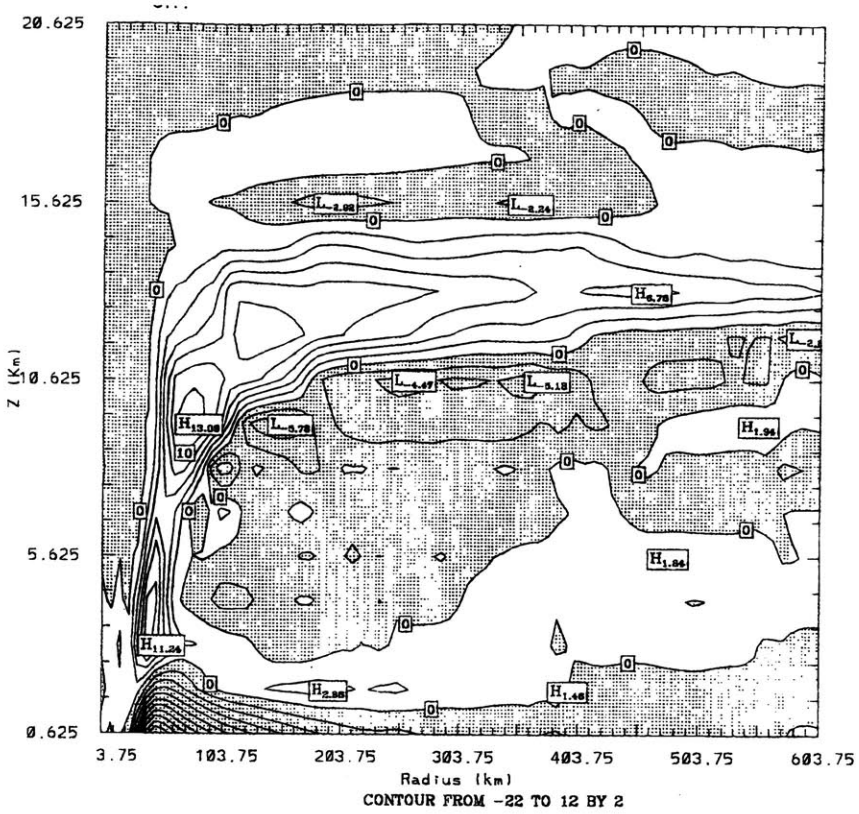

Figure 2-13: Five hour averaged radial velocity of EXP1 at t=150 hours. Negative areas are shaded.

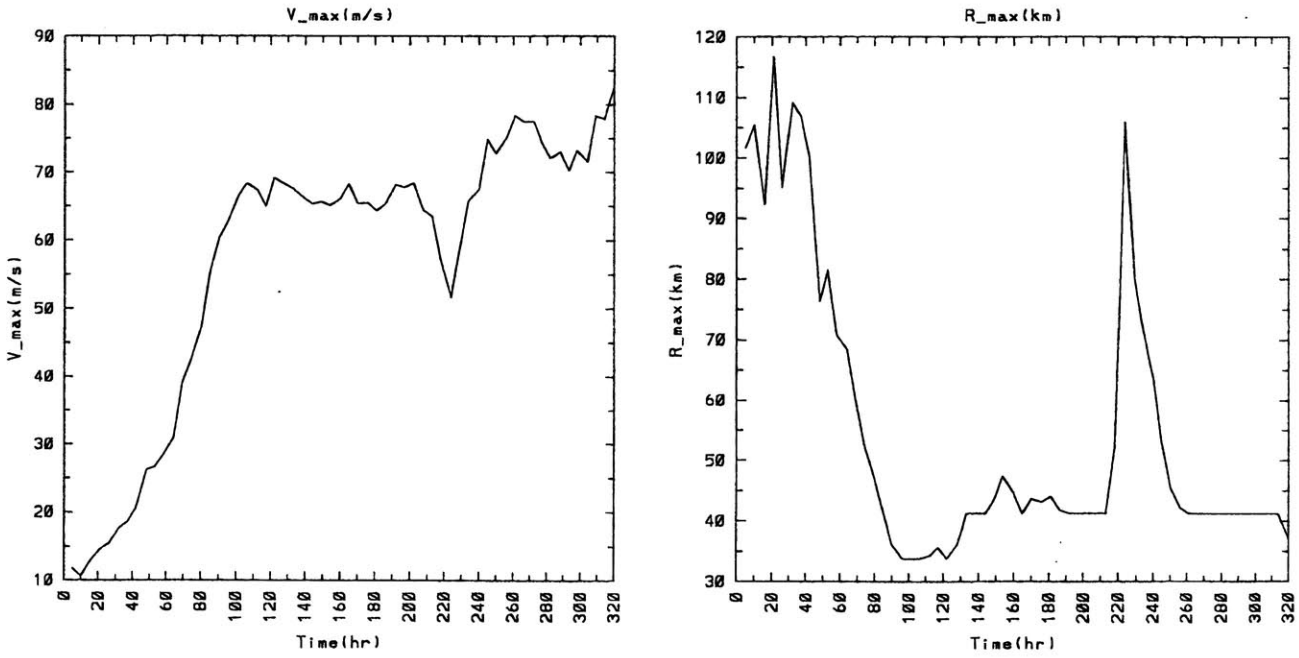

Figure 2-14: Time evolution of v_{max} (a) and r_{max} (b) of EXP3.

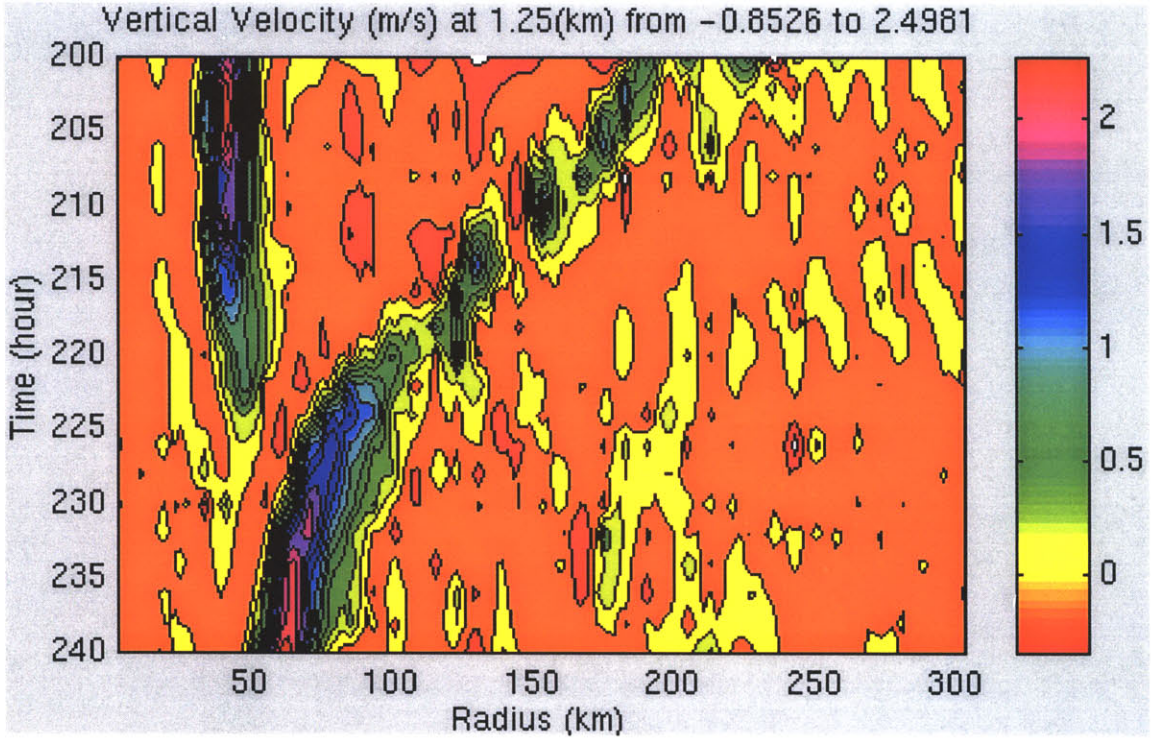

(a)

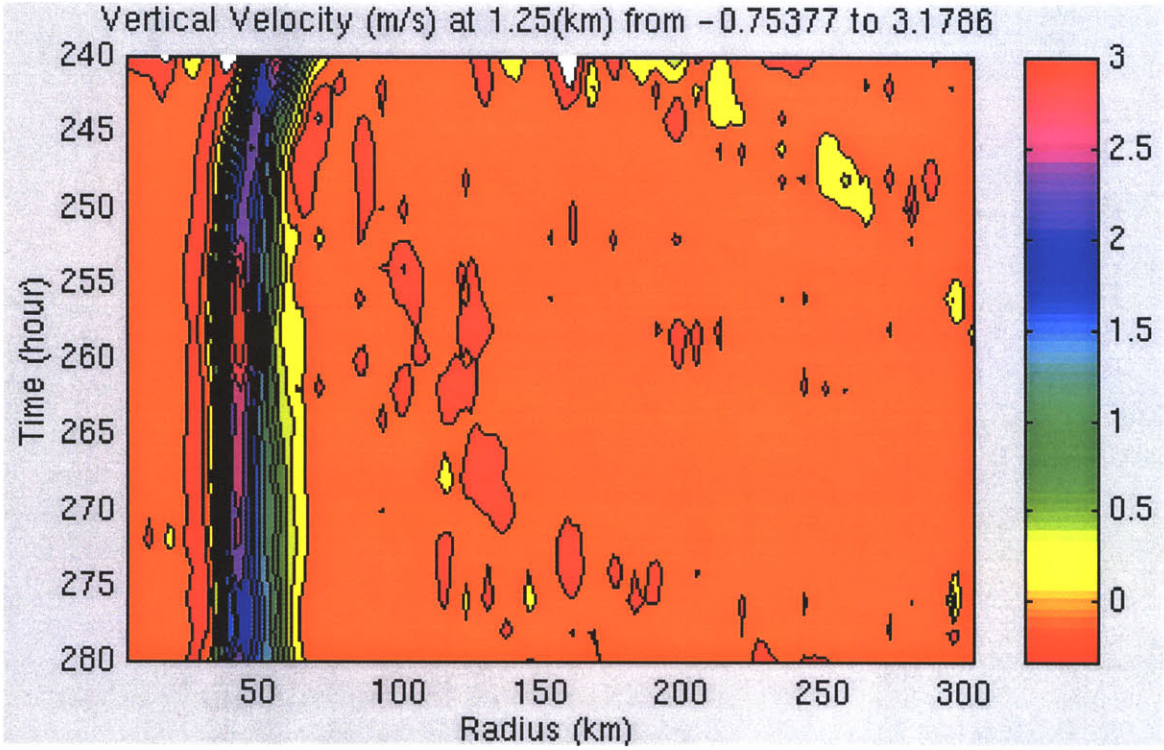

(b)

Figure 2-15: Radius via time plots of vertical velocity of EXP3 at 1250m between 200 and 240 hours (a) and between 240 and 280 hours (b);

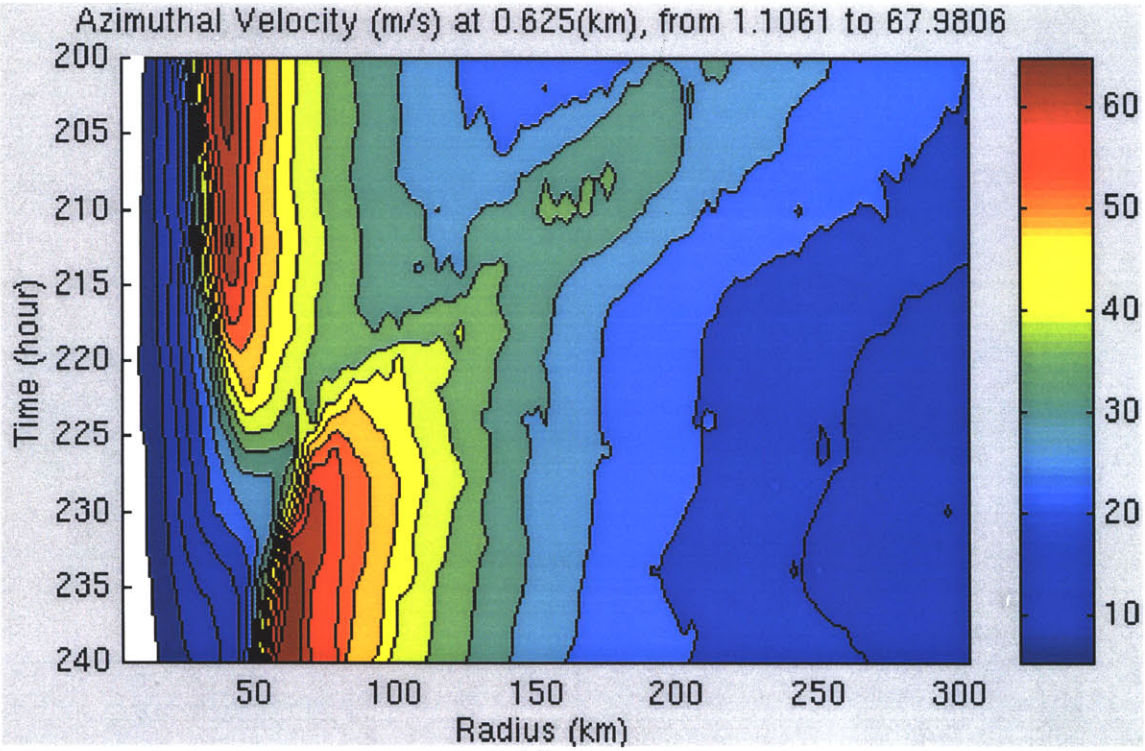

(c)

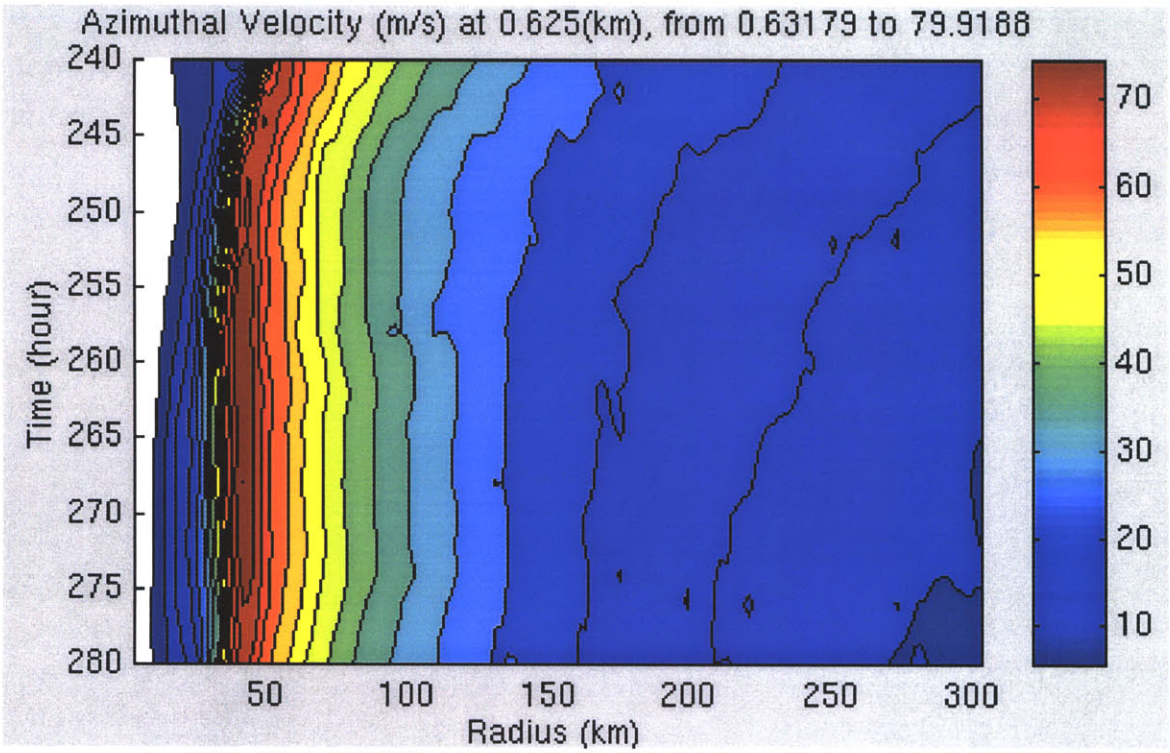

(d)

Figure 2-15:Radius via time plots of azimuthal velocity of EXP3 at 625m between 200 and 240 hours (c) and between 240 and 280 hours (d).

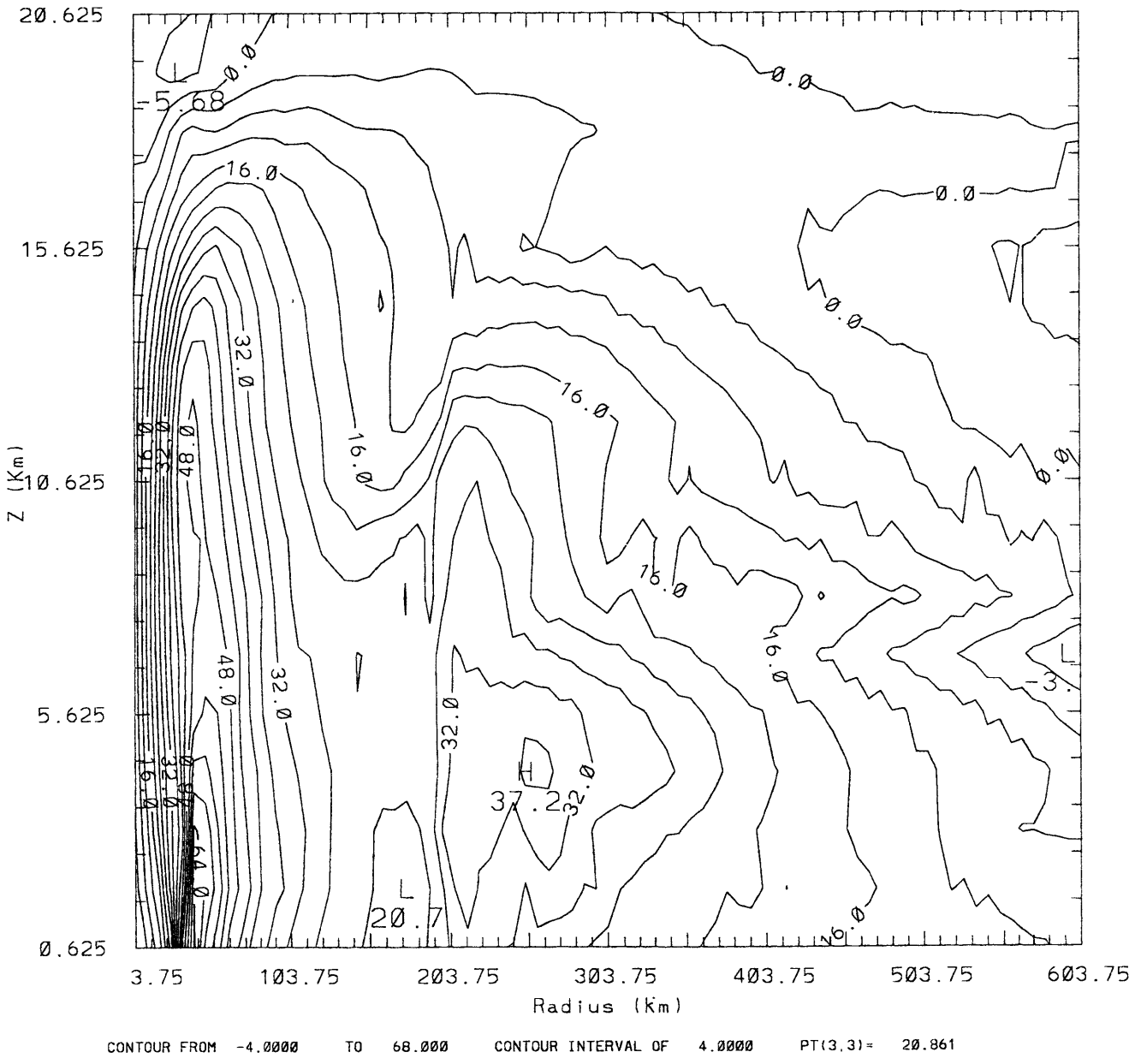

Figure 2-16: (a) Five hour averaged tangential velocity of EXP3 at 200 hours.

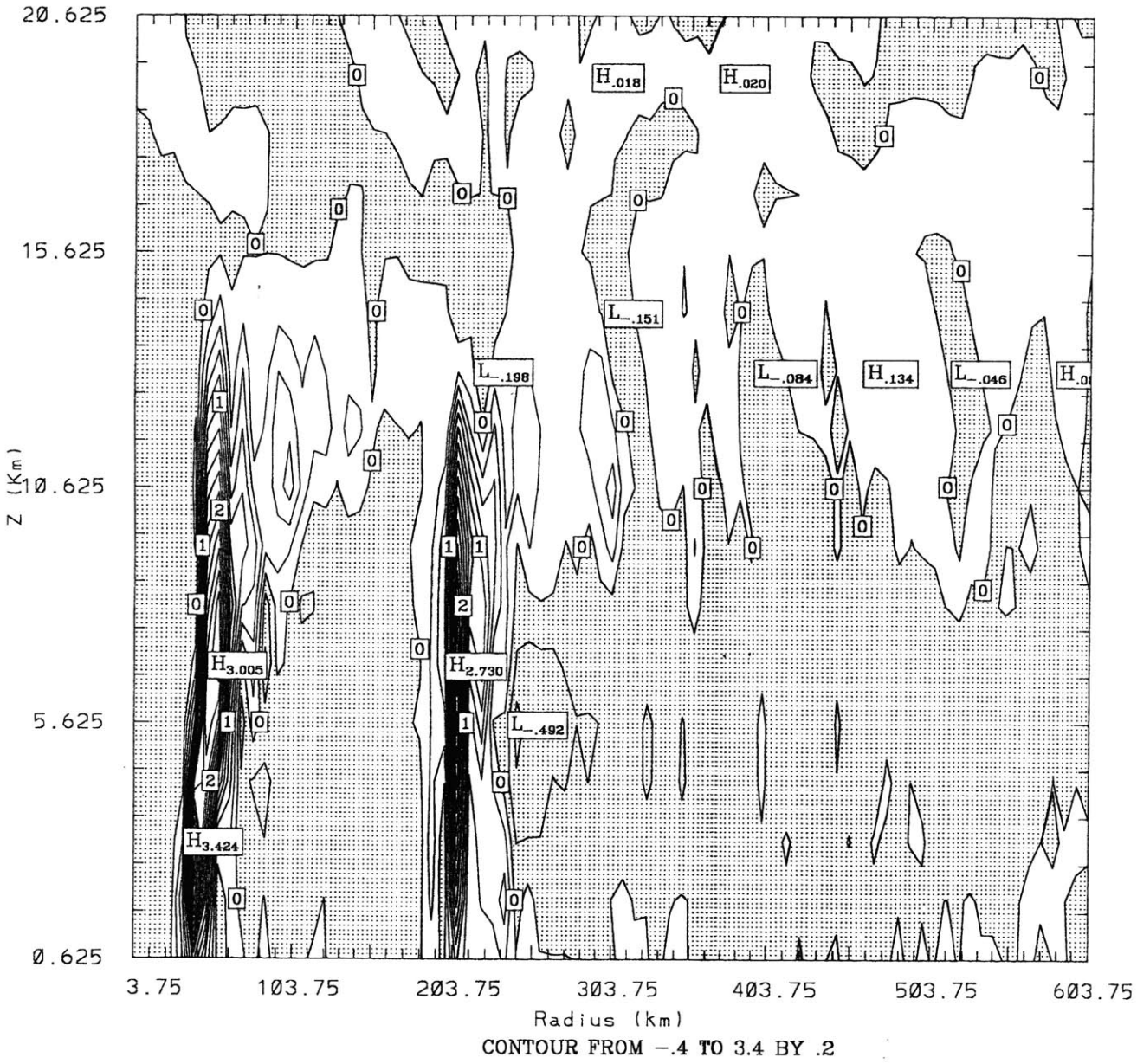

Figure 2-16: (b) Five hour averaged vertical velocity of EXP3 at 200 hours. Negative area are shaded.

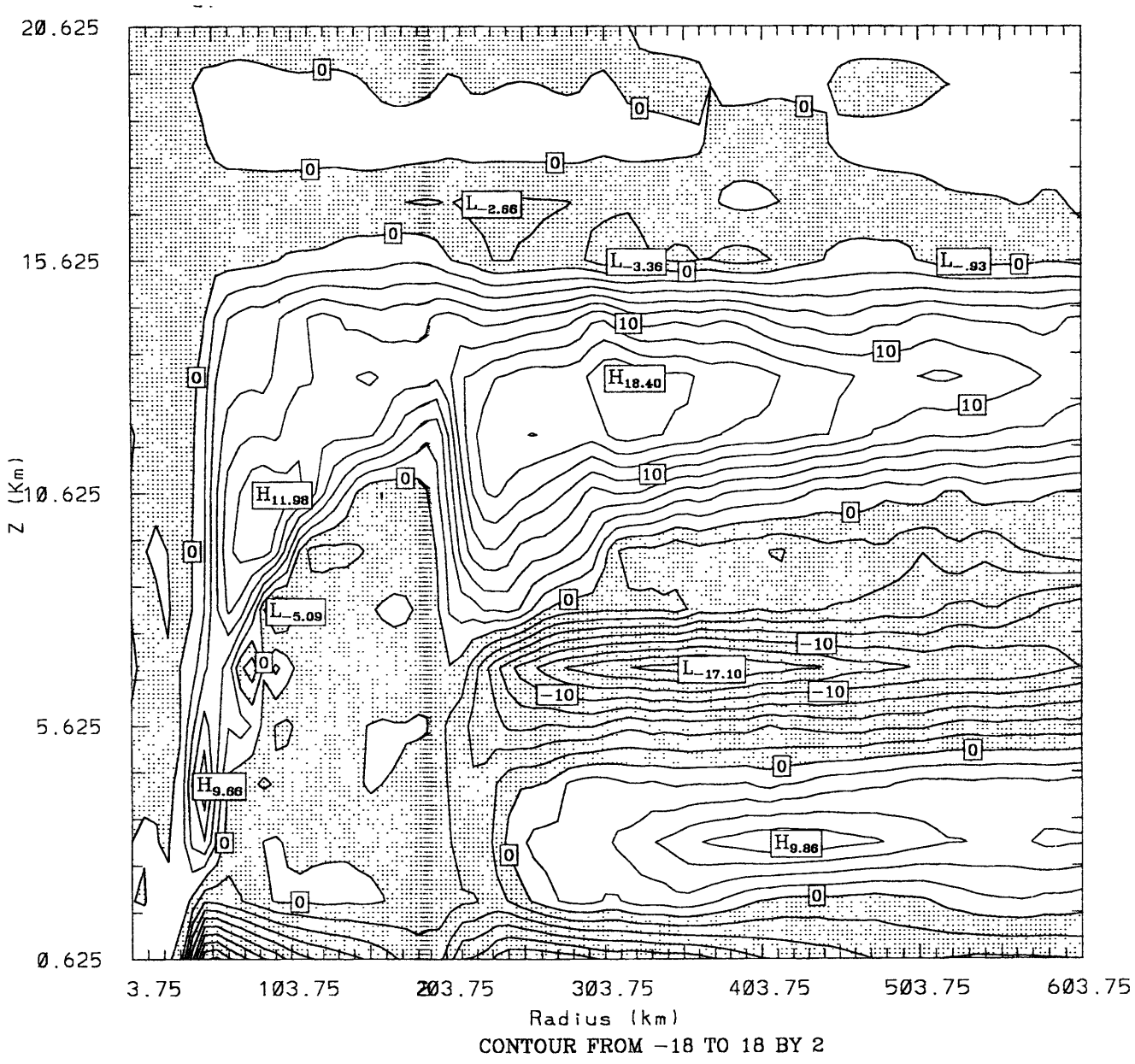

Figure 2-16: (c) Five hour averaged radial velocity of EXP3 at 200 hours. Negative area is shaded.

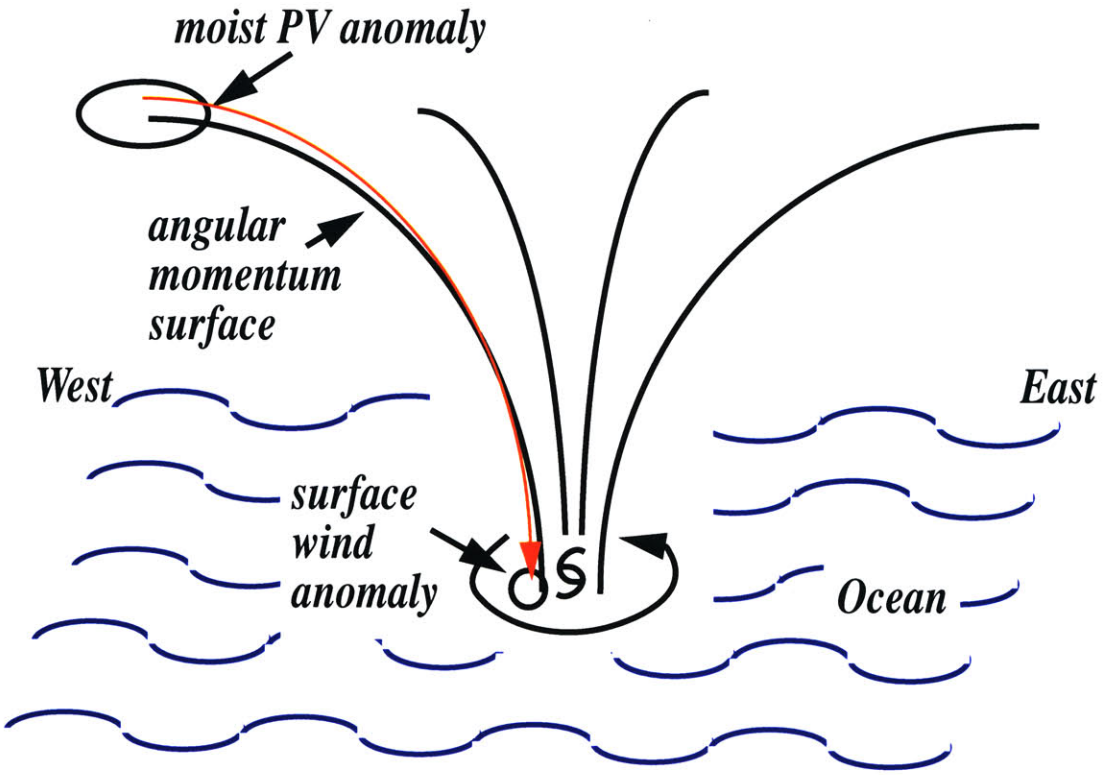

Figure 2-17:Schematic illustration of how an upper-level moist PV anomaly induces a surface wind anomaly. The red arrow indicates that the upper-level PV anomaly projects a cyclonic component downward along the angular momentum surface to the ocean surface. Note that the upper-level PV anomaly is not necessary at the northwest quadrant. It could be at the other quadrants, as pointed out by Prof. Newell at MIT (private communitation).

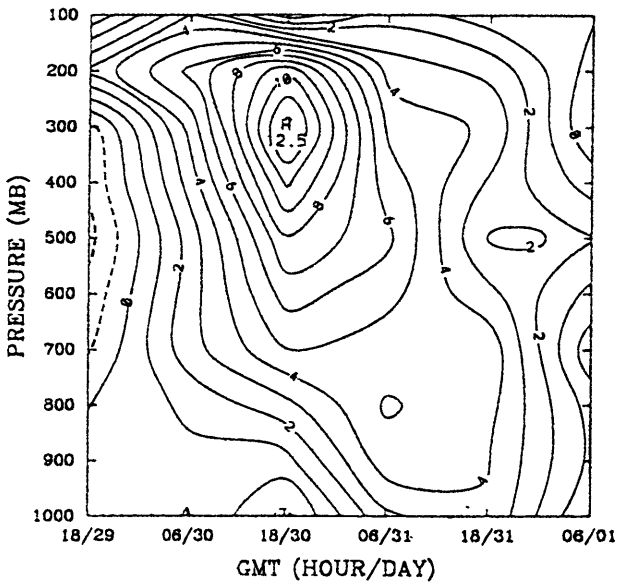

Figure 2-18: Pressure-time series of the time rate of change of the azimuthally averaged tangential velocity at the 500km radius. Values are for 12 hours periods centered on the times shown on the abscissa. Negative contours are dashed.Unit:m/s/day (from Molinari et al.(1990)).

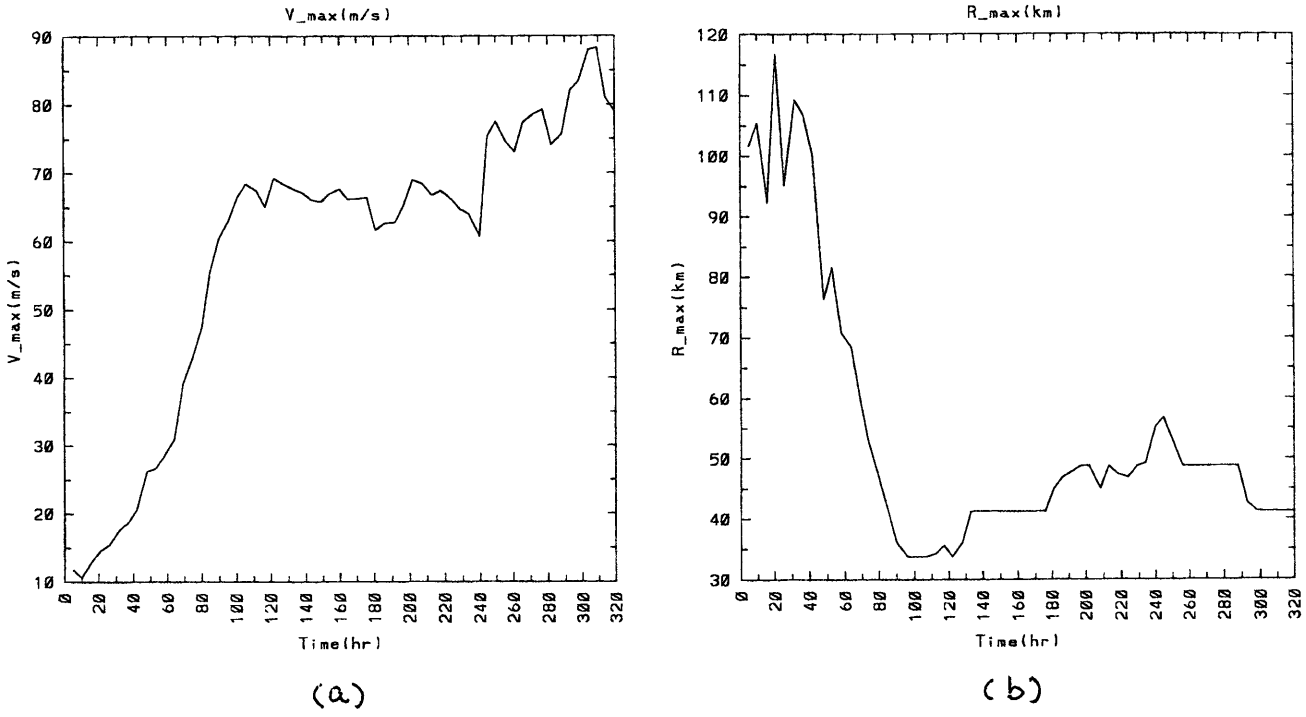

Figure 2-19: Time evolution of v_{max} (a) and r_{max} (b) of EXP4.

Chapter 3

Case Studies

In this chapter we will test our hypothesis by doing case studies. More particularly, by checking isentropic potential vorticity and calculating eddy PV fluxes near the tropopause, we should be able to determine whether an upper-level synoptic-scale percusor always exists before the genesis of a concentric eyewall cyclone.

3.1 Difficulties in the Case Studies of Tropical Cyclones

Tropical cyclones occur predominantly over tropical oceans where observational data are scarce. The destructive nature of tropical cyclones makes their observation not only dangerous but also difficult. It is risky collecting data in an area with intermittent strong upward and downward motion. The difficulties arise not only from the dynamic nature of tropical weather systems including tropical cyclones themselves but also from technical hurdles in the data collection.

Synoptic-scale circulations in the tropics are nearly non-divergent (and thus are well represented by the rotational wind component alone). The scale analysis of Holton (1992) shows that: 1) geopotential perturbations associated with equatorial synoptic-scale disturbances are an order of magnitude smaller than those of mid-latitude systems of similar scale; 2) synoptic-scale temperature fluctuations are prac-

tically negligible for deep tropical systems; 3) in the absence of precipitation, the vertical motion is constrained to be even smaller than in extratropical synoptic systems of a similar scale. In reality, however, weather-producing systems have considerable divergence. The requirement to observe and analyze the divergent component of the wind makes tropical analysis more difficult than that in the mid-latitudes. Also much of the energy of the divergent motions in the tropics is derived from the release of latent heat. Consequently, observations of the moisture field assume a much greater importance than in the midlatitudes.

Secondly, only a weak balance exists between the wind and the mass field in the tropics. The quasi-geostrophic constraint that is essential to analysis in the mid-latitudes is not valid throughout most of the tropics. The observational errors in geopotential height from rawinsondes often obscure the fluctuating signal because of the smallness of the horizontal pressure gradients in the tropics.

Thirdly, as stated in the very beginning of this thesis, tropical cyclones comprise a range of important horizontal scales. The inner core of the mature tropical cyclone has a large gradient of temperature and vorticity over tens of kilometers, whereas the outer circulation may extend to a radius of 2000km. The scale of spiral rainbands is of the order of 100 km. In the vertical direction, the circulation of tropical cyclones extends upward of 18 km. Although the inner core of tropical cyclones is almost symmetric, significant asymmetries exist in the surrounding fields of wind, moisture and convection. The asymmetry occurrs when the tropical cyclones move into a strongly vertically-sheared environment, such as during recurvature into the mid-latitude westerlies; or even when the cyclones are still in the tropics.

In a word, we need simultaneous high-quality three-dimensional wind and thermodynamic data in order to depict the multi-scale kinematic structure of tropical cyclones.

To monitor tropical cyclones today, people use reconnaissance aircraft and conventional observations, which include surface, rawinsonde and radar observations. Conventional data are only available when tropical cyclones are approaching coastal regions, and the tropical cyclones generally spend most of their life cycle over data-

spare areas. So the best way to observe the tropical cyclones is by direct observations from reconnaissance aircraft, particularly for monitoring location and intensity. Much of the knowledge about the inner region of the tropical cyclones has been obtained from aircraft measurements. According to Gray et al. (1991), the aircraft reconnaissance program operated by the U.S. delivers cost-effective accurate observations of tropical cyclones to support both forecasting and research.

But there are shortcomings in the reconnaissance aircraft observations. First, aircraft cannot continuously measure the storm intensity, while, as we have discussed in Chapter 1.1, very substantial fluctuations in intensity occur on time scales as small as 12 hours in association with concentric eyewall cycles. Second, the Air Force C-130's and NOAA WP-3D's are limited to altitudes below 10km. Thus it is impossible to collect data directly in the upper troposphere or lower stratosphere where important interactions between a tropical cyclone and its synoptic environment are likely to happen. A reconnaissance aircraft typically penetrates a tropical cyclone at the 700hPa level ($\sim$3km altitude). If turbulent conditions permit in weaker systems, the aircraft may fly at 500m altitude. Although accurate measurements of 700mb winds are obtained, there are frequently questions regarding the accuracy of the surface winds that must be inferred from these higher-level measurements. Finally, the cost of acquiring and maintaining a dedicated reconnaissance program is high. The U.S. Air Force spends on the order of $35 million annually to perform air reconnaissance of Atlantic hurricanes (Emanuel et al., 1995a). In August 1987, the Department of Defense (DOD) terminated long-standing routine aircraft reconnaissance into tropical cyclones in the northwest Pacific mainly due to budgetary considerations.

Given the above disadvantages of aircraft observations, satellite observations are becoming more and more popular. Since they became available as an observational tool for tropical cyclones in the mid-1960s, satellite-based observations have had an enormous influence on global detection, analysis and forecasting of tropical cyclones. All significant tropical cloud clusters are now routinely observed through both geostationary and polar-orbiting satellites, and those showing signs of organization are closely monitored for intensification. Tropical cyclone forecasters everywhere use

some version of the Dvorak technique (Dvorak (1984)) to estimate the position and intensity of tropical cyclones. In many regions, satellite data serve as the only observational evidence of the existence of a tropical cyclone, and the Dvorak technique is the only method available for analysis.

Although extremely useful and widely used, satellite data cannot be viewed as a complete substitute for conventional and reconnaissance aircraft observations. There are difficulties involved in translating radiance into required parameters for tropical cyclone description. The translation is either a manual or an automatic procedure of subjective interpolations. Martin (1988), Sheets and McAdie (1988), Guard (1988), and Mayfield et al. (1988) compared reconnaissance aircraft and satellite information on positioning and intensity estimates. They have found limits to how accurately the current satellite systems can measure the location and surface wind structure of some tropical cyclones under operational conditions. For example, there were many cases in which the cirrus shield obscures the circulation center in the visible or infrared imagery. Large errors may occur when the Dvorak technique alone is used to estimate the intensity of tropical cyclones. In practice, satellite analysts frequently rely on available aircraft reconnaissance information to calibrate their satellite-derived position fixes. Currently, an aircraft is the only platform that can measure inner and outer radius winds where significant precipitation is occurring. As we have discussed earlier in this section, a good measurement of vertical humidity profiles is needed in order to understand the dynamics of the tropics completely. The key limitation in the remote sensing of humidity fields is the lack of vertical resolution, although fields of total precipitable water can be determined. Some fine-tuning of the satellite profiles is possible if "ground-truth" observations from an independent source are present. This is usually not good enough for any meaningful study.

Special Sensing Microwave/Imager (SSM/I) data became available in July 1987. SSM/I satellites utilize passive microwave sensors to observe radiation emanating from the atmosphere below the cirrus shield. The observed radiance may then be used to estimate parameters such as total content of water vapor, cloud liquid water, precipitation intensity, and regions of convective activity. For example, using 85 GHz

imagery can better locate centers of tropical cyclones than conventional visible or infrared images when the centers are obscured by cirrus overcast. However, there still exist some drawbacks associated with SSM/I data, e.g., contamination of the wind speed signal by atmospheric moisture, an upper limit on wind speed of 25m/s, noisy data, navigation error, and the lack of sensitivity within 50km of a coastline (Foley 1995). Furthermore, SSM/I data are not generally available to most operational forecasting centers as well as ordinary research people like a graduate student at MIT PAOC (personal experience).

In brief, carrying out case studies of tropical cyclones is hindered by the lack of high quality three-dimensional data, the high costs in association with acquiring such data if possible, and the unavailability of the existing data.

3.2 Data Sources

In the past, case studies have been hampered by a scarcity of data. But doing case studies can help gain significant insight into the dynamics of tropical cyclones. Tremendous advances have been made in understanding the dynamics of mid-latitude weather systems through numerous case studies based on observations. As a matter of fact, many researchers have managed to perform observational studies with limited data. Their studies have made marked progress in the knowledge of many aspects of tropical cyclone dynamics.

The purpose of our case studies is to test our hypothesis and to look for any upper-level synoptic-scale precursors before the genesis of concentric eyewalls. To fulfill this purpose, we put forward four basic requirements of dataset. These requirements are: (1) the location of the storm in the data set should be close to its true location in nature, as much as possible; (2) the maximum vorticity with a tropical cyclone should occur at the same point throughout the lower and middle troposphere, as it must in the mature stages of a hurricane; (3) the dataset should have very good coverage at high altitudes; and (4) the dataset should have high time resolution and should be long enough and consistent in time.

The rationales behind these requirements are straightforward. We need to represent a tropical cyclone as correctly as possible in the dataset before we study it. This turns out to be a tough task for existing global numerical models. Demanding good coverage at upper levels ensures the ability to analyze the outflow layer of a tropical cyclone at multiple vertical levels. In the past, data have been available only at 200mb so the vertical structure of the eddy forcing could not be determined, and thus many of their conclusions based on such analyses should be treated cautiously. Any meaningful analysis should include other levels. Finally, we need high time resolution to resolve concentric eyewalls.

Given the above requirements, we have decided to use the reanalysis datasets from NCEP/NCAR and ECMWF. Both datasets have two unique features:

- The length of the period covered is from 1957-1996 for the NCEP/NCAR reanalysis. For the ECMWF reanalysis, the time range is from 1979-1993. The second phase of the ECMWF reanalysis will be from 1958 to the present time. Both reanalyses have 6 hourly data output.

- With a frozen data assimilation system, the datasets assimilate very comprehensive observational data which includes land surface, ship, rawinsonde, pibal, aircraft, satellite, and other data.

These two features meet the last two requirements of our study. We will check the first two requirements with calculations.

There are several benefits of using the reanalysis datasets. The first is that it allows us to bypass the steps of data collection, data quality determination, and objective analysis. The second one is that the reanalyses take advantage of sophisticated initialization techniques which insure that wind and mass fields obey some dynamical balances. The last one is that reanalyses use the strength of one observational method to offset the weakness of another one through the assembly of all available observational data.

Before we evaluate the reanalysis datasets, we would like to introduce them based on the report written by Kalnay et al. (1996, hereafter K96) and ECMWF reanalysis

web site[1]. Details of the NCEP/NCAR reanalysis are can be found in K96.

3.2.1 An Overview of the NCEP/NCAR Reanalysis

The NCEP/NCAR Reanalysis Project is a joint project between the National Centers for Environmental Prediction (NCEP, formerly known as the National Meteorological Center (NMC)) and the National Center for Atmospheric Research (NCAR). The goal of this joint effort, according to K96, is to produce new atmospheric analyses using historical data (1957 onwards) and as well to produce analyses of the current atmospheric state. The reanalysis system consists of three main components: the data preprocessor, the data assimilation module and the reanalysis distribution module.

The data preprocessor reformats the data coming from many different sources into a uniform BUFR(binary universal format representation) format before the execution of the assimilation module. The data used in the reanalysis are: global rawinsode data, COADS (Comprehensive Ocean-Atmosphere Data Set) surface marine data, aircraft data, surface land synoptic data, satellite sounder data, satellite cloud drift winds and SSM/I surface wind speeds [2].

The preprocessor also prepares the surface boundary conditions (SST, sea ice, etc.). The following analyses and climatologies are used for the boundary fields: optimal interpolation SST reanalysis (Reynolds and Smith (1994)) starting from 1982 and UKMO (United Kingdom Meteorological Office) GISST (Global Ice and Sea Surface Temperature dataset) for earlier periods, NESDIS weekly snow cover analyses and climatology, SSMR (Scanning Multichannel Microwave Radiometer)/SSMI derived sea ice, albedo from Matthews (1985), soil wetness updated during the analysis cycle[3], and SiB (Simple Biosphere Model) roughness length and vegetation resistance.

The central module is the data assimilation, which has the following characteris-

[1]The web address of ECMWF reanalysis is http://www.ecmwf.int/html/ERA/index.html.

[2]Due to technical problems, SSM/I winds have not been used in the first phase of the reanalysis. The SSM/I winds will be used in the second phase of the reanalysis

[3]Soil moisture is not nudged when concurrent data is used. A very small coefficient is used to nudge the soil moisture toward climatology. Interannual variability but no long-term drift is found in soil moisture fields.

tics:

1. The T62[4]/28-level NCEP global spectral model is used in the assimilation system, as implemented in the NCEP operational system in December 1994. The model equations are in the sigma coordinate system. There are five vertical levels in the boundary layer and about seven levels above 100hPa. The model consists of parameterizations of all types of clouds, boundary layer physics, and an interactive surface hydrology, and vertical and horizontal diffusion processes. The convection scheme is a simplified Arakawa-Schubert convective parameterization scheme developed by Pan and Wu (1994) and based on Grell (1993).

2. The spectral statistical interpolation (SSI), a three-dimensional variational analysis scheme (Parrish and Derber 1992; Derber et al. 1991), is used as the analysis module. An important advantage of SSI is that the balance imposed on the analysis is valid throughout the globe, thus obviating nonlinear normal-mode initialization. Since its final implementation in January 1995, SSI has led to major improvements in analysis and forecast, especially in the Tropics, and a major reduction in the precipitation spinup. The analysis scheme also includes improved error statistics and the use of the full tendency of the divergence equation in the cost function.

3. Several quality control methods are employed to ensure the quality of the input data. The complex quality control (CQC) method is used to control the quality of the rawinsonde heights and temperatures. The OIQC (optimal interpolation quality control) method screens all final observational data that will be assimilated into the model. The optimal averaging method computes temporal and spatial averages of several parameters over a number of prescribed areas, which provides more accurate averages and estimates of the average (Gandin 1993).

4. One-way coupled ocean model 4D assimilation is used for the time after 1982.

[4]equivalent to a horizontal resolution of about 210km

The last main component of the reanalysis system is the data output and distribution. The major part of the output is archived in synoptic format. The data is output at four synoptic times, 0000, 0600, 1200 and 1800UTC, on a 2.5^o latitude-longitude grid. The original model output is on sigma levels, but is interpolated to 17 pressure levels. These levels are 1000.0mb, 925.0mb, 850.0mb, 700.0mb, 600.0mb, 500.0mb, 400.0mb, 300.0mb, 250.0mb, 200.0mb, 150.0mb, 100.0mb, 70.0mb, 50.0mb, 30.0mb, 20.0mb, and 10.0mb. This thesis will use the pressure level data[5].

3.2.2 An Overview of ECMWF Reanalysis

ECMWF used the following observational data sources in their first phase reanalysis project:

- ECMWF archive of real time WMO World Weather Watch data (3 day cut-off);
- COADS ship and buoy observations;
- FGGE (First GARP (Global Atmospheric Research Program) Global Experiment (1979)) and ALPEX Level II-B data;
- TOGA COARE data,
- Australian PAOB surface pressure pseudo-observations from the Bureau of Meteorology;
- NOAA TOVS (TIROSN Operational Vertical Sounder) cloud cleared radiance data from 1979 to 1993;
- GMS (geostationary meteorological satellite) cloud winds, AIREP and TEMP data supplied by Japan Meteorological Agency;
- NOAA SST analyses after November 1981, and UKMO's SST analyses for the early period; Sea ice cover derived from SMMR and SSM/I data.

[5]The data was originally obtained from CDC on tapes. But due to a technical difficulty in retrieving data from the tapes at MIT PAOC, we had to copy the whole datasets ($\sim 80GB$) bit by bit from Jeremy Pal at Parsons Laboratory of MIT who generously offered the source tapes and his tape drive.

The ECMWF reanalysis data assimilation system is a special version of the ECMWF operational data assimilation system. The reanalysis system includes:

- A spectral T106 ($\sim 1.125^o$ latitude-longitude resolution) forecast model with 31 hybrid vertical levels, and a full three-dimensional semi-lagrangian advection scheme.

- Intermittent statistical optimum interpolation analysis with a cycle of 6 hours and no FGAT.

- A diabatic, non-linear normal mode initialization scheme which has five modes vertically.

- One dimensional variational (1D-VAR) physical retrieval of TOVS satellite radiance below 100hPa, and NESDIS operational retrievals above. No TOVS data are used above 100hPa between 20^oN, and 20^oS.

- A physical parameterization package which has:

  - a planetary boundary layer whose parameterization is based on similarity;
  - mean orography with a compatible parameterization taking into account the effects of sub-grid scale orography;
  - a four-layer prognostic soil temperature and soil moisture scheme without any external forcing but with nudging of the moisture from boundary layer atmospheric humidity analyses;
  - an interactive cloud/radiation scheme including the representations of cloud water content, ice content and cloud cover;
  - ECMWF operational radiation parameterization scheme in which the concentrations of aerosols, CO_2 and O_3 are prescribed. The concentration of O_3 varies geographically and seasonally; the aerosols are geographically and vertically dependent. The CO_2 is held constant.

This thesis will use the 6 hourly data on 17 pressure levels[6]. The resolution of the data has been reduced to 2.5^o latitude-longitude by ECMWF [7].

3.3 Equations for Calculating Eddy Fluxes

Following an air parcel, we can express the time rate change of Ertel's potential vorticity q in the following general form:

$$\frac{dq}{dt} = Source - Sink, \tag{3.1}$$

where typical sources and sinks arise from the processes such as condensation, evaporation, radiation and friction (including turbulent mixing). The expression for q in an isobaric coordinate system is:

$$q = -g(f\mathbf{k} + \nabla_p \times \mathbf{v}) \cdot \nabla_p \theta. \tag{3.2}$$

where $\mathbf{k}$ is a unit vertical vector, $\mathbf{v}$ is the three-dimensional velocity, θ is the potential temperature, and ∇_p is the three-dimensional gradient operator in the pressure coordinate system.

In observational studies of tropical cyclones, it is necessary to develop the equations in a storm-following coordinate (Molinari et al., 1993) in order to produce correct flux terms. Molinari and his colleagues calculated all eddy flux quantities such as the eddy relative angular momentum fluxes and convergence, and the eddy potential vorticity fluxes and convergence, in the coordinate moving with the storm. For the convenience of comparison and for the reasons we will present below, we will follow the pratical rule in this thesis and choose to calculate all eddy quantities in a cyclindrical coordinate system moving with a tropical cyclone.

[6]Upper air levels, 1000mb, 925mb, 850mb, 775mb, 700mb, 600mb, 500mb, 400mb, 300mb, 250mb, 200mb, 150mb, 100mb, 70mb, 50mb, 30mb, and 10mb.

[7]The original output is in 1.125^o resolution. But 2.5^o resolution output is the only available ECMWF reanalysis data currently at NCAR. The data were kindly provided by Prof. Chang at MIT PAOC who retrieved the data.

In the storm-following coordinate system, we can rewrite Equation 3.1 in flux format:

$$\frac{\partial q}{\partial t} = -\frac{1}{r}\frac{\partial(ruq)}{\partial r} - \frac{1}{r}\frac{\partial(vq)}{\partial \lambda} - \frac{\partial(\omega q)}{\partial p} + Source - Sink \tag{3.3}$$

where u,v,and ω are radial, tangential, and vertical velocity components in the cylindrical coordinate system r (radius), λ (azimuth), and p (pressure). We have made use of the continuity equation when deriving the above equation.

Next we define

$$u(r,\lambda,p,t) = \overline{u}(r,p,t) + u^{'}(r,\lambda,p,t) \tag{3.4}$$

$$v(r,\lambda,p,t) = \overline{v}(r,p,t) + v^{'}(r,\lambda,p,t) \tag{3.5}$$

$$\omega(r,\lambda,p,t) = \overline{\omega}(r,p,t) + \omega^{'}(r,\lambda,p,t) \tag{3.6}$$

$$q(r,\lambda,p,t) = \overline{q}(r,p,t) + q^{'}(r,\lambda,p,t) \tag{3.7}$$

where

$$\overline{(\,)} = \frac{1}{2\pi}\int_0^{2\pi}(\,)d\lambda. \tag{3.8}$$

Substituting the above equations into Equation 3.3 and azimuthally averaging gives the final form of the equation for azimuthal mean storm-relative Ertel's PV

$$\frac{\partial \overline{q}}{\partial t} = -\frac{1}{r}\frac{\partial(r\overline{u}\,\overline{q})}{\partial r} - \frac{\partial(\overline{\omega}\,\overline{q})}{\partial p} - \frac{1}{r}\frac{\partial(r\overline{u'q'})}{\partial r} - \frac{\partial(\overline{\omega'q'})}{\partial p} + \overline{Source - Sink}. \tag{3.9}$$

The right-hand-side terms represent, respectively, the lateral and vertical flux convergence of Ertel's PV by the azimuthal mean flow, the lateral and vertical storm-relative eddy flux convergence and the azimuthally averaged source and sink terms.

We then integrate over the cyclone mass and apply Gauss' divergence theorem to derive a formulation for the lateral eddy PV flux (or EPF for short) as

$$EPF = \int_{p_1}^{p_2}\int_0^{2\pi}\int_0^{r}(-\frac{1}{r}\frac{\partial(r\overline{u'q'})}{\partial r})rdrd\lambda(-\frac{dp}{g}) = -\frac{2\pi r}{g}\int_{p_2}^{p_1}\overline{u'q'}dp. \tag{3.10}$$

where p1 and p2 are the pressures at two different altitudes. In the following calculation, p1 is equal to 1000mb and p2 70mb.

To calculate EPF from the reanalysis datasets, we approximate Ertel's potential vorticity by neglecting the products of horizontal vorticity components and horizontal gradients of potential temperature. Our calculations show that the error owing to this neglection is less than 5 percent of entire Ertel's potential vorticity north of 10^oN where the upper-level interaction is normally observed. So we believe that such neglect is acceptable. It greatly simplifies our calculation of EPF. The approximated Ertel's potential vorticity (or AEPV for short) takes the following form:

$$AEPV = -g[f + \frac{\partial(rv)}{r\partial r} - \frac{\partial u}{r\partial\lambda}]\frac{\partial\theta}{\partial p}, \tag{3.11}$$

where the Coriolis parameter f is evaluated at the storm center. As a consequence, the approximated EPF (or AEPF for short) is expressed as:

$$\begin{aligned} AEPF &= -\frac{2\pi r}{g}\int_{p_2}^{p_1}\overline{u'(AEPV)'}dp, \\ &= A + B + C + D + E + F + G; \end{aligned} \tag{3.12}$$

where Terms A, B, C, D, E, F, and G are:

$$A = 2\pi\int_{p2}^{p1}\frac{\partial(r^2\overline{u'v'})}{r\partial r}\frac{\partial\overline{\theta}}{\partial p}dp, \tag{3.13}$$

$$B = -2\pi\int_{p2}^{p1}\overline{rv'\frac{\partial ru'}{r\partial r}}\frac{\partial\overline{\theta}}{\partial p}dp, \tag{3.14}$$

$$C = 2\pi\int_{p2}^{p1}[f + \frac{\partial(r\overline{v})}{r\partial r}]\overline{ru'\frac{\partial\theta'}{\partial p}}dp, \tag{3.15}$$

$$D = 2\pi\int_{p2}^{p1}r\overline{u}\overline{\frac{\partial(rv')}{r\partial r}\frac{\partial\theta'}{\partial p}}dp, \tag{3.16}$$

$$E = -2\pi\int_{p2}^{p1}r\overline{u}\overline{\frac{\partial u'}{r\partial\lambda}\frac{\partial\theta'}{\partial p}}dp, \tag{3.17}$$

$$F = 2\pi\int_{p2}^{p1}\overline{ru'\frac{\partial(rv')}{r\partial r}\frac{\partial\theta'}{\partial p}}dp, \tag{3.18}$$

$$G = -2\pi\int_{p2}^{p1}\overline{ru'\frac{\partial u'}{r\partial\lambda}\frac{\partial\theta'}{\partial p}}dp. \tag{3.19}$$

In above equations, we have defined and use

$$\theta(r, \lambda, p, t) = \overline{\theta}(r, p, t) + \theta'(r, \lambda, p, t) \tag{3.20}$$

In Equation 3.12, Term A is the vertical integral of the product between the azimuthal mean stability and the lateral convergence of eddy relative angular momentum fluxes; Term B is the vertical integral of the product between the mean stability and the correlation between the lateral eddy convergence and the eddy relative angular momentum; Term C is the vertical integral of the product between the mean absolute vertical vorticity and the radial advection of eddy stability by the eddy circulation; the sum of Terms D and E is the vertical integral of the product between the mean radial velocity and the correlation between the eddy vertical relative vorticity and the eddy stability; the sum of Terms F and G is the vertical integral of the azimuthal average of the eddy radial transportation of the correlation between eddy vertical relative vorticity and the eddy stability. Except for Terms A and B which involve the mean stability, the other terms involve the vertical derivative of eddy potential temperature.

To derive eddy relative angular momentum fluxes (or ERAMF for short), we multiply Equation 2.4 by the radius r and integrate over the cyclone mass. After applying the Gauss' divergence theorem again to the integral, we have the formulation for ERAMF as:

$$ERAMF = -\frac{2\pi r^2}{g} \int_{p2}^{p1} \overline{u'v'} dp. \tag{3.21}$$

So ERAMF is the volume integral of relative angular momentum by the Lagrangian azimuthal eddies at a certain radius. Compared with Equation 3.13, we can see that the lateral convergence ERAMF is part of Term A in Equation 3.12.

Our calculation procedure consists of the following steps: (1) A bicubic spline technique is used to interpolate data on the original 2.5 degree latitude-longitude grid to a new 1.0 degree latitude-longitude grid; (2) The position and the translation speed of the storm are derived from the best track data archive which will be introduced below; (3) the bicubic spline technique is employed again to interpolate data from

1^o-grid to a grid moving with a tropical cyclone;(4) storm-relative winds can then be computed; (5) the bicubic spline technique is used again to interpolate data from the moving latitude-longitude grid to a cylindrical grid with 0.5 latitude degree [8] radial and 10^o azimuthal resolution, out to a radius of 20 latitude degree; (6) various eddy terms are then calculated within this cylindrical grid. Effects of the earth's curvature are neglected in the calculations. According to Molinari and Vollaro (1989), this will only bring a maximum error in radial distance of 3.1% around 20 latitude degree radius.

3.4 Evaluation of Data

Before we proceed with case studies, it is wise to evaluate our datasets first. For convenience, we abbreviate the NCEP/NCAR reanalysis to NNRA and the ECMWF reanalysis to ERA. Unless we specify otherwise, all our calculations are done using the NNRA's dataset.

The tracks of the tropical cyclones studied in this thesis are based on the best track data archive available from National Hurricane Center (NHC) and National Climatic Data Center[9]. The best track data consist of the latitude and longitude of the tropical cyclone center, central pressure and maximum wind speed every 6 hours. All "best track" statistics are determined in a post-analysis of all available data by NHC.

Since we do not have real synoptic observational data for hurricanes, we have to compare our calculations with other observational results. After a thorough search of the literature, we have found the following observational case studies on the synoptic environment of tropical cyclones. These cases are Hurricane Debby of 1982 by Lord and Franklin (1987, hereafter LF87), Hurricane Elena of 1985 and Hurricane Allen of 1980 by Molinari and his colleagues, and Hurricane Gabrielle and Dean of 1989 by DeMaria et al.(1993, hereafter D93). Among these hurricanes, Elena, Allen and

[8]The length of 1 latitude degree is 111 km.

[9]One may access the best track data at http://weather.unisys.com/hurricane/atlantic/index.html

Gabrielle have been reported as having concentric eyewall cycles in their life time. Dean is the only Category 2 hurricane which is the weakest tropical cyclone among these five hurricanes. Debby was a Category 4 hurricane. The categories for the other three can been found in Chapter 1.1.

3.4.1 Hurricane Debby of 1982

Figs. 3.1 and 3.2 show the fields of relative vorticity (vertical component) and horizontal divergence at 0000UTC 16 September at 850mb, 500mb and 200mb of Hurricane Debby (LF82). To satisfy the boundary condition $\omega = 0$ at the surface and p=100mb, Lord and Franklin corrected the horizontal divergence by adding a constant divergence at all analysis levels. At 0000UTC 16 September, Debby was located at 30.5^{o}N and 67.5^{o}W and had a central pressure of 966mb with an observed maximum wind of 50m/s. Two days later, Debby reached its maximum intensity with maximum sustained winds of 58m/s and a minimum central pressure of 950mb.

The primary data sources for the analysis were from Omega dropwindsondes (ODWs) dropped during the Synoptic-Flow Experiment (SFE) from 1900UTC 15 September to 0300UTC 16 September, rawinsondes in the continental United States and Carribean, and VAS (Visible Infrared Spin-Scan Radiometer Atmospheric Sounder) satellite-derived winds. Supplementary data were NOAA WP-3D flight-level data, surface data from ships of opportunity, commercial aircraft winds, and flight-level data and dropsondes from USAF C-130 reconnaissance aircraft, and National Meteorological Center (NMC) operational analyses at 100mb and 150mb. Detailed descriptions of the data sources and the preliminary processing and error-checking procedures can be found in LF87. The basic analysis method in LF87 is a two-dimensional least-square fitting algorithm together with a derivative constraint serving as a spatial low-pass filter on the analyzed field (Ooyama, 1987).

At both 800mb and 500mb pressure surfaces (Figs. 3.1a and 3.1b), the vorticity maxima associated with Debby are well defined. At the 200mb level (Fig. 3.1c), there is no distinct feature connected to the hurricane itself. The maximum vorticity is related to a cutoff low which formed previously and was the primary subject of

interest in this SFE. The cyclonic vorticity with the cutoff low extends south and south-westward through the Bahamas at all levels. The vorticity feature near 27^oN and 66^oW, according to the analyses in LF87, connects to a convective band southeast of Debby. Detailed resolution of features on this scale is made impossible by the horizontal ODWs data density.

The divergence field at 850mb (Fig. 3.2a) indicates that maximum convergence happens in a region between Debby's inner core and the convective band to the southeast. The field at the 500mb level (Fig. 3.2b) is characterized by weak convergence/divergence patterns throughout the whole domain. Maximum convergence occurrs near the hurricane center and in the northeast corner. The analyzed divergence field at 200mb (Fig. 3.2c) is very different from those at lower levels. Stronger divergence occurrs over the hurricane and in the cirrus outflow to the northeast. The strongest convergence is located at the northern boundary of the domain, and it may be an artifact of the boundary conditions used in LF87.

Figs. 3.3 and 3.4 show our calculations for the same time at the same three levels from the NNRA's dataset. Roughly speaking, major observed features in the vorticity field are captured by NNRA. For example, the hurricane center is close to the vorticity maxima at 850mb and 500mb levels (Figs. 3.3a and 3.3b), which means the NNRA's dataset meets our first two basic requirements we gave before. The cyclonic vorticity with the cutoff low is present at the 200mb level (Fig. 3.3c) and stretching southwestward through the Bahamas. When it comes to the divergence field, at the 850mb level (Fig. 3.4a), the hurricane center is within a region of maximum convergence. And at the 200mb level (Fig. 3.4c), the center is in a divergence region and close to a maximum divergence center.

However, several discrepancies can also be found between the NNRA's and the observational results. The obvious one is that at lower levels, the hurricane center does not coincide with the NNRA's maximum vorticity center, while it overlaps the observed maximum vorticity center. The cyclonic vorticity of the cutoff low is weaker in Fig. 3.3c than in Fig. 3.1c. The NNRA's cutoff low tilts more north-eastward than the observed one does. The NNRA's divergence field at the 200mb level shows

the maximum divergence center east of the hurricane. The hurricane center is at the zero divergence line outside of at the 500mb level in the NNRA's results (Fig. 3.4b). The most severe discrepancy is in the divergence field. The NNRA's divergence is about one order of magnitude less than the observed. This is a common problem for many operational analyses (K96 and Hollingsworth et al. 1989). Even though both NNRA and ERA have made many efforts to correct this problem, they still have not produced a good divergence field.

3.4.2 Hurricane Elena of 1985

To further assess the NNRA's and ERA's capability of representing tropical cyclones, we calculate the relative vertical vorticity and divergence for Elena's case. Figs. 3.5 and 3.6 show the calculations at 850mb and 500mb levels for 1200UTC 29 August, 0600UTC 31 August and 0000UTC 2 September from NNRA's and ERA's datasets respectively. The observed storm location is marked with a crossmark. From Fig. 1.10a, we can see that at 1200UTC 29 August, Elena just became a hurricane; one hour before 0600UTC 31 August, a secondary wind maximum was forming 120km from the center; and at 0000UTC 2 September, Elena reached its maximum intensity.

Comparison of these two figures reveals similarities as well as differences. Both datasets have an analogous vorticity distribution pattern. But ERA (Fig. 3.6) has a stronger vortex at low- and mid-levels than NNRA (Fig. 3.5) does. The observed hurricane center is undoubtedly close to its counterpart in both reanalysis datasets. The location of a storm in operational analyses is normally defined by the maximum midtropospheric relative vorticity. But the ERA's center is closer to the observed one than the NNRA's. At the end, the maximum vorticity appears at almost the same point in lower and middle troposphere in both datasets. Again, ERA does better a job than NNRA does, for example, at 1200UTC 29 August.

Shown in Fig. 3.7 are the azimuthally averaged tangential velocity and radial velocity at 200mb, and the ERAMF of Elena from Molinari and Vollaro (1989). The convergence of the eddy momentum flux (called eddy spin up rate or ESUR for short) has been shown in Fig. 1.11a. The data sources of Molinari and Vollaro's

analysis are the international rawinsonde network and upper-level satellite-derived cloud motion vectors generated operationally by NHC. Their analysis was only done at the 200mb level since the upper-level cloud motion vectors were assumed valid at this level. The procedure for their objective analysis is a successive-correction method with anisotropic weighting functions, following Benjamin and Seaman (1985). Our calculations of the same physical variables are given in Figs. 3.8 (NNRA) and 3.9 (ERA). After comparing the observational results (Figs. 1.11a and 3.7) with the calculations from both reanalysis datasets (Figs. 3.8a-d and 3.9a-d), we conclude that the reanalysis results strongly resemble the observational ones while there exist some subtle differences between them.

A very similar pattern can be seen in the field of mean tangential velocity (Figs. 3.7a-3.9a). The pattern clearly shows a retreat of anticyclonic rotation after an inward shift of positive eddy forcing (Figs. 3.7c-3.9c). The retreat is followed by a development of cyclonic rotation. However, the cyclonic rotations of the observations, NNRA and ERA are different in their strengths. ERA has the strongest cyclonic rotation of the three, NNRA is in the middle, and the observed is the weakest. Interestingly this order is reversed for the strength of the anticyclone. The observed anticyclone is the strongest, and the ERA's is the weakest.

The fields of azimuthally averaged radial velocity (Figs. 3.7b-3.9b) all show an inward propagation of an outflow maximum after 0000UTC 31 August. An extended period of deepening was set off at the end of this inward shifting (Fig. 1.10a). Note that the ERA's inward shifting ends 12 h earlier the other two. Starting around 1200UTC 29 August, both ERA and the observations show an outflow maximum over the inner 1200km for 12 hours. The value of the ERA's outflow, however, is about one-third of the observed maximum value. NNRA shows an outflow maximum near $\sim$ 1200km radius for the same period. But the NNRA's outflow maximum is far away from the storm core compared with the other two. Centering around 2 September at 500km radius there is one more outflow maximum which only appears in NNRA's results. The reality of this outflow maximum needs to be confirmed by more detailed observational study. Finally, the magnitude of the observed mean radial

velocity is the largest, which means that both datasets also undervalue the divergent component of the wind here.

All eddy momentum fluxes (Figs. 3.7c-3.9c) show two local maximum centers. The first one is located at ~2000km radius late on 28 August. This maximum is too far away from the hurricane center to influence Elena's intensity significantly. The second one which we are interested in is situated around 1300km from the hurricane center on 31 August. Molinari and Vollaro (1989) found this maximum having a high correlation with Elena's intensity change about 30 hours later. ERA has the weakest EARMF, and the observation has the most intense interaction. NNRA is in the middle. At the end we would like to point out the analysis sensitivity tests done by Molinari and Vollaro revealed that their eddy momentum fluxes beyond 800km carry a high degree of confidence.

Eddy spin up rates are very much alike at the 200mb level in the observations (Fig. 1.11a) and both reanalyses (Figs. 3.8d and 3.9d). All have a major cyclonic event around 31 August. They differ only in terms of magnitude and occurrence locations. The NNRA's ESUR has the largest magnitude but is the farthest away from the storm center. The ERA's ESUR has the smallest magnitude but is closest to the storm center. The observed ESUR is in the middle.

The ESUR's vertical structure cannot be calculated by using only 200mb observational data. So we have to compare our calculations (Figs. 3.8e-f and 3.9e-f) with Molinari et al's results (Figs. 1.11b-c). Their calculations were based on the ECMWF operational analysis (See Chapter 1.4.2). In general, all calculations indicate that the positive ESUR frist increases with height, maximizes around 200mb, and then decreases with height again. The maximum values of ESUR from all calculations are compatiable. But the ESURs from both reanalyses have larger negative spin up rate than that from the ECMWF reanalysis.

3.4.3 Hurricane Allen of 1980

Allen is the most notable concentric eyewall hurricane that has been observed so far. It became a hurricane at 0000UTC 3 August and reached its maximum intensity

48 h later with a MSLP of 911mb and maximum surface wind of 71m/s. It then experienced three complete concentric eyewall cycles before landfall. Its intensity history has been given in Fig. 1.6.

Fig. 3.10 shows the radius-time series of azimuthally averaged radial velocity at 200mb in Allen of 1980 (Molinari 1992), computed from the objectively analyzed winds. The data sources of this analysis are objective analyses of the outflow layer and gridded analyses from ECMWF. The objective analyses made use of conventional international rawindsonde winds, commercial aircraft winds, operationally derived upper tropospheric cloud motion vectors from NHC, and an enhanced set of cloud motion vectors from the late Harry Hawkins. The objective analysis procedure is the same successive-correction method as that of Elena.

Three major outflow events occurred in Allen. All lasted about 24 hours. The first one occurred on 4 August, and maximized at 1200UTC on the same day. The second one appeared on 5 August, and also reached its maximum strength in the middle of the day. The last one occurred between 1200UTC 8 August and 1200UTC 9 August, and its peak value was at 0000UTC 9 August. Furthermore, the last outflow maxima is larger than the first two which almost have the same peak value. After comparing with the history of Allen's intensity (Fig. 1.6), we can see that each outflow event always happens near or at the end of each period of rapid deepening. We suspect that each of these outflow maximum might be the result of each rapid deepening. There is a little weaker outflow maximum occurring between 1200UTC 5 August and 0000UTC 6 August at 700km radius. It happened during a period of rapid weakening of the hurricane. This maximum may be the product of the development of a secondary eyewall.

Shown in Fig. 3.11 is the radius-time series of NNRA's mean radial velocity. There also exist three major outflow events in the NNRA's results . The first and last events occur at the same time and location as their observed counterparts do. But the second outflow maximum happens about 12 hours earlier than the observed second one does. NNRA entirely misses the minor outflow maximum observed between 1200UTC 5 August and 0000UTC 6 August at 700km radius (Fig. 3.10). Furthermore, the peak

values of all outflow maxima are smaller than those seen on Fig. 3.10. This is just one more indication of underestimation of the divergent part of wind in the NNRA's dataset.

3.4.4 Hurricanes Dean and Gabrielle of 1989

Dean became a hurricane at 1200UTC 2 August and reached its peak intensity at 0000UTC 7 August. Its MSLP was 968mb, and its maximum surface wind was 46m/s. Gabrielle strengthened into a hurricane at 0000UTC 1 September. Its peak intensity started at 0600UTC 5 September and lasted 12 h. The MSLP of Gabrielle was 941mb and the maximum surface was 64m/s. A secondary eyewall was observed on the radar composite of 1941-2011 UTC 3 September.

Fig. 3.12 illustrates the ESURs at 200mb as a function of radius and time for Dean and Gabrielle separately (D93). The data in the analysis included rawinsondes, satellite cloud-track winds, and aircraft observations from both U.S. Air Force reconnaissance and NOAA research missions. The objective analysis scheme is the spline-fitting technique described in LF87. Our calculation is given in Fig. 3.13.

For Dean's case (Fig. 3.12a), the region of enhanced eddy forcing first showed up on 4 August at 1500km radius. It then moved inward for the next two days. It peaked on 6 August about 650km from the hurricane center. After 24 hours, Dean reached its maximum intensity. This suggests that there may exist a connection between the enhanced eddy forcing and Dean's intensification. There is a short period of eddy forcing with a value less than 10m/s/day on 1 August. This eddy forcing may assist Dean's early development. On 1 August Dean was developing from an initial easterly wave into a tropical storm, and Dean was a hurricane 24 hours later. A look at the NNRA's result for Dean (Fig. 3.13a) indicates that NNRA fails to produce the first episode on 1 August, though it does produce the second episode starting on 4 August. However, the NNRA's ESUR is weaker and more diffuse than the observed one.

In Gabrielle's case (Fig. 3.12b), the period of enhanced eddy forcing began on 5 September. The observed eddy forcing reached its first maximum on 7 September and the second maximum on 8 September. The peak value of the eddy forcing occurred in

the second maximum and was 48m/s/day. In the reanalysis calculation (Fig. 3.13b), the NNRA's eddy forcing begins to increase on 6 September, one day later than the observed one. This eddy forcing reaches it first maximum at 1200UTC 7 September, 12 hours later than its observed counterpart, and reaches its second maximum on 8 September with a peak value less than 40m/s/day. Also the locations of both NNRA's maxima are about 150km further away from the hurricane center compared with the observations. Furthermore, the reanalysis ESUR has a small region of anticylonic spin-up between 3 September and 5 September while we see an observed cyclonic spin-up in the same region for the same time period. This contradiction remains mysterious to us.

3.4.5 Summary of Data Evaluation

To summarize this section, we have compared our calculations using two reanalysis datasets with five observational case studies, in which two different types of objective analysis methods are used. The preliminary comparison leads us to the following conclusions:

1. Both reanalyses produce storm tracks close to the true storm tracks. The performance of the ECMWF reanalysis is better than that of the NCAR/NCEP reanalysis.

2. The maximum vorticity associated with a storm in both reanalysis datasets occurrs nearly at the same point throughout the lower and middle troposphere, although its magnitude is smaller than that of the observed in the NNRA's dataset.

3. NNRA shows some skill in producing the low-level convergence and high-level divergence associated with a hurricane. But the values are underestimated and noisy in general.

4. Both reanalysis datasets represent the rotational component of the wind well. The magnitude in both reanalyses is compatible with that of the observed ro-

tational wind. This is the because the rotational wind is largely balanced flow, which should be well represented in the analyzed fields.

5. The divergent wind is undervalued in both reanalysis datasets. A possible reason is that the divergent wind is unbalanced, and it can be well determined only with a good knowledge of the vertical distribution of heating in the Tropics. Since both reanalysis systems are reported to have difficulty with spin-up of precipitation fields, they are unlikely to overcome such weakness without a significant improvement of the convection parameterization scheme. Within the two reanalyses, NNRA has stronger outflow than ERA does.

6. In general, the eddy forcing from both reanalysis datasets is similar to the observed one in terms of location and timing. The reason for the similarity is as follows: the eddy forcing arises from the interaction between a hurricane and its upper-level synoptic environment, typically, a midlatitude trough northwest of the hurricane. Most of or perhaps the largest eddy wind components occur within the trough which can be well observed by the U.S. rawinsonde network and thus should be accurately described in both reanalysis datasets. Therefore, most of the eddy forcing can be well represented in both reanalyses. NNRA seems to have stronger interaction than ERA does.

3.5 Case Studies for Concentric Eyewall Hurricanes

Having gained some confidence in the reanalysis datasets, we turn to look at isentropic potential vorticity and eddy PV fluxes near tropopause for the concentric eyewall hurricanes[10] listed in Chapter 1.1. We will first discuss four individual cases with different AEPF patterns in detail. These four cases are Hurricane Elena of 1985, Hurricane Opal of 1995, Hurricane Gilbert of 1988, and Hurricane Emily of 1993. Calculations will be done using both NNRA's and ERA's datasets except for Opal.

[10]Due to the time consuming nature of the calculations, we have not studied Ella of 1978, Debbie of 1969, Beulah of 1967, Carla of 1961, and Donna of 1960.

As we will see below, there are three types of interaction between a hurricane and its upper-level environment. Then we will present summarized results for all other cases.

3.5.1 Hurricane Elena of 1985

Elena has been studied extensively by Molinari and his colleagues. Their results have been presented throughout this thesis. For the comparison purpose, we will do a parallel case study based on both reanalysis datasets.

Elena began as tropical wave that crossed the Atlantic and passed over Cuba into the Gulf of Mexico. It made landfall near Biloxi, Mississippi at 1300UTC 2 September. As shown in Fig.1.10b, before 31 August, the intensification of Elena was slow. On 31 August and 1 September, passage of a mid-latitude trough induced an anticyclonic track loop in Apalachicola Bay. The interaction between this trough and Elena is thought to have led to the development of a secondary eyewall observed on 1 September (Willoughby 1990).

Fig. 3.14a-f displays the time evolution of isentropic potential vorticity (IPV) on the $\theta = 350K$ surface from 060UTC 30 August to 1800UTC 1 September at 12 hours interval. Fig. 3.15a-f shows cross sections of IPV from northwest to southeast through Elena's center for the same time period. The center at each time is taken from the best track data archive. The interaction between Elena and its synoptic environment is clearly discernible from Figs. 3.14 and 3.15.

Elena's outflow anticyclone is well established at 0006UTC 30 August (Fig. 3.14a). A broad region of low-PV air exists around the storm. There is a trough to the north-northwest of Elena over the central United States. The strip of high PV over the southern United States is the remains of previous Rossby wave breaking on 28-29 August. The vertical PV structure at this time (Fig. 3.15a) shows a local PV anomaly associated with Elena, which extends from 310K surface to 340K surface. The detailed PV structure of Elena's inner core, of course, cannot be depicted by such coarse resolution data. In Gloria's case (Fig. 1.13b), the PV in its inner core is of the order of 25-50 PVU (1PVU= $1 \times 10^{-6} m^2 K s^{-1} kg^{-1}$). Nevertheless, the presence of such a low-level PV anomaly should assist us in tracking the strengthening of the

interaction later on.

By 1800UTC 30 August, Elena has intensified. This is evident from an increase of the strength of the low-level PV anomaly (Fig. 3.15b). The trough is now directly north of the hurricane (Fig.3.14b). The flow ahead of the trough smoothly passes north of the storm and then perhaps fortifies the outflow jet to the storm's northeast. PV contour lines show wavelike structure north of the storm. After 12 hours (Fig. 3.14c), the main trough's body keeps traveling to the east but the base of the trough is retarded and invaded by Elena. The trough tilts further north-eastward with respect to the north-south plane. There is a little sign of thinning of the entire trough compared to 12 hours ago. The low-level PV anomaly leans with height a little bit toward the south-east (Fig. 3.15c) perhaps owing to the vertical shear brought about by the trough.

The interaction becomes even more distinguishable by 1800UTC 31 August. The upper-level PV anomaly associated with the base of the trough is now almost directly over the low-level PV anomaly (Fig. 3.15d). The trough's base still remains at the storm's west side (Fig. 3.14d). Elena's well-defined anticyclonic outflow now is replaced by a weak cyclonic circulation. This replacement process can also be seen in Figs. 3.8a and 3.9a. Twelve hours later, Elena is right at the base of the trough (Fig. 3.14e). The PV anomaly with the trough's base has apparently been eroded by the storm. The low-level PV anomaly (Fig. 3.15e) inclines further south-eastward with height. After another 12 hours, the low-level PV anomaly (Fig. 3.15f) is nearly vertical again. There is an indication of the reappearance of the anticyclonic outflow (Fig. 3.14f). Elena achieved at its maximum intensity around 0000UTC 2 September (Fig. 1.10a).

Figs. 3.14 and 3.15 depict a clear example of an "equatorward Rossby wave breaking" (Thorncroft et al., 1993) followed by partial superposition of the resulting PV anomaly and the storm. This synoptic-scale wave breaking has some interesting features, such as, southward penetration, lagging of the base of the trough, and a subsequent thinning of the midlatitude trough. During the wave breaking, the hurricane outflow anticyclone acts as a block high. Based on ECMWF operational

analyses, Molinari et al. (1995) found a similar wave breaking process when studying the synoptic environment of Elena. This gives us some confidence in the NNRA's dataset.

The interaction shown in Figs. 3.14 and 3.15 can also be described by the local PV time tendency. We calculate the PV tendency by interpolating the PV from the original latitude-longitude grid to a latitude-longitude grid moving with the storm at each time, then using a centered time difference scheme to calculate the PV time tendency. Fig. 3.16 shows the time series of PV tendency for the same time period as in Fig. 3.14. All features of the synoptic-scale wave breaking can be easily found on this figure, especially the retardation and thinning of the trough. From this figure we learn that the interaction occurrs at multiple levels and the strongest is at 200mb. Furthermore, after 1800UTC 31 August (Figs. 3.16e and 3.16f), the hurricane is entering or already in an area of negative PV tendency. This means that the deepening of the hurricane is underway and an anticyclonic outflow is about to develop.

After having studied the interaction with the aid of isentropic potential vorticity and PV tendency maps, we now turn to a more quantitative approach, calculating the eddy terms during the interaction. Our calculations of ERAMF and ESUR have been presented in the previous section (Figs. 3.8c-f and Figs. 3.9c-f). Here we will focus on the evolution of eddy PV fluxes. Before showing AEPF for Elena, we would like to compare the relative importance of each term in Equation 3.12 first.

Fig. 3.17 presents radius-time series of each term on the right hand side of Equation 3.12, the sum of all terms and the ERAMF. The first impression of this figure is that around 31 August when the interaction is happening, all terms show some dramatic changes, e.g., the appearance of a local maximum in Terms A, B, and D or a strip of high value extending toward the center with time in Terms C, E, F and G. Furthermore, Terms A, B, C, F and G are almost of the same order of magnitude, while Terms D and E are one order smaller. Among Terms A, B, C, F and G, Terms A and C are the largest. The smallness of Terms D and E is because the eddy radial velocity is much larger than the mean radial velocity.

A closer examination of Fig. 3.17 reveals that Term B partially cancels Term G,

and Term C partially cancels Term F. Therefore the sum of all terms (Fig. 3.17h) is dominated by the pattern of Term A which has a direct and close connection with the ERAMF. This is proven true by comparing Fig. 3.17i (ERAMF) and Fig. 3.17j (AEPF or the sum of all individual terms). The dominance of Term A in AEPF implies that the effect of eddy heat fluxes is less important than eddy angular momentum fluxes. Note that the AEPF propagates further toward the storm center than the ERAMF does. Also it is less noisy than the ERAMF.

Fig. 3.18 is the same as Fig. 3.17 except that its calculation is based on the ERA's dataset. Basically, all corresponding individual terms show similar geometry and magnitude except for Term C. ERA's Term C has the same maximum value as NNRA's Term C does, whereas the former is more organized and thus less noisy than the latter. Regarding AEPF, ERA's AEPF is stronger and closer to the storm center than NNRA's AEPF. Also ERA's AEPF has an extra local maximum centered at $\sim$1700km radius around 1200UTC 30 August. This local maximum may reflect the interaction between Elena and an upper-level trough southeast of the hurricane. This trough can be seen on Figs.3.15a and 3.15b. It is not clear why the NNRA's AEPF does not capture the local maximum even though the trough shows up in NNRA's results.

3.5.2 Hurricane Opal of 1995

Hurricane Opal of 1995 originated from a tropical wave that emerged from the west coast of Africa on 11 September (Lawrence et al.1998). It strengthened into a hurricane near 1200UTC 2 October while centered 275km west of Merida, Mexico. Opal intensified into a category four hurricane near 1000UTC 4 October at which time a small, 18-km-diameter eye was observed by reconnaissance aircraft. The minimum central pressure was 916mb with maximum sustained surface winds of 67m/s. Soon after Opal reached its peak intensity; it is reported that the small inner eyewall diminished as an outer eyewall became more dominant. The outer eyewall was initiated late on 3 October or early on 4 October. Opal weakened during this eyewall replacement process, but was still a marginal category 3 hurricane when it made landfall at

Pensacola Beach, Florida, near 2200UTC 4 October.

The time evolution of IPV on the $\theta = 355K$ surface is shown in Fig. 3.19. The time period is from 0000UTC 3 October to 1200UTC on 4 October at an interval of 12 hours. Fig.3.20 displays the northwest-southeast cross sections of IPV through the observed center of the hurricane for the same time period.

At 0000UTC 3 October (Fig. 3.19a), a large upper-level anticyclone is well established over the Gulf of Mexico. A large amplitude and broad mid- to upper-level trough is positioned over the central United States. This trough turned Opal slowly toward the north in the following days. There is a low-level PV anomaly evident in Fig. 3.20a. It is related to the hurricane itself, as shown in Elena's case (Fig. 3.15a). The low-level PV anomaly extends from the $\theta = 300K$ surface to the $\theta = 360$ surface. It is deeper than that of Elena. After 12 hours, the trough keeps moving to the east but there is some indication of retardation of its base by Opal (Fig. 3.19b). The upper-level anticyclone has been blown to the east of Opal by the trough, and plays the role of a blocking high as in Elena's case. The low-level PV anomaly at this time (Fig. 3.20b) merges into the PV anomaly associated with the trough.

At 0000UTC 4 October, the trough starts to tilt toward the northeast with respect to the north-south plane (Fig. 3.19c). But there is little sign of thinning of the trough. The PV tendency maps (not shown here) indicate no sign of thinning either. The base of the trough is captured by Opal. The mid- to upper-level PV anomaly at the trough's base is not over the low-level PV anomaly (Fig. 3.20c). The pattern seen at 0000UTC 4 October continues for the next 12 hours (Figs.3.19d and 3.20d).

Comparing the time development of the synoptic environment in the Opal and Elena cases, we can see similarities and differences. The similarities are, for example, the involvement of a mid-latitude upper-level trough, the retardation and detention of the trough's base in both cases. The differences arise mainly due to the fact that the trough in Opal's case is much stronger than that in Elena's case (Fig. 3.14). So the deformation of the trough is not as significant as that in the Elena case. Consequently, no partial superposition of low-level and upper-level PV anomalies occurrs in Opal's case. As argued by Molinari et al. (1998), the thinning of the approaching trough

(positive PV anomaly) is a key element of the partial superposition that occurrs later on.

The differences between Opal and Elena are also revealed by eddy quantities. Fig. 3.21 shows the mean tangential and radial velocities at 200mb, ERAMF, and ESUR at 200mb, 150mb and 100mb levels. Fig. 3.22 gives AEPF and ERAMF [11]. All eddy quantities exhibit two events of inward propagation of a local maximum eddy value starting from a radius of about 2200km. The first event occurrs around 1200UTC 2 October, and has been discussed above. In particular, as the mid- to upper-level trough (Fig. 3.19) moves closer to the hurricane, the interaction and its effect becomes stronger and more remarkable (Fig. 3.22b). The first event seems to end early on 4 October. After a very short period of negative AEPF (and ERAMF), the second event occurrs around 1200UTC 4 October. The persistent positive eddy fluxes at large radii differs from what we have seen in Elena's case (Figs. 3.17i, 3.17j, 3.18i and 3.18j).

It is quite interesting to note that at the 200mb level (Fig. 3.21a), mean cyclonic rotation always exists within 500km radius of the storm except for an 18 h interruption on 4 October. Mean anticyclonic rotation dominates outside 500km radius. Around 1650km there is a band-shape anticyclonic maximum embedded with two local maxima. This band-shaped anticyclonic rotation is owing to the enhancement of Opal's original anticyclonic circulation by the southwesterly wind ahead of the trough (Fig. 3.19). This is different from what we saw in Elena's case (Figs. 3.8a and 3.9a), in which Elena's anticyclone is completely destroyed during the interaction process. Also there is no "equatorward Rossby wave breaking" in Opal case since we do not see any deformation of the trough. But we still see the interaction between low- and upper-level PV anomalies. We suspect that the working mechanism demonstrated in Fig. 2.17 is actually in operation here.

Finally the field of mean radial velocity (Fig. 3.21b) clearly shows an inward shift of the outflow maximum after 3 October. This is consistent with the deepening of Opal on 4 October. This pattern is similar to that of Elena's mean radial outflow

[11] For easy of comparison between AEPF and ERAMF, we always present them together.

(Figs. 3.8b and 3.9b).

3.5.3 Hurricane Gilbert of 1988

The synoptic history of Gilbert has been described previously in Chapter 1.1. Here we will discuss the time evolution of the synoptic environment before the appearance of a secondary tangential wind maximum at 2200UTC 13 September (Fig. 1.4a).

Fig. 3.23 presents the time series of IPV on the $\theta = 360K$ surface, and Fig. 3.24 the northwest-southeast cross sections of IPV through the observed center of the hurricane. The time period for both figures is from 0000UTC 12 September to 0000UTC 14 September with a time increment of 12 hours.

In Fig. 3.23, we find the familiar upper-level pattern we have seen in the two previous cases, such as low PV air surrounding the hurricane center and a well defined anticyclonic outflow. However, the most striking feature revealed by the figure is that instead of having a significant midlatitude trough, Gilbert is embeded in a very broad midlatitude ridge. This becomes more clear as time goes by. The existence of the ridge can also be seen on Fig. 3.24 which also shows a notable PV wave around $\theta = 380K$ surface. The low-level PV anomaly associated with the hurricane is at the rear (or west) part of the PV wave ridge at the beginning (Fig. 3.24a), and it slowly moves toward the base of the ridge later on.

In Fig. 3.23, there is a strip of high PV anomaly west of the storm. The strip is originally from a cut-off low that formed two days previously. Part of its vertical structure can be found at the left side of the cross sections on Fig. 3.24. The distance between this upper-level PV anomaly and the low-level anomaly rarely changes, so that the partial superposition discovered in Elena's case does not occur. So we again suspect that the working mechanism illustrated in Fig. 2.17 may help start the initial secondary surface wind maximum observed in nature (Fig. 1.4a).

The lack of interaction is also evident in eddy quantities. Fig. 3.25 shows ERAMF and AEPF, and Fig. 3.26 displays mean azimuthal and radial velocities at the 200mb level, ERAMF, and ESUR at three different pressure levels. Figs. 3.27 and 3.28 presents the same physical variables as in Figs. 3.25 and 3.26 but from the ERA's

dataset. It is not surprising to see the absence of any remarkable local maximum in eddy PV or momentum fluxes (Figs. 3.25 and 3.27) after the above discussion of Gilbert's synoptic environment. Both ERAMF and AEPF organize themselves into a band-shaped area lasting from 0000UTC 11 September to 1200UTC 13 September. They never show any sign of inward shifting of maximum values.

The eddy quantities from both reanalyses differs in their strengths. The NNRA's AEPF is more pronounced than that of ERA. But this is not true for ERAMF. The ERA's ERAMF is larger than that of NNRA. This suggests that the eddy heat fluxes are different in both reanalyses.

The distribution patterns of ESUR are almost the same at the 200mb level for both reanalysis datasets (Figs. 3.26d and 3.28d). But ERA has stronger ESUR than NNRA does. NNRA's and ERA's ESURs are completely different at the 150mb and 100mb levels (Figs. 3.26e, 3.26f, 3.28e, and 3.28f). For example, at the 150mb level, NNRA has negative ESUR between 1200UTC 11 September and 13 September within the 700km radius, while ERA has positive ESUR for the same time period within 1100km radius. It is unknown which result is closer to the reality.

Comparison of Fig. 3.26a and Fig. 3.28a reveals that ERA has stronger cyclonic rotation than NNRA does inside 700km radius. This is in agreement with a stronger positive ESUR found in the ERA's dataset. Outside 700km radius, both reanalyses show dominant anticyclonic rotation with roughly the same strength. In Opal's case, we already see such distribution pattern of a cyclonic circulation inside a certain radius and an anticyclonic circulation outside this radius.

In the end, the field of mean radial velocity exhibits similar pattern for both reanalyses (Figs. 3.26b and 3.28b). But ERA has smaller mean outflow than NNRA does, which is consistent with what we have found in Elena's case.

3.5.4 Hurricane Emily of 1993

Hurricane Emily of 1993 (Pasch and Rappaport 1995) originated from a cloud cluster associated with an easterly wave of African origin. Emily briefly reached hurricane intensity on 26 August and then weakened to a tropical storm for about 18 hours.

Emily regained hurricane strength late on 27 August. At 1700UTC 28 August, flight-level data revealed an outer wind maximum (Fig. 3.29a). The radar composite of 1910-2030UTC on the same day (Fig. 3.29b) shows a partial outer eyewall forming in the northern half of the storm at a radius of about 76km from the center. The inner eyewall is only visible on the northwest side of the storm. After two days, an eyewall replacement was well in progress. The outer wind maximum became stronger than the inner one (Fig. 3.29c). The MSLP rose from 973 at 0000UTC to 979mb at 1200UTC on 29 August. By 1200UTC 30 August, only the outer wind maximum remained at 50km radius with 40m/s maximum wind (Fig. 3.29d). The radar composite of 2040-2214UTC on 30 August (Fig. 3.29e) shows a clear, closed eyewall. The distributions of wind and D values are broad. The D value is defined as the departure of a selected isobaric height from the corresponding value in the standard atmosphere. After the eyewall replacement, Emily's MSLP began to fall at a rate of a millibar every 3 hours. At 2349UTC 31 August, Emily reached its maximum intensity with a 960mb MSLP and a maximum wind of 51m/s. The eyewall replacement of Emily is analogous with the one of Elana of 1985. Both happened before the hurricane reached its maximum intensity, which differs from the classical eyewall replacement described by Willoughby (1982).

Fig. 3.30 shows the time evolution of IPV on the $\theta = 355K$ surface between 0000UTC 27 August and 0000UTC 29 August with a 12 h interval, and Fig. 3.31 gives west-northwest-east-southeast cross sections through the observed center of the hurricane for the corresponding time period.

At 0000UTC 27 August (Fig. 3.30a), Emily is between three notable upper-level PV anomalies. The one to the west and the one to the south are both originally from a cut-off low that formed before 27 August. The one to the east is from a midlatitude trough. The eastern one is stronger and more organized than the other two. To the northwest of Emily over the central United States, there is a very broad high pressure ridge. Within the ridge, there are several other PV anomalies. Gilbert (Fig. 3.23a) had a somewhat similar synoptic environment as we just see for Emily. But unlike in Gilbert's case, Emily is very close to its surrounding PV anomalies.

The synoptic environment of 0000UTC 27 August evolves with time (Figs. 3.30b-3.30e). The PV anomaly west of Emily intensifies first but drops back to its original strength at the end. Its maximum center rotates clockwise around the hurricane. The orientation of its major axis is changed from west-east direction to southwest-northeast direction. The one to the south remains unchanged during the entire period. The PV anomaly east of the hurricane is about to cut off from its major body in midlatitudes (Fig. 3.30e). It actually becomes a cutoff low at midday on 29 August. The ridge north of Emily passes the hurricane and moves to the north-northeast of the storm. The most interesting thing is that Emily's anticyclonic outflow develops during this time period, which we have not seen in previous three cases.

Three positive PV anomalies are present in cross section plots (Fig. 3.31a). The low-level PV anomaly is associated with Emily, as we have seen before. The upper-level PV anomaly to the left belongs to the PV anomaly west of the hurricane. Another upper-level PV anomaly to the right is related to the trough east of Emily. At 0000UTC 27 August (Fig. 3.31a), Emily is closer to the upper-level PV anomaly to the right than the one to the left. As time passes by (Figs. 3.31b-3.31d), the low-level PV anomaly moves from the trough toward the PV anomaly west of Emily. At the end (Fig. 3.31e), there is a partial superposition between the upper-level PV anomaly west of Emily and the low-level PV anomaly, as we have discovered in the case of Elena.

At this point we have discussed qualitatively the interaction between Emily and its upper-level synoptic environment. We now examine such interaction quantitatively through calculating eddy PV fluxes. Figs. 3.32 and 3.33 display ERAMF and AEPF from the NNRA's and ERA's datasets respectively. Both NNRA's and ERA's results show small positive or even negative values of ERAMF and AEPF before and after the appearance of the outer wind maximum (Figs. 3.29a and 3.29b). This indicates a weak interaction compared to the above three cases we have studied so far. This is a very surprising result given the apparently strong interactions on the isentropic charts.

Calculations of "local" eddy quantities as a function of azimuth and radius reveal

that while there is an inward transport of positive PV from the PV anomaly west of Emily, there is an outward transportation of positive eddy PV toward the PV anomaly east of the hurricane. The outward is larger than the inward. The sum and the azimuthal average is what we see on Figs. 3.32 and 3.33. Actually there is a weakening of the PV anomaly west of Emily and a strengthening of the PV anomaly east of Emily, which supports our calculations. Another direct indication is the development of anticyclonic outflow clearly documented in Fig. 3.30. It is easy to find out that the setting of Emily's synoptic environment at 0000UTC 27 August (Fig. 3.30a) is very suitable for the future development of an anticyclone circulation later. This is proven true in Fig. 3.34 which displays the radius-time series of mean tangential velocity from both reanalyses at the 200mb level.

We learn two important lessons we from Emily's case. The first is that a seemingly strong interaction on IPV maps is not necessarily a strong one in terms of eddy PV fluxes. This suggests that IPV maps alone may not be adequate enough to describe the interaction processes. The second is that when studying the interaction between the cyclone and its upper-level environment, we should check the whole surrounding synoptic environment of a tropical cyclone. If we just look at the the synoptic environment northwest of the cyclone, we may reach the wrong conclusion.

3.5.5 Results of Other Case Studies

Up to now, we have thoroughly discussed the upper-level interactions of four individual cases before the appearance of a secondary wind maximum. Based on the AEPF patterns in these cases, we may classify the interaction intensities of the other cases into three categories: strong interaction as in Elena and Opal, medium interaction as in Gilbert, and weak (or close to no) interaction as in Emily. Since the results from ERA are like those of NNRA, we will only use the NCEP/NCAR reanalysis data in the following calculations. Table 3.1 presents our final classification for all the concentric eyewall hurricane cases we have calculated.

At this point we would like to mention three issues. The first is that we classify all calculated AEPF patterns in terms of the AEPF patterns seen in the cases of Elena,

Upper Level Signal (AEPF)	Hurricanes
Strong	1996:Bertha; 1995:Felix, Luis, Marilyn, Opal; 1990:Gustav; 1985:Elena, Gloria; 1980:Allen; 1977:Anita.
Medium	1996:Edouard, Fran; 1992:Andrew; 1988:Gilbert; 1984:Diana.
Weak to None	1996:Hortense; 1993:Emily; 1991:Claudette; 1989:Gabrielle, Hugo; 1983:Alicia; 1979:David.

Table 3.1: Summary for other case studies

Opal, Gilbert and Emily. The classification is not purely subjective since AEPF patterns in the four cases are distinctive enough. We confess that we have not done any test to check whether the uncertainty in the reanalysis data would move a case from one category to another category. But since we have found very similar AEPF patter for one category using two different reanalysis dataset, we suspect that such thing could happen.

The second is that both Figs.3.13b and 3.14b shows an inward increase of eddy momentum fluxes between 7 September and 9 September. But the observed outer eyewall occurred between 1941UTC and 2011UTC on 3 September, during which period no significant eddy momentum fluxes are present. That is why Gabrielle belongs to the weak to none category.

The third issue is that even though Gabrielle had a 48m/s/day eddy spin up rate, it did not have any eyewall replacement cycle. On the other hand, Elena had a clear eyewall replacement cycle with a 26m/s/day eddy spin up rate. So there is no direct relationship between the strength of eddy forcing and the genesis of a secondary eyewall.

3.6 Case Study for A Non-concentric Eyewall Hurricane

In the previous section, we have learned that for there exists a variety of degree of interactions between concentric eywall hurricanes and their upper-level synoptic environments. We will discuss the eddy PV fluxes associated with an intense hurricane that did not have concentric eyewall cycles in its life time. This was Hurricane Frederic of 1979 (Willoughby et al. 1982). Frederic is the only hurricane definitely without an eyewall replacement cycle known to us so far.

Frederic (Hebert, 1980) developed from a tropical wave originally from the west African coast late on 27 August, and was upgraded to a hurricane about 0600UTC 1 September near $13^oN, 49^oW$. At this time, Hurricane David of 1979 became a very intense hurricane. David's outflow stifled Frederic's outflow so that Frederic weakened to a tropical storm at 0000UTC 2 September. At around 1200UTC 10 September, Frederic regained hurricane intensity again. At this time, it was over warm sea with a sea surface temperature of $29^o - 30^oC$, and a large anticyclone was taking shape at 200mb over the storm. These factors probably contributed to the intensification for the next 48 h. About 1200UTC 12 September, Frederic arrived at its maximum intensity with 943mb MSLP and 59m/s maximum surface wind.

Fig. 3.35 gives the time evolution of isentropic potential vorticity on the $\theta = 360K$ surface at 0000UTC 2 September, 1200UTC 4 September, 0000UTC 6 September, 1200UTC 6 September, 0000UTC 10 September, and 0000UTC 11 September. Fig. 3.36 displays cross sections of IPV from northwest to southeast through Frederic's center for the same six times. Both figures clearly show the development of Frederic's synoptic environment at upper levels.

As we can see, at 0000UTC 2 September (Fig. 3.35a), Frederic is located at the rear part of a mid-latitude trough. It is under the influence of the outflow from Hurricane David of 1979 and the northwest wind from the trough. David at this time is at 21.3°N and 75.2°W. There is no sign of low-level PV anomaly associated with Frederic (Fig. 3.36a). After 50 hours (Fig. 3.35b), Frederic is within the

main body of the trough. At this time, a low-level PV anomaly coincides with the storm (Fig. 3.36b). The low-level PV anomaly may be the combination of the local PV anomaly with the storm and downward extension of the PV anomaly with the trough. Another 36 hours later (Fig. 3.35c), a cut-off low is breaking away from the trough's main body. Frederic now has its own PV anomaly (Fig. 3.36c). At 1200UTC 6 September (Fig. 3.35d), Frederic is between the cut-off low and the trough's main body, which is suitable for the development of its anticyclonic outflow. But interestingly the low-level PV anomaly with the storm disappears (Fig. 3.36d). At 0000UTC 10 September (Fig. 3.35e), there is another mid-latitude trough to the east of the storm. Frederic's anticyclone has been well established. A broad region of low-PV air surrounds the storm. The vertical structure at this time indicates two PV anomalies (Fig. 3.36e). The upper-level one is with the trough's base. The low-level one is with the storm. This setting of the synoptic environment implies that an interaction is about to happen. Indeed the interaction does happen. The trough's base has been retarded (Fig. 3.35f). A partial superposition, however, does not occur (Fig. 3.36f). At 1200UTC 12 September, Frederic reached its maximum intersity. So we suspect that the machanism illustrated in Fig. 2.17 may help intensify the storm after 10 September, but does not produce any concentric eyewall cycles.

Again we calculate eddy quantities to quantify the interaction. Fig. 3.37 shows ERAMF and AEPF as a function of radius and time. Compared with the AEPF patterns we have seen before, Frederic's AEPF has its own remarkable features. There are three events of inward shifting of *negative* maximum eddy PV fluxes in addition of two events of inward propagation of *positive* maximum eddy PV fluxes. We have not seen the former three events before, while we have seen the latter two events in previous cases. The enhanced eddy PV flux event between 8 September and 12 September is believed to have some effects on the strengthening of the storm for this period, and we suspect that the two negative events around 2 September and 6 September have some impact on the weakening of the storm around those times. The last negative event has nothing to do with the intensity change of Frederic since it is too far away from the storm center.

Shown in Fig. 3.38 are the radius-time series of mean tangential velocity and radial velocity at 200mb, ERAMF, and ESUR at 200mb, 150mb and 100mb. The field of mean azimuthal velocity (Fig. 3.38a) reveals the presence of cyclonic rotation between 4 September and 6 September, which we have seen from the IPV maps. The development of Frederic's anticyclone after 6 September is evident from the same plot. The field of mean radial velocity is noisy. ESUR at 200mb clearly shows two events of inward shift of *negative* spin up rates around 2 September and 6 September, which is consistent with what we have found from the AEPF map. At the 200mb and 150mb levels, around 1300km radius, there exists a band-shaped positive ESUR. This enhanced ESUR starts around 9 September, and it is believed that it has some impact on the intensification of Frederic after 9 September. ESUR at 100mb is unorganized.

We wish we could find more intense hurricanes without eyewall replacements so that we could develop more confidence in the AEPF pattern seen in Frederic's case. But it turns out that this is a daunting task. But with Frederic's result and results from concentric eyewall hurricanes, we can certainly conclude that the interaction between a tropical cyclone and its upper-level synoptic environment is neither sufficient nor necessary for the genesis and development of concentric eyewall.

3.7 Conclusions from the Case Studies

Difficulties in observational studies in the Tropics lead us to adopt the analysis output from global numerical models to do case studies. With the available reanalysis data from NCEP/NCAR and ECMWF, we have conducted an extensive set of case studies.

More specifically, we first calculate the eddy potential vorticity flux in a storm-following system. Then we use this physical quantity to quantify the interaction seen from IPV maps. In total, we have studied 22 concentric eyewall hurricanes in the Atlantic basin. Based on what we have learned from these cases, we have identified three distinct types of eddy PV flux patterns before the formation of an outer wind maximum. Four individual cases are then discussed in detail to illustrate the three characteristic eddy PV flux patterns. Finally we sort all our results on the basis of

these three patterns.

We have also found an intense hurricane without concentric eyewall cycles. This is the only case known to us definitely without an eyewall replacement cycle. After calculating the eddy PV flux and comparing the result with those of the concentric eyewall hurricanes, we have gained more insight into the relationship between the eddy forcing at upper levels and the genesis of a secondary eyewall.

During the long course of our calculations, we also evaluate the reanalysis datasets we use. The following are our basic conclusions:

1. Both reanalyses are able to closely reproduce a storm track from the best track data. ECMWF reanalysis does a better job than the NCEP/NCAR reanalysis.

2. The NNRA's vorticity matches the observed vorticity fairly well in terms of magnitude and distribution. But this conclusion does not apply to the divergence field. The magnitude of convergence/divergence is at least one order less than that of the observed one even though the distribution pattern is more or less reproduced correctly.

3. The rotational component of the wind is more realistically represented than the divergent part of the wind in both reanalyses. The strength of the rotational wind is commensurate with that of the observed one, while the magnitude of the divergent wind is underestimated in both reanalyses.

4. Azimuthal eddy fluxes of relative angular momentum in both analyses quantitatively differ, but qualitatively resemble, the observed eddy fluxes at the 200mb level. This conclusion is generally true for the eddy spin up rates too.

5. The lack of observational eddy PV fluxes precludes us from drawing any conclusion directly from our calculated eddy PV fluxes. After calculating each individual term in the eddy PV fluxes, we find that the eddy PV fluxes are dominated by the eddy relative angular momentum fluxes. Therefore we conclude that our calculated eddy PV fluxes are also good enough to describe the upper-level interaction accurately.

6. Three different patterns of eddy PV fluxes have been identified. They are employed to classify the degree of interaction between a concentric eyewall hurricane and its upper-level synoptic environment before genesis of a secondary surface wind maximum. This classification is somewhat different from what we observe in the IPV maps. For example, a seemingly strong interaction on IPV maps, as in the Emily's case, turns out to be a weak (or close to zero) interaction in AEPF. Another example is that a seemingly weak interaction on IPV maps, as in the Opal case, shows a very strong interaction signal in AEPF.

7. The AEPF pattern of a strong interaction is characterized by an inward shifting of maximum eddy PV fluxes before and during the initial formation and development of an outer wind maximum. A period of significant intensification often follows the end of this inward shifting. 10 out of the 22 cases we have studied have strong interaction.

8. A medium degree of interaction does not have the inward increase of eddy PV fluxes. Its AEPF pattern shows the existence of a band-shaped maximum of eddy PV or momentum fluxes. This band-shaped geometry usually centers around a certain radius ($\sim$1000km) and appears a couple days before the genesis of a secondary eyewall. 5 cases show medium interaction, including the famous case of Andrew in 1992.

9. A weak interaction does not have any organized positive eddy PV or momentum fluxes before the appearance of an outer eyewall. Its typical AEPF pattern includes well-defined negative eddy fluxes outside $\sim$1000km radius, and scattered positive eddy fluxes inside that radius. 7 out of 22 cases are in this category.

10. Synoptic-scale wave-breaking is not always observed during the interaction, nor is the final break-down of the upper-level anticyclone. In both cases of Opal and Gilbert, the anticyclone survives the interaction process. In Emily's case, an anticyclone develops during the interaction.

11. The interaction does not always lead to partial superposition of the upper-

level PV anomaly with a trough or a cutoff low and the low-level PV anomaly associated with a tropical cyclone. No partial superposition happened in the Opal and Gilbert cases. Emily had a weak interaction, as indicated by the eddy PV fluxes, and a partial superposition occurred.

12. The results from Frederic tell us the interaction between a tropical cyclone and its upper-level synoptic environment is not sufficient for the genesis and development of concentric eyewall cycles in reality. The results from concentric eyewall hurricanes tell us that the interaction is not necessary.

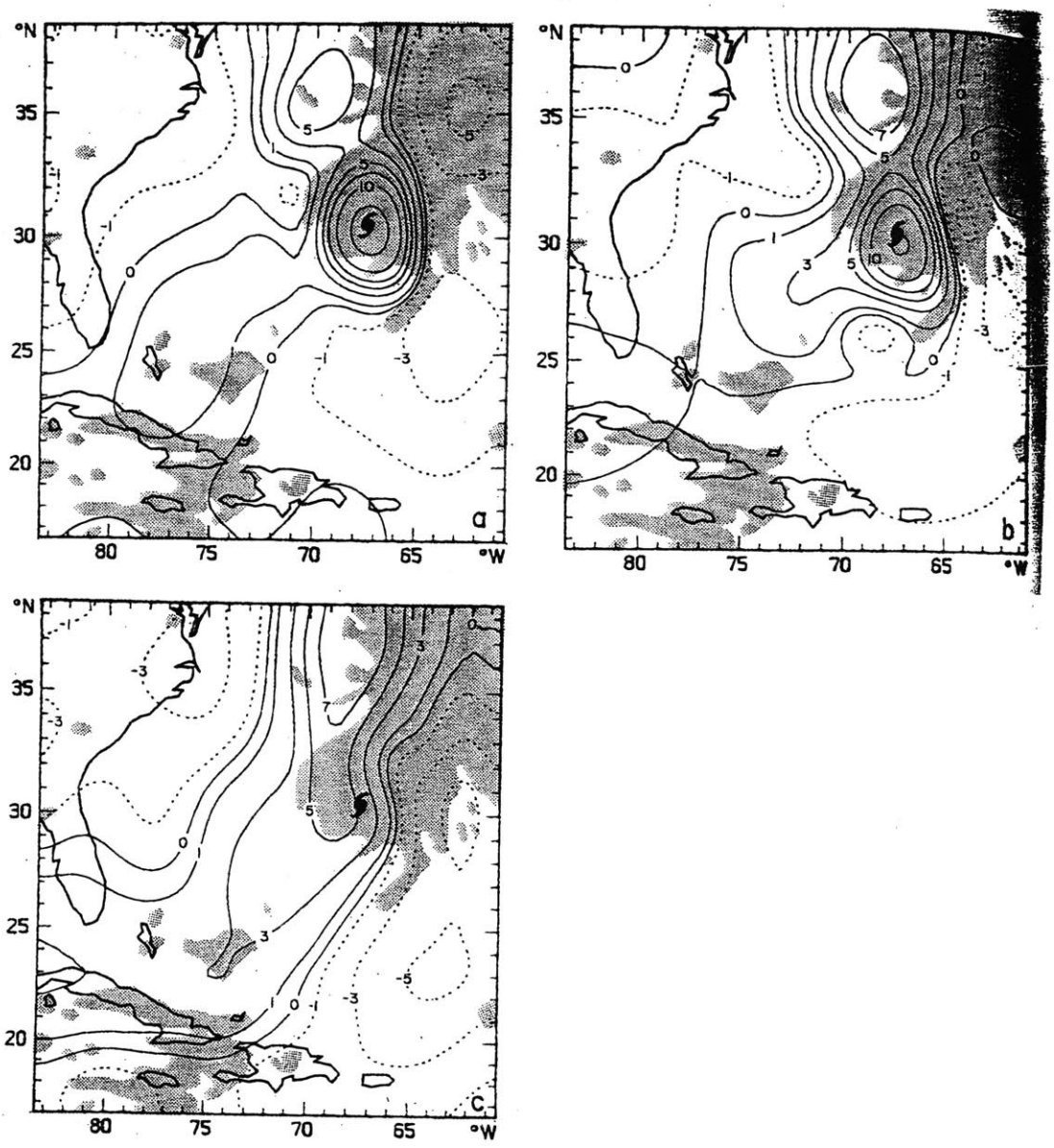

Figure 3.1: Relative vorticity of Hurricane Debby of 1982 for (a) 850mb, (b) 500mb, (c) 200mb at 0000UTC 16 September. Isolines are at 0, $\pm 1, \pm 3, \pm 5, 7, 10, 15 (\times 10^{-5} s^{-1})$. Debby's location is indicated by the hurricane symbol. The shaded area indicates the region of cloud cover (from Lord and Franklin (1987)).

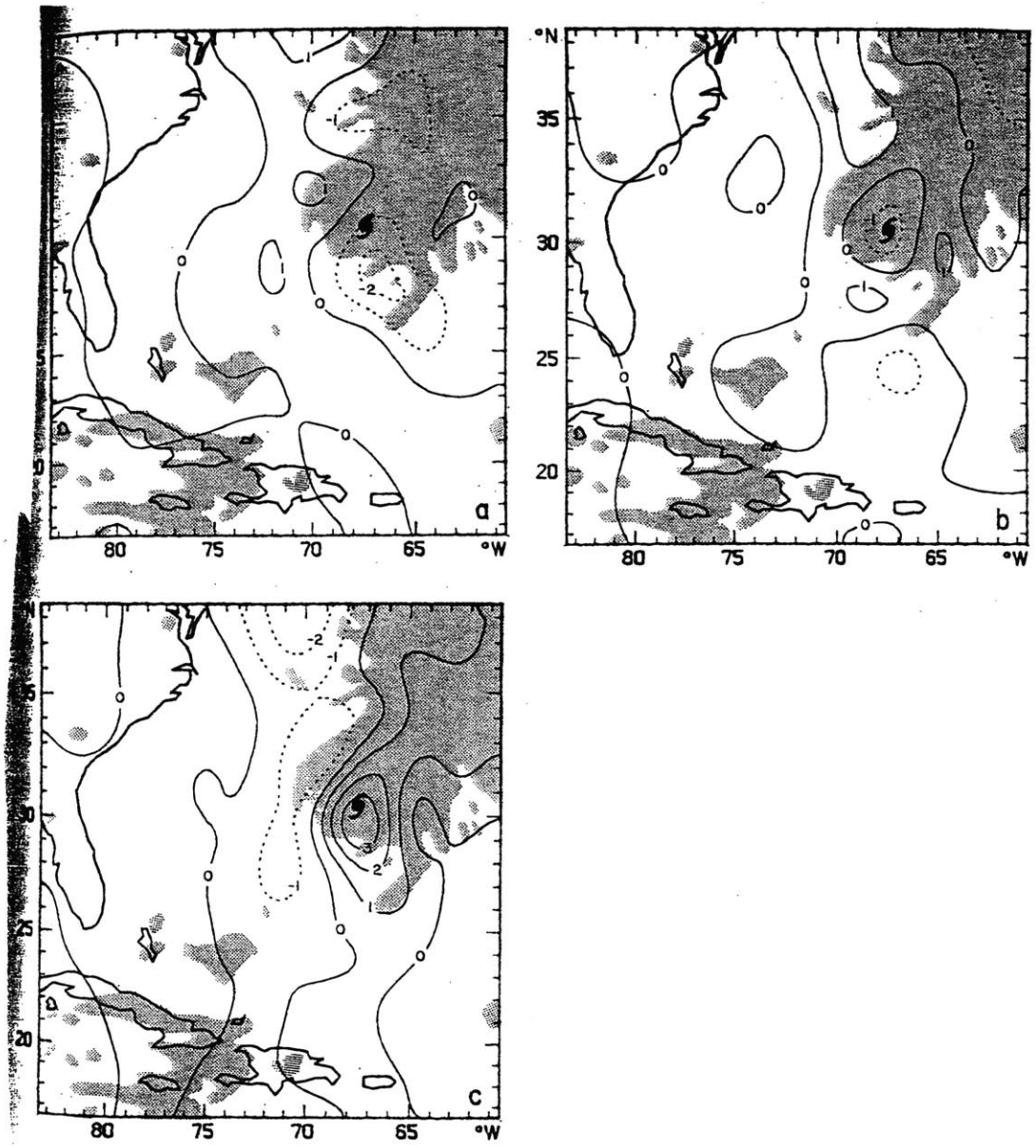

Figure 3.2: As in Fig. 3-1 except for corrected divergence. Isolines are at 0, $\pm 1, \pm 2, \pm 3$ ($\times 10^{-5} s^{-1}$).(from Lord and Franklin (1987))

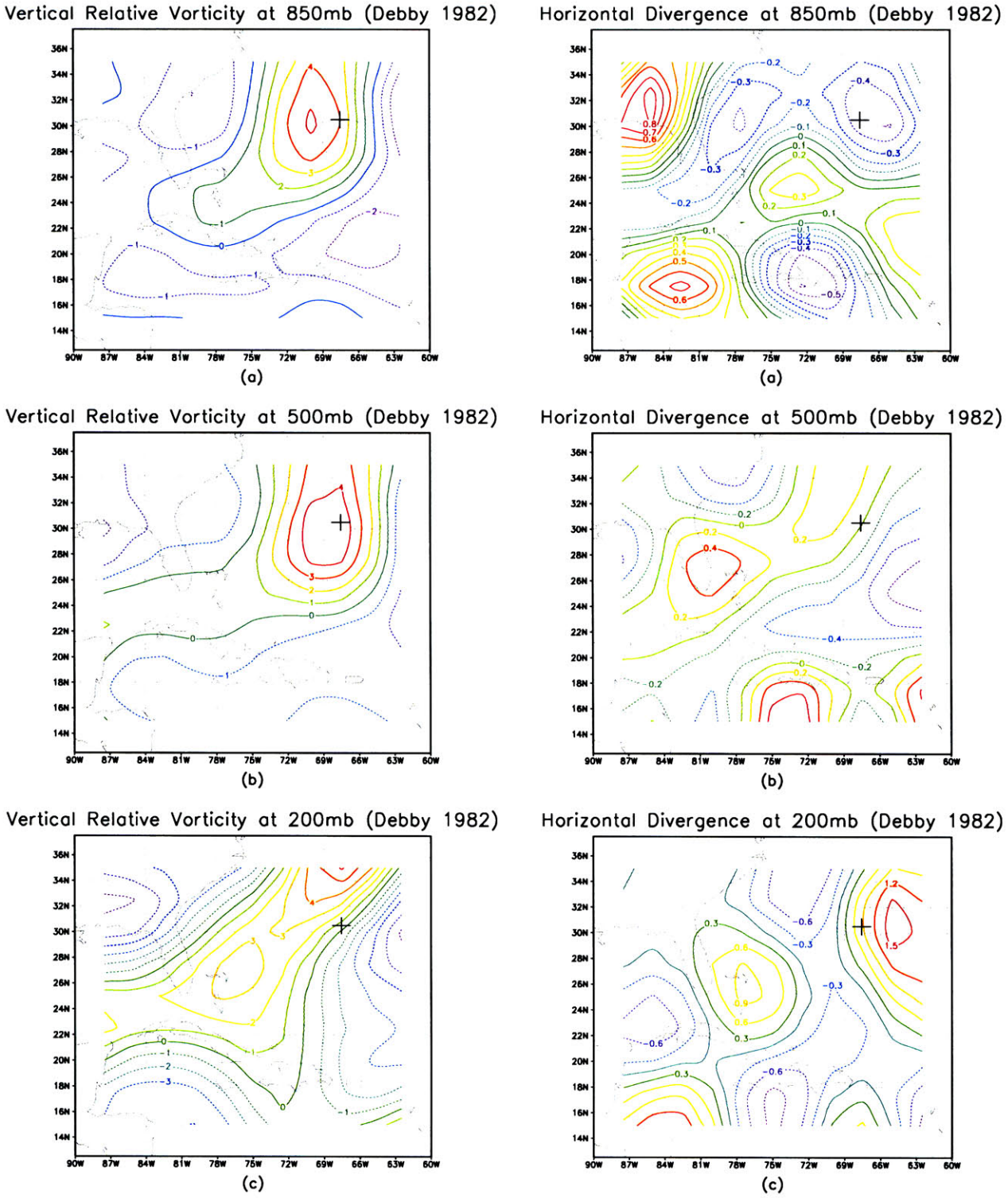

Figure 3.3: (left panel) NNRA's relative vorticity for Debby of 1982. Unit:$10^{-5}s^{-1}$ at (a) 850mb, (b) 500mb, and (c) 200mb. Debby's location is indicated by the crossmark.
Fig. 3-4 (right panel): As in Fig. 3-3 but for the divergence.

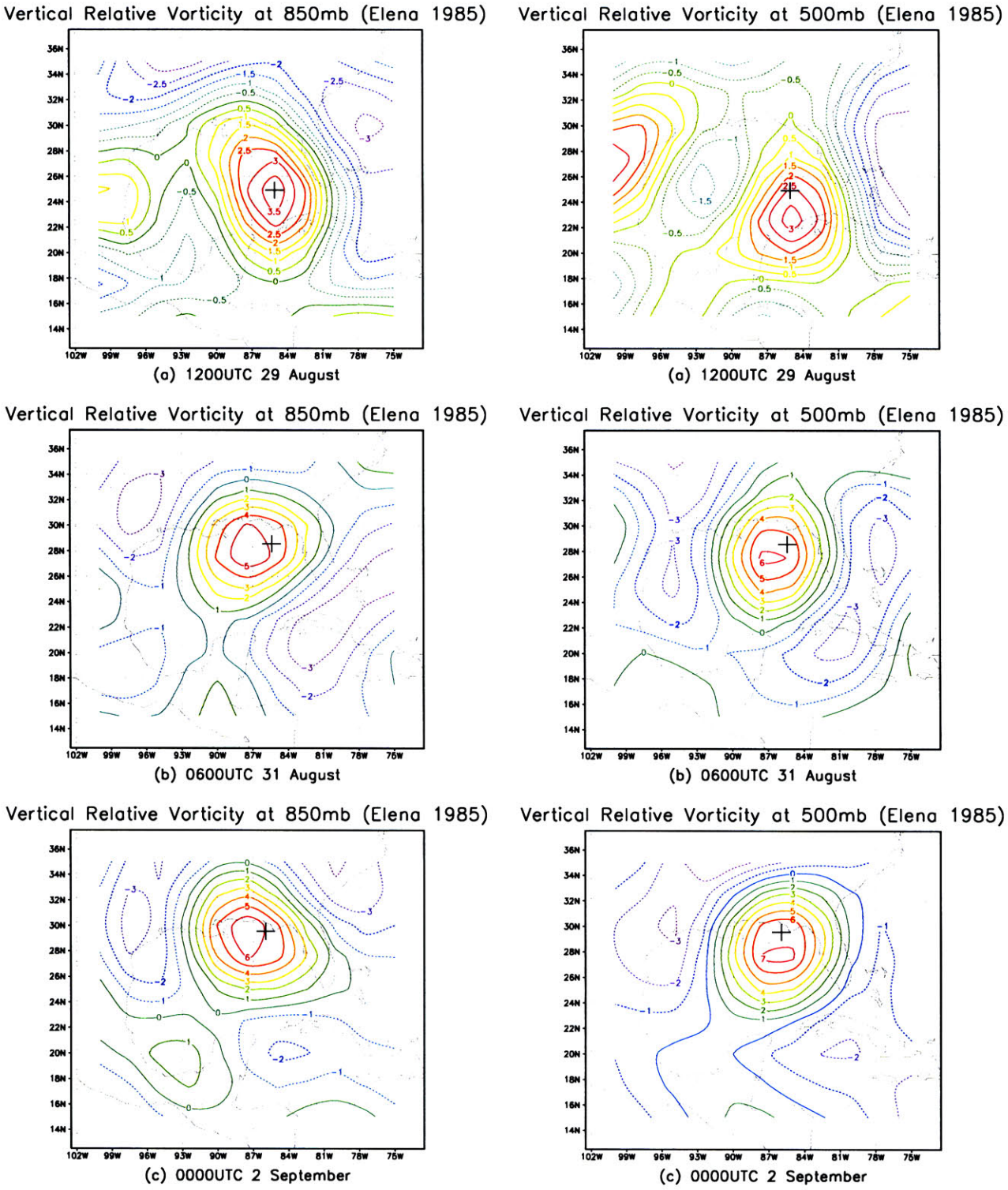

Figure 3.5: NNRA's vertical relative vorticity of Elena for 850mb (left panel) and 500mb (right panel) at (a) 1200UTC 29 August, (b) 0600UTC 31 August, and (c) 0000UTC 2 September. Unit:$10^{-5}s^{-1}$. Elena's location is indicated by the crossmark.

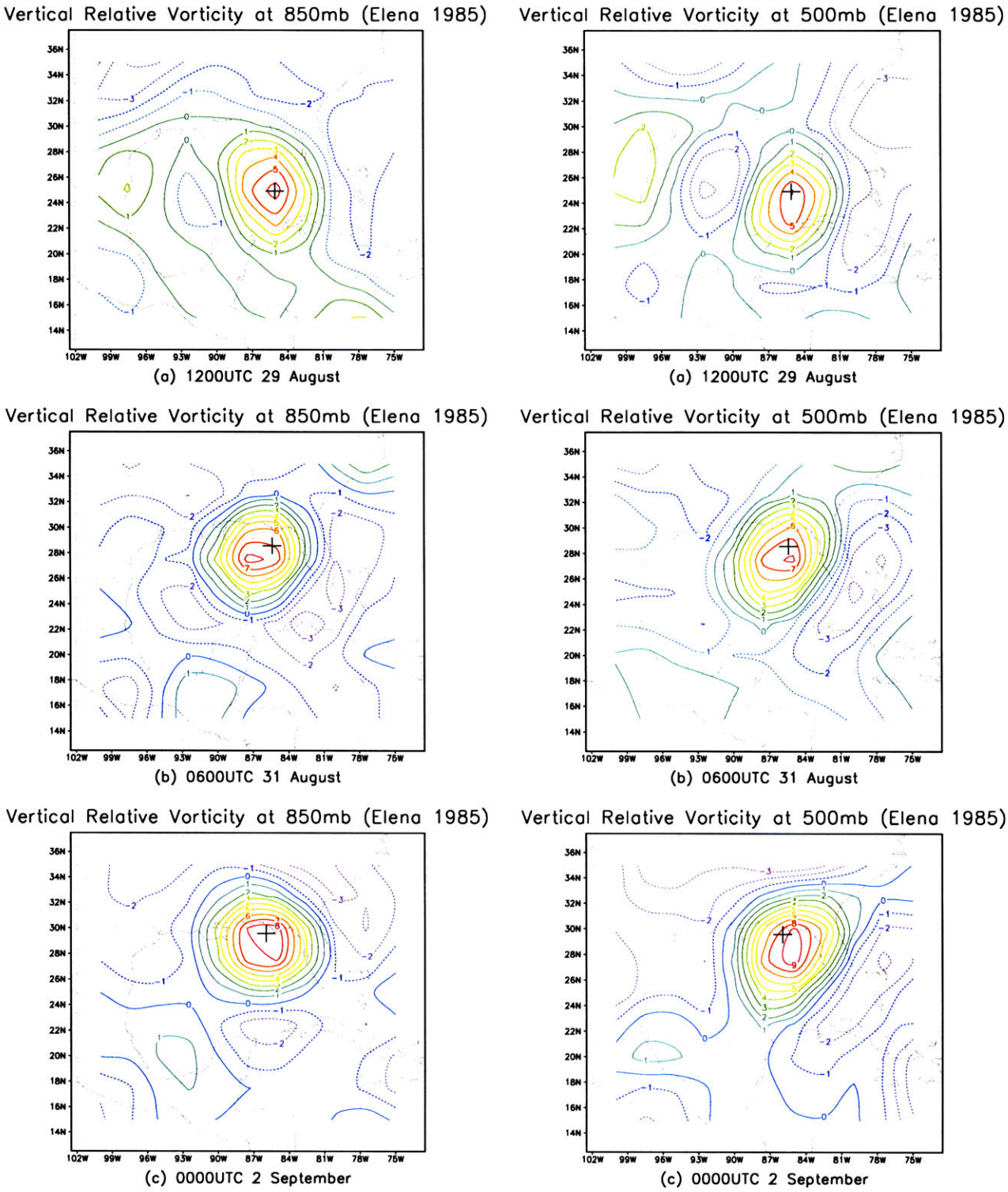

Figure 3.6: As in Fig. 3-5 but from ERA.

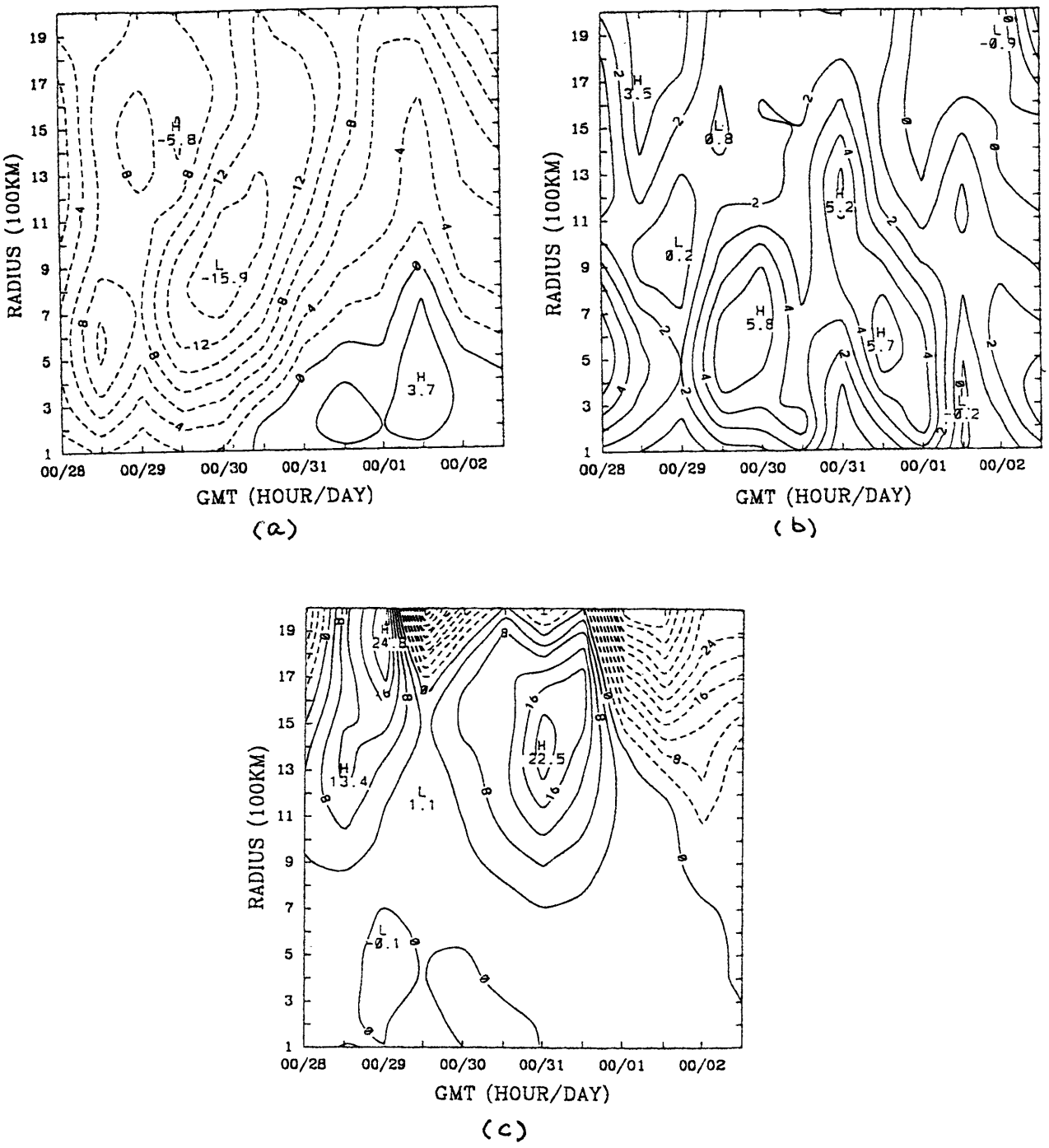

Figure 3.7: Elena's radius-time series of azimuthally averaged (a) tangential velocity with $2ms^{-1}$ contour increment, (b) radial velocity with $1ms^{-1}$ contour increment, and (c) eddy relative angular momentum fluxes with $4 \times 10^{17} kgm^2 s^{-2}$ contour increment at 200mb (from Molinari and Vollaro (1990)).

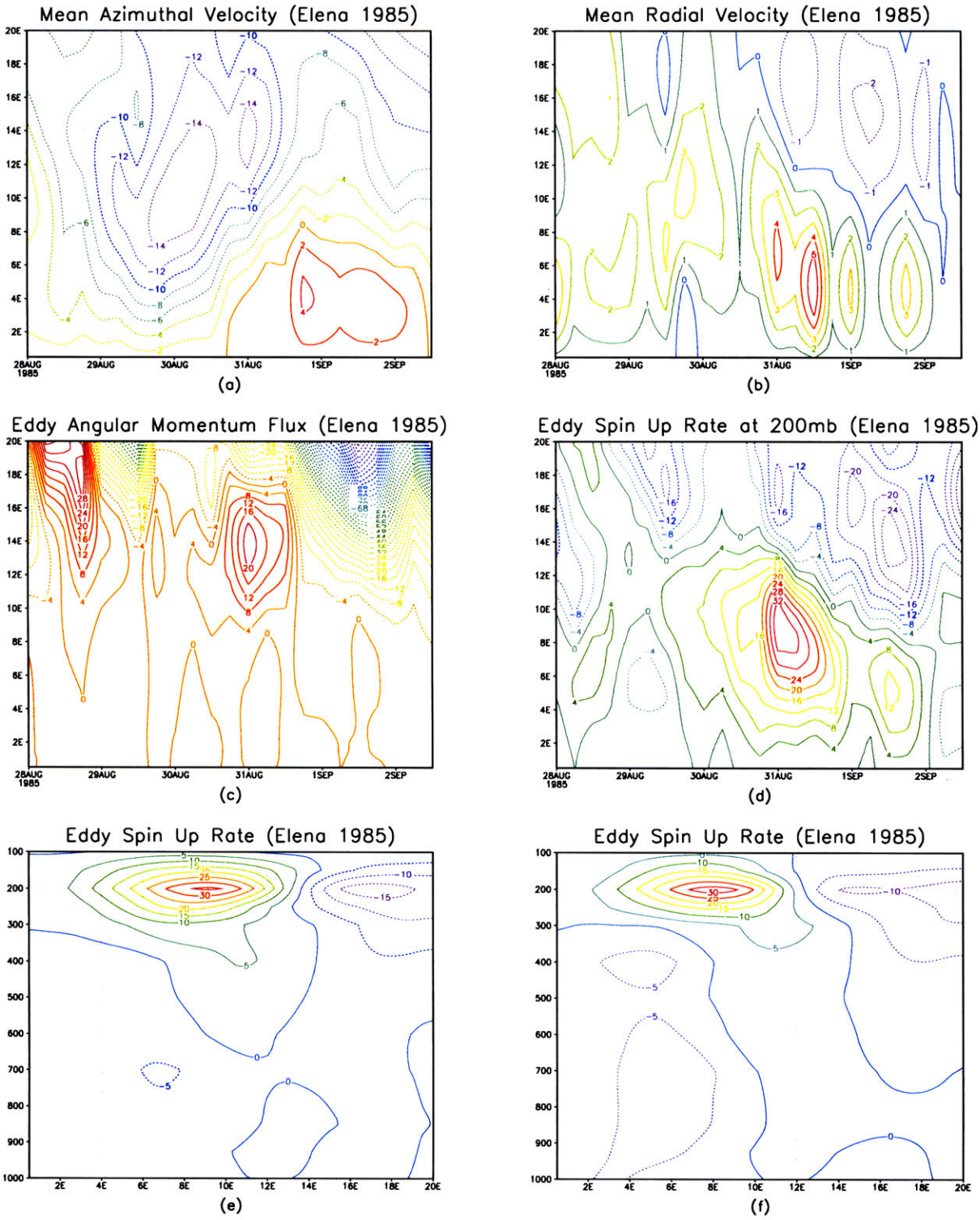

Figure 3.8: Radius-time series of mean (a) azimuthal velocity (m/s) and (b) radial velocity (m/s) at 200mb, (c) eddy relative angular momentum fluxes ($10^{17} kgm^2 s^{-2}$), and eddy spinup rates (m/s/day) at (d) 200mb for Elena of 1985. Eddy spin up rate at (e) 0000UTC 31 August and (f) 0600UTC 31 August for Elena. The calculation is based on the NNRA dataset. 1E in plots is equal to 1 latitude degree which is equal to 111km.

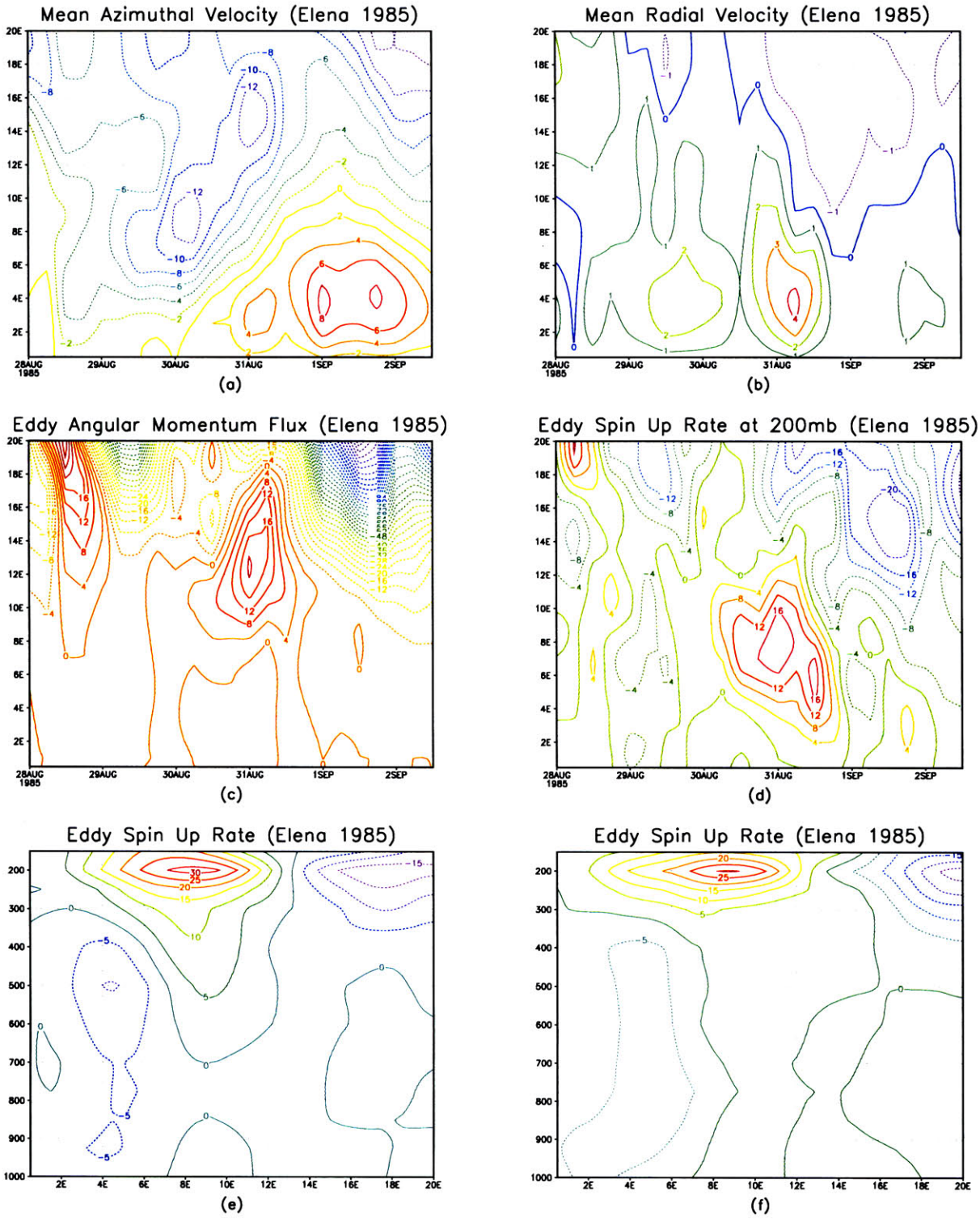

Figure 3.9: As in Fig. 3-8 but the calculation is based on the ERA dataset.

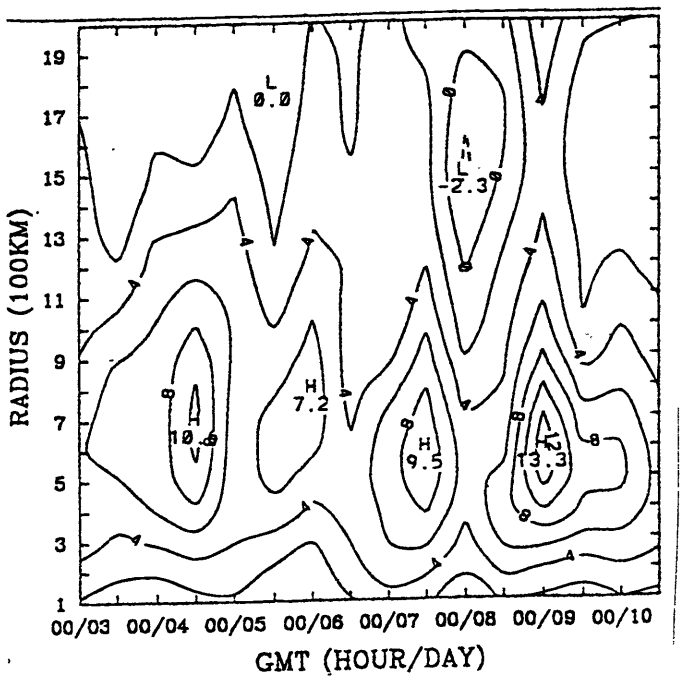

Figure 3.10: Radius-time series of azimuthally averaged radial velocity (m/s) at 200mb in Allen of 1980, computed from the objectively analyzed winds (from Molinari (1992)).

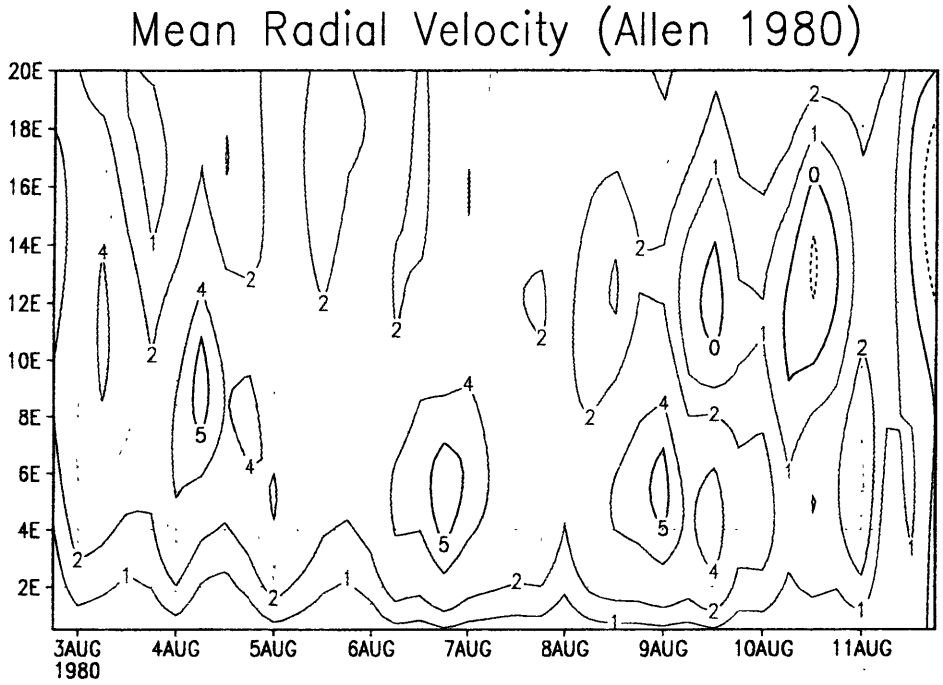

Figure 3.11: As in Fig. 3-10 but the calculation is based on the NNRA dataset.

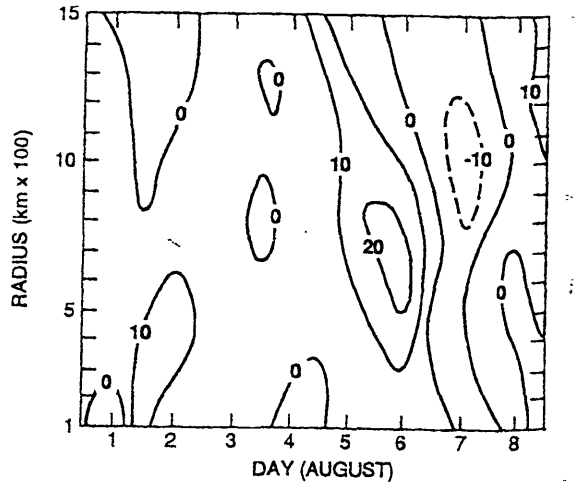

Figure 3.12: Radius-time series of eddy spin up rate (m/s/day) at 200mb for (a) Dean of 1989, and (b) Gabrielle of 1989 (from Demaria et al.(1993)).

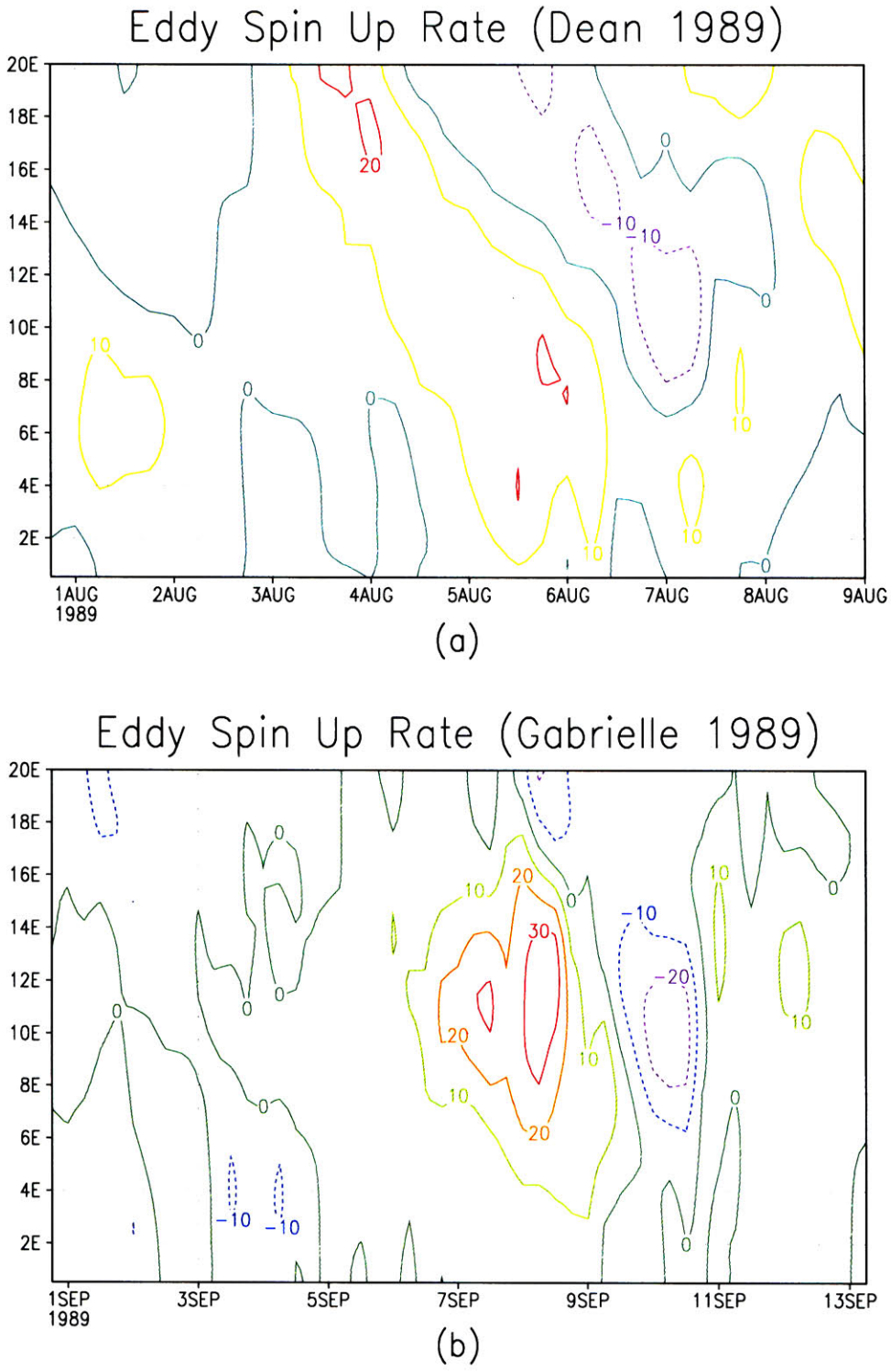

Figure 3.13: As in Fig. 3-12 but the calculation is based on the NNRA dataset.

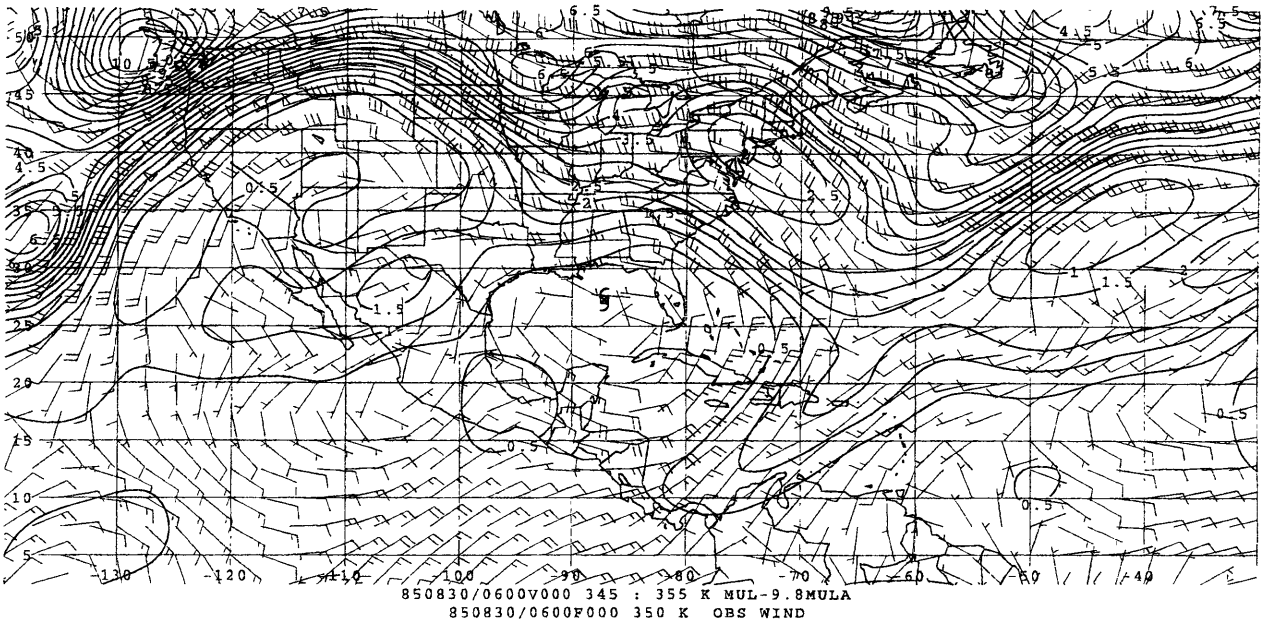

Figure 3.14: Wind barbs (m/s) and Ertel's potential vorticity (PVU) on the $\theta = 350K$ surface for Elena at (a) 0600UTC 30 August (Elena's location is indicated by the hurricane symbol);

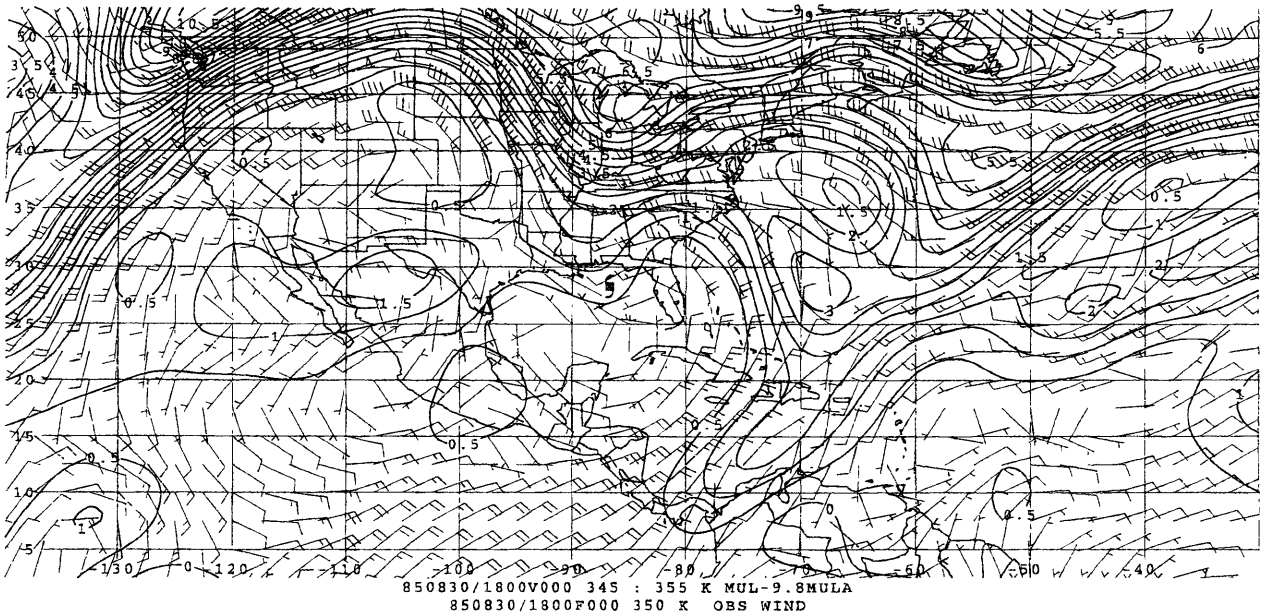

Figure 3.14: (b) 1800UTC 30 August;

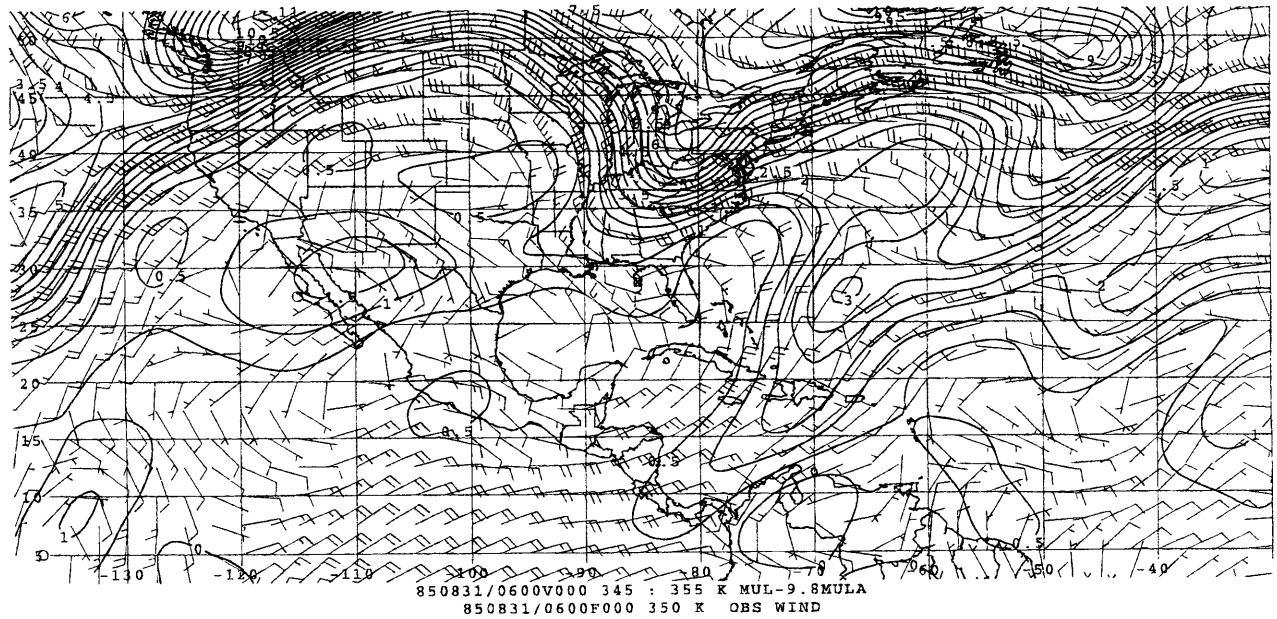

Figure 3.14: (c) 0600UTC 31 August;

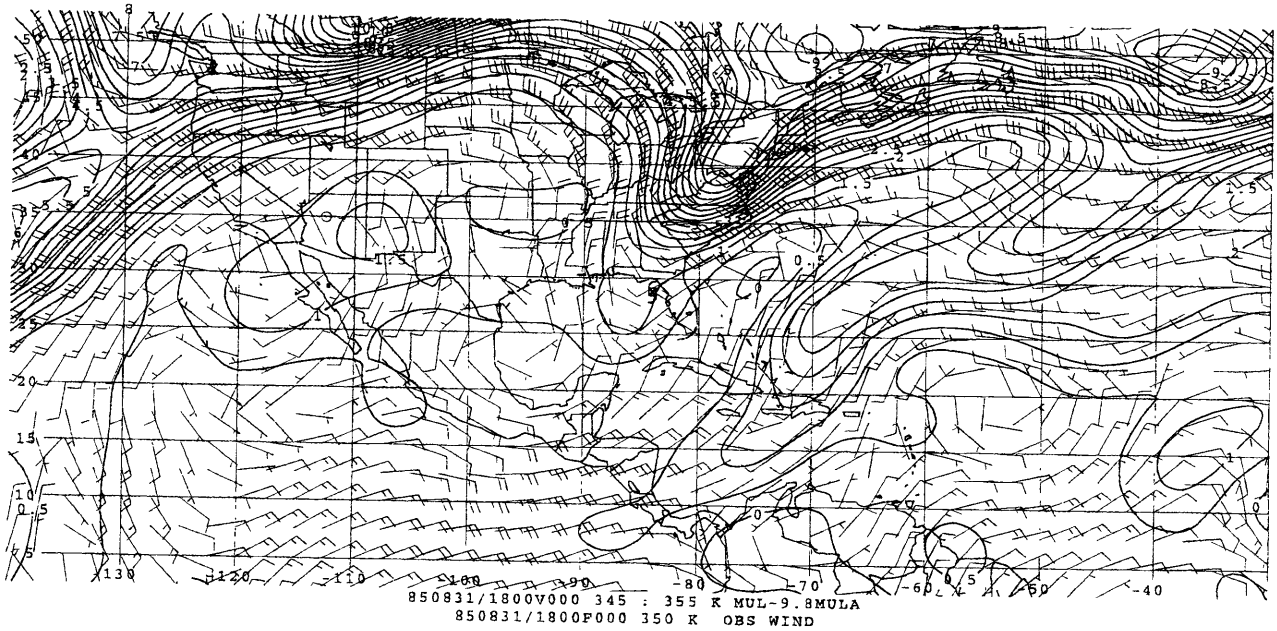

Figure 3.14: (d) 1800UTC 31 August;

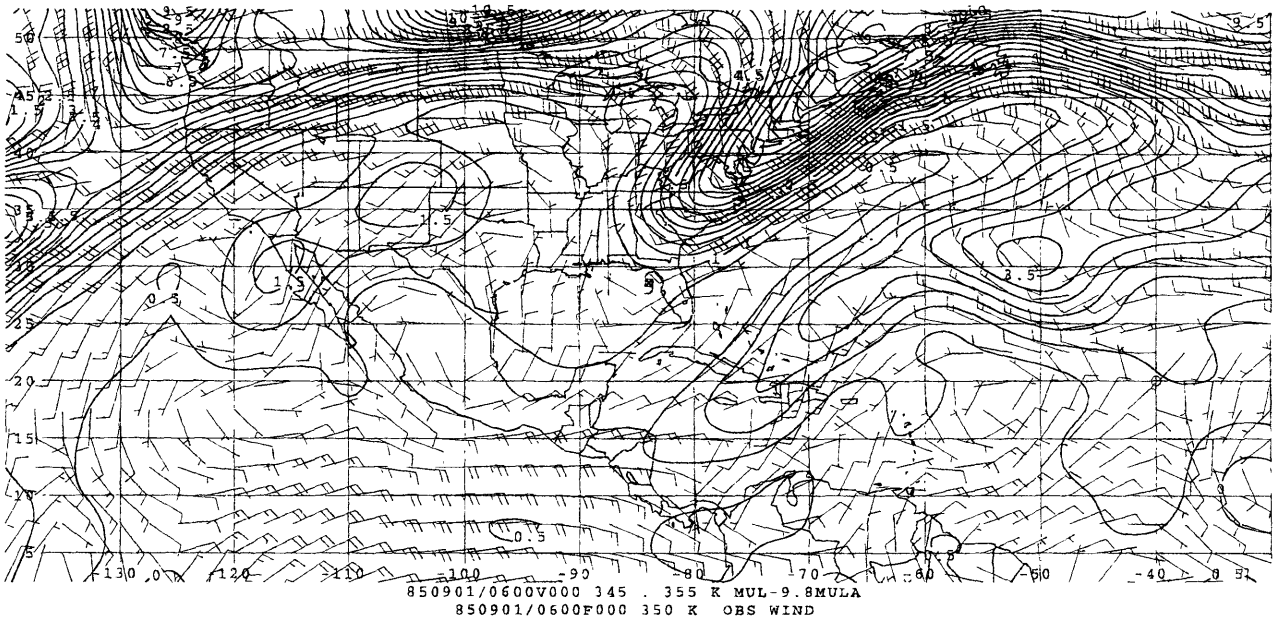

Figure 3.14: (e) 0600UTC 1 September;

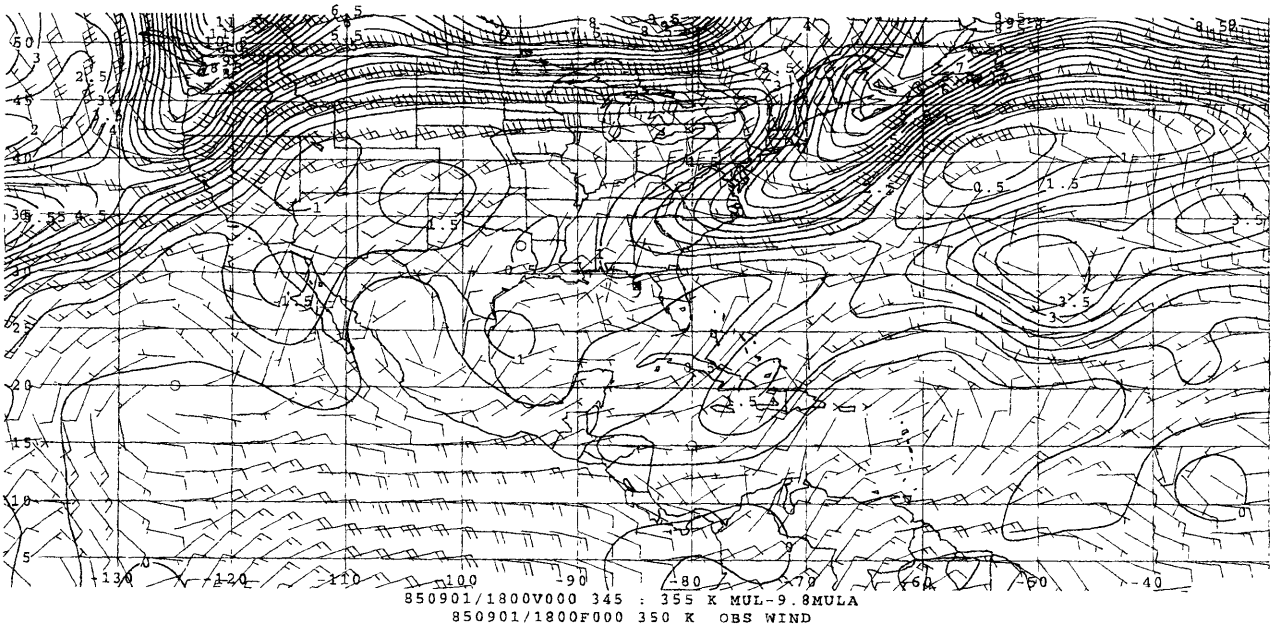

Figure 3.14: (f) 1800UTC 1 September.

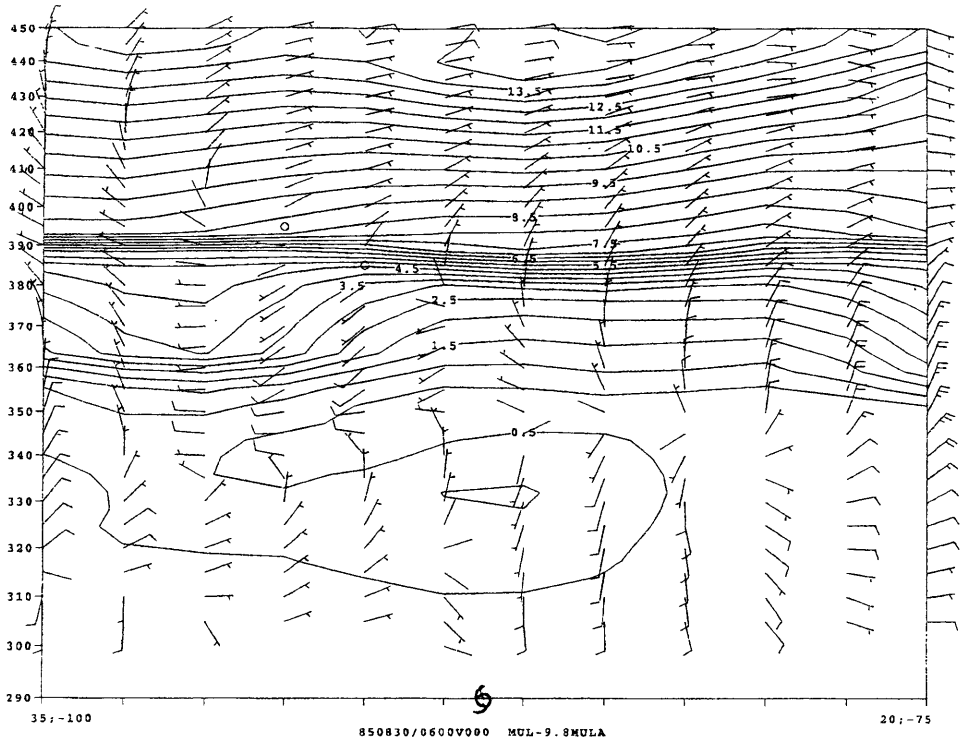

Figure 3.15: Cross sections of IPV (PVU) from northwest (left) to southeast (right) through the observed center of Hurricane Elena at (a) 0600UTC 30 August (Elena's location is indicated by the hurricane symbol;

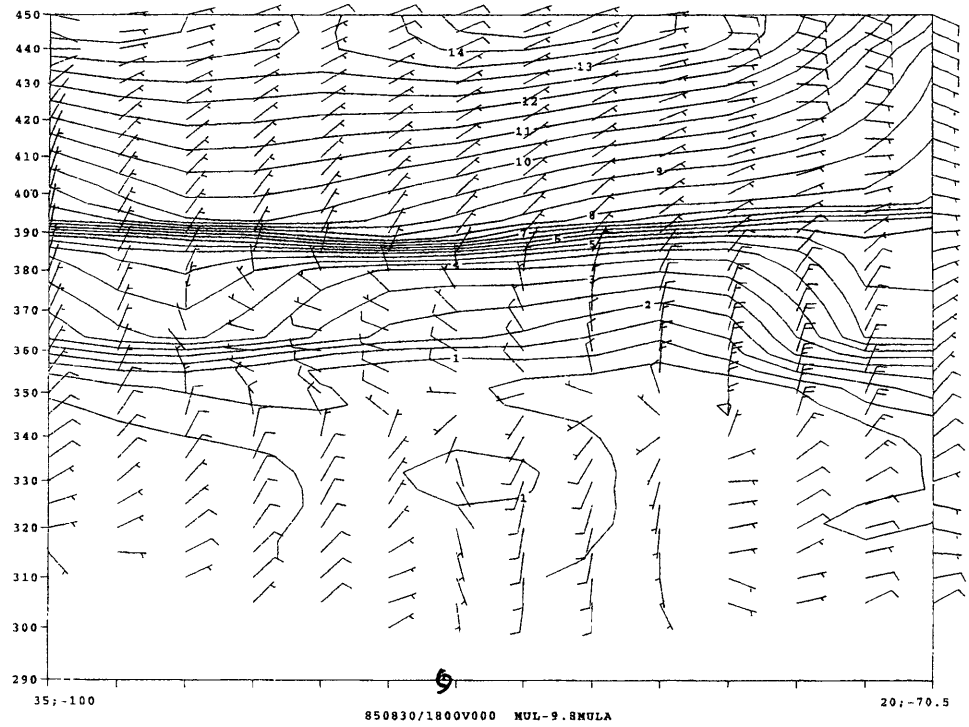

Figure 3.15: (b) 1800UTC 30 August;

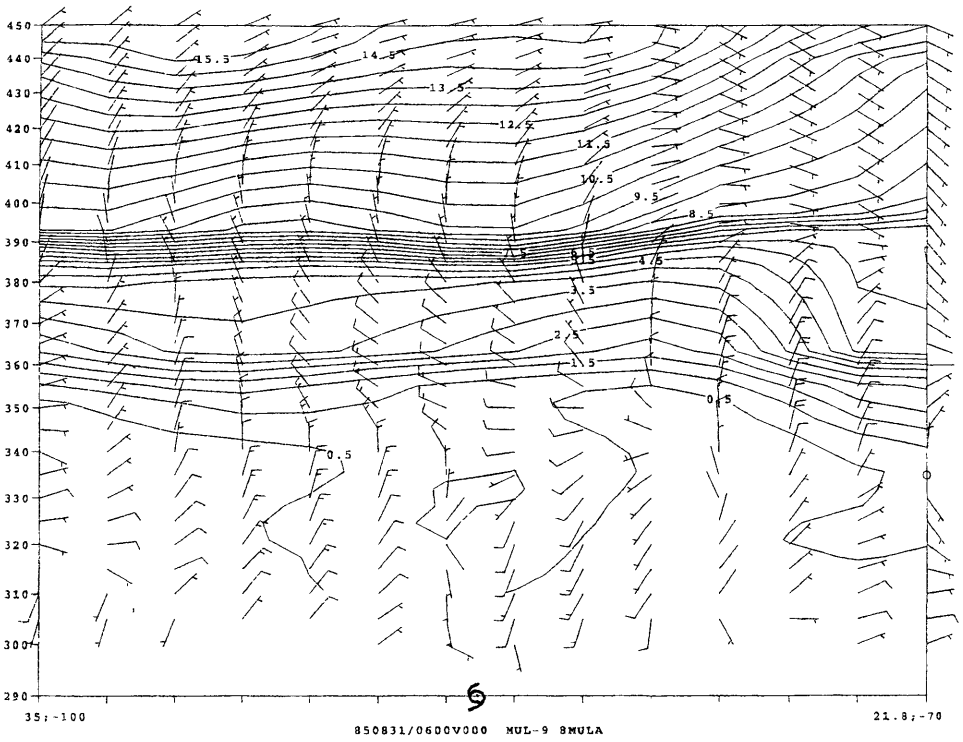

Figure 3.15: (c) 0600UTC 31 August;

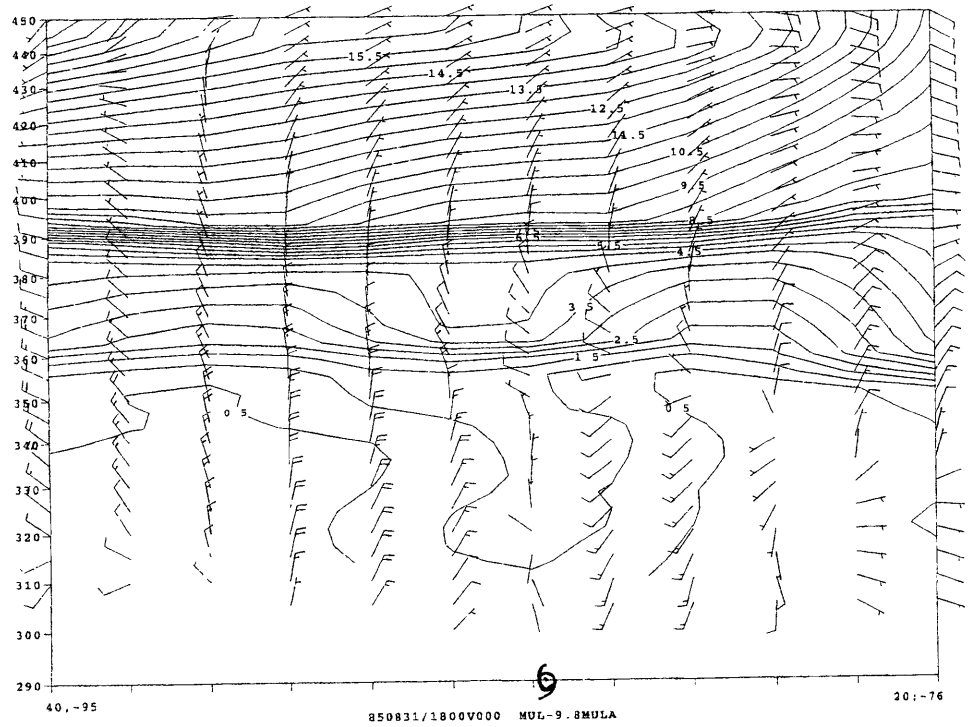

Figure 3.15: (d) 1800UTC 31 August;

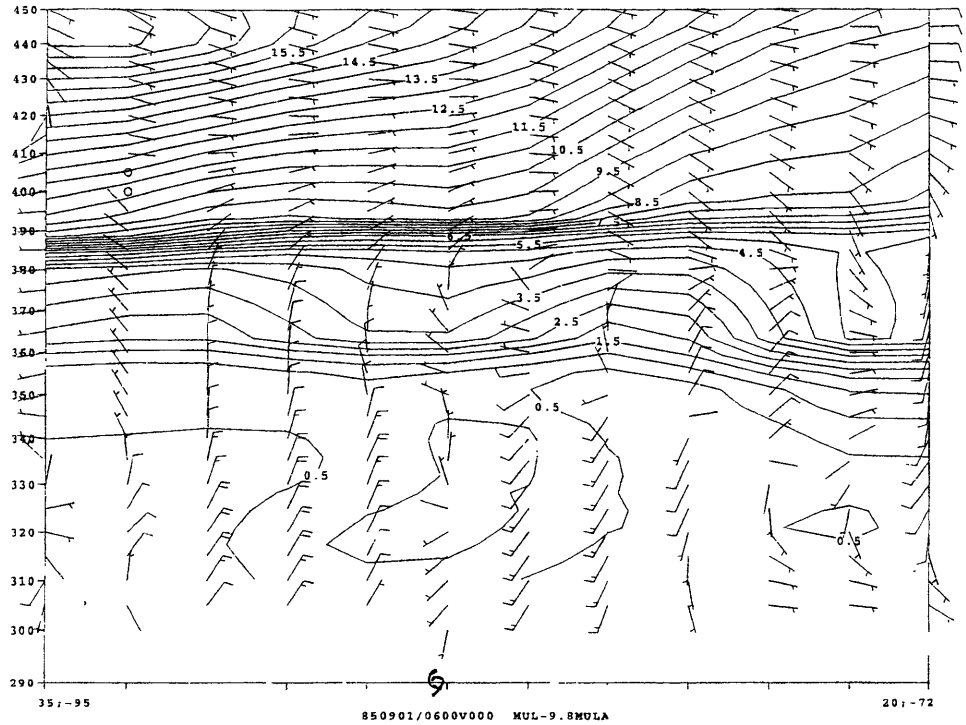

Figure 3.15: (e) 0600UTC 1 September;

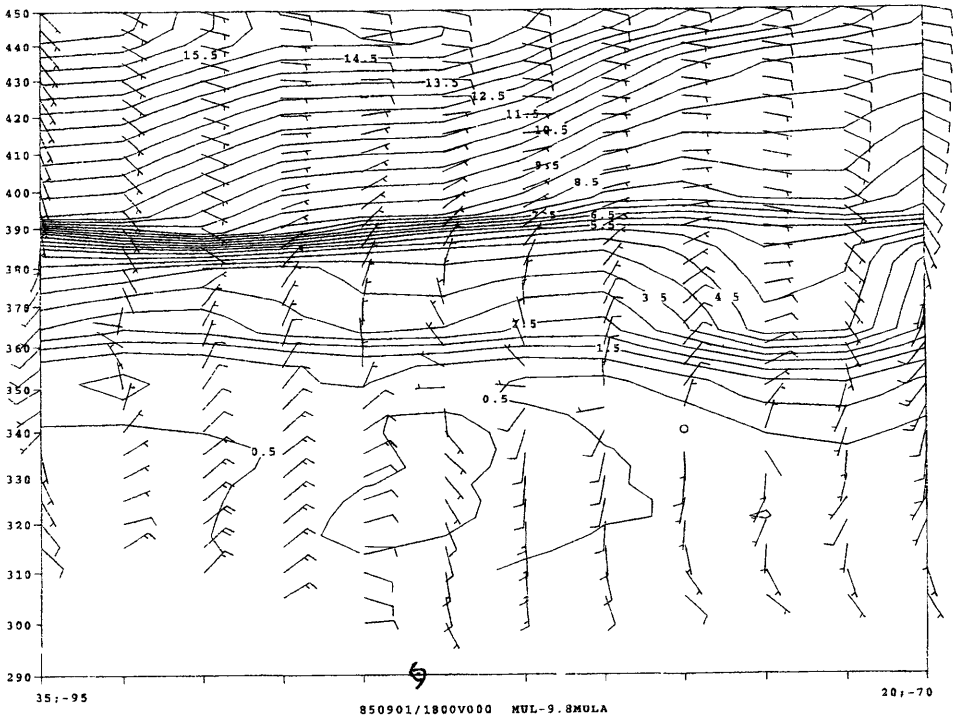

Figure 3.15: (f) 1800UTC 1 September.

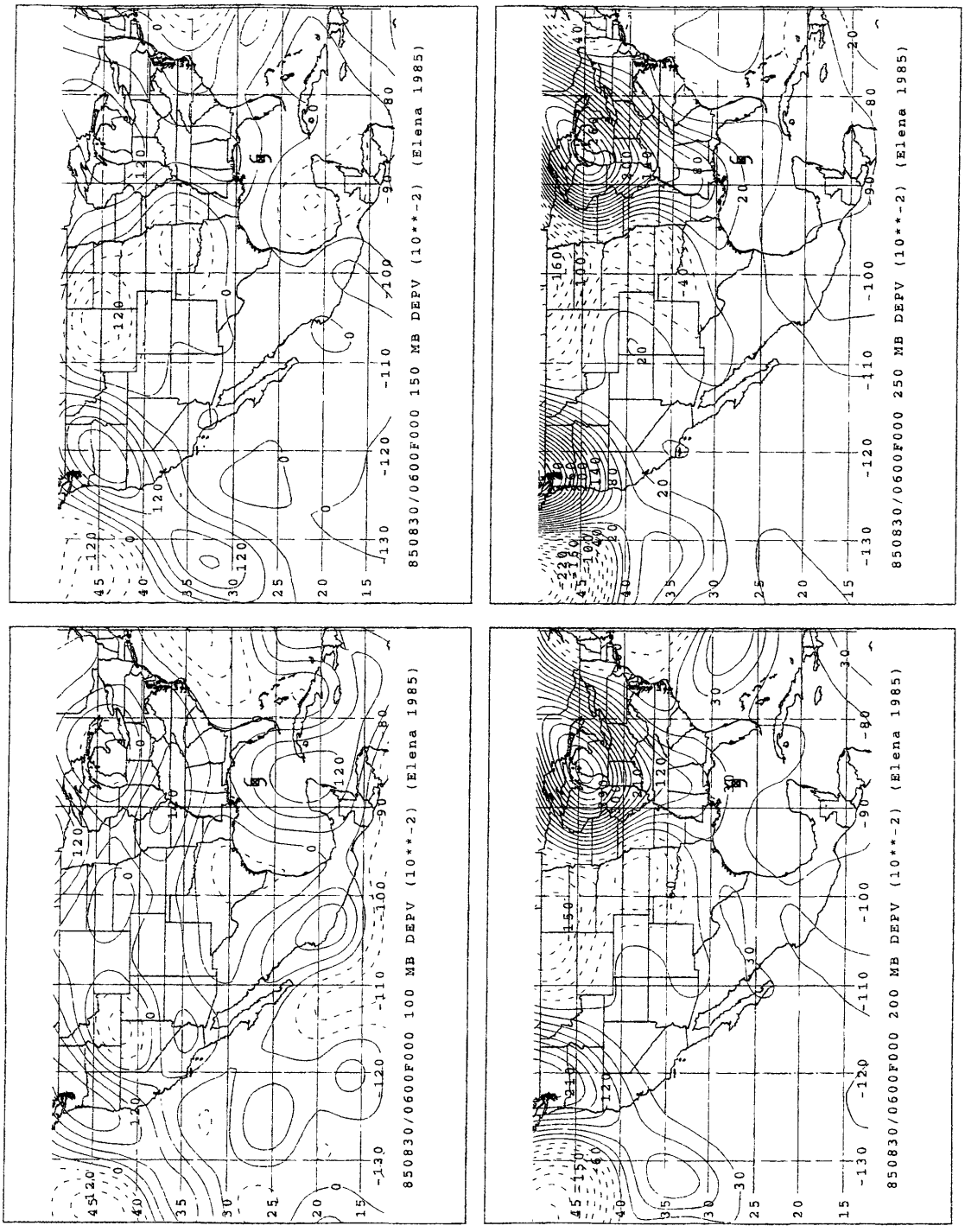

Figure 3.16: Local PV tendency (10^{-2}PVU/12h) on 100mb, 150mb, 200mb and 250mb for Elena of 1985 at (a) 0600UTC 30 August (Elena's location is indicated by the hurricane symbol);

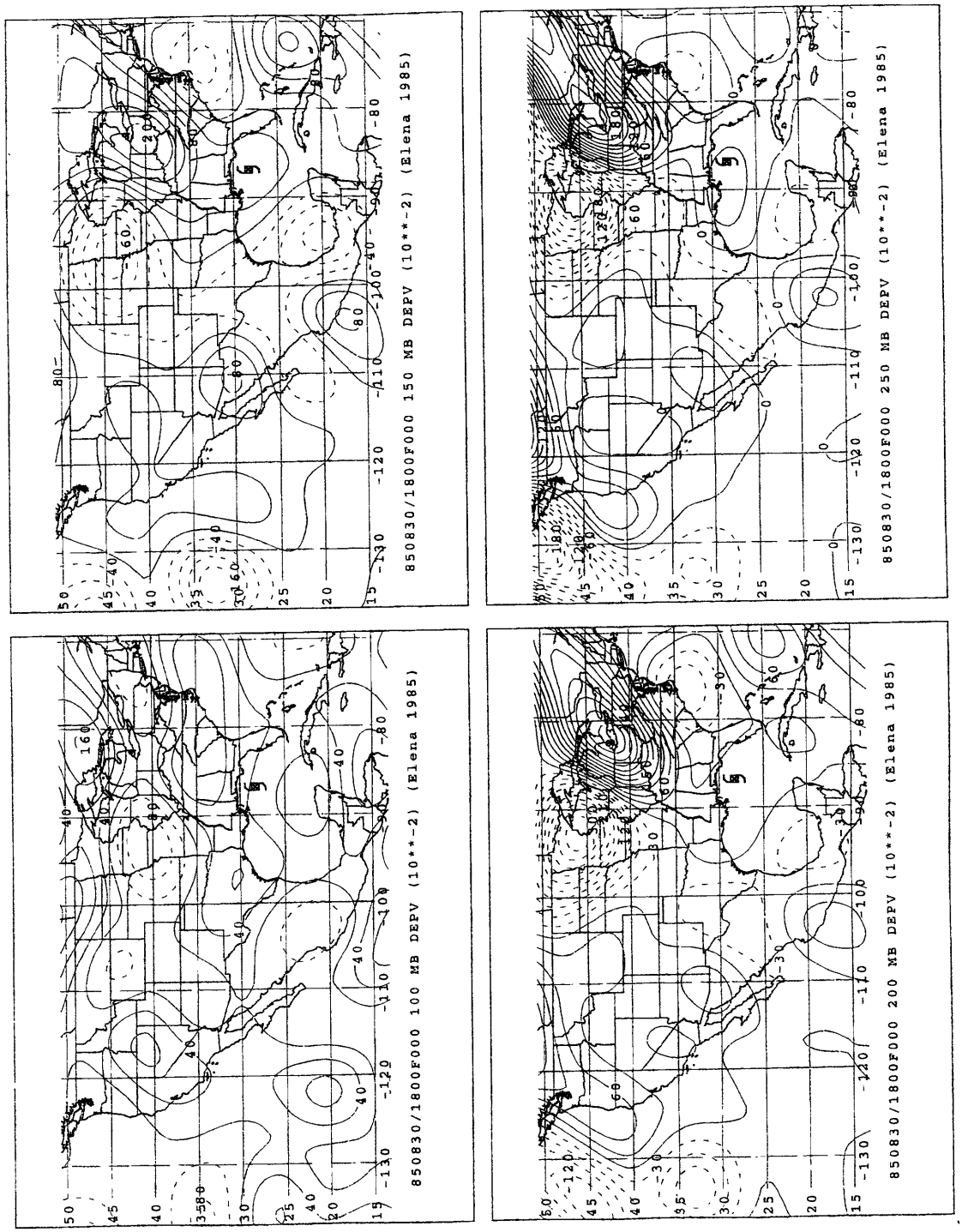

Figure 3.16: (b) 1800UTC 30 August;

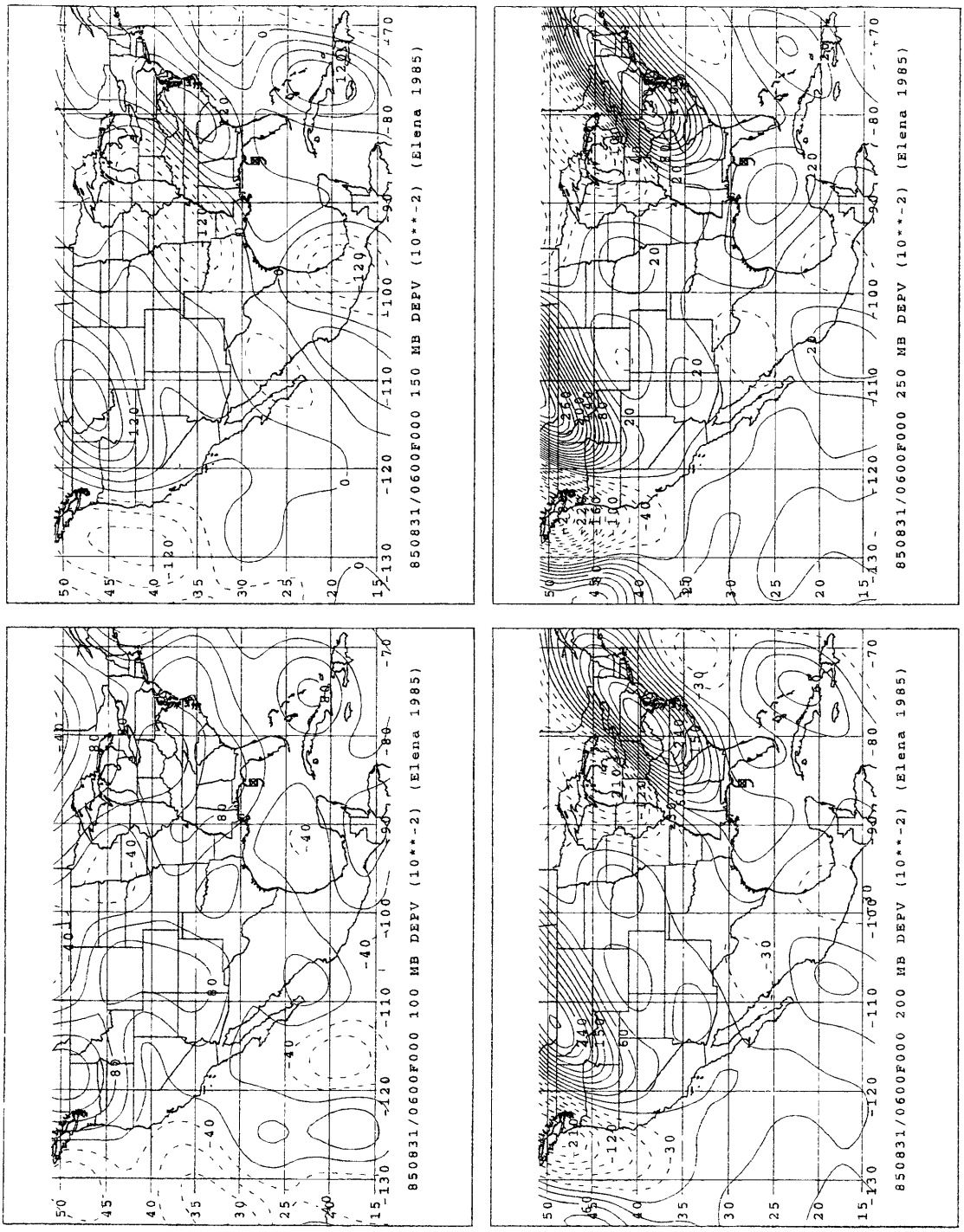

Figure 3.16: (c) 0600UTC 31 August;

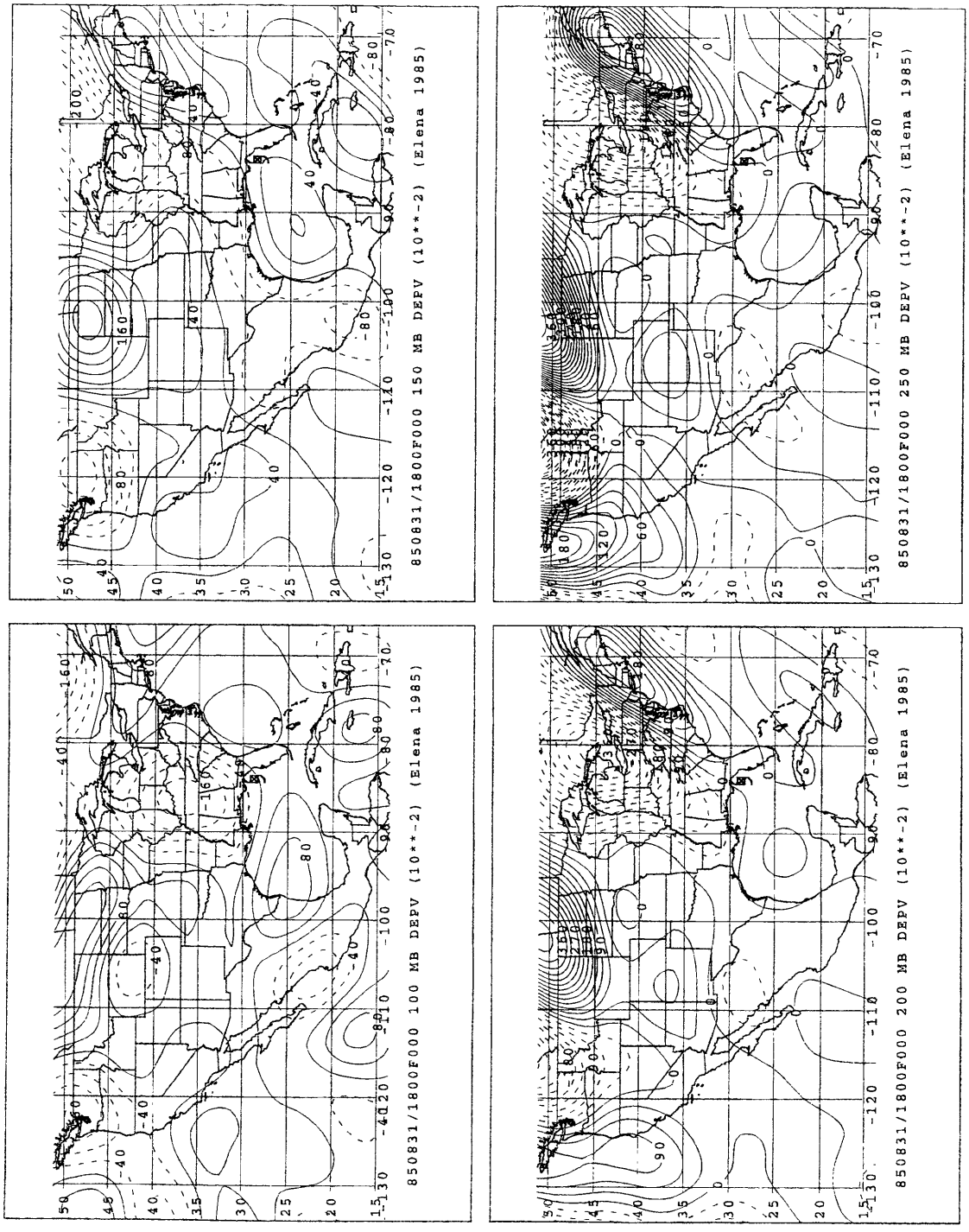

Figure 3.16: (d) 1800UTC 31 August;

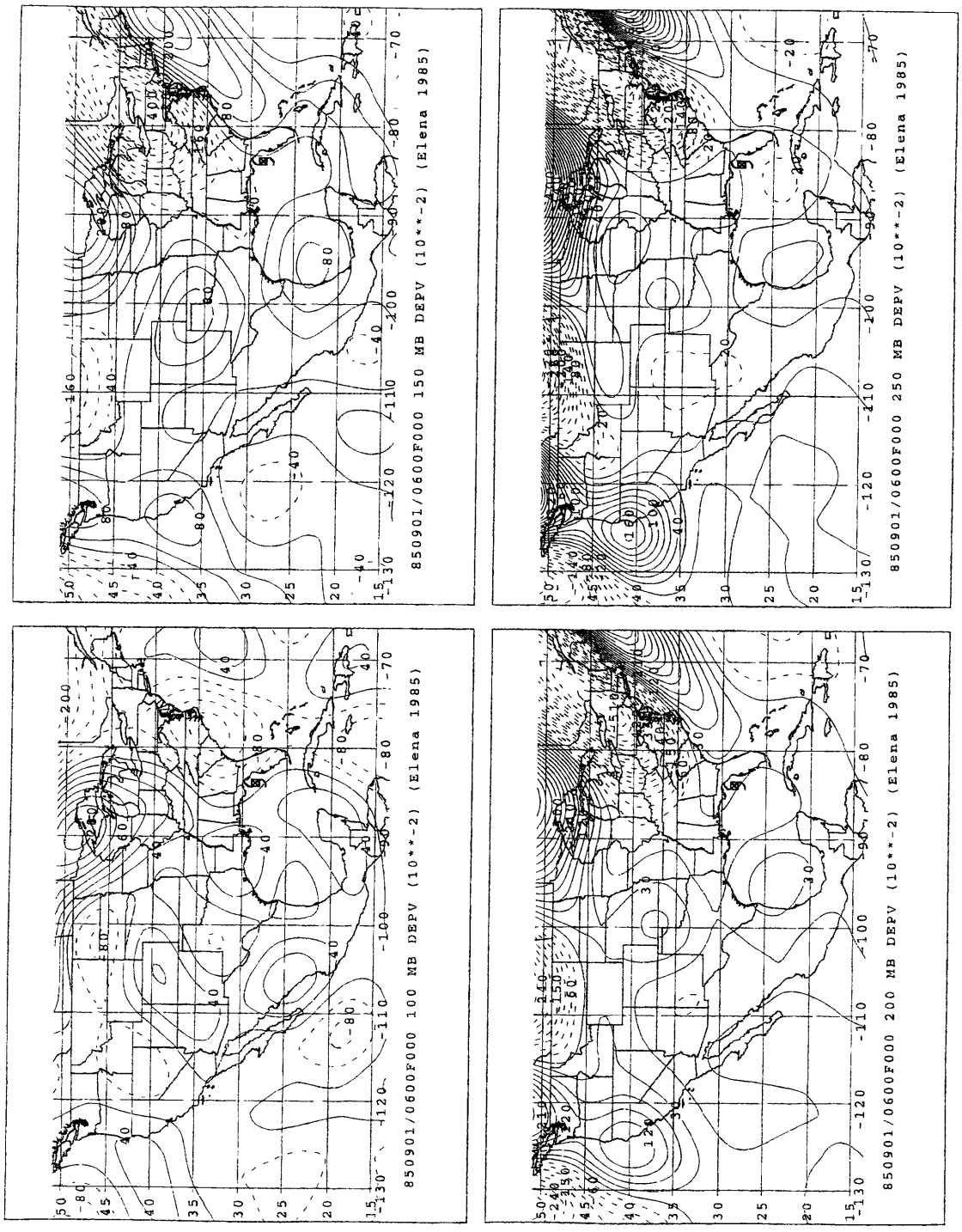

Figure 3.16: (e) 0600UTC 1 September;

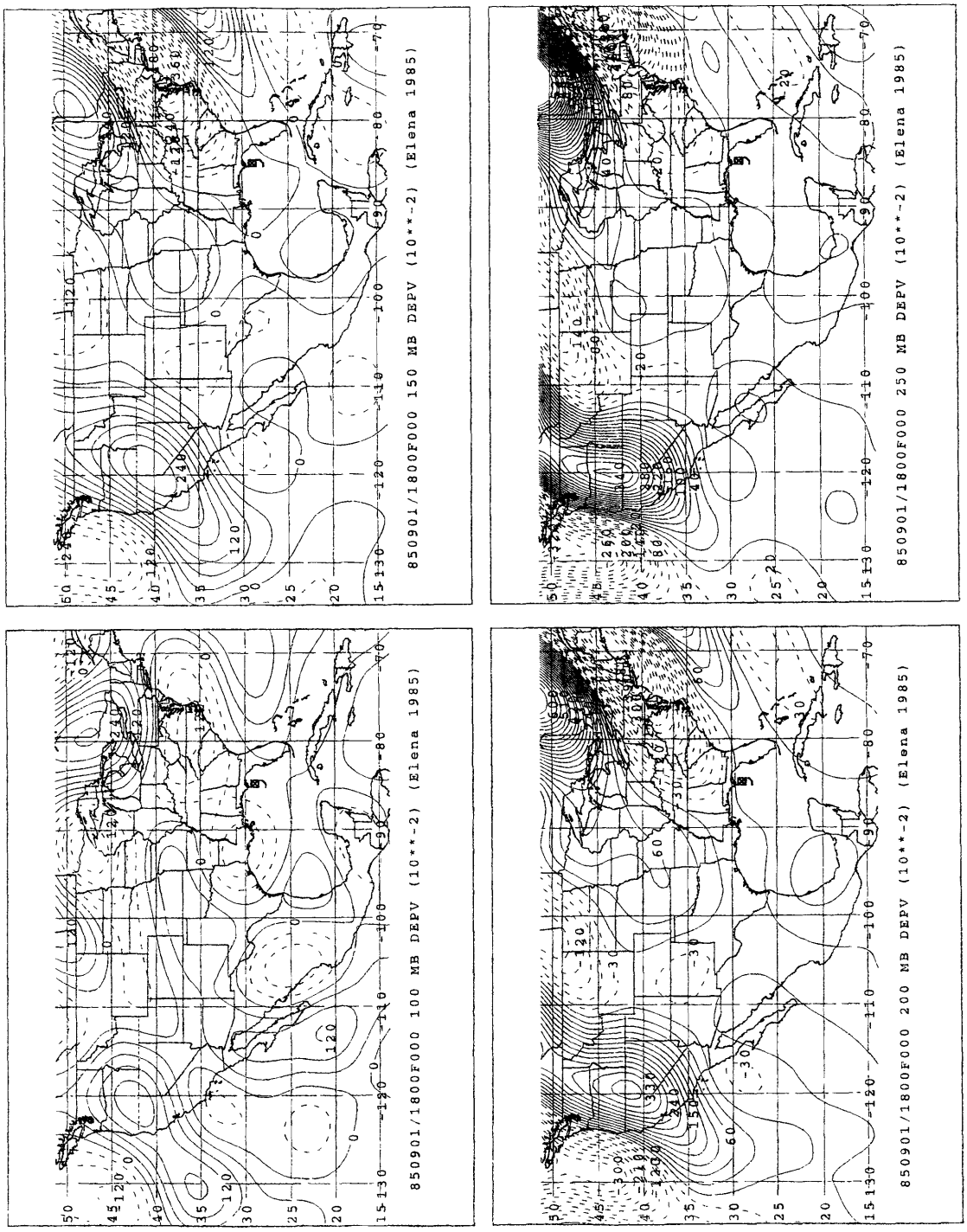

Figure 3.16: (f) 1800UTC 1 September.

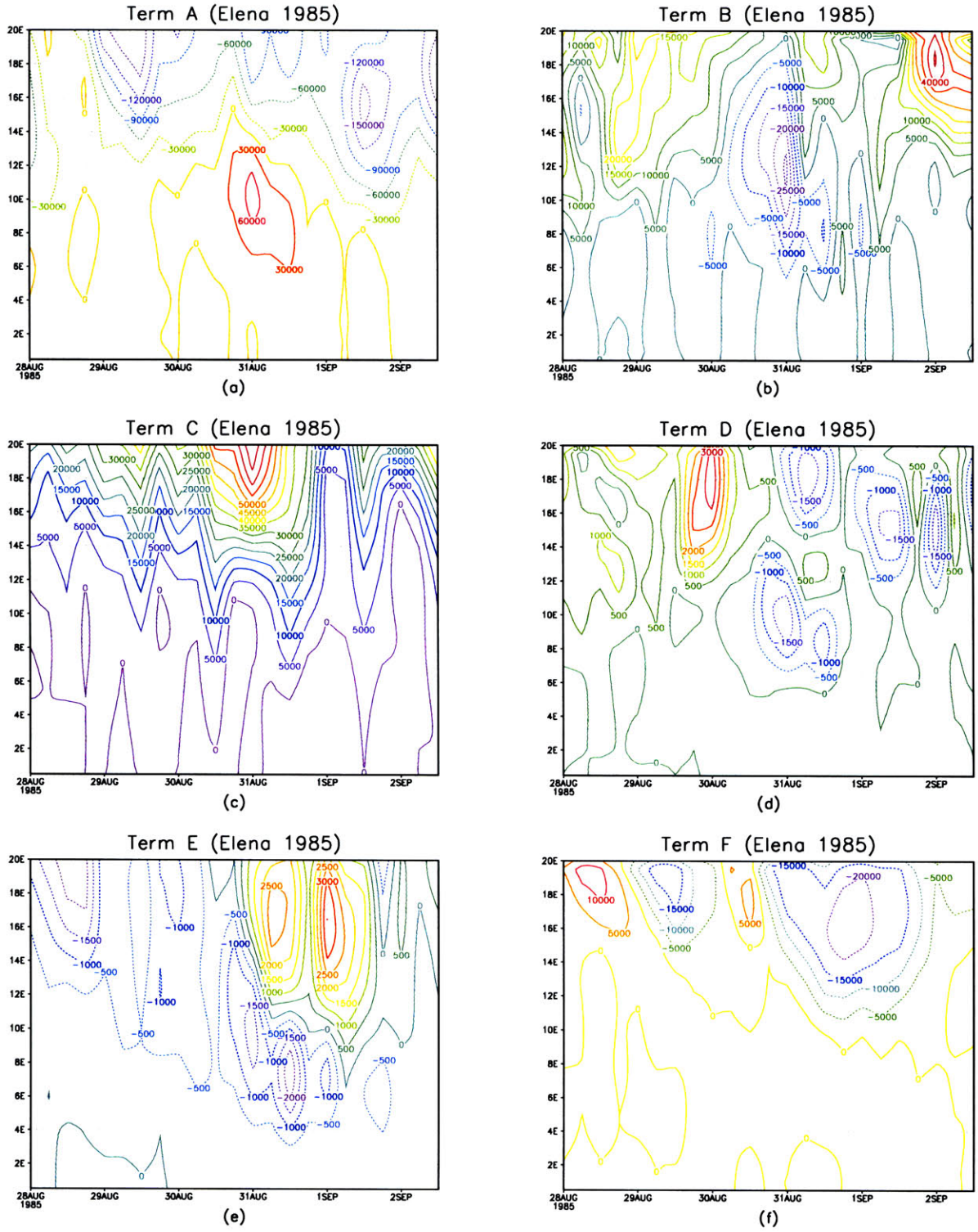

Figure 3.17: Radius-time series of individual terms (mK) in Equation 3.12 for Elena based on the NNRA dataset. (a) Term A, (b) Term B, (c) Term C, (d) Term D, (e) Term E, (f) Term F,

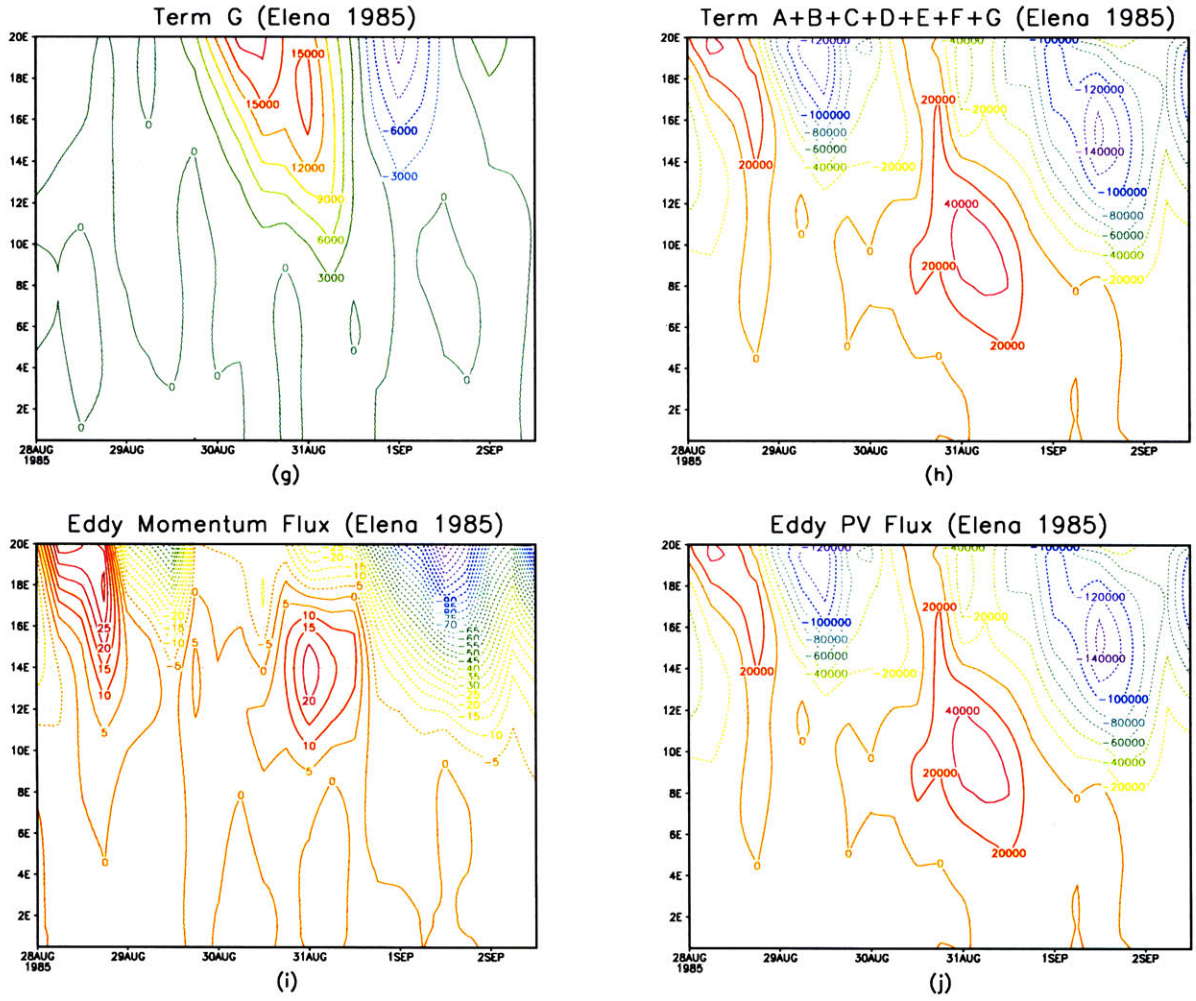

Figure 3.17: (continued) (g) Term G, (h) sum of all individual terms, (i) eddy relative angular momentum fluxes ($10^{17} kgm^{-2}s^{-2}$), (j) eddy PV fluxes (mK) (exactly equal to the sum in (h)).

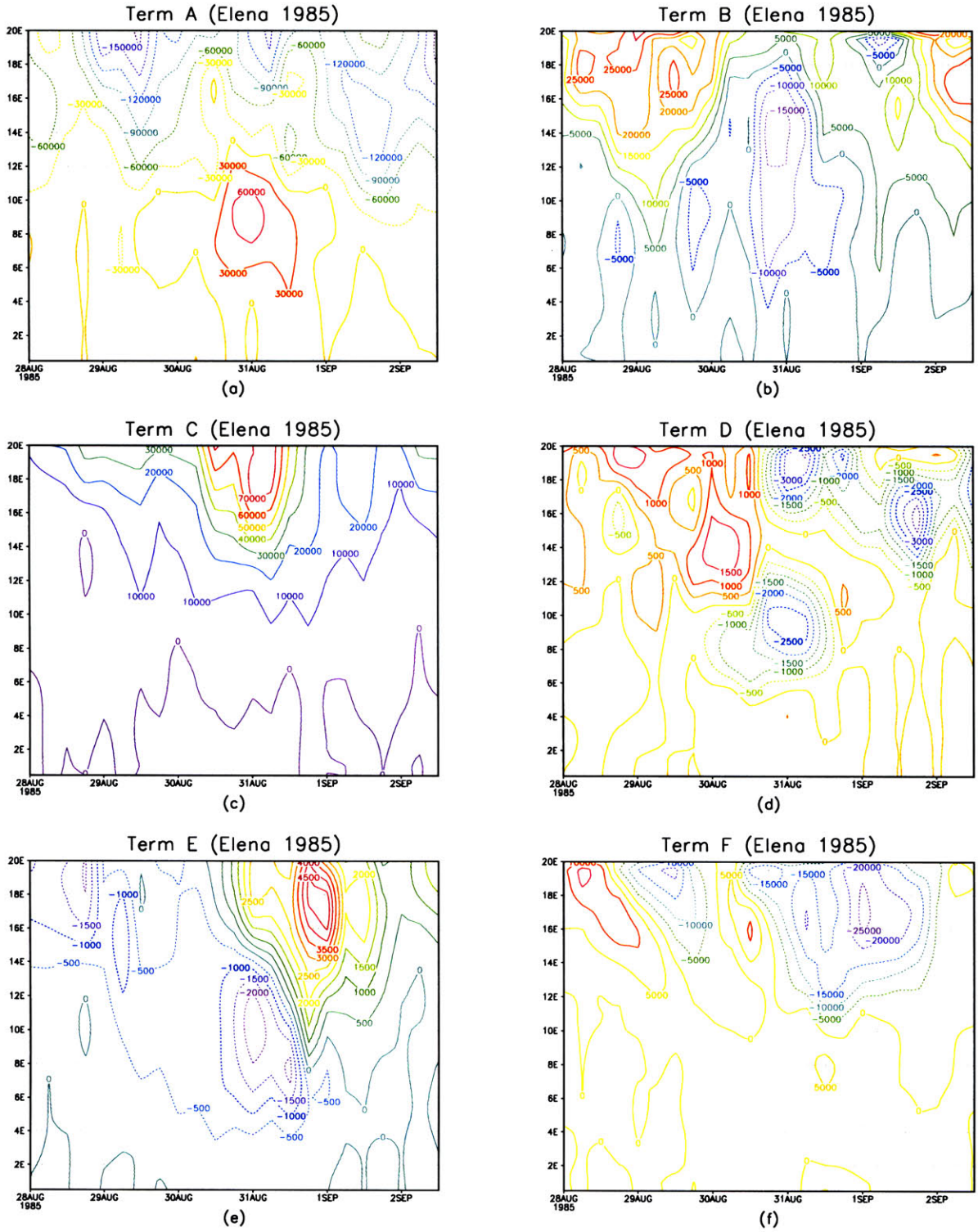

Figure 3.18: As in Fig. 3-17 but the calculation is based on the ERA dataset.

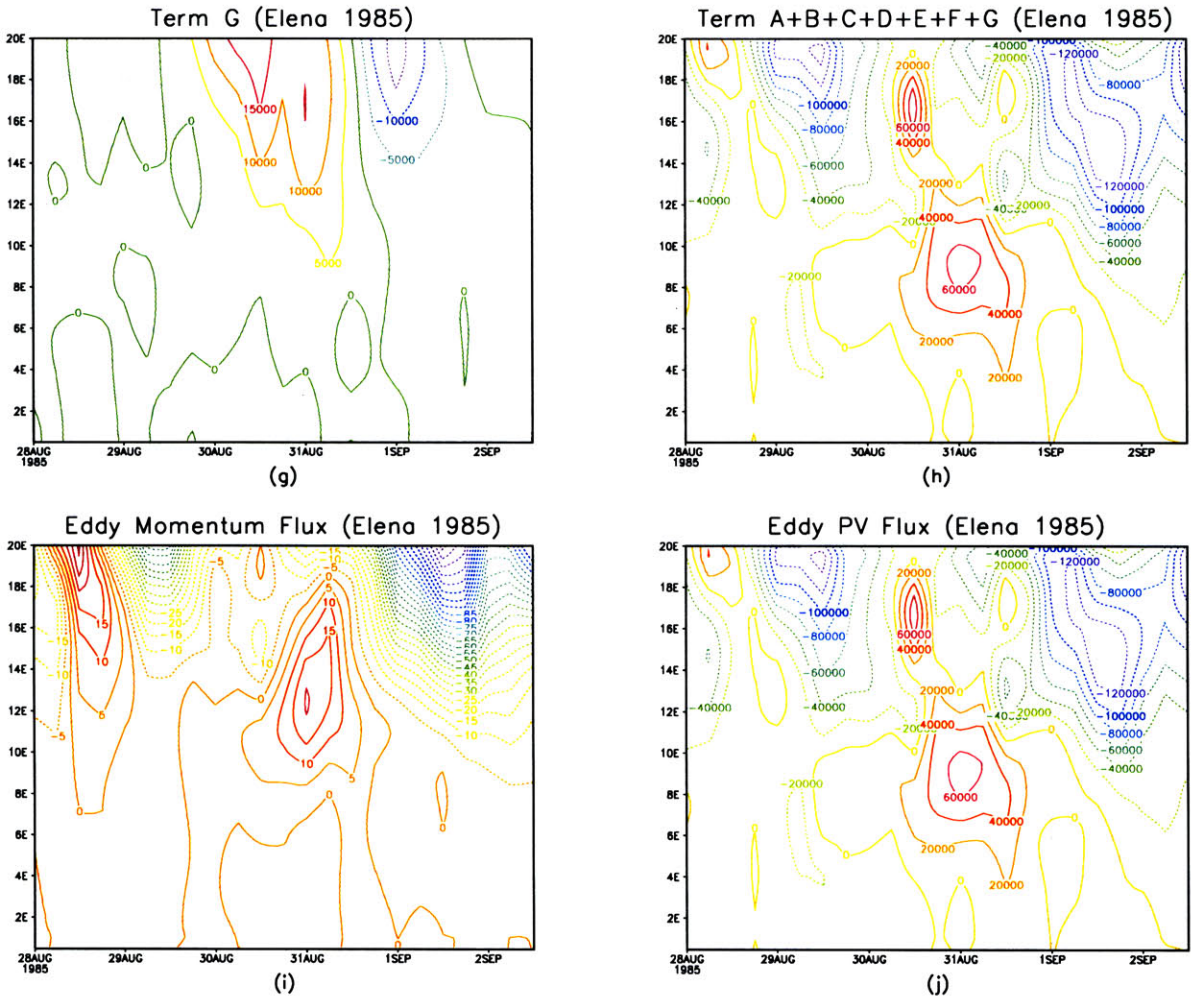

Figure 3.18: (continued)

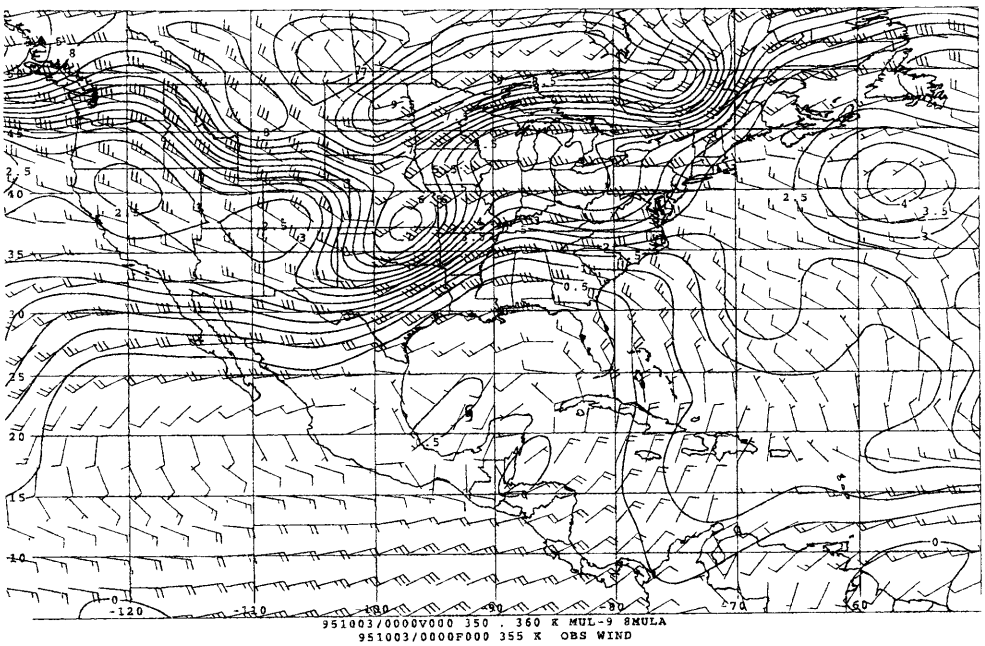

Figure 3.19: Wind barbs (m/s) and Ertel's potential vorticity (PVU) on the $\theta = 355K$ surface for Opal at (a) 0000UTC 3 October (Opal's location is indicated by the hurricane symbol);

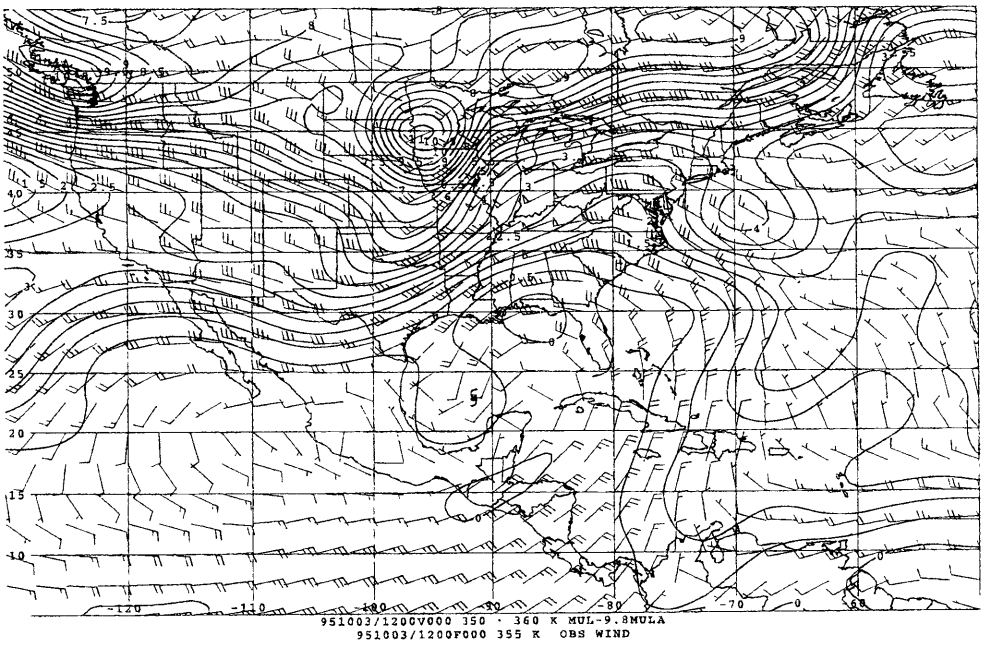

Figure 3.19: (b) 1200UTC 3 October;

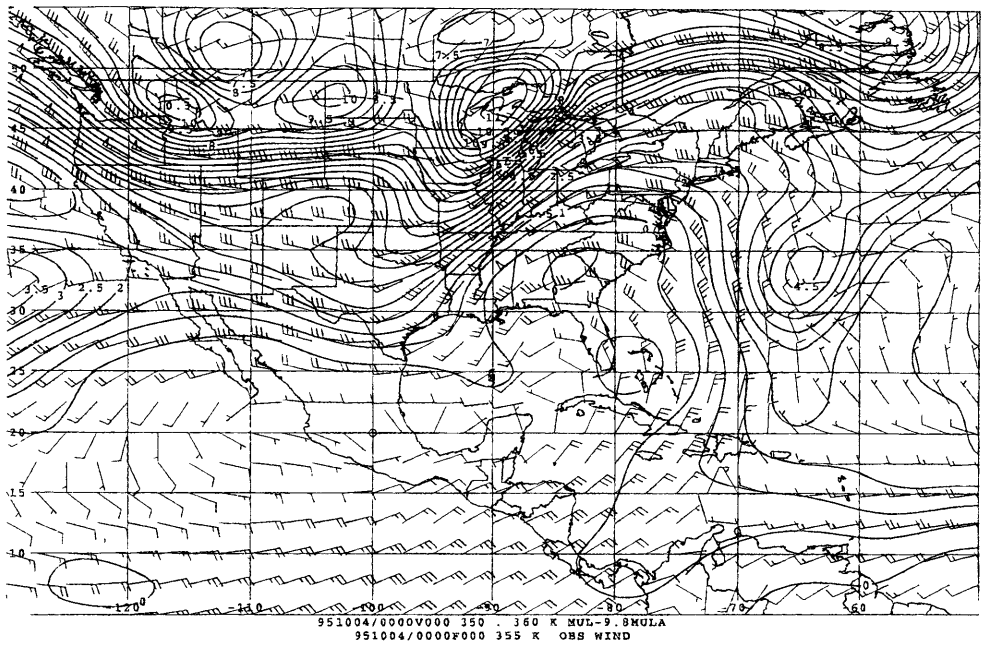

Figure 3.19: (c) 0000UTC 4 October;

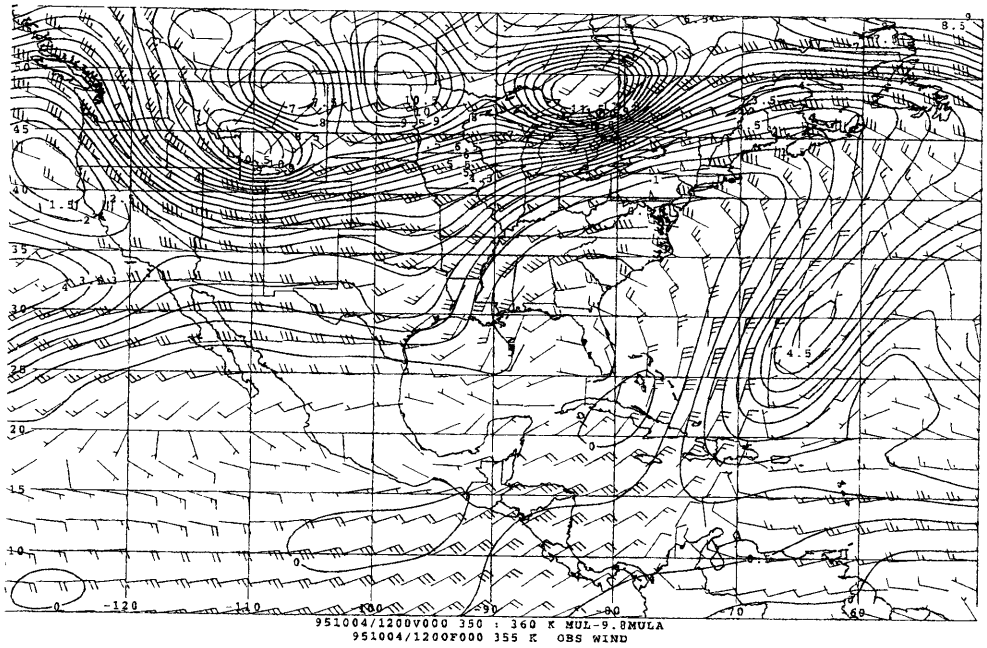

Figure 3.19: (d) 1200UTC 4 October.

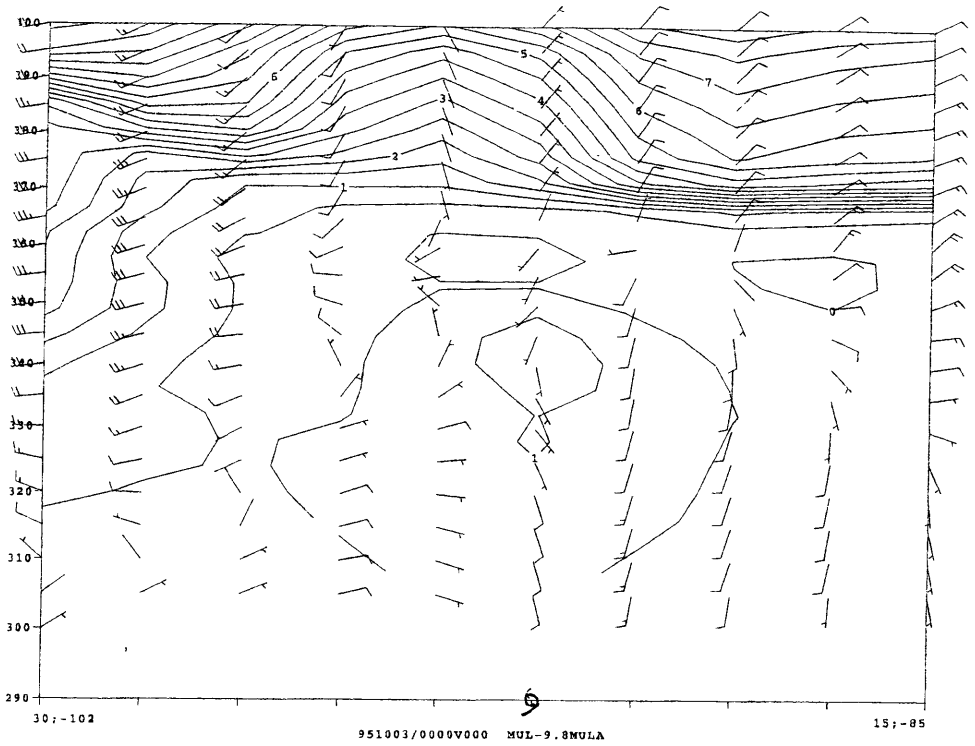

Figure 3.20: Cross sections of IPV (PVU) from northwest (left) to southeast (right) through the observed center of Hurricane Opal at (a) 0000UTC 3 October (Opal's location is indicated by the hurricane symbol);

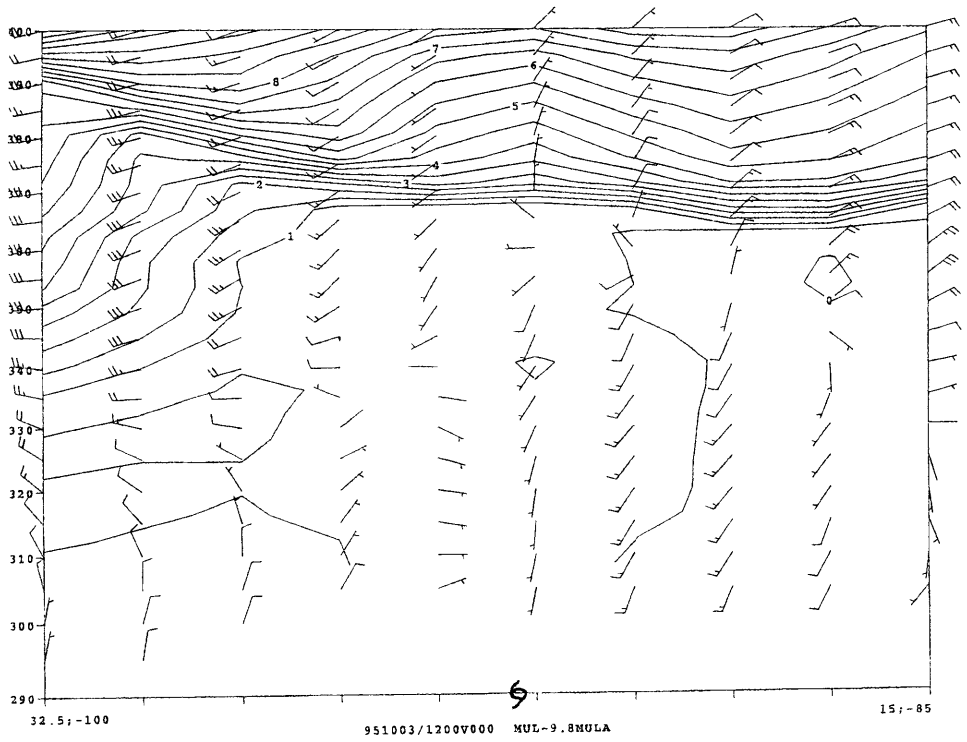

Figure 3.20: (b) 1200UTC 3 October;

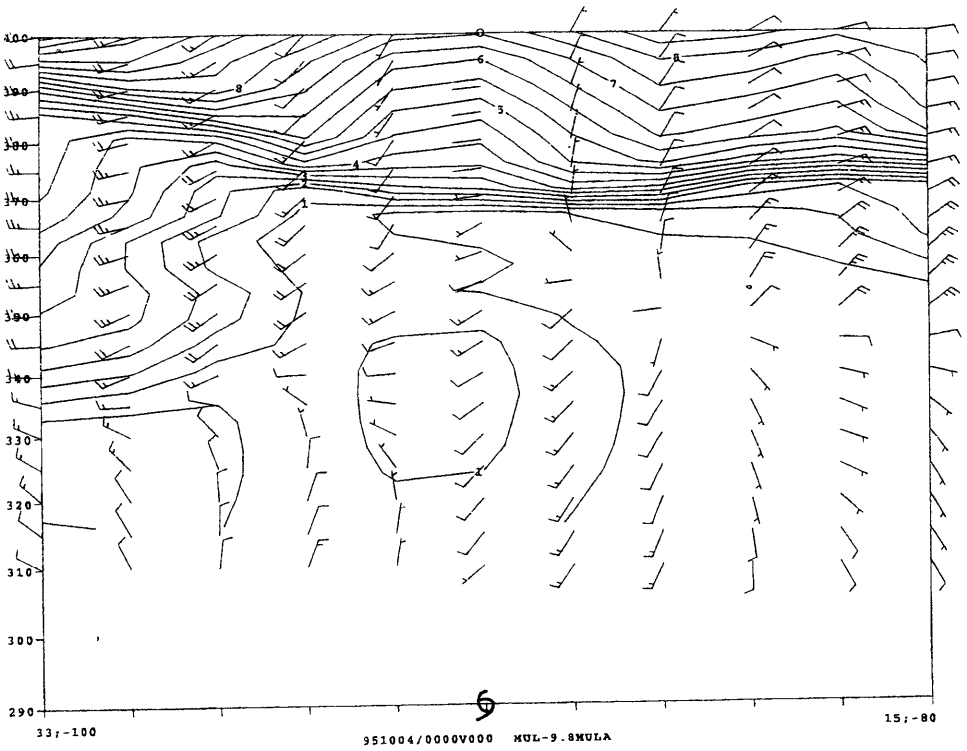

Figure 3.20: (c) 0000UTC 4 October;

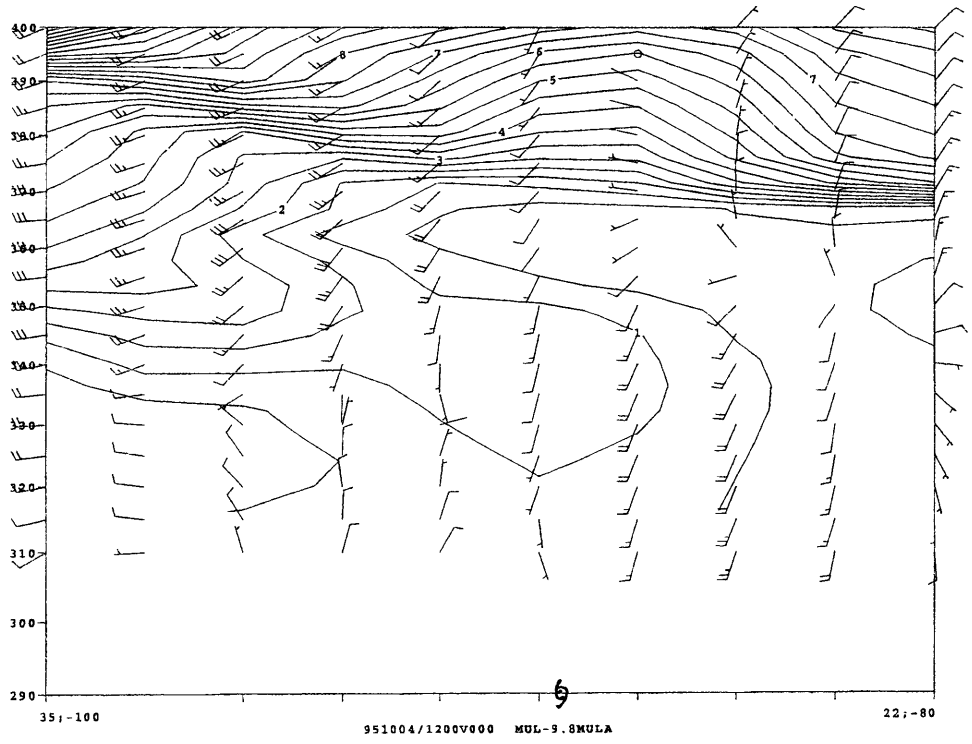

Figure 3.20: (d) 1200UTC 4 October.

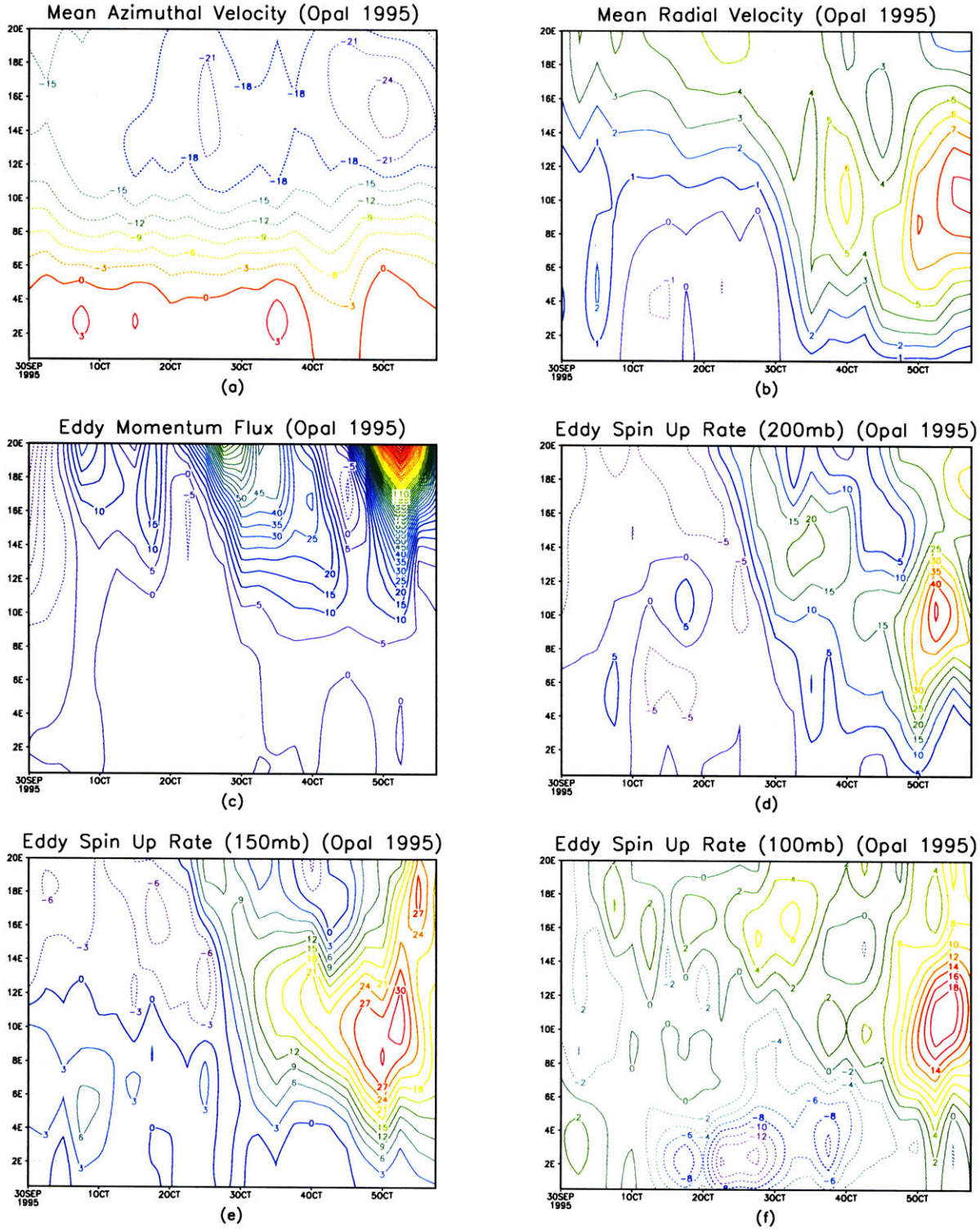

Figure 3.21: Radius-time series of mean (a) azimuthal velocity (m/s) and (b) radial velocity (m/s) at 200mb, (c) eddy relative angular momentum fluxes ($10^{17} kgm^2 s^{-2}$), and eddy spin up rates (m/s/day) at (d) 200mb, (e) 150mb and (f) 100mb for Opal of 1995. The calculation is based on the NNRA dataset.

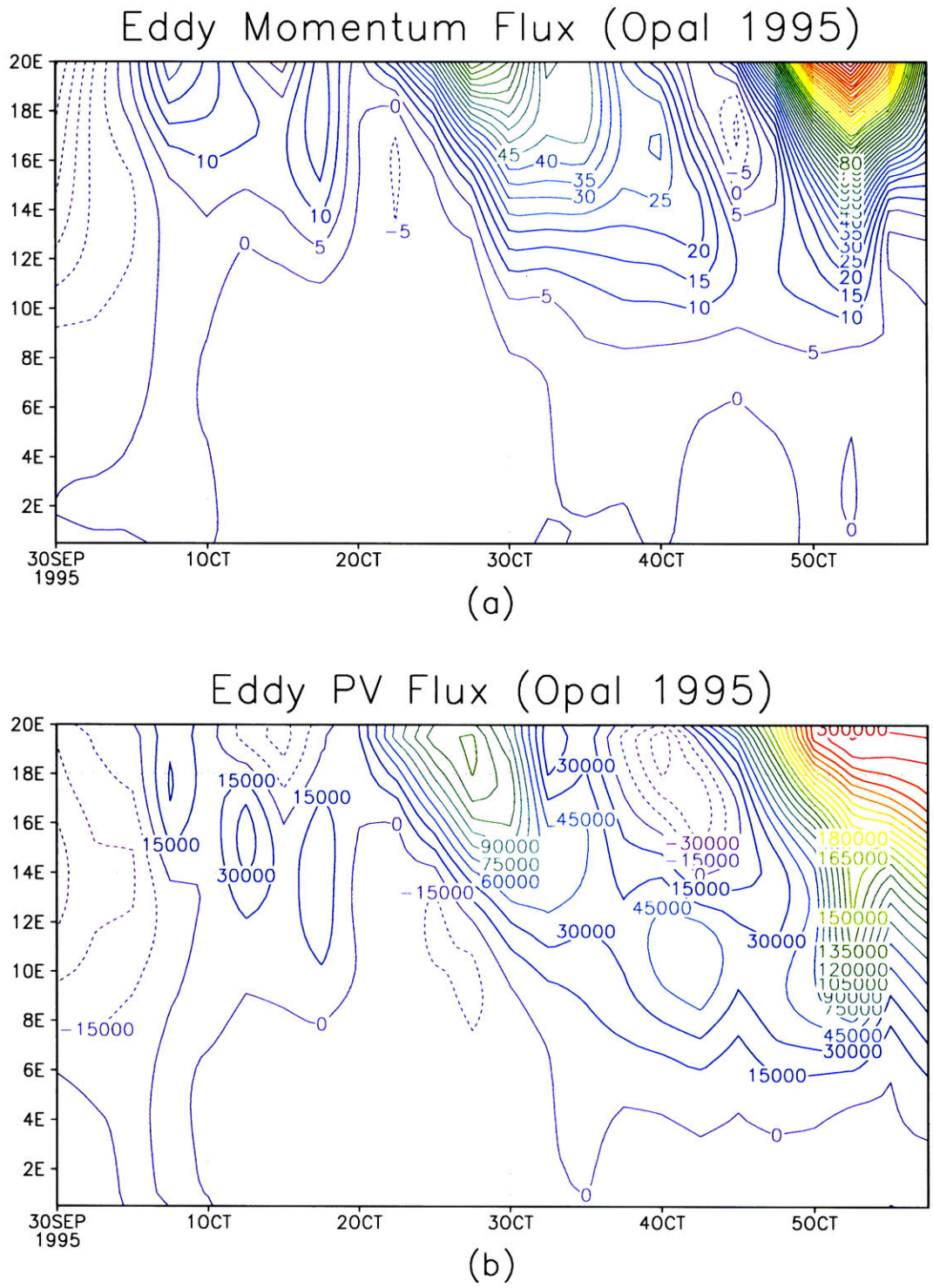

Figure 3.22: Radius-time series of (a) eddy relative angular momentum fluxes ($10^{17} kgm^2 s^{-2}$), and (b) eddy PV fluxes (mK) for Opal of 1995. The calculation is based on the NNRA dataset.

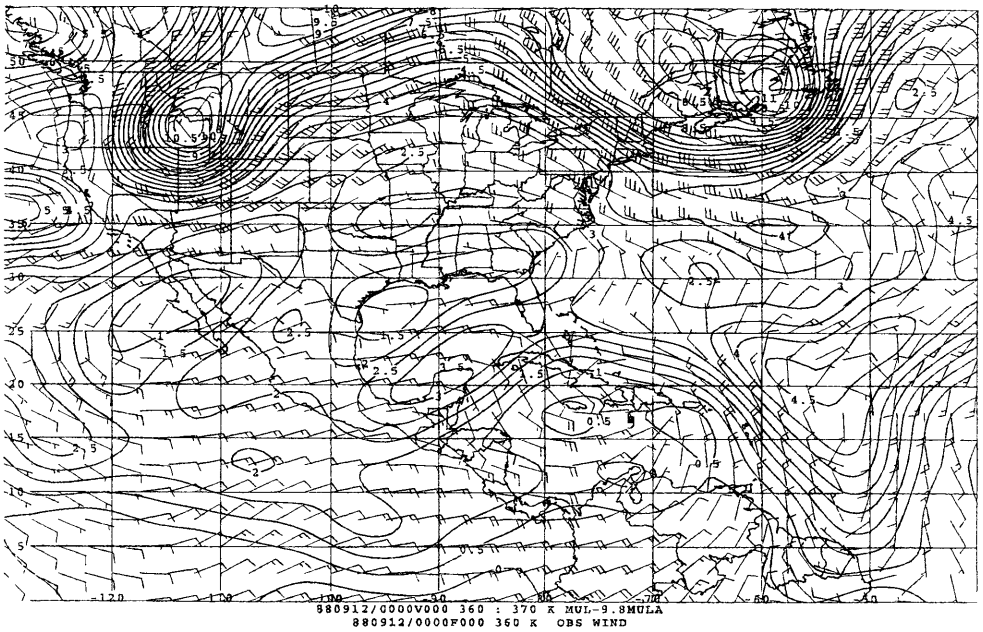

Figure 3.23: Wind barbs (m/s) and Ertel's potential vorticity (PVU) on the $\theta = 360K$ surface for Gilbert at (a) 0000UTC 12 September (Gilbert's location is indicated by the hurricane symbol);

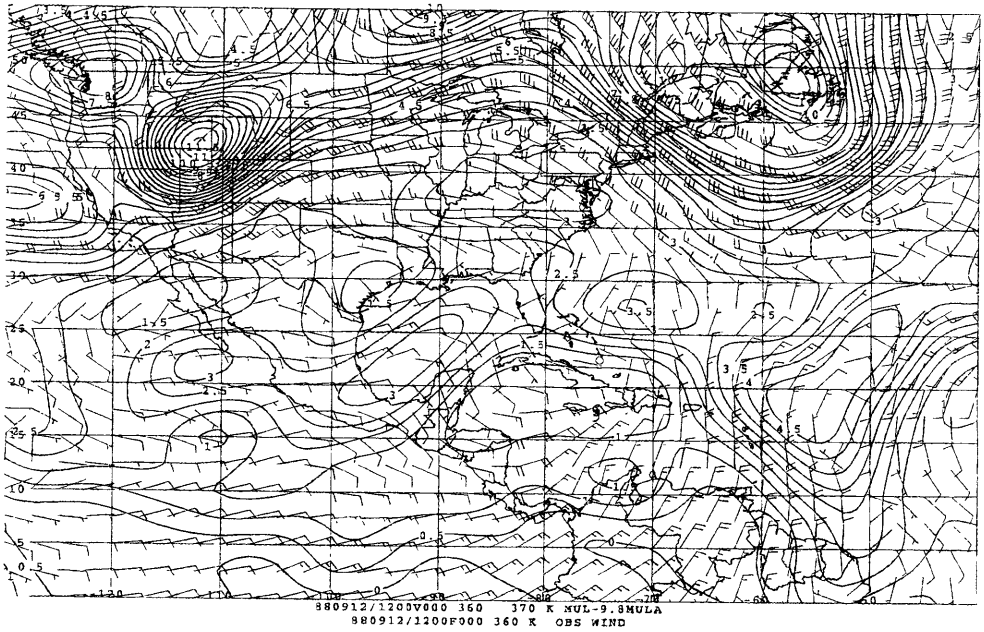

Figure 3.23: (b) 1200UTC 12 September;

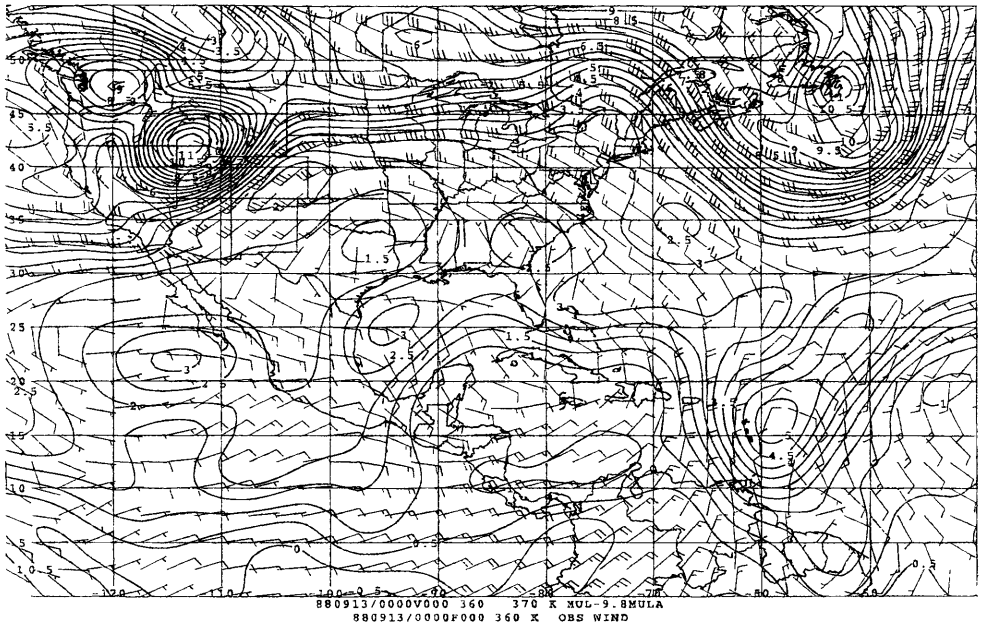

Figure 3.23: (c) 0000UTC 13 September;

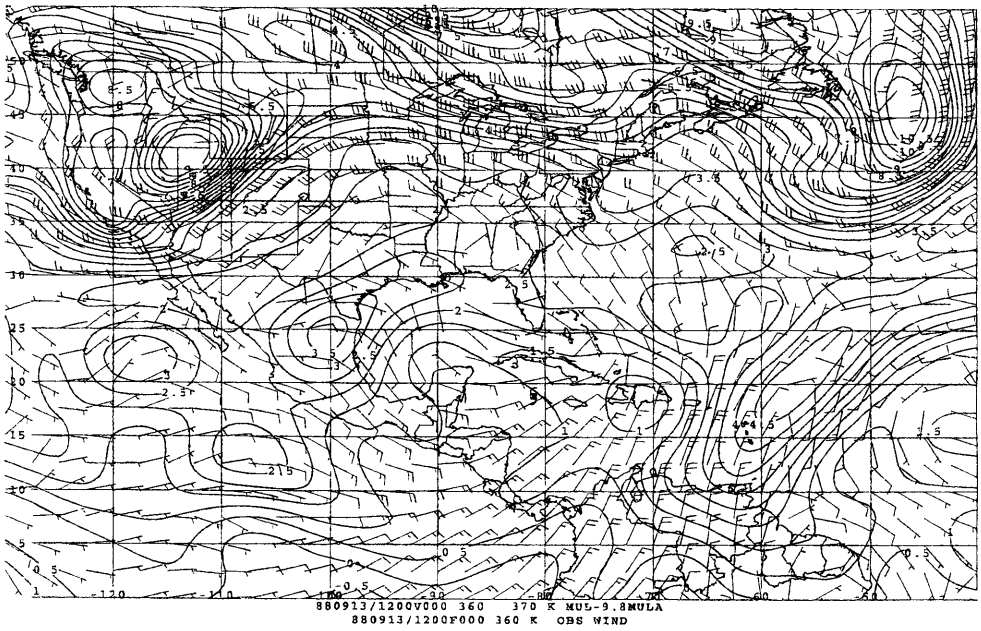

Figure 3.23: (d) 1200UTC 13 September;

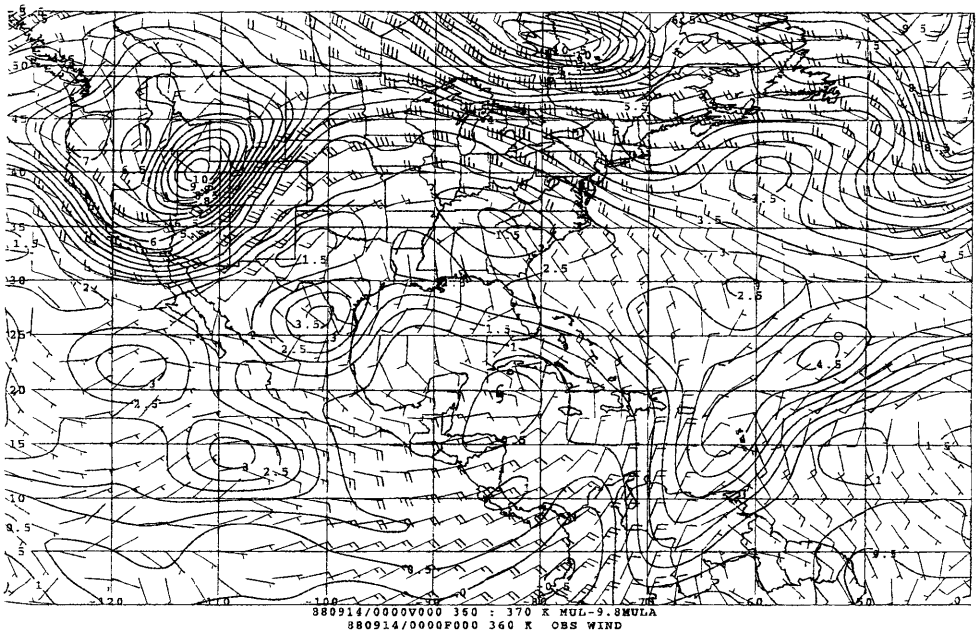

Figure 3.23: (e) 0000UTC 14 September.

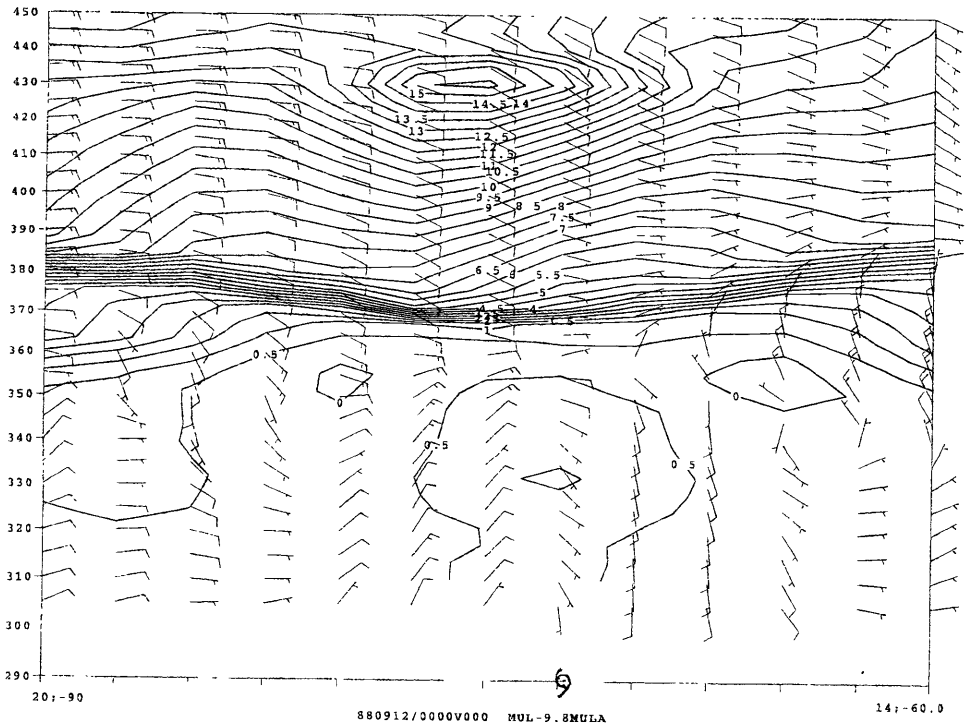

Figure 3.24: Cross sections of IPV (PVU) from northwest (left) to southeast (right) through the observed center of Hurricane Gilbert at (a) 0000UTC 12 September (Gilbert's location is indicated by the hurricane symbol);

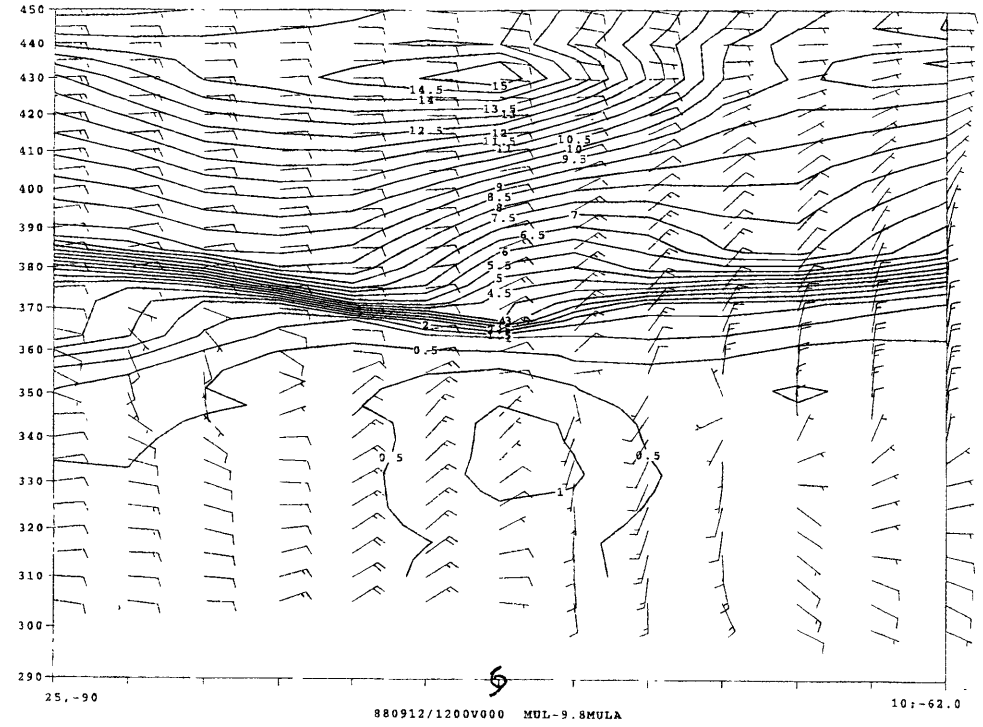

Figure 3.24: (b) 1200UTC 12 September;

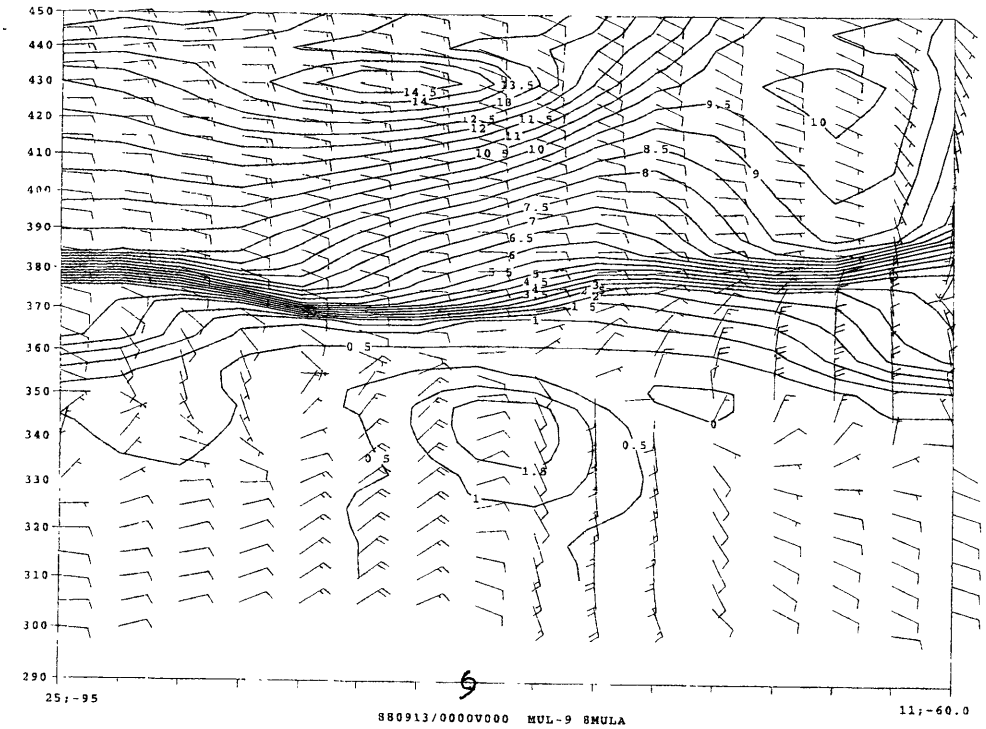

Figure 3.24: (c) 0000UTC 13 September;

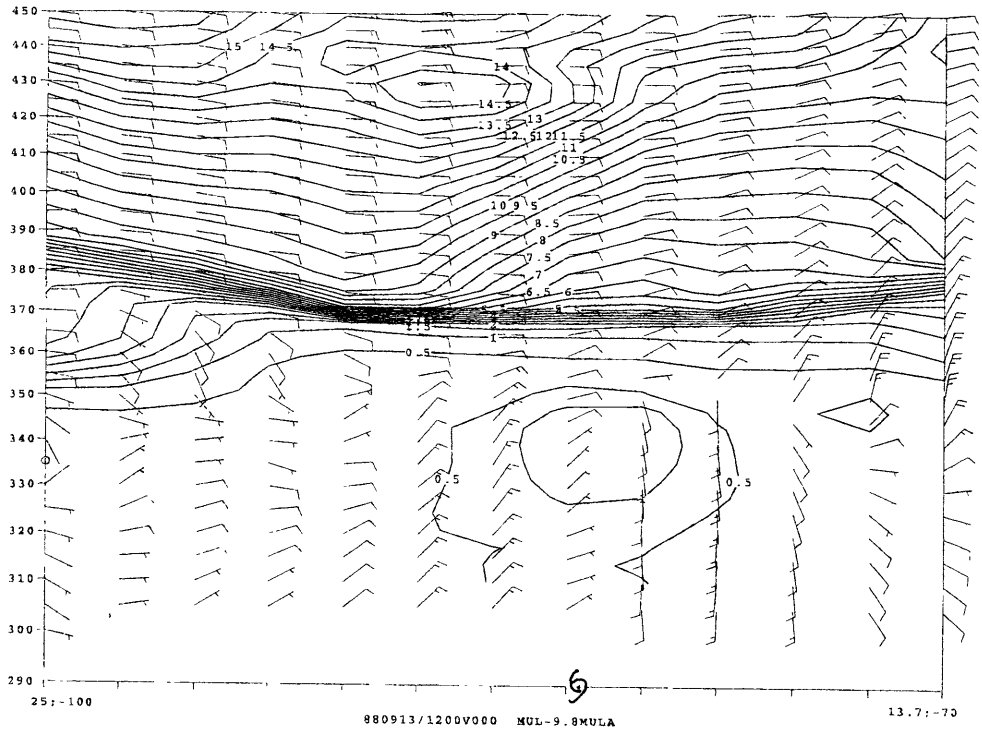

Figure 3.24: (d) 1200UTC 13 September;

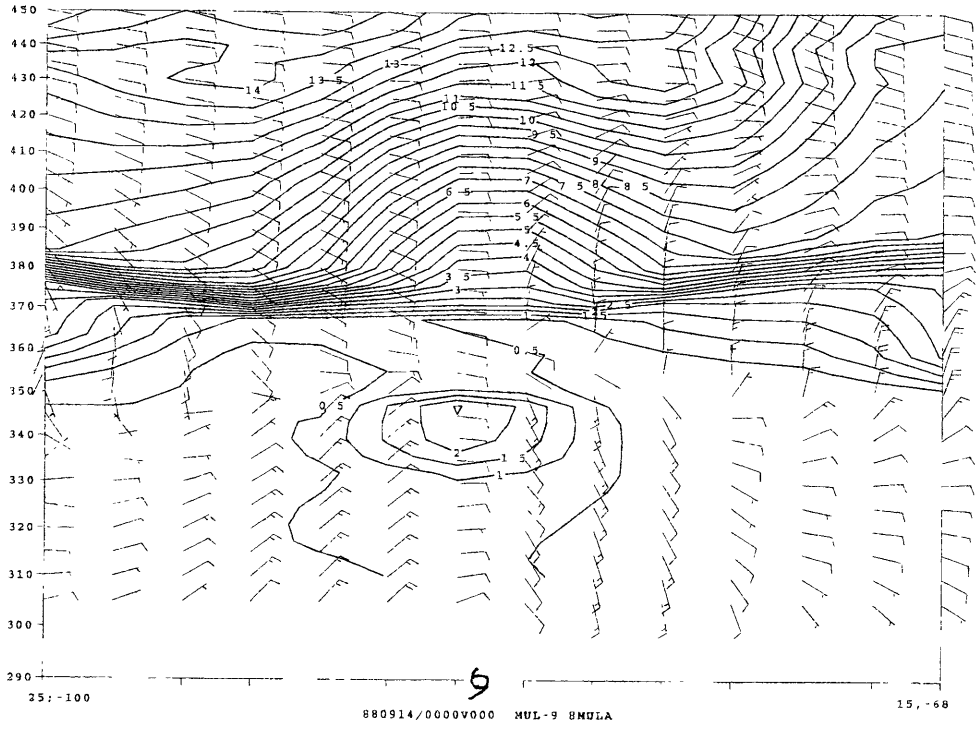

Figure 3.24: (e) 0000UTC 14 September.

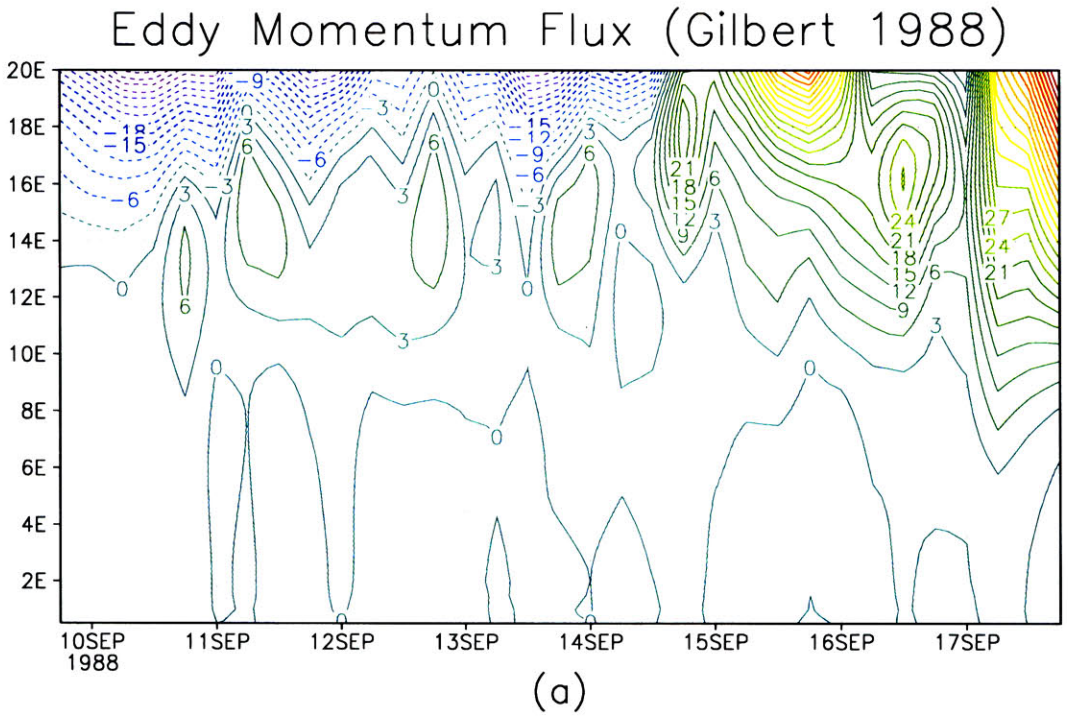

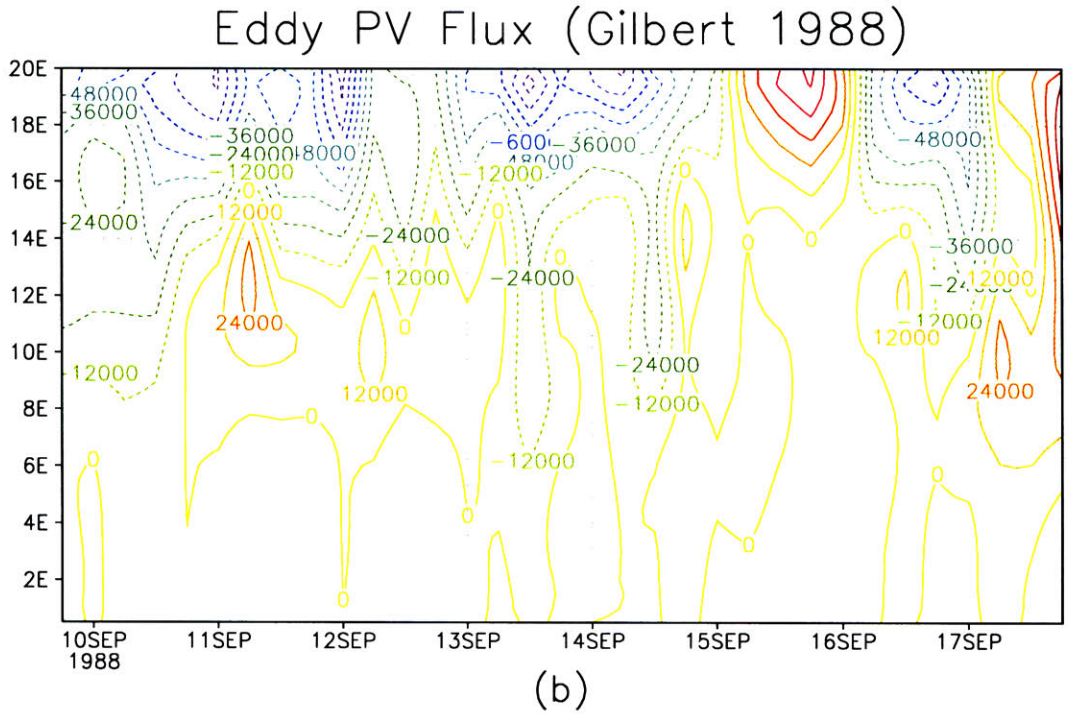

Figure 3.25: Radius-time series of (a) eddy relative angular momentum fluxes ($10^{17} kgm^2 s^{-2}$), and (b) eddy PV fluxes (mK) for Gilbert of 1988. The calculation is based on the NNRA dataset.

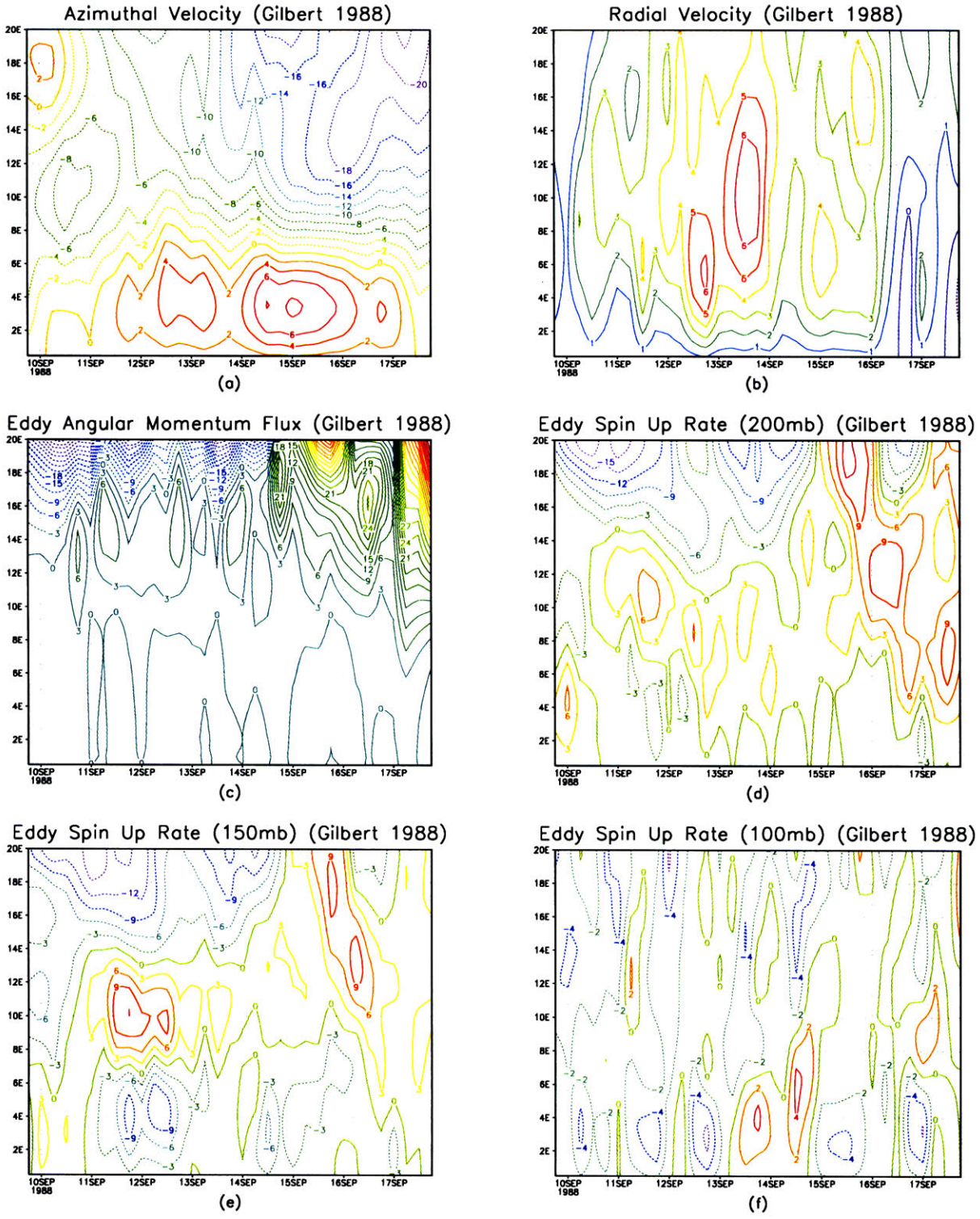

Figure 3.26: Radius-time series of mean (a) azimuthal velocity (m/s) and (b) radial velocity (m/s) at 200mb, (c) eddy relative angular momentum fluxes ($10^{17} kgm^2 s^{-2}$), and eddy spinup rates (m/s/day) at (d) 200mb, (e) 150mb and (f) 100mb for Gilbert of 1988. The calculation is based on the NNRA dataset.

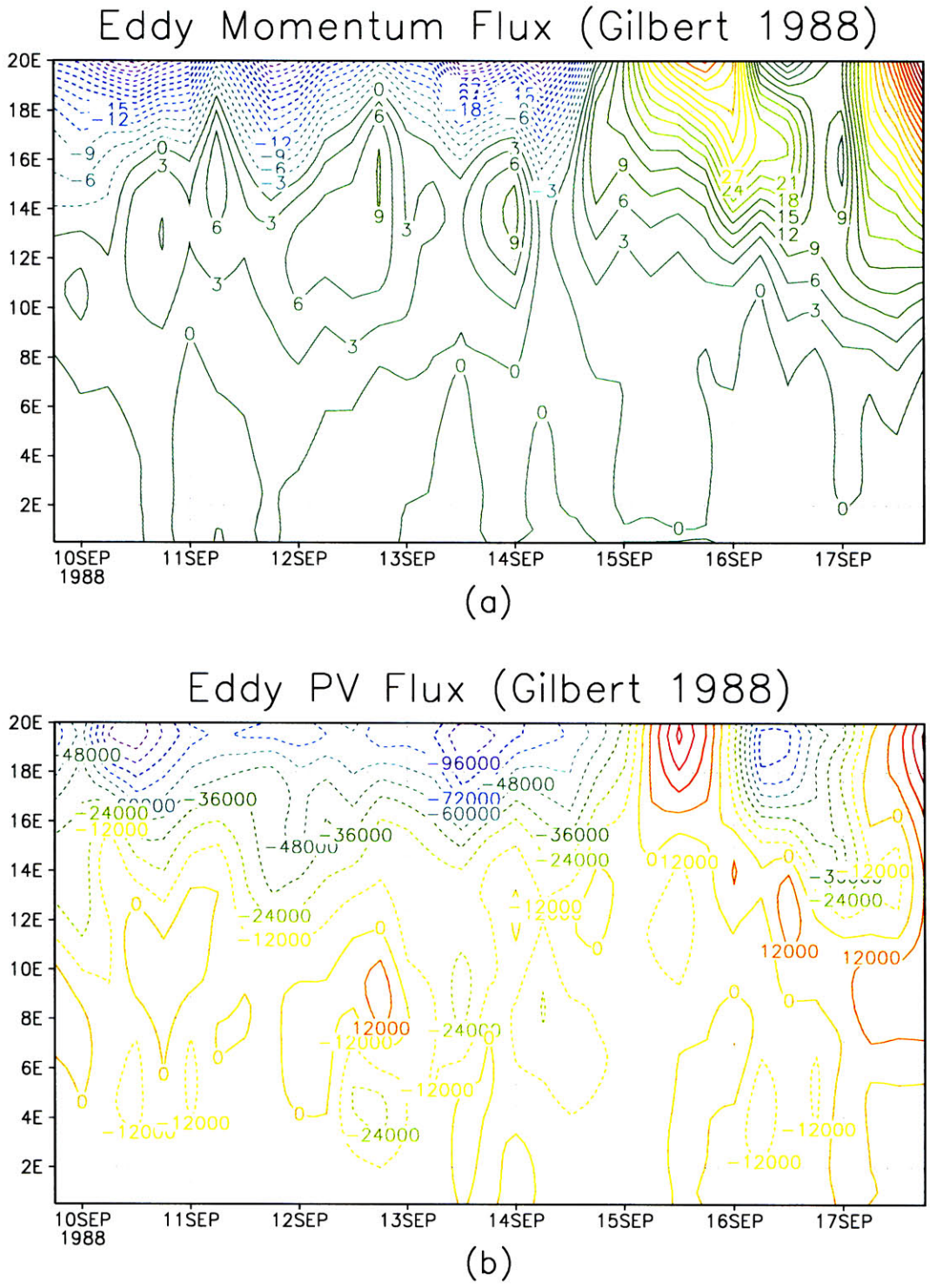

Figure 3.27: As in Fig. 3-25 but the calculation is based on the ERA dataset.

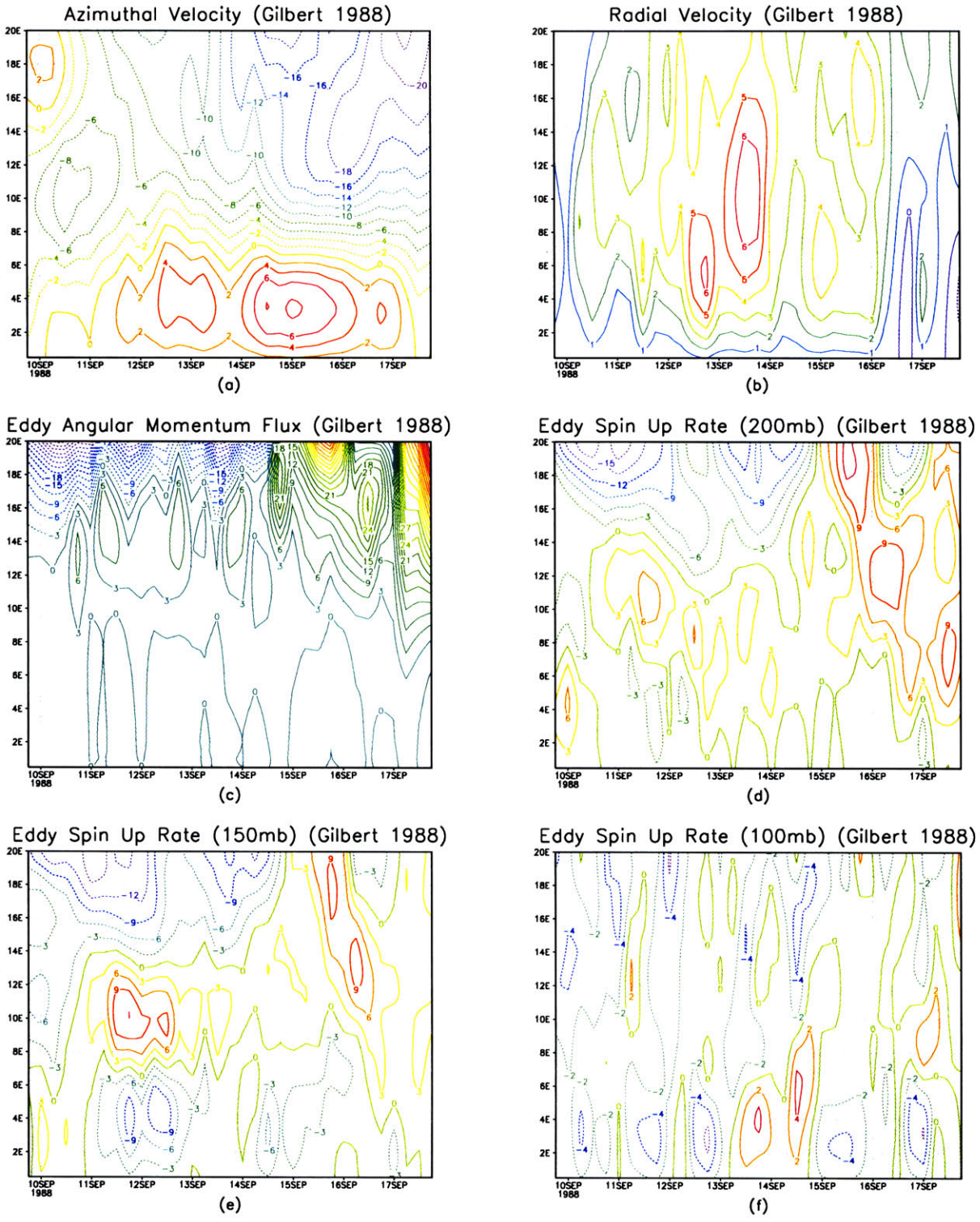

Figure 3.28: As in Fig. 3-26 but the calculation is based on the ERA dataset.

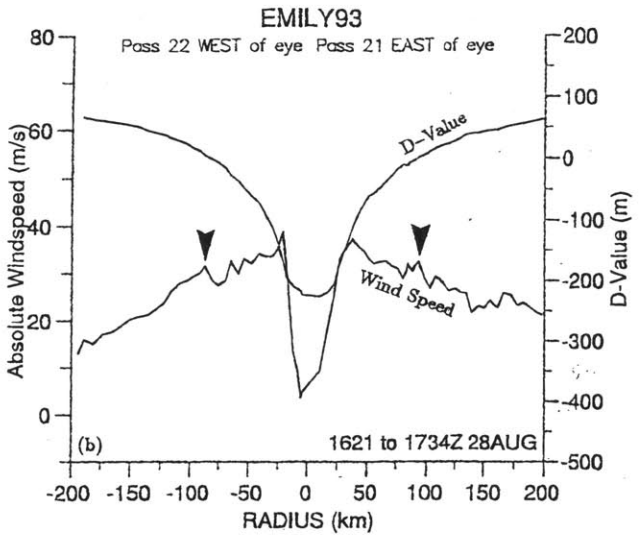

Figure 3.29: (a) Flight-level wind speed and D values reported in real time for Hurricane Emily when an outer eyewall, indicated by arrow, first became well defined (from Burpee et al. (1994)).

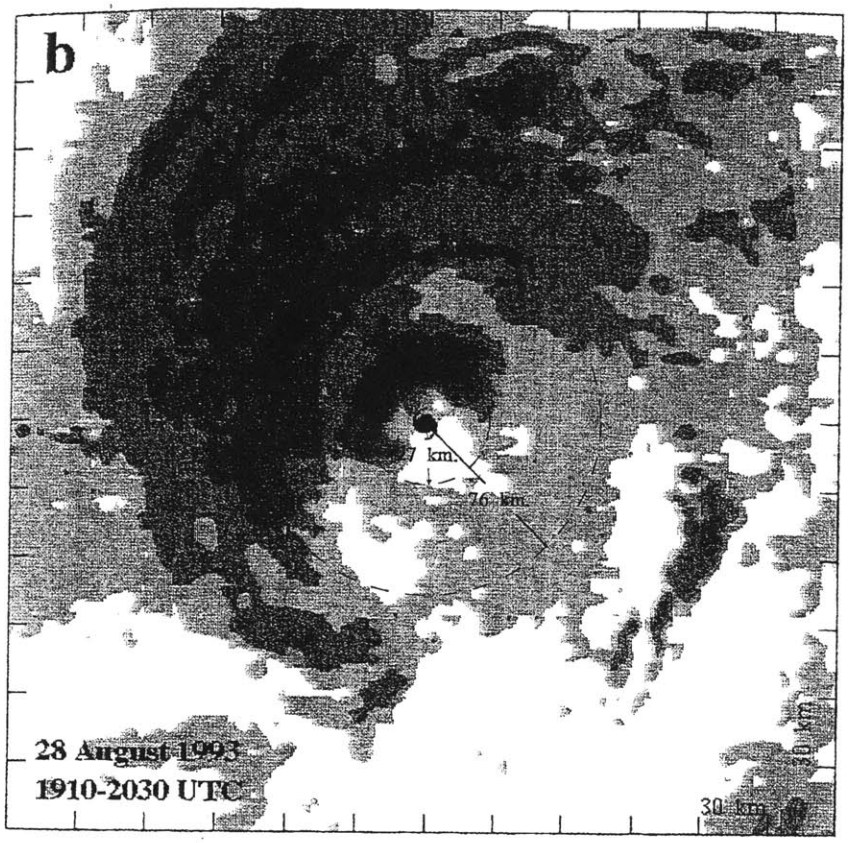

Figure 3.29: (b) Radar composite calculated for 1910-2030UTC 28 August. The white area indicates reflectivities below the minimum detectable signal. The contour levels in the gray area are 15, 21, 28 ,35, 41, and 48 dBZ. The domain size is 360km by 360km and is positioned on the eye center at the time of the last radar sweep in the composite. North is at the top. (from Burpee et al. (1994))

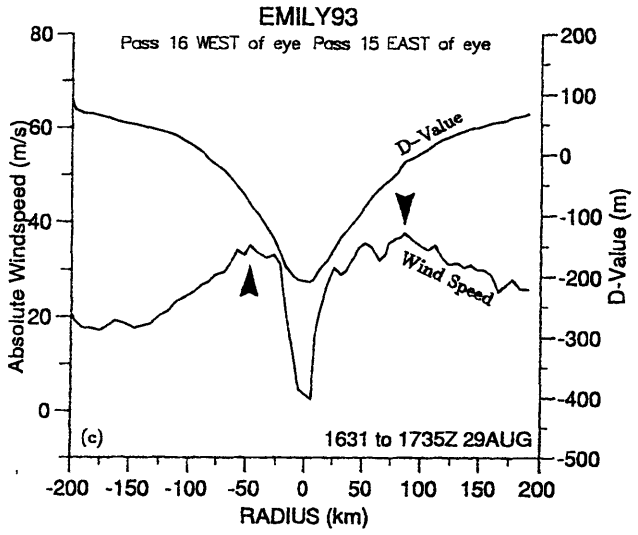

Figure 3.29: (c) As in (a) but the outer eyewall is replacing the inner one. The outer wind maximum is stronger than the inner one. (from Burpee et al. (1994))

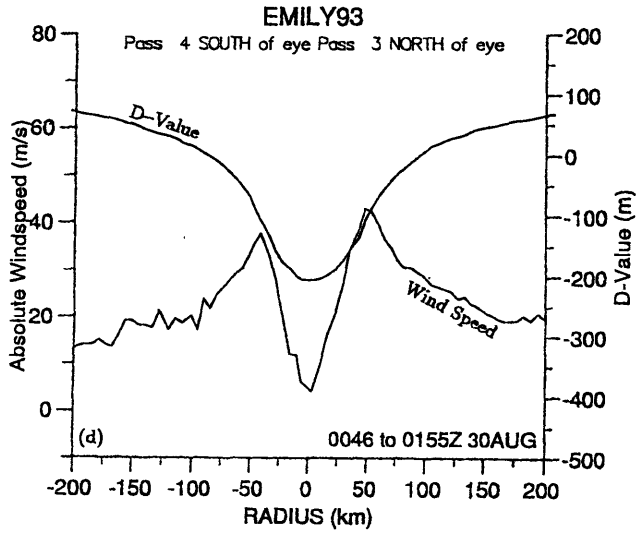

Figure 3.29: (d) As in (a) but only the outer eyewall remained. (from Burpee et al. (1994))

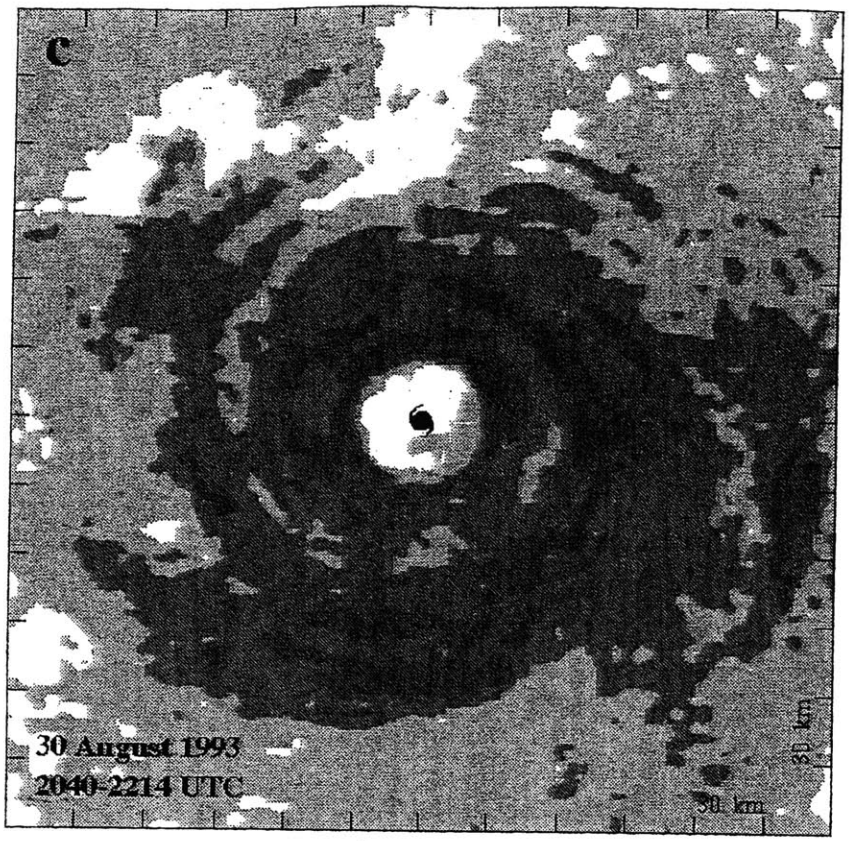

Figure 3.29: (d) As in (b) but for 2040-2214UTC 30 August. (from Burpee et al. (1994))

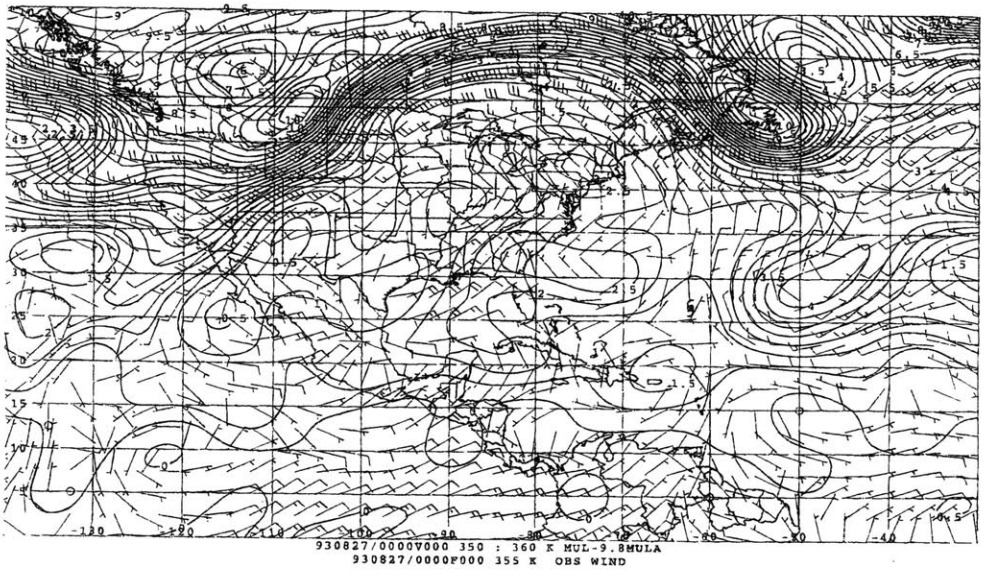

Figure 3.30: Wind barbs (m/s) and Ertel's potential vorticity (PVU) on the $\theta = 355K$ surface for Emily at (a) 0000UTC 27 August (Emily's location is indicated by the hurricane symbol);

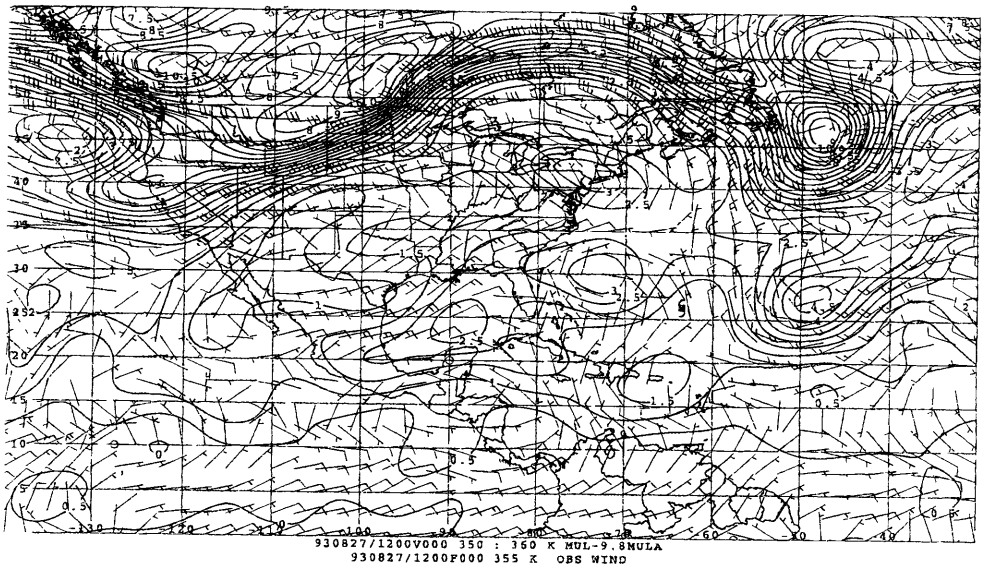

Figure 3.30: (b) 1200UTC 27 August;

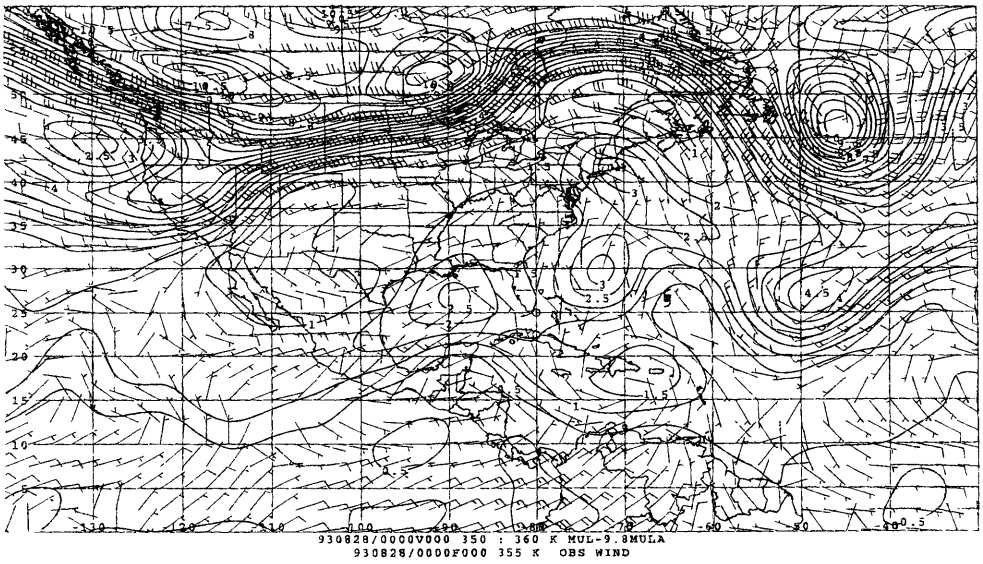

Figure 3.30: (c) 0000UTC 28 August;

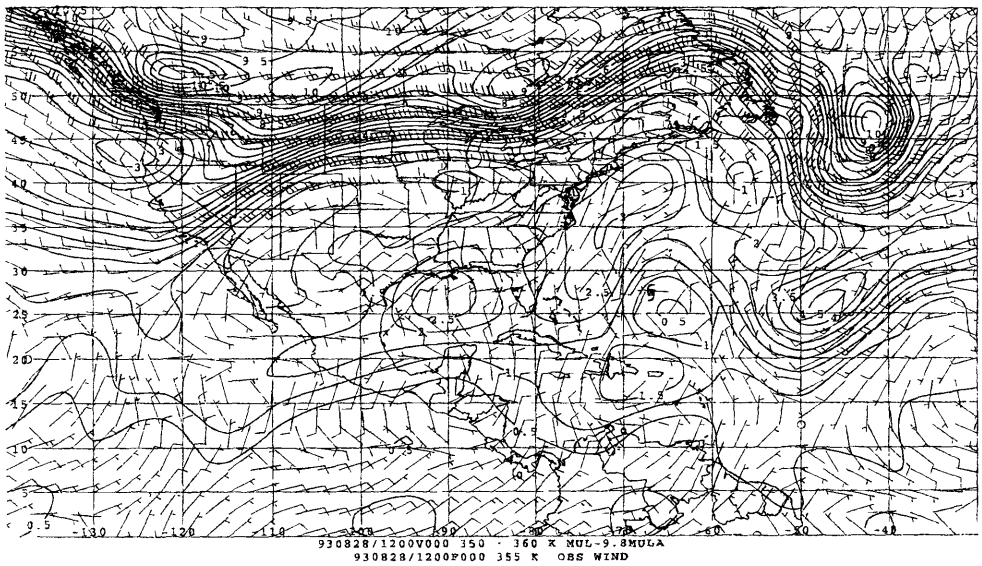

Figure 3.30: (d) 1200UTC 28 August;

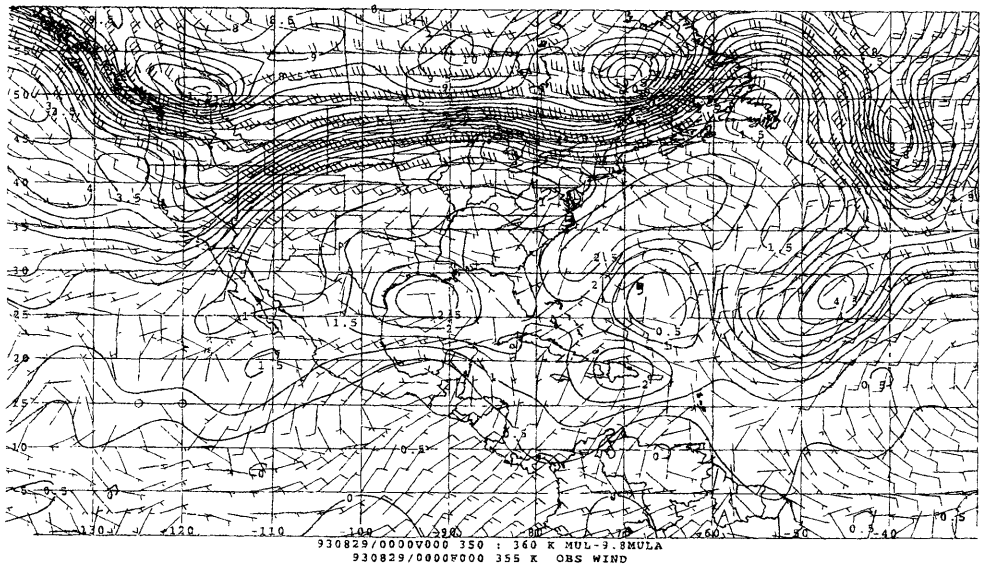

Figure 3.30: (e) 0000UTC 29 August.

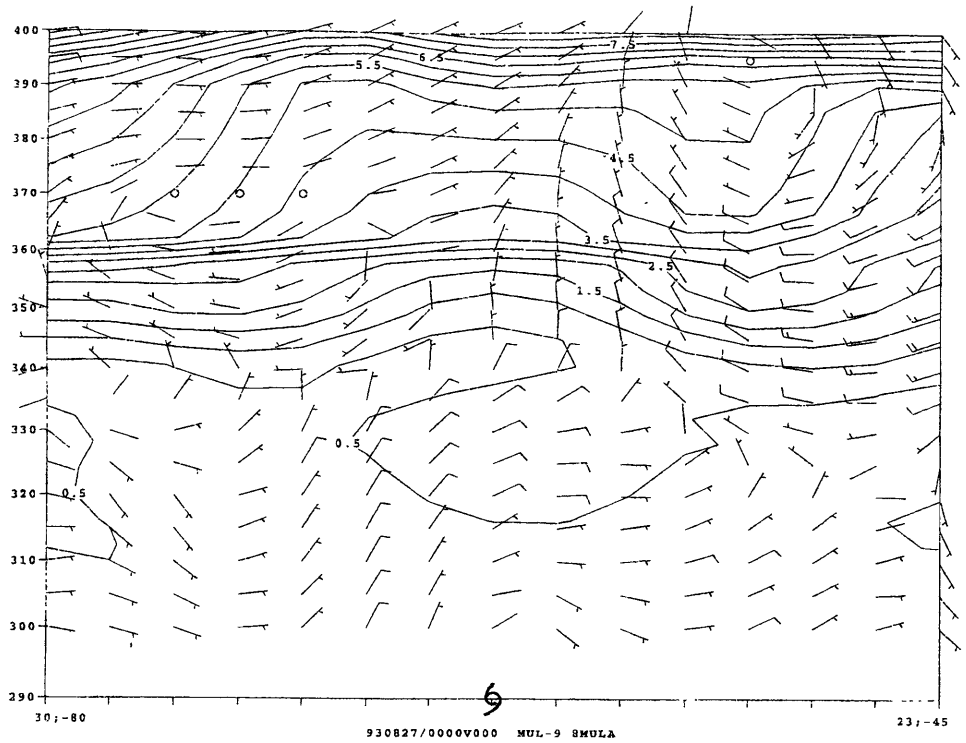

Figure 3.31: Cross sections of IPV (PVU) from west-northwest (left) to east-southeast (right) through the observed center of Hurricane Emily at (a) 0000UTC 27 August (Emily's location is indicated by the hurricane symbol);

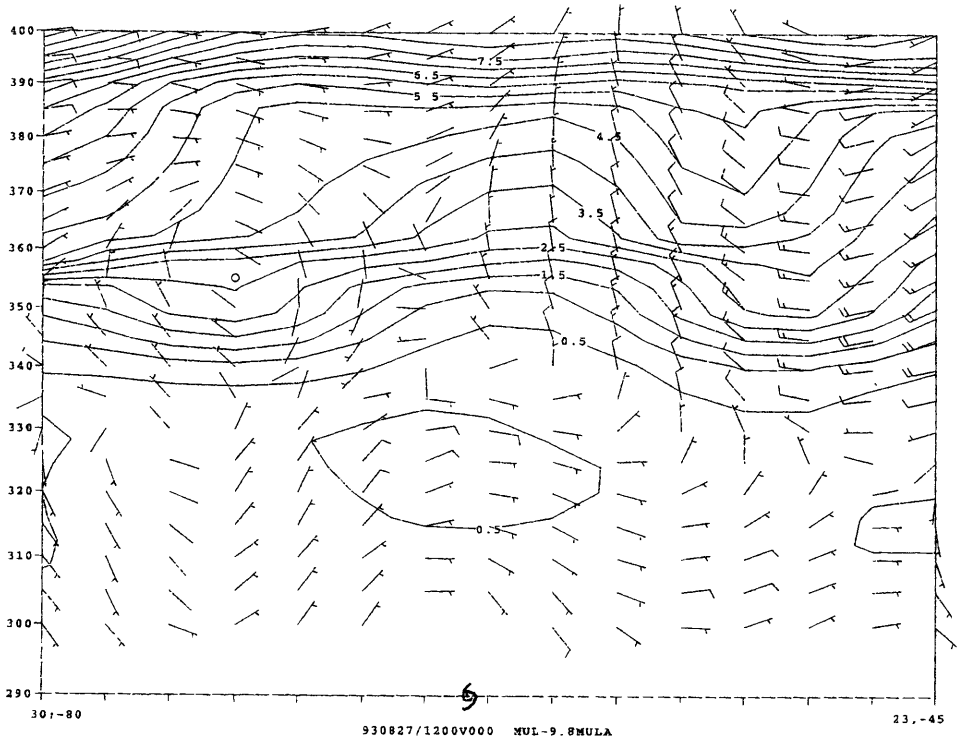

Figure 3.31: (b) 1200UTC 27 August;

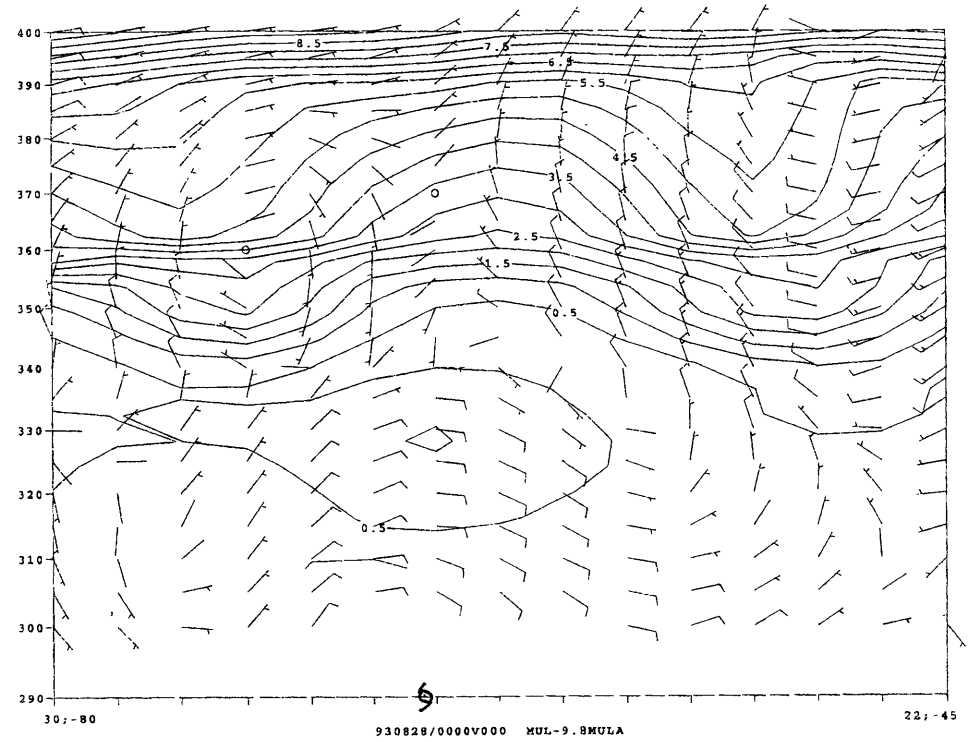

Figure 3.31: (c) 0000UTC 28 August;

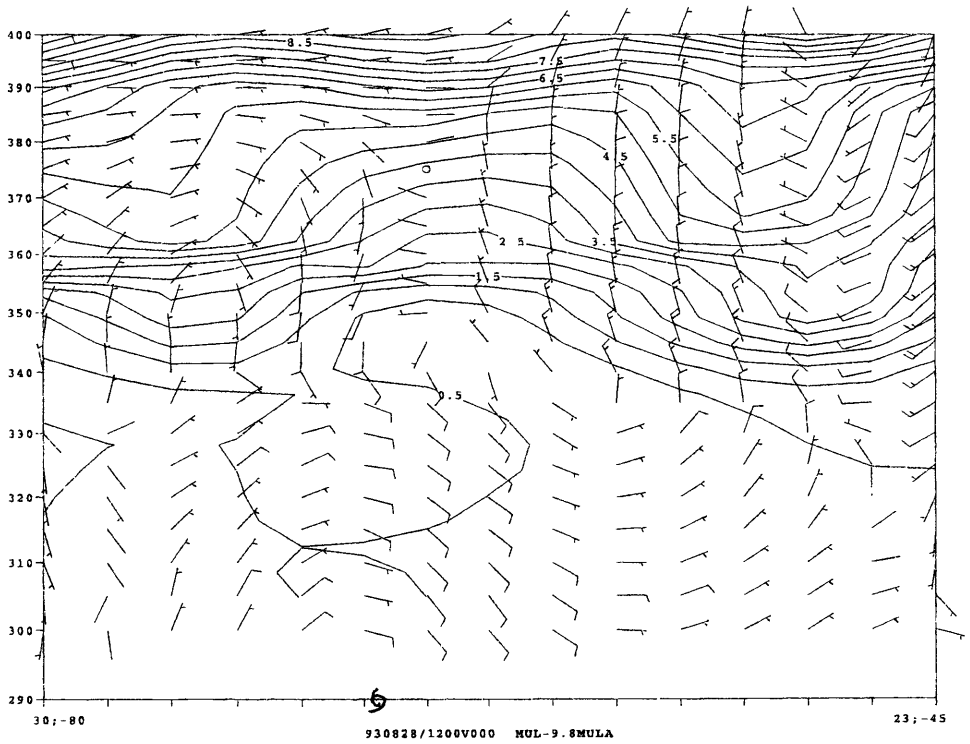

Figure 3.31: (d) 1200UTC 28 August;

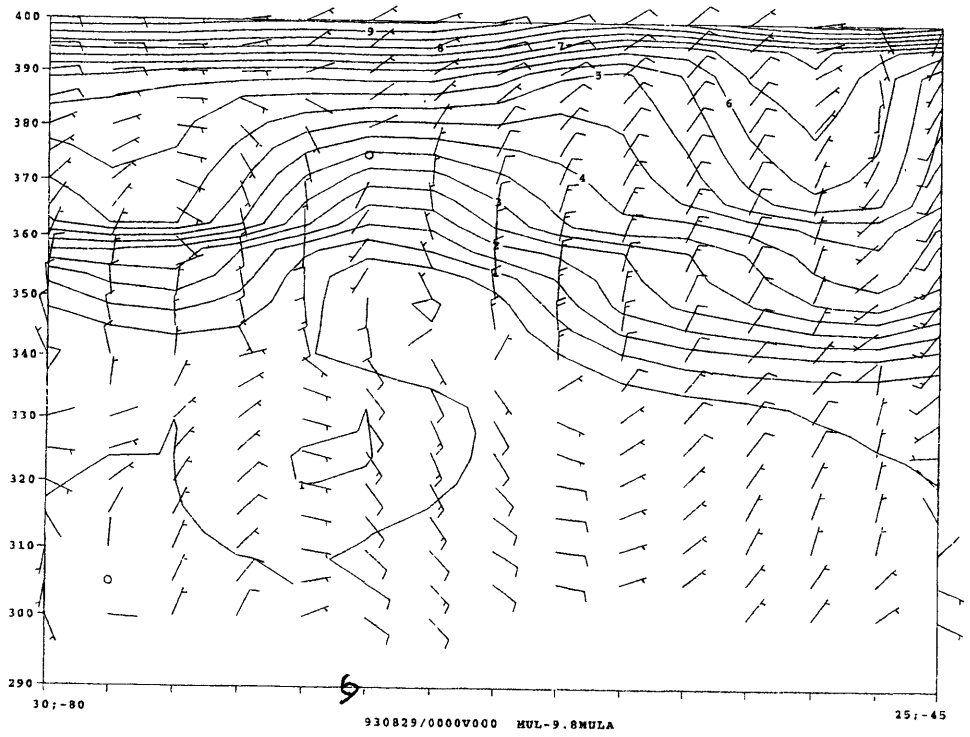

Figure 3.31: (e) 0000UTC 29 August.

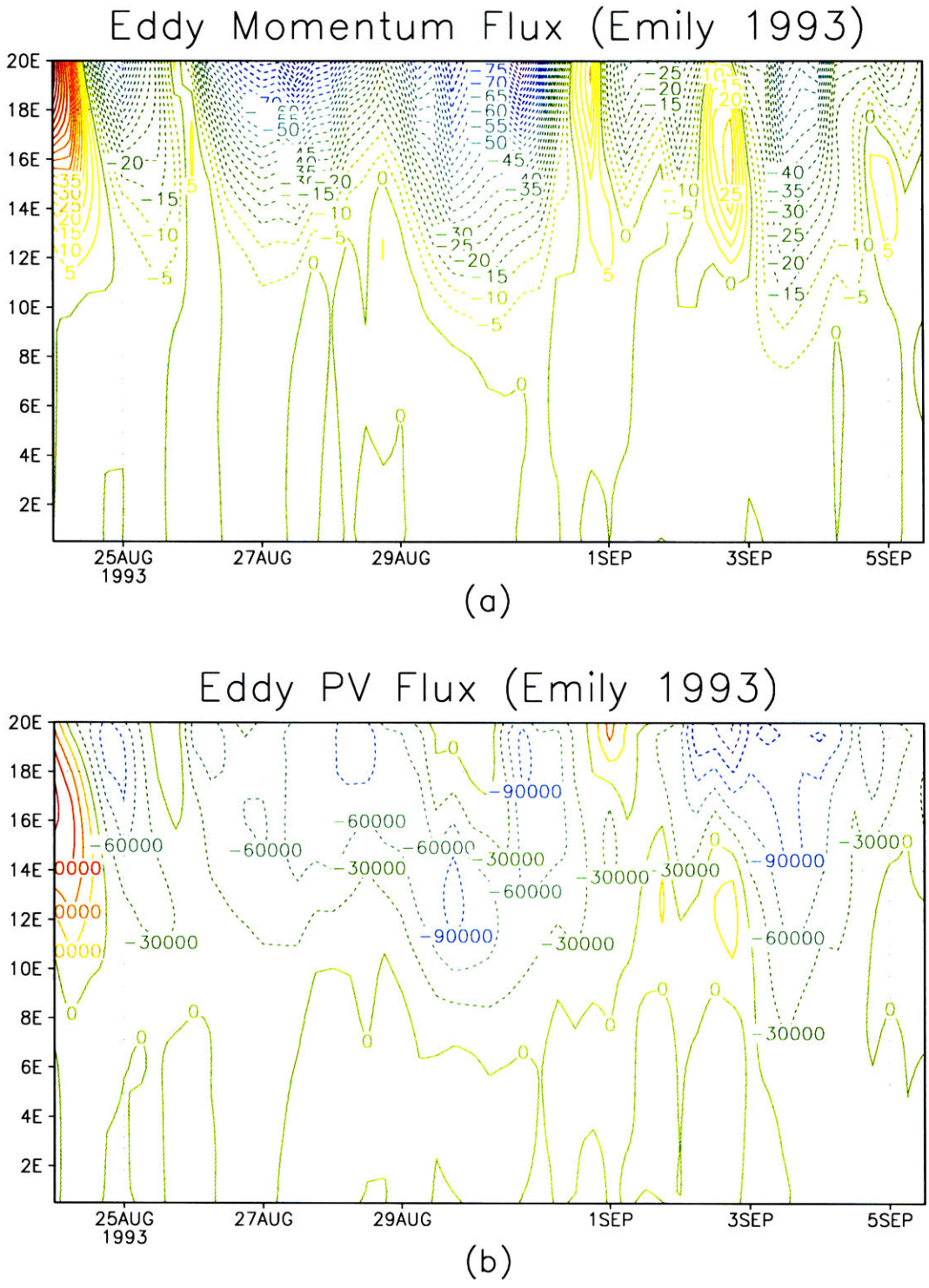

Figure 3.32: Radius-time series of (a) eddy relative angular momentum fluxes ($10^{17} kgm^2 s^{-2}$), and (b) eddy PV fluxes (mK) for Emily of 1993. The calculation is based on the NNRA dataset.

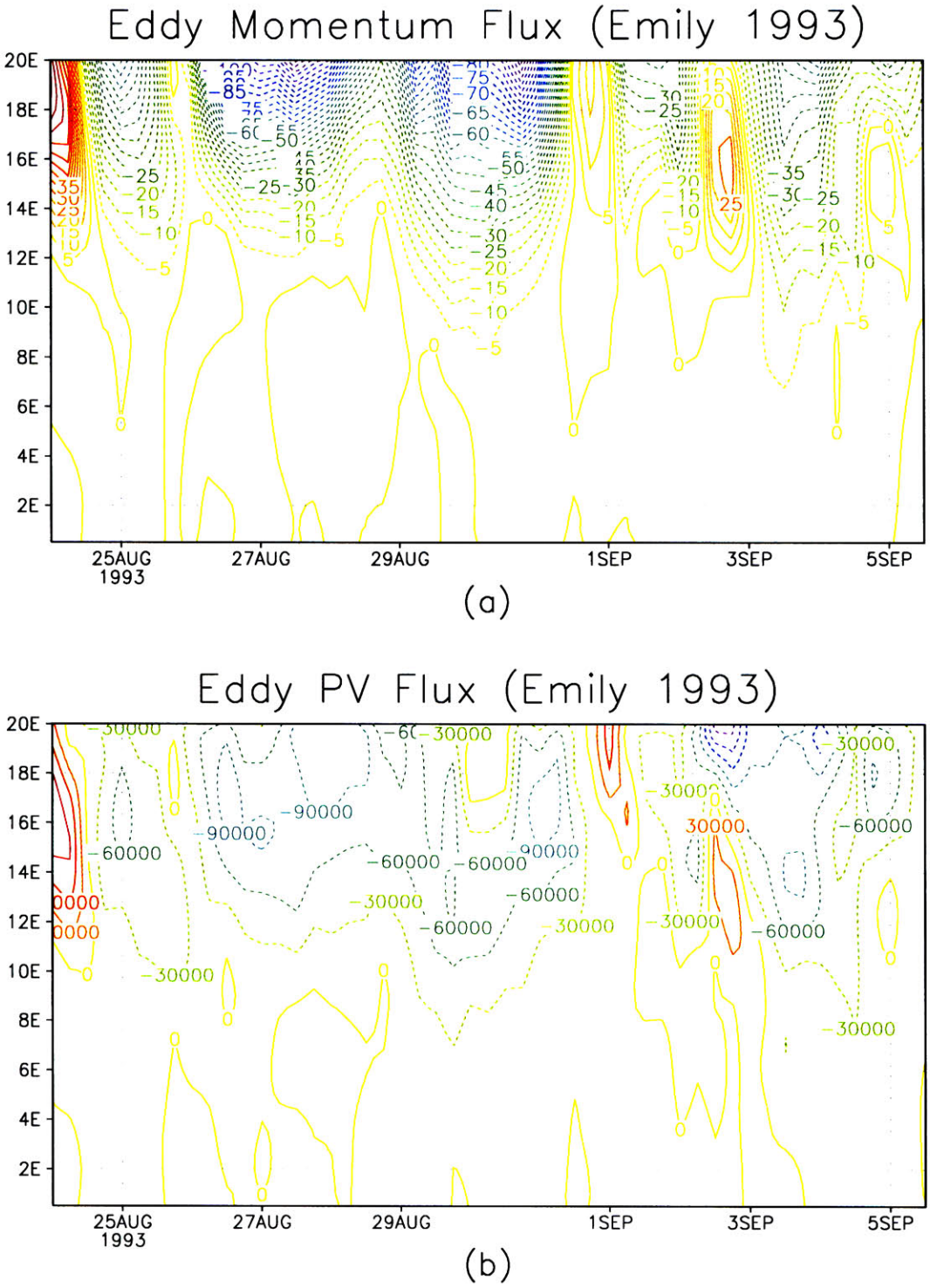

Figure 3.33: As in Fig. 3-32 but the calculation is based on the ERA dataset.

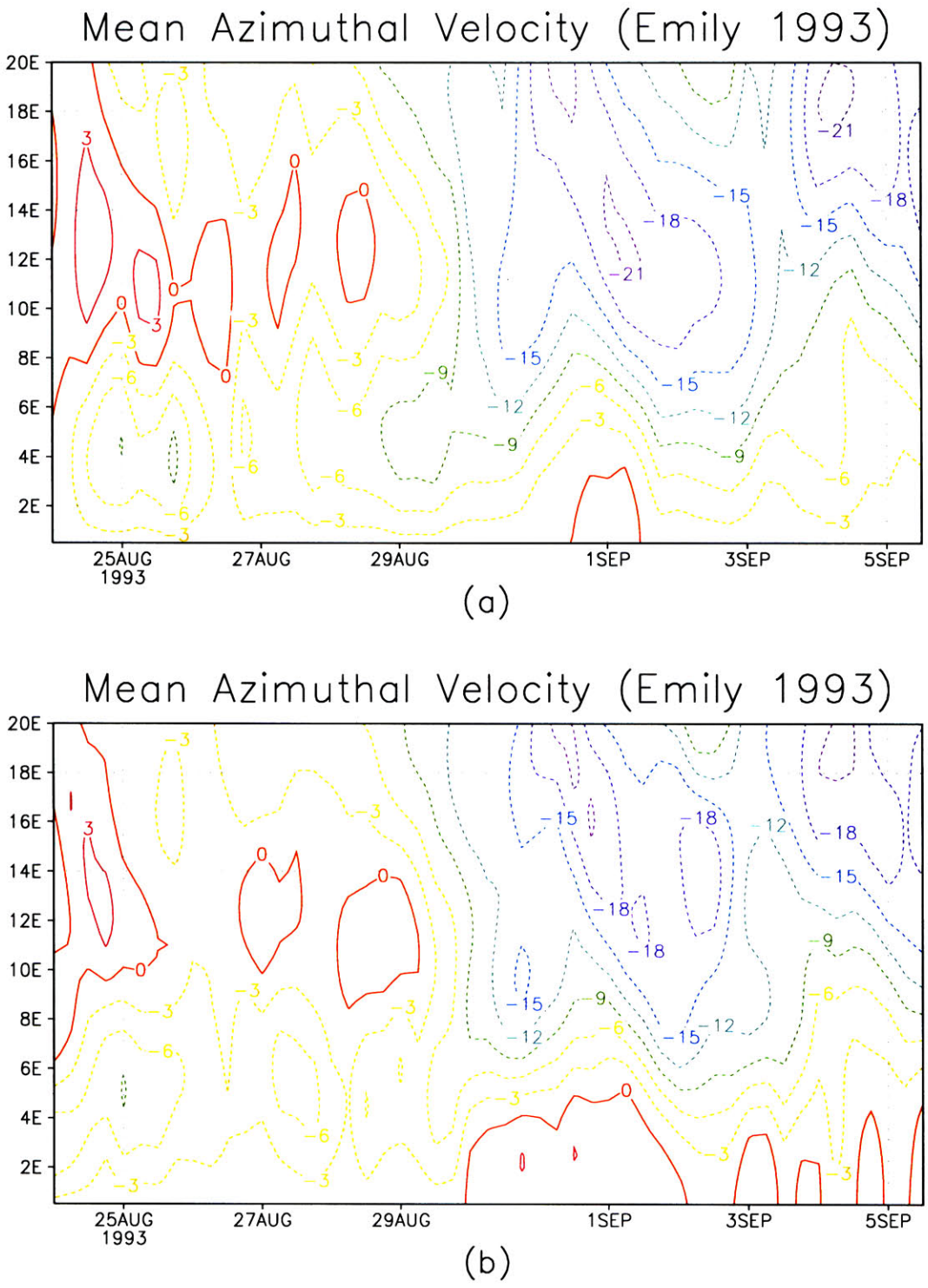

Figure 3.34: Radius-time series of azimuthally averaged tangential velocity (m/s) from (a) NNRA and (b) ERA.

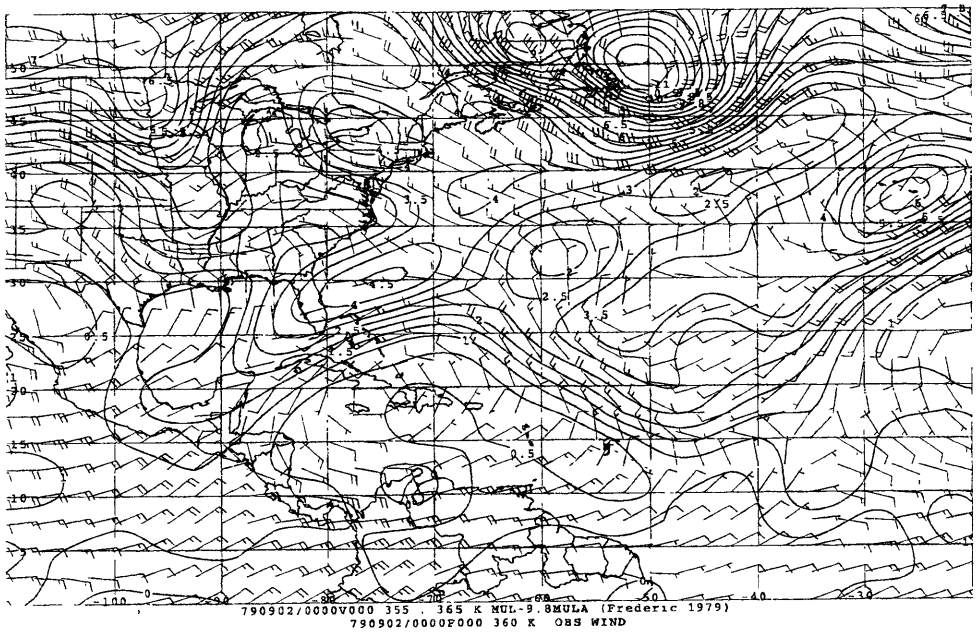

Figure 3.35: Wind barbs (m/s) and Ertel's potential vorticity (PVU) on the $\theta = 355K$ surface for Frederic at (a) 0000UTC 2 September (Frederic's location is indicated by the hurricane symbol);

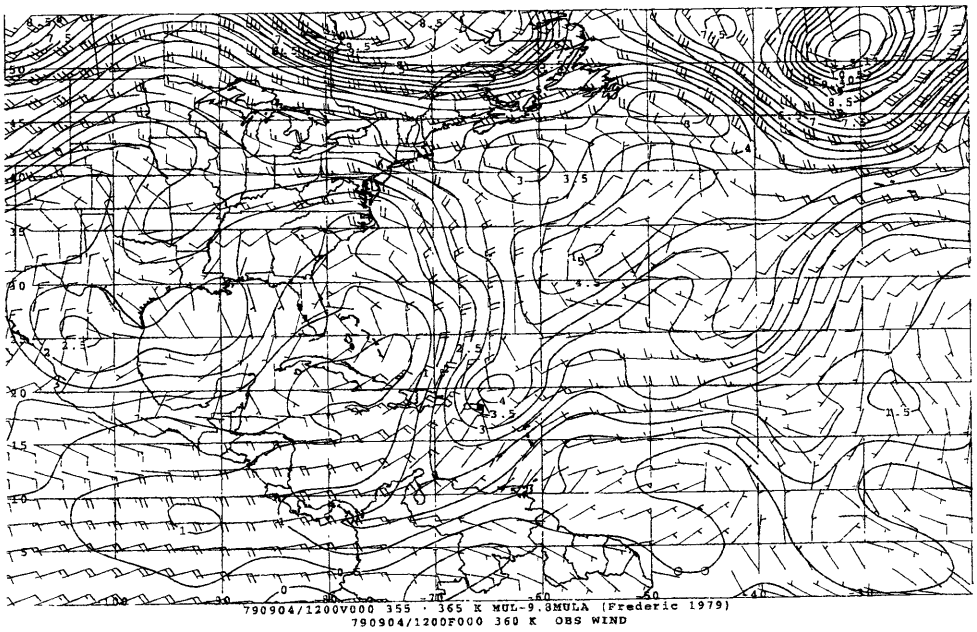

Figure 3.35: (b) 1200UTC 4 September;

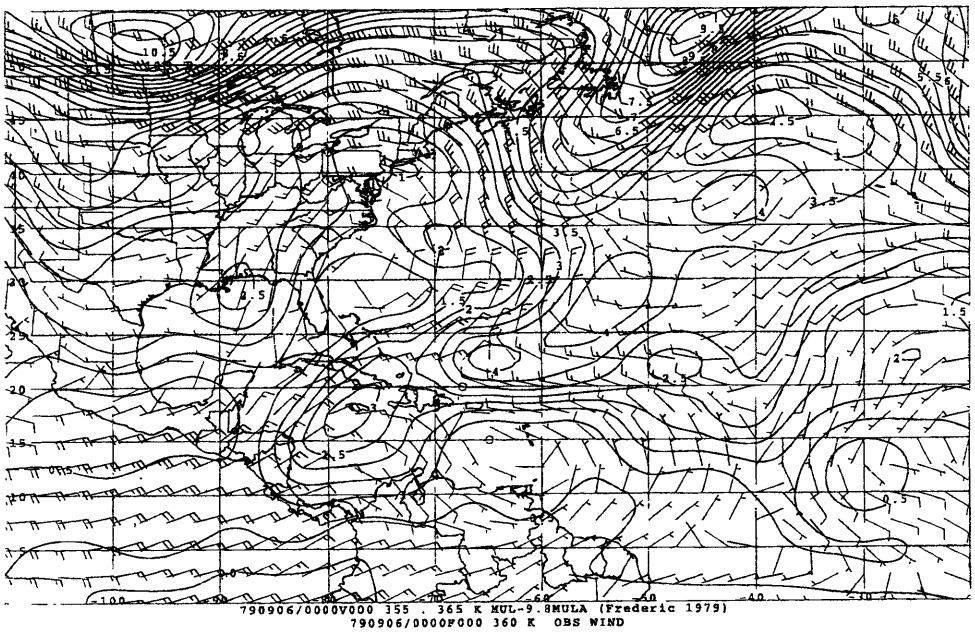

Figure 3.35: (c) 0000UTC 6 September;

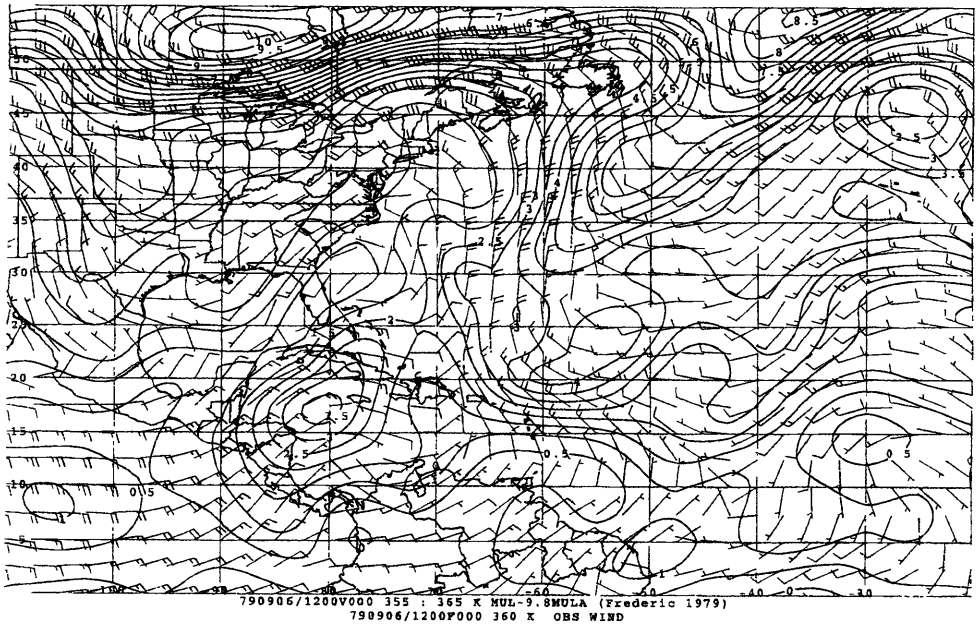

Figure 3.35: (d) 1200UTC 6 September;

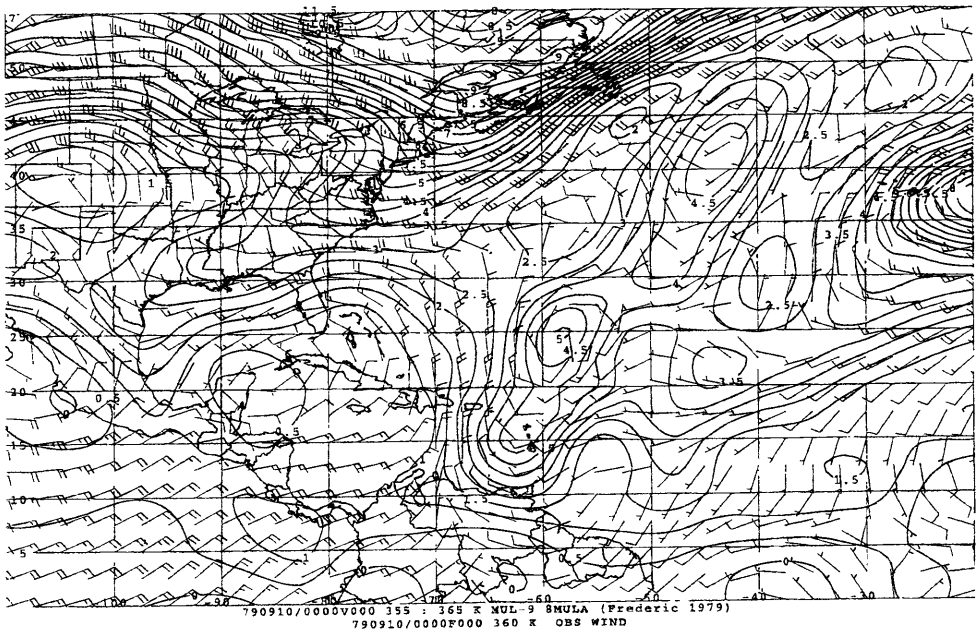

Figure 3.35: (e) 0000UTC 10 September;

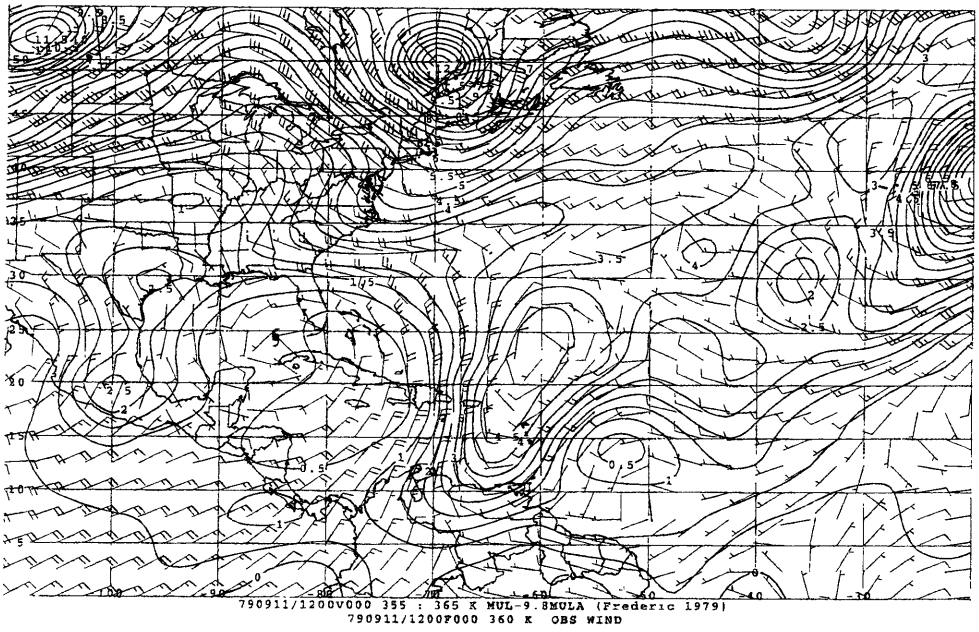

Figure 3.35: (f) 1200UTC 11 September.

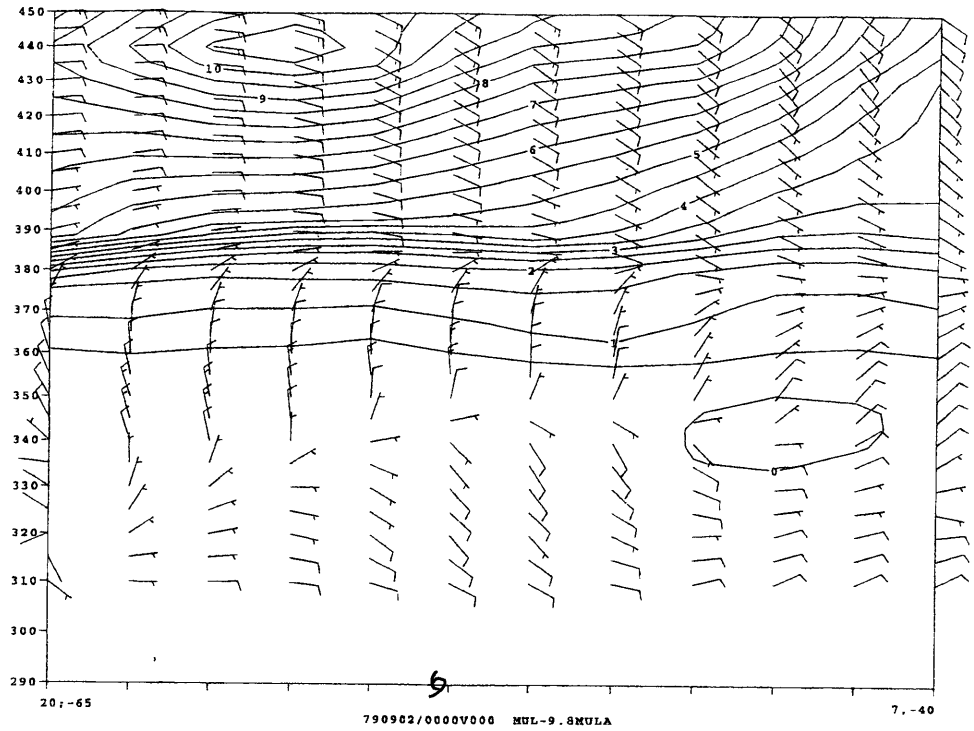

Figure 3.36: Cross sections of IPV (PVU) from west-northwest (left) to east-southeast (right) through the observed center of Hurricane Frederic at (a) 0000UTC 2 September (Frederic's location is indicated by the hurricane symbol);

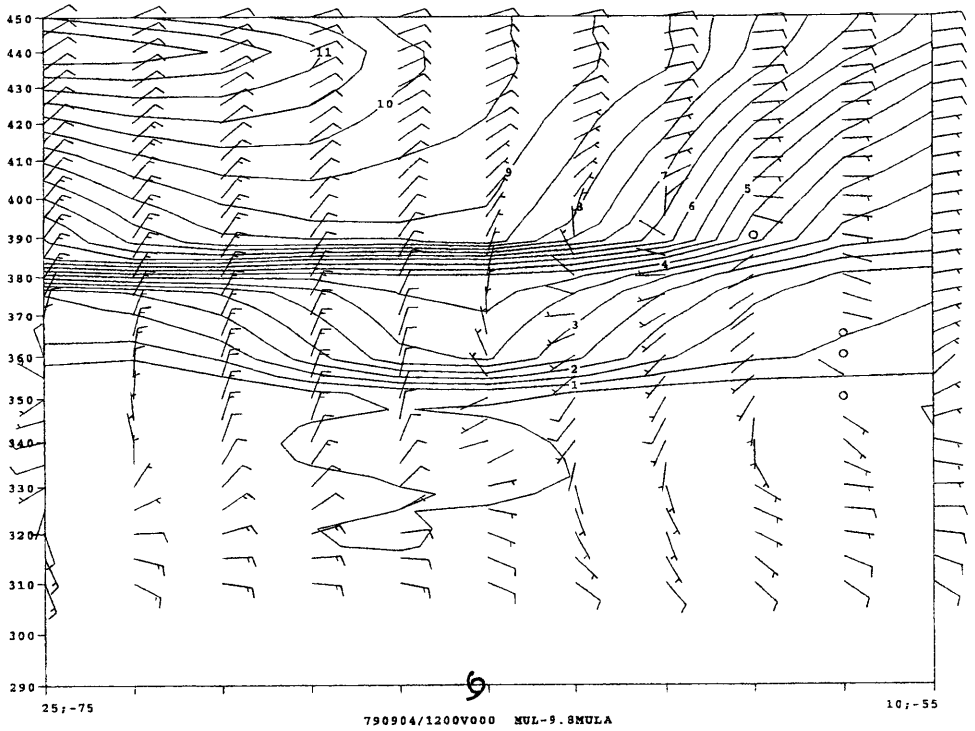

Figure 3.36: (b) 1200UTC 4 September;

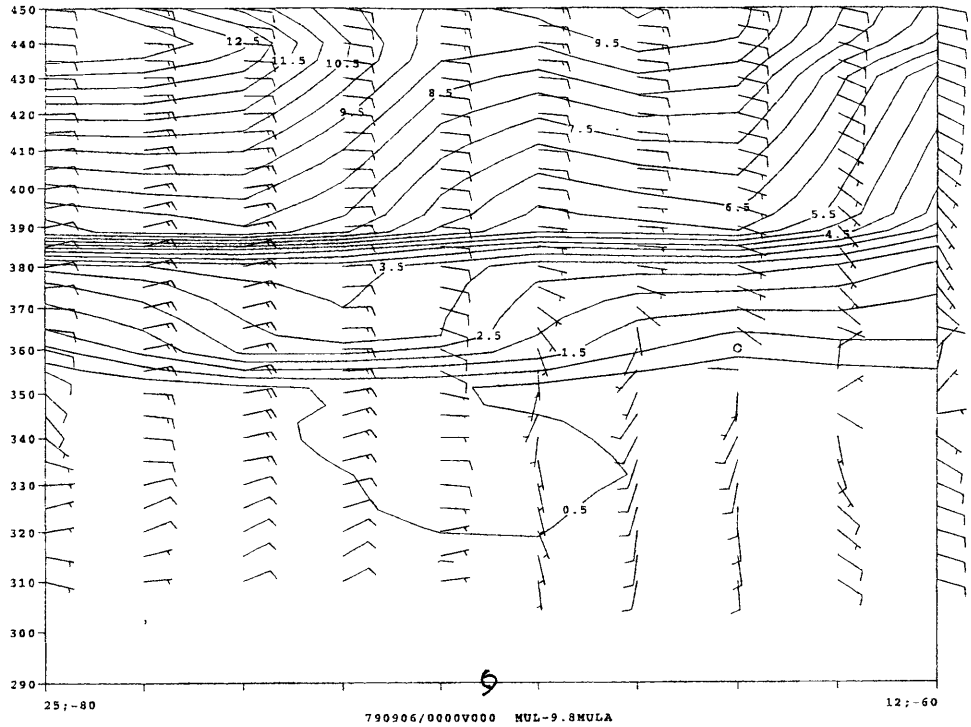

Figure 3.36: (c) 0000UTC 6 September;

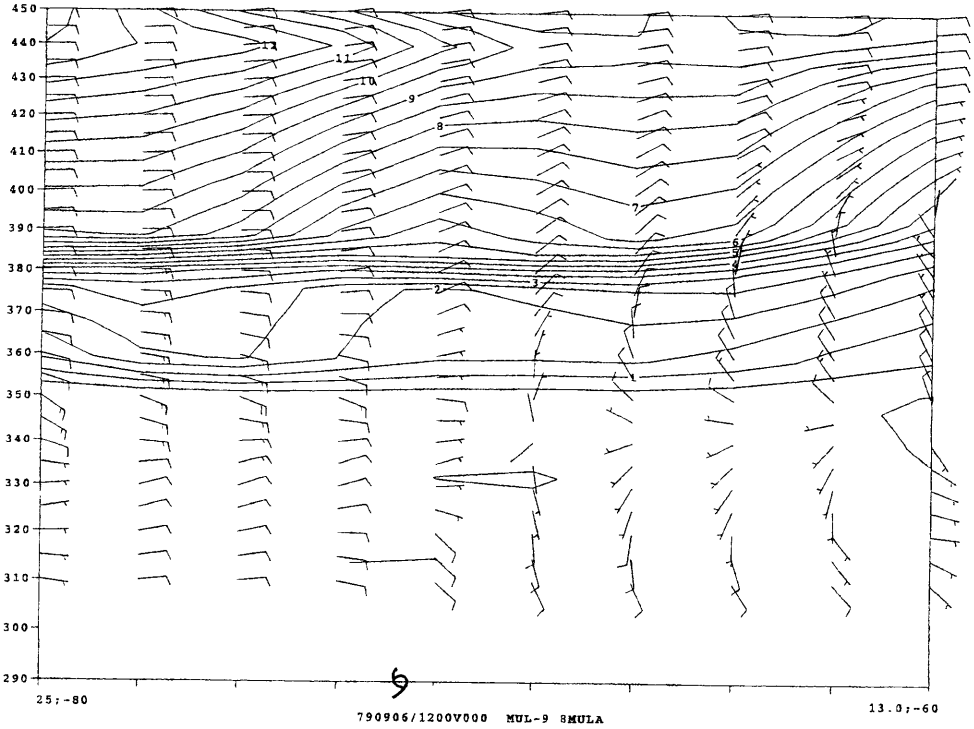

Figure 3.36: (d) 1200UTC 6 September;

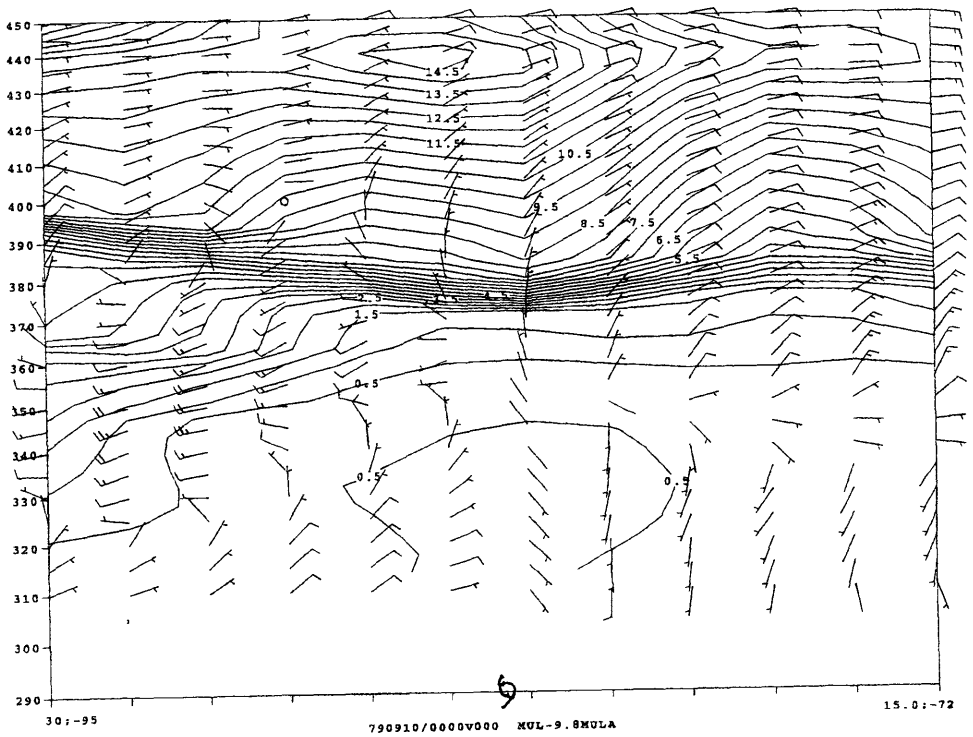

Figure 3.36: (e) 0000UTC 10 September;

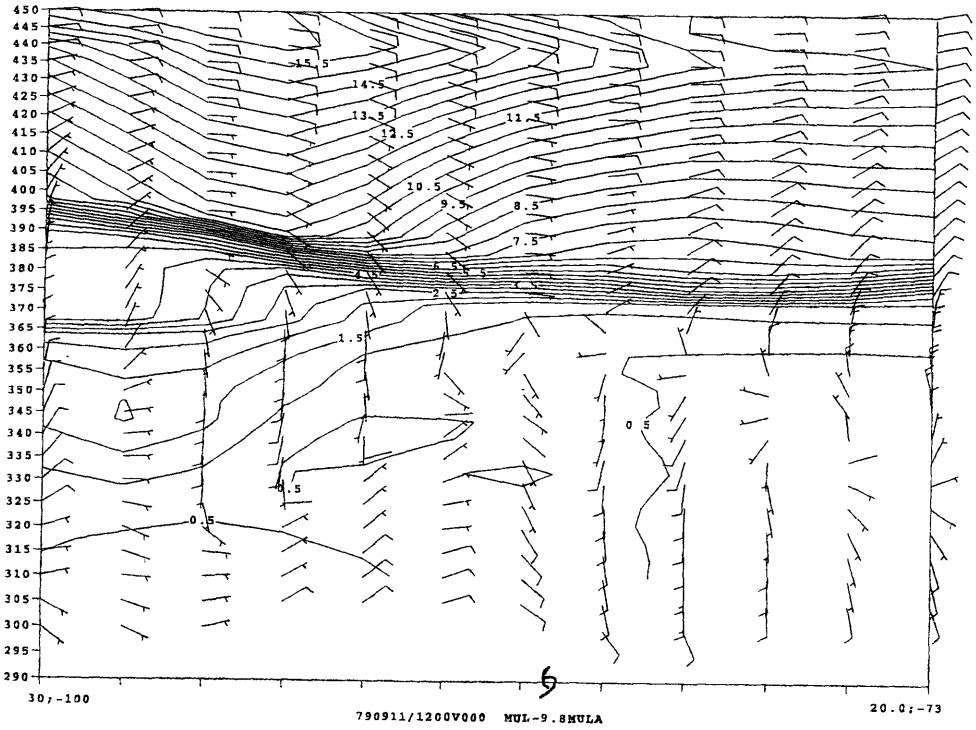

Figure 3.36: (f) 1200UTC 11 September.

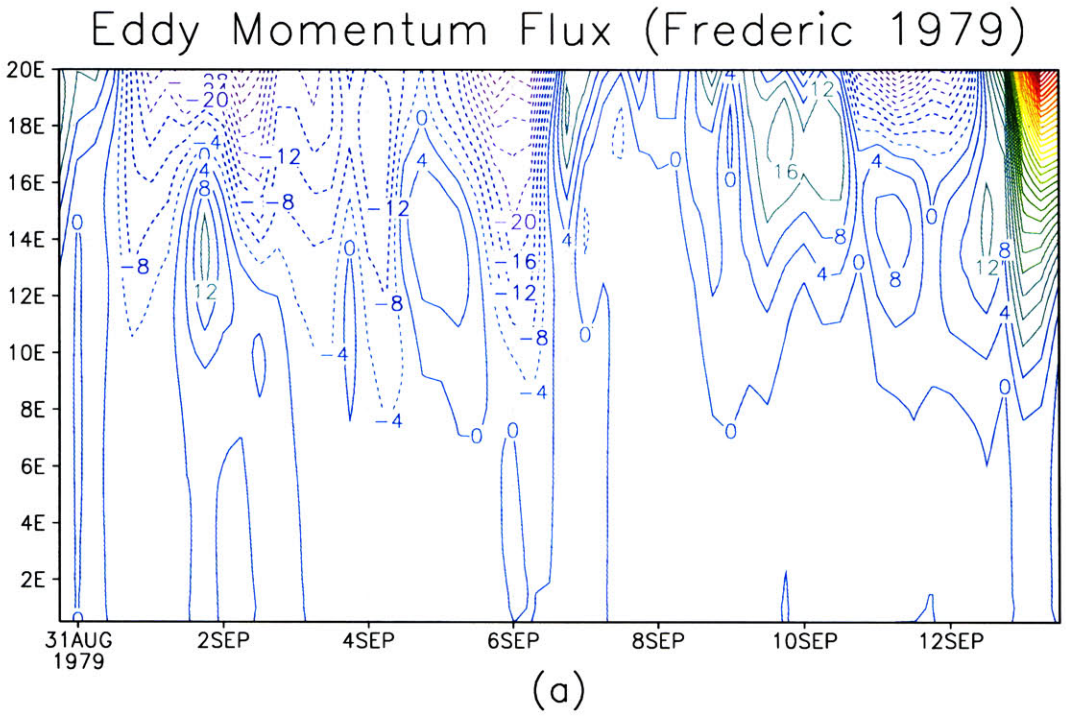

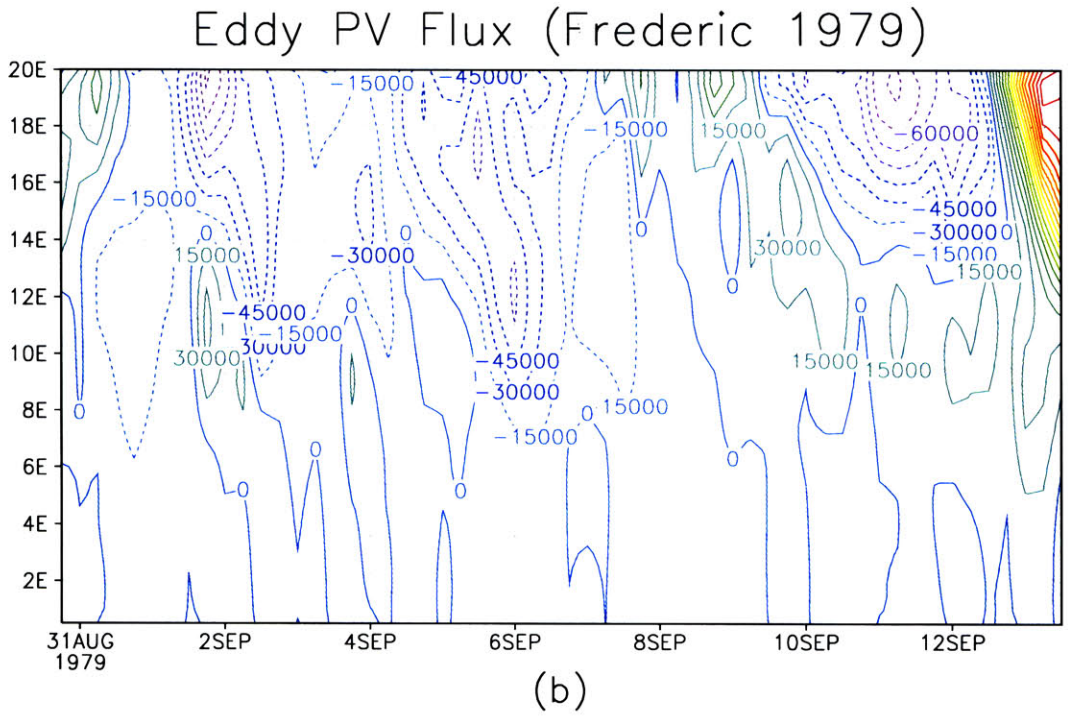

Figure 3.37: Radius-time series of (a) eddy relative angular momentum fluxes ($10^{17} kgm^2 s^{-2}$) and (b) eddy PV fluxes (mK) for Frederic of 1979. The calculation is based on the NNRA dataset.

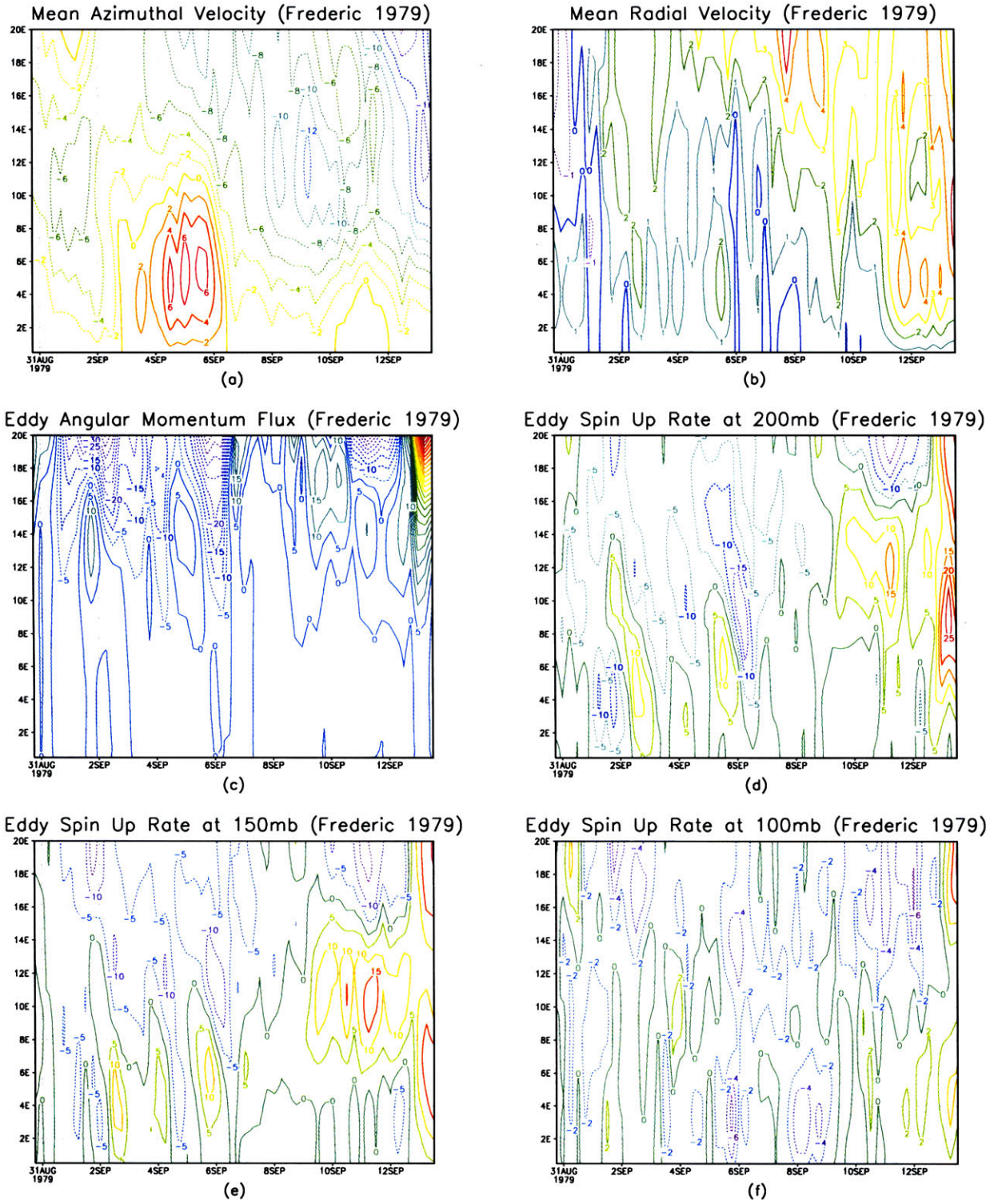

Figure 3.38: Radius-time series of mean (a) azimuthal velocity (m/s) and (b) radial velocity (m/s) at 200mb, (c) eddy relative angular momentum fluxes ($10^{17} kgm^2 s^{-2}$), and eddy spinup rates (m/s/day) at (d) 200mb, (e) 150mb and (f) 100mb for Frederic of 1979. The calculation is based on the NNRA dataset.

Chapter 4

Conclusions

This work attempts to understand the dynamics of the genesis of concentric eyewall hurricanes. More specifically, we focus on the effects of external eddy forcing associated with upper-level wave asymmetries in the environment of tropical cyclones, and through what processes these effects can be achieved. Our approach is a combination of numerical modeling and observational case studies. We have made use of two numerical models, namely a simple two-layer model and a two-dimensional cloud resolving non-hydrostatic model. The latter is called the full physics model for short. Owing to the lack of direct measurements of upper-level atmospheric conditions, we choose to use reanalysis data from NCEP/NCAR and ECMWF. A somewhat lengthy evaluation suggests that both datasets are marginally suitable for case studies of tropical cyclones.

Through our study, we have come to the following conclusions with some discussion:

1. The numerical simulations suggest that the WISHE mechanism plays a critical role in the development of an outer wind maximum. The fundamentals of this mechanism are the augmentation of wind speed-dependent sea-to-air enthalpy transfer above ambient values. Such wind speed-dependent transfer makes possible a positive feedback between an intense vortex-scale flow and the surface fluxes. The importance of the feedback has been borne out convincingly by nu-

merical results from the experiments in which the WISHE is purposely turned off. No disturbance in both models can develop outside the primary eyewall without the positive feedback of the surface wind anomalies and the anomalous surface entropy fluxes.

Randomized experiments with the simple model further suggest that unless the low troposphere is very moist, a sufficiently strong disturbance is necessary for the ultimate formation of a secondary eyewall, which is in accord with the finite-amplitude nature of tropical cyclongenesis. The reason is that the precipitation-induced downdrafts stabilize the outer region, which extends from the radius of maximum winds to an outer radius where azimuthal winds vanish, by depleting the subcloud-layer entropy. This effect is crucial to the development and maintenance of a tropical cyclone. But at the same time it is detrimental to the genesis of concentric eyewall hurricanes. The significance of a moist lower and middle troposphere becomes apparent at this point. If the lower and middle troposphere is moist enough in the simple model, we reduce the cooling effect due to the downdrafts so that disturbances can develop.

The full physics model, however, does not spontaneously produce concentric eyewall hurricanes,even when the initial moisture in the troposphere is increased. Numerical results reveal three unique features which we believe contribute to this. These three features are a relatively quick drain of the initial extra moisture, a remarkable temperature inversion layer at the top of boundary layer of the outer region, and a radial inflow in the upper-middle model troposphere. The overall effect of these features is that the primary eyewall becomes even more stable, while any infinitesimal perturbations dissipate.

In brief, results from the simple and full-physics models suggest that the genesis of concentric eyewall hurricane results from finite-amplitude WISHE instability of the tropical atmosphere.

2. Where can one find the finite-amplitude perturbations that trigger the concentric eyewall cycles? We have proposed that the perturbations are induced by

external factors, for example, tropospheric and low stratospheric environmental forcing. It has been known and accepted in varying degrees that the tropical cyclone environment has a decisive role in the intensity change of the tropical cyclone. After we introduce time varying eddy fluxes of angular momentum after the peak intensity of the model hurricane, we produce concentric eyewall cycles in the full physics model. The cycles like the observed ones in reality. The secondary eyewall contracts and intensifies, while the primary eyewall weakens and dissipates. A significant fluctuation is found in the model hurricane intensity during the eyewall replacement, which is consistent with that of concentric eyewall hurricanes in nature. Note that the time variation of the eddy fluxes is bell-like to mimic the observed eddy flux convergence. Sensitivity tests show that the external forcing should last long enough, be close to the vortex center and the surface, and be broad enough in space.

The working mechanism, illustrated in Fig. 2.17, is that when there is an upper-level trough several hundred kilometers to the west and poleward of a hurricane, as argued by Emanuel (1997), the cyclonic vorticity associated with the trough may project a component to on the surface. This can be accomplished downward along angular momentum surfaces, which function as characteristic surfaces in moist potential vorticity inversion. Once there is a local surface wind maximum, it amplifies through the WISHE mechanism.

In short, the role of the eddy forcing is like the catalyst in a chemical reaction at the beginning. It helps manifest finite-amplitude internal instabilities which themselves are driven by surface enthalpy fluxes later on.

3. According to the results from extensive case studies, a causal relationship does not always exist between environmental forcing and genesis of a secondary eyewall, as suggested by Molinari and his colleagues. The relationship is inconclusive indeed.

   Some cases clearly show the existence of the causal relationship. A few examples are Allen of 1980, Elena of 1985, and Opal of 1995. The characteristic of eddy

PV fluxes in these cases is a pattern of organized maximum eddy fluxes shifting inward toward the inner core of the storm before the first observational report of an outer wind maximum. On the other hand, there are some other cases showing no sign of inward shifting of eddy fluxes at all, for example, David of 1979 and Emily of 1993. The eddy PV fluxes in these cases display a pattern of scattered weak positive or negative eddy fluxes before the first appearance of an outer surface wind maximum. We also found some cases having medium strength interaction between hurricanes and their upper-level synoptic environments.

With Frederic's result and results from concentric eyewall hurricanes, we can conclude that the interaction between a tropical cyclone and its upper-level synoptic environment is neither sufficient nor necessary for the genesis and development of concentric eyewall cycles in reality.

4. It is not always true that the interaction will lead to wave-breaking or scale reduction of the upper-level PV trough followed by superposition, as in the case of Opal. In the same case, the strong trough did not weaken the storm. On the other hand, as in Emily's case, the seemingly strong interaction based on IPV maps turns out to be a weak interaction in the eddy PV fluxes. An important lesson is that when studying upper-level interactions, we should not use IPV maps solely. The IPV maps only provide qualitative information on the occurrence of the interaction. The strength of the interaction should be determined quantitatively by the eddy PV fluxes. Indeed two other physical quantities, the Eliassen-Palm flux and its convergence, are more useful than the eddy PV fluxes alone. The E-P flux can tell us the relative importance of eddy momentum flux and eddy heat flux, and its vector can reveal the direction of both eddy fluxes. So these two quantities may help us gain insights into the genesis than the eddy PV flux does. Due to the time limit of this thesis, the author does not calculate the E-P flux and its convergence.

We would like to mention two more issues. The first is that we calculate all our eddy terms in a storm-moving system, as other investigators have. Since Ertel's PV

is Galilean-invariant, we should be able to calculate Ertel's PV independently outside any moving coordinate first. Then we interpolate the PV to a moving cylindrical system and calculate eddy PV fluxes using the left-hand side of Equation 3.12. The eddy radial velocity in the same equation is also made storm relative. The result for Elena's case is shown in Fig. 4.1. This figure also presents the result based on the right hand side of Equation 3.12 for an easy comparison. Without doubt, the results from two methods are totally different. We reach the same conclusion using the ERA dataset. Calculations from ERA is shown in Fig. 4.2. We also compare the results from two calculation methods for other cases and reach the same conclusion. It seems to us that the acceleration of the movement of a hurricane does have considerable impact on the calculation of eddy PV fluxes.

The second issue concerns the use of the PV inversion technique (Davis and Emanuel 1991) to study the effects of upper-level PV anomalies associated with troughs. The technique has proven useful in studying diagnostically synoptic-scale systems based on the distribution and evolution of Ertel's PV anomaly. We tried to use this technique to invert the upper-level PV anomaly to see whether there would be surface wind disturbances due to the anomaly. Since we did not take into account the effects of moisture, we did not find any meaningful results. However, since we do not have a good knowledge of either vertical distribution of latent heating or the observed accumulation of surface precipitation for any of the concentric eyewall hurricanes, we still cannot apply the PV inversion technique usefully. Maybe we can do moist PV inversion in the future.

In this thesis we have found a discrepancy between the results from the full physics model and those from our case studies. This discrepancy does not mean that our numerical results are wrong, since we still have a substantial number of cases to support the conclusions from the full physics model. On the contrary, the discrepancy implies that the nature of the interaction is complex. Numerical simulations by Challa et al. (1998) show that the effect of eddy momentum and heat fluxes depends on the direction of the water vapor transport into or out of the vortex core. Also the discrepancy suggests that there exist other mechanisms for eyewall genesis, for

example, the interaction between a tropical cyclone and its underlying ocean.

It is well known that tropical cyclones climatologically develop only over warm oceans with sea surface temperature (SST) of 26°C or higher. The maximum hurricane intensity is very sensitive to SST. The interaction between a tropical cyclone and the ocean underneath consists of positive and negative feedbacks. The positive feedback is the mutual enhancement between surface heat and moisture fluxes and the storm's surface wind, which is the WISHE mechanism. The negative feedback is the deepening of the ocean mixed layer due to the increased surface wind stress with the storm's intensification. The deepening is due to turbulent mixing, which is the primary mechanism for the SST decrease. The decrease of SST then reduces the surface fluxes from ocean to atmosphere. As a result, the storm's intensity decreases. This might, to some extent, help the development of disturbances in the outer region.

Another possible mechanism is the tilting of the low-level PV associated with tropical cyclones. The slant is present in the cross-sections of all four cases we have discussed in the previous chapter. The slant is caused by the environmental vertical shear. In Gloria's case, we have seen the PV of the inner core is as large as 40 PVU (Fig. 1.13b). So when there is a tilting of such high PV inner core, we can imagine that the cyclonic vorticity associated with the PV anomaly, defined as the deviation from the azimuthally averaged PV at a certain radius, may project a component down to the ocean surface. The cyclonic vorticity can also be brought down by convective downdrafts. The surface wind disturbance then intensifies through with the WISHE mechanism. But if the vertical shear is strong, the initial surface wind disturbance may not develop, as is true in the case of tropical cyclongenesis. One simple way to test this hypothesis is to identify in which quadrant an outer wind maximum is first observed. This might be difficult since it requires continuous surveillance of all possible candidates from the beginning. Another way would be by using a three-dimensional numerical model to examine this hypothesis.

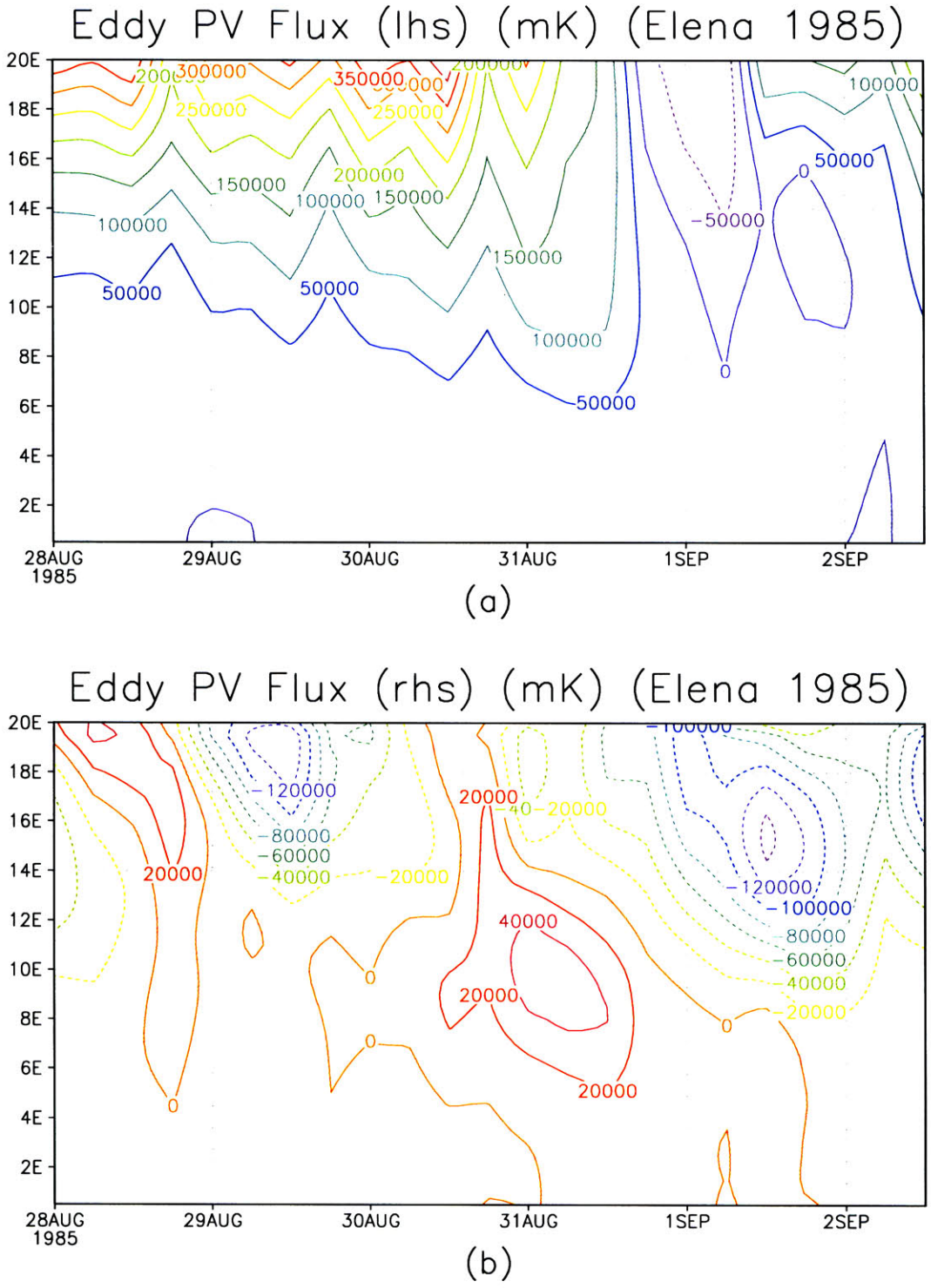

Figure 4.1: Radius-time series of eddy PV fluxes (mK) for Elena of 1985. The fluxes are calculated using (a) the left hand side of Equation 3.12, and (b) the right hand side of Equation 3.12. The calculation is based on the NNRA dataset.

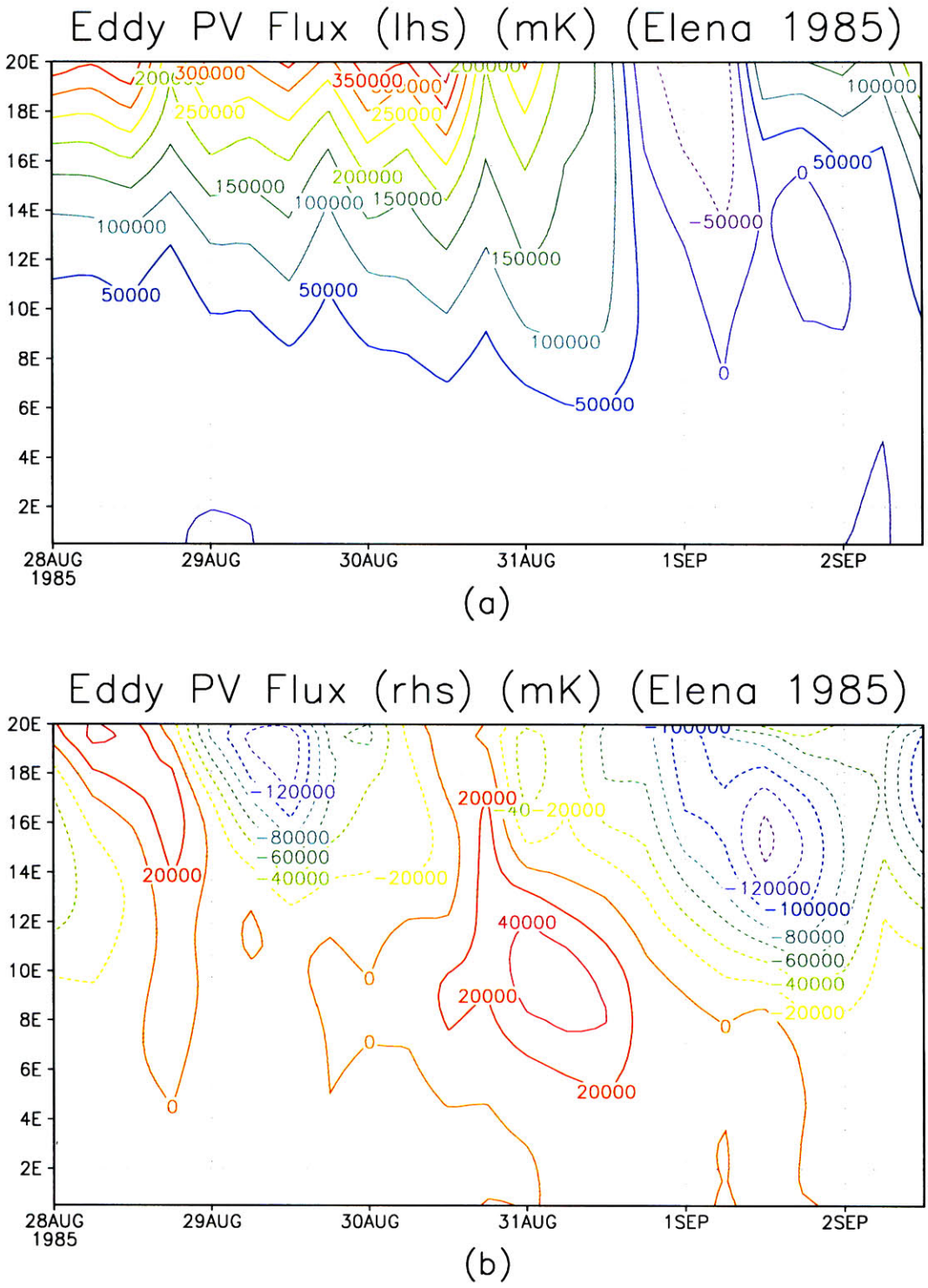

Figure 4.2: As in Fig. 4-1 but the calculation is based on the ERA dataset.

Bibliography

[1] Benjamin, S. G., and N. L. Seaman, 1985: A simple scheme for objective analysis in curved flow. *Mon. Wea. Rev.* **113**, 1184-1198.

[2] Bennetts, D. A., and B. J. Hoskins, 1979: Conditional symmetric instability — a possible explanation for frontal rainbands. *Quart. J. Roy. Meteor. Soc.* ,**105**, 945-962.

[3] Bister, M., 1996: Development of tropical cyclones from mesoscale convective systems. Ph.D.thesis, 112pp., Massachusetts Institute of Technology, Cambridge.

[4] Black, M. L. and H. E. Willoughby, 1992: The concentric eyewall cycle of Hurricane Gilbert. *Mon. Wea. Rev.* , **120**, 947-957.

[5] Bosart, L. F., and J. A. Bartlo, 1991: Tropical storm formation in a baroclinic environment. *Mon. Wea. Rev.* **119**,1979-2013.

[6] Burpee, R.W., S.D. Aberson, P.G. Black, M.Demaria,J.L. Griffin, S.H. Houston, J. Kaplan, S.J. Lord, F.D. Marks Jr., M.D. Powell, and H. Willoughby, 1994: Real-time guidance provided by NOAA's hurricane research division to forecasters during Emily of 1993. *Bull. Amer. Met. Soc.* **75**, 1765-1783.

[7] Challa, M., and R. L. Pfeffer, 1990: Formation of Altantic hurricanes from cloud clusters and depressions. *J. Atmos. Sci.* **47**, 909-927.

[8] —, —, Qiang Zhao, and Simon W. Chang, 1998: Can eddy fluxes serve as a catalyst for Hurricane and Typhoon formation?. *J. Atmos. Sci.* **55**, 2201-2219.

[9] Craig, G. C., 1996: Numerical experiments on radiation and tropical cyclones. *Quart. J. Roy. Meteor. Soc.* **122**, 415-422.

[10] Davis, C. A., and K. Emanuel, 1991: Potential vorticity diagnostics of cyclogenesis. *Mon. Wea. Rev.* **119**, 1929-1953.

[11] DeMaria, M.,J. -J. Baik, and J. Kaplan 1993: Upper-level eddy angular momentum fluxes and tropical cyclone intensity change. *J. Atmos. Sci.* **50**, 1133-1147.

[12] Derber, J. D., D. F. Parrish, and S. J. Lord, 1991: The new global operational analysis system at the National Meteorological Center. *Wea. Forecasting*, **6**, 538-547.

[13] Dvorak, V. F., 1984: Tropical cyclone intensity analysis using satellite data. *NOAA Tech. Rep.*, NESDIS 11, 47pp.

[14] Eliassen, A., 1951: Slow thermally or frictionally controlled meridional circulation in a circular vortex. *Astrophys. Norv.*, **5**, 19-60.

[15] Emanuel, K. A., 1979: Inertial instability and mesoscale convective systems. Part 1: Linear theory of inertial instability in rotating viscous fluids. *J. Atmos. Sci.* **36**, 2425-2449.

[16] —, 1989: The finite-amplitude nature of tropical cyclogenesis. *J. Atmos. Sci.* , **46**, 3431-3456.

[17] —, 1993:The effects of convective response time on WISHE modes. *J. Atmos. Sci.* , **50**, 1763-1775.

[18] —, and J.D. Needlin, and C.S.Bretherton, 1994: On large-scale circulations in convecting atmospheres.*Quart. J. Roy. Meteor. Soc.* , **120**, 1111-1143.

[19] — et al., 1995a: Report of the first prospectus development team of the U.S. weather research program to NOAA and the NSF. *Bull. Amer. Met. Soc.* **76**, 1194-1208.

[20] —, 1995b: The behavior of a simple hurricane model using a convective scheme based on subcloud-layer entropy equilibrium. *J. Atmos. Sci.* , **52**, 3960-3968.

[21] —, 1997: Some aspects of hurricane inner-core dynamics and energetics. *J. Atmos. Sci.* **54**, 1014-1026.

[22] Foley, G. R., 1995: Observations and analysis of tropical cyclones. *Global perspectives on tropical cyclones.* Report No. TCP-38, World Meteorological Organization, Geneva, 289pp.

[23] Fortner, L. E., 1958: Typhoon Sarah, 1956. *Bull. Amer. Met. Soc.* **39**, 633-639.

[24] Gandin, L. S., 1993: Optimal averaging of meteorological fields. NMC Office Note 397, 45pp.[Available from NOAA/NCEP, 5200 Auth Rd., Washington, DC 20233.]

[25] Gray, W. M., 1988: Environmental on tropical cyclones. *Aus. Met. Mag.*, **36**, 127-139.

[26] —, C. Neumann, and T. L. Tsui, 1991: Assessment of the role of aircraft reconnaissance on tropical cyclone analysis and forecasting. *Bull. Amer. Met. Soc.* **72**, 1867-1883.

[27] Grell, G. A., 1993: Prognostic evaluation of assumptions used by cumulus parameterizations. *Mon. Wea. Rev.* **121**, 764-787.

[28] Guard, C. P., 1988: Results of a tropical cyclone accuracy study using polar orbiting satellite data. Office of the Federal Coordinator, Tropical Cyclone Studies Report, FCM-R11-1988, Part 3.

[29] Hawkins, H. F., 1983: Hurricane Allen and island obstacles. *J. Atmos. Sci.* **40**, 1360-1361.

[30] Herbert, P. J., 1980: Atlantic Hurricane season of 1979. *Mon. Wea. Rev.* **108**, 973-990.

[31] Holliday, C. R., 1977: Double intensification of Typhoon Gloria, 1974. *Mon. Wea. Rev.* **105**, 523-528.

[32] Holland, G. J., 1988: Mature Structure and structure change. *A Global View of Tropical Cyclones*, R. L. Elsberry, Ed., Naval Postgraduate School, 13-52.

[33] —, and R. T. Merrill, 1984: On the dynamics of tropical cyclone structural changes. *Quart. J. Roy. Meteor. Soc.* **110**, 723-745.

[34] Holton, J. R., 1992: An introduction to dynamic meteorology. *Academic Press*, 511pp.

[35] Kalnay, E. et. al., 1996: The NCEP/NCAR 40-year reanalysis project. *Bull. Amer. Met. Soc.* **77**, 437-471.

[36] Klemp, J.B., and R. B. Wilhelmson, 1978: The simulation of three-dimensional convective storm dynamics. *J. Atmos. Sci.* **35**, 1070-1096.

[37] Kurihara, Y., 1975: Budget analysis of a tropical cyclone model simulated in a axisymmetric numerical model. *J. Atmos. Sci.* **32**, 25-59.

[38] Lawrence, M. B. and J. M. Gross, 1989: Atlantic hurricane season of 1988. *Mon. Wea. Rev.* **117**, 2248-2259.

[39] Lilly, D.K., 1962: On the numerical simulation of buoyant convection. *Tellus*, **14**, 148-172.

[40] Lin, Y. -L., R. D. Farley, and H. D. Orville, 1983: Bulk parameterization of the snow field in a cloud model. *J. Climate App. Meteor.*, **22**, 1065-1092.

[41] Lord, S. J., H. E. Willoughby, and J. M. Piotrowicz, 1984: Role of a parameterized ice-phase microphysics in an Axisymmetric, nonhydrostatic tropical cyclone model. *J. Atmos. Sci.* **41**, 2836-2848.

[42] —, J. L. Franklin, 1987: The environment of Hurricane Debby (1982). Part I: Winds. *Mon. Wea. Rev.* **115**, 2760-2780.

[43] Mason, P. J., and R. I. Sykes, 1982: A two-dimensional numerical study of horizontal roll vortices in an inversion capped planetary boundary layer. *Quart. J. Roy. Meteor. Soc.* , **108**, 801-823.

[44] Martin, J. D., 1988: Tropical cyclone observation and forecasting with and without aircraft reconnaissance. Dept. Of Atmos. Sci. Paper No. 428. Colo. State Univ., Fort Collins, Colorado, 114pp.

[45] Matthews, E., 1985: Atlas of archived vegetation, land-use and seasonal albedo data sets. NASA Tech. Memo. 86199, 53pp. [Available from Goddard Space Flight Center, Greenbelt, MD 20771.]

[46] Mayfield, M., C. McAdie, and A. Pike, 1988: A preliminary evaluation of the dispersion of tropical cyclone position and intensity estimates determined from satellite imagery. NOAA NHC research paper, 16pp.

[47] McBride, J. L., and R. Zehr, 1981: Observational analysis of tropical cyclone formation. Part II: Comparison of non-developing versus developing systems. *J. Atmos. Sci.* , **38**, 1132-1151.

[48] Merrill, R. T., 1988a: Characteristics of upper-tropospheric environmental flow around hurricanes. *J. Atmos. Sci.* **45**, 1665-1667.

[49] —, 1988b: Environmental influences on hurricane intensification. *J. Atmos. Sci.* **45**, 1678-1687.

[50] Miller, B. I., 1958: On the maximum intensity of hurricanes. *J. Meteor.*, **15**, 184-195.

[51] Molinari, J., and D. Vollaro, 1989a: External influences on hurricane intensity. *J. Atmos. Sci.* , **46**, 1093-1105.

[52] —, and —, 1989b: Interaction of a hurricane with a baroclinic wave. Preprints, *18th Conf. on Hurricane and Tropical Meteorology,* San Diego, CA, Amer. Meteor. Soc. 50-51.

[53] —, and —, 1990: External influences on hurricane intensity. Part 2: Vertical structure and response of the hurricane vortex. *J. Atmos. Sci.* , **47**, 1902-1918.

[54] —, 1992: Environmental controls on eye wall cycles and intensity change in Hurricane Allen(1980). In *Tropical cyclone disasters.* Eds. J. Lighthill, Z. Zhemin, G.Holland and K. Emanuel. Peking University Press, Beijing

[55] —, D. Vollaro, and S. Skubis, 1993: Application of the Eliassen balanced model to real-data tropical cyclones. *Mon. Wea. Rev.*; **121**, 2409-2419.

[56] —, S. Skubis, and D. Vollaro, 1995: External influences on hurricane intensity. Part III: potential vorticity structure. *J. Atmos. Sci.* **52**, 3593-3606.

[57] Montgomery, M. T., and B. F. Farrell, 1993: Tropical cyclone formation. *J. Atmos. Sci.* **50**, 285-310.

[58] Ooyama, K. V., 1987: Scale-controlled objective analysis. *Mon. Wea. Rev.* **115**, 2479-2506.

[59] Orville, H. D., and F.J. Kopp, 1977: Numerical simulation of the history of a hailstorm. *J. Atmos. Sci.* **34**, 1596-1618.

[60] Pan, H. L., and Wan-Shu Wu, 1994: Implementing a mass flux convective parameterization package for the NMC medium-range forecast model. Preprints, *10th Conf. on Numerical Weather Prediction*, Portland, OR, Amer. Meteor. Soc., 96-98.

[61] Parrish, D. F., and J. C. Derber, 1992: The National Meteorological Center's spectral statistical interpolation analysis system. *Mon. Wea. Rev.* **120**, 1747-1763.

[62] Pfeffer, R. L., 1958: Concerning the mechanics of hurricanes. *J. Met.*, **15**, 113-120.

[63] —, and M. Challa, 1981: A numerical study of the role of eddy fluxes of momentum in the development of Atlantic hurricanes. *J. Atmos. Sci.* **38**, 2393-2398.

[64] Raymond, D. J., 1995: Regulation of moist convection over the west Pacific warm pool. *J. Atmos. Sci.* **52**, 3945-3959.

[65] Reilly, D. H., and K. A. Emanuel, 1991: Evidence of upper tropospheric triggering of tropical cyclogenesis. Preprints, *19th Conf. on Hurricanes and Tropical Meteorology*, Miami, FL, Amer. Meteor. Soc., 202-205.

[66] Reynolds, R. W., and T. M. Smith, 1994: Improved global sea surface temperature analyses using optimum interpolation. *J. Climate* **7**, 929-948.

[67] Riehl, H., 1979: Climate and Weather in the Tropics. *Academic Press*, 661.

[68] Rosenthal, S. L., 1978: Numerical simulation of tropical cyclone development with latent heat release by resolvable scales. I: Model description and preliminary results. *J. Atmos. Sci.* **35**, 258-271.

[69] Rotunno, R., and K. A. Emanuel, 1987: An air-sea interaction theory for tropical cyclones. Part II, *J. Atmos. Sci.* **44**, 5542-561.

[70] Sadler, J. C., 1976: A role of the tropical upper tropospheric trough in early season typhoon development. *Mon. Wea. Rev.* **104**, 1266-1278.

[71] Samsury, C. E., and E. J. Zipser, 1995: Secondary wind maxima in hurricane: airflow and relationship to rainbands. *Mon. Wea. Rev. 123*, 3502-3517.

[72] Schubert, W. H., and B. T. Alworth, 1987: Evolution of potential vorticity in a three-layer model. *Quart. J. Roy. Meteor. Soc.* **113**, 147-162.

[73] Shapiro, L. J., and H.E. Willoughby, 1982: The response of balanced hurricanes to local sources of heat and momentum. *J. Atmos. Sci.* **39**,378-394.

[74] —, and J.L. Flanklin, 1995: Potential vorticity in Hurricane Gloria. *Mon. Wea. Rev.* **123**, 1465-1475.

[75] Sheets, R. C., 1985: Hurricane tracking using a mass field envelop approach-impacts of forecast tracks. Extended Abstracts Volume, *16th Conf. on Hurricanes*

and Tropical Meteorology, 14-17 May 1985, Houston, Texas, Amer. Meteor. Soc., 38-40.

[76] Thrope, A. J., 1985: Diagnosis of balanced vortex structure using potential vorticity. *J. Atmos. Sci.* **42**, 397-406.

[77] Thorncroft, C. D., B. J. Hoskins, and M. E. McIntyre, 1993: Two paradigms of baroclinic-wave life-cycle behavior. *Quart. J. Roy. Meteor. Soc.* **119**, 17-55.

[78] Willoughby, H. E., 1979: Excitation of spiral bands in hurricane by interaction between the symmetric mean vortex and a shearing environmental steering current. *J. Atmos. Sci.* **36**, 1226-1235.

[79] —, and J. A. Clos, and M. G. Shoreibah, 1982: Concentric eyewalls secondary wind maxima, and the evolution of the hurricane vortex. *J. Atmos. Sci.* ,**39**, 395-411.

[80] —, H-L. Jin, S.J. Lord and J. M. Piotrowicz, 1984: Hurricane structure and evolution as simulated by an axisymmetric, nonhydrostatic numerical model. *J. Atmos. Sci.* ,**41**, 1169-1186.

[81] —, 1988: The dynamics of the tropical cyclone core. *Austr. Meteor. Mag.* , **36**, 183-192.

[82] —, 1990: Temporal changes of the primary circulation in tropical cyclones. *J. Atmos. Sci.* ,**47**, 242-264.

[83] —, P. G. Black, 1996: Hurricane Andrew in Florida: Dynamics of a Disaster. *Bull. Amer. Met. Soc.* **77**, 543-549.